Seasonal Variation of Atmospheric Muons in KM3NeT Detectors

Exploring the Connection Between Atmospheric Temperatures and Muon Flux Detected in KM3NeT's ORCA and ARCA Detectors

Cas Hahnraths

Delft University of Technology

TU Delft

Seasonal Variation of Atmospheric Muons in KM3NeT Detectors

Exploring the Connection Between Atmospheric Temperatures and Muon Flux Detected in KM3NeT's ORCA and ARCA Detectors

by

Cas Hahnraths

to obtain the degree of Master of Science

at the Delft University of Technology, in the KM3NeT group at Nikhef,

to be defended publicly on Monday January 23, 2025 at 14:00.

Student number:	4894367	
Project duration:	May 1, 2024 – January 1, 2025	
Thesis committee:	Dr. E. J. Buis,	TU Delft, supervisor
	Ir. R. A. Verzijlbergh,	TU Delft
	Dr. R. Bruijn,	University of Amsterdam and Nikhef, supervisor

Cover: Air showers by Ars Electronica (Thomas Bergauer) [1]

TU Delft

Summary

In this study, the seasonal variation of atmospheric muons detected by the KM3NeT ORCA and ARCA detectors is investigated. Both detectors are still under construction; therefore, only specific configurations of the detects are available for analysis. The main focus is on the impact of atmospheric temperatures on the detected muon rate. The muon rates are correlated with the effective atmospheric temperature above the KM3NeT detectors to calculate an effective temperature coefficient (α). The effective temperature is a weighted average over all pressure levels in the raw temperature data sets. In this study, the AIRS and ERA5 temperature datasets are used to calculate two effective temperatures over time. An effective temperature analysis is needed to account for the fact that most muons are produced in the upper parts of the atmosphere. The KM3NeT detectors experience a high degree of background rate. Therefore, not the muon rate gets correlated with the effective temperature but the ratio of the muon rate with the muon rate out of run-by-run Monte Carlo simulation. This simulation should account for all the factors that impact the true muon rate, except for the temperature variation. Multiply approaches are taken to the calculation of the effective temperature coefficient to see the impacts of it. A positive correlation between muon rate and atmospheric temperature has been found for all approaches, but for most detector configurations studied, the correlation is stronger than expected. The analysis remains difficult because of the lack of a multi-year stable dataset. The data set show a decrease in the mean ratio, pointing to some problems with the Monte Carlo simulations. The Monte Carlo simulations probably do not accurately account for all influences on the detected rate such as efficiency losses of the detector and other periodic variations in the rata. In all data sets used in this study, a linear downward trend was found in the ratio data. This trend can be removed, and the effective temperature coefficient can then be recalculated. After detrending, the correlation between the muon rate and atmospheric temperature moves closer to the expected value for most detector configurations, but it still deviates significantly. The linear downward trend can be caused by an overestimation of detector efficiency in the upward direction by the Monte Carlo simulations. In addition to this, in one of the analyses, it is found that the Monte Carlo simulation underestimates the rates for smaller zenith angles and overestimates the rates for larger zenith angles.

Contents

1

Introduction

The atmosphere of the Earth has been studied since ancient times, with one of the first meteorological descriptions dating back to Aristotle, who wrote the book Meteorologica. Since then, a lot has changed in the research on the atmosphere. With inventions such as thermometers, barometers, and weather balloons, our understanding of the atmosphere has greatly increased. Nowadays, these tools together with the computer, radar, and satellites are used to give us an even better understanding of our atmosphere. By combining measurements from all of these instruments, complex models of the atmosphere can be made. These include atmospheric density profiles, which relate temperature to atmospheric densities.

The field of Cosmic Ray Physics started up a bit later. In the early 20th century scientists believed that a constant, low-level radiation, which could be detected at ground level, originated from radioactive materials in the Earth. However, this started to change when Wulf did a series of measurements on the top of the Eiffel Tower in 1909. Wulf expected that the radiation on top of the Eiffel Tower would decrease significantly with the levels found on the ground. However, the decrease was much smaller than expected. In 1912 Victor Hess was inspired by these results and decided to use balloons to measure the radiation at much higher levels. His results clearly showed that radiation increased with altitude, which led him to conclude that the increase in radiation with altitude must come from extraterrestrial sources. He also concluded that the Sun was not a direct source because he found no difference between day- and night-time observations. In 1913 Kolhöster verified and improved Hess' findings [2, 3]. In the figure below, the results of the measurements of Hess and Kolhöster are shown.

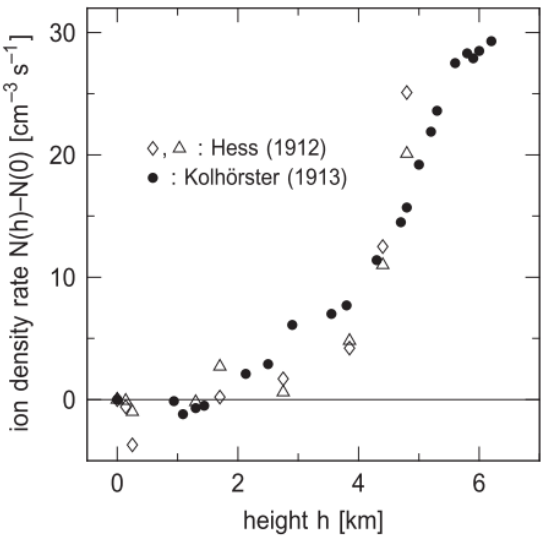

Figure 1.1: Radiation measurements by Hess and Kolhöster using weather balloons [2].

A bit later in 1939, Pierre Auger found that air showers created by primary cosmic rays are extensive, which means that they cover a large area up to hundreds of metres in diameter [4]. Primary cosmic rays are high-energy particles that travel through space. If a primary cosmic-ray particle collides with an atmospheric particle it creates a cascade of reactions creating secondary particles. This process is called an air shower.
In 1952 Barrett et al. did research into the nature and origin of secondary cosmic rays detected far underground. They found that at these depths the predominantly detected particle was the muon, which is a type of meson. The muon has a long lifetime and a low chance of interacting. This causes muons to reach much farther than other components of the air showers. In addition to this, they also found the first clue that the muon intensity varied with atmospheric temperature [5].
Since this first hint of variation of muon intensity with atmospheric temperature, a lot of research has been done on it. The development of more sophisticated detectors and better atmospheric data and models has helped to better investigate the muon intensity variation. Experiments such as IceCube, MINOS, MACRO, NOvA, and Daya Bay have all investigated this phenomenon and helped to better understand cosmic rays and their interaction with the atmosphere [6, 7, 8, 9, 10].

This study will look at the two detectors, ORCA and ARCA, currently under construction by the Cubic Kilometres Neutrino Telescope (KM3NeT) project. The goal of these detectors is to detect neutrinos. Because neutrinos are much harder to detect than muons, the detectors are built at the bottom of the Mediterranean Sea at a depth of around 3 kilometres. The water above the detector will stop the low-energy muons, but the high-energy muons are still able to pass through the water layer and be detected. The goal is to better understand how variations in atmospheric temperature influence high-energy muons detected by the KM3NeT detectors. This is important because these muons are the main background signal for neutrino measurements [11]. The main question of this study is then as follows: How does the muon rate at the KM3NeT ORCA and ARCA detectors correlate with atmospheric temperature?

1.1. Relevance to society

Both neutrino and muon research may seem a bit abstract at first glance, but they do hold a relevance for society. Muon tomography, for example, can be used to inspect cargo for smuggled nuclear materials in a non-invasive way. It can also be used to explore the internal structure of large historical structures such as ancient burial chambers or pyramids. A good example of this was when researchers used muon tomography to discover a large space in the Great Pyramid of Giza and a hidden chamber in the underground Hellenistic necropolis of Neapolis [12, 13]. Cosmic muons can also be used for geology and volcano monitoring. By mapping the variations in volcano density, scientists can get a better idea

of the movement of the magma and identify potential hazards. In general, better understanding of how volcanoes work and monitoring are crucial factors in predicting eruptions. Muons also have industrial applications; for example, they can be used to inspect blast furnaces to improve safety and efficiency. It can also be used in the mining industry to better map mineral deposits and identify hazards [14]. In addition to this, another benefit of KM3NeT research is that many innovations that are made in the development of detectors can later be implemented in other fields that may have a more direct link to society.

Chapter 2 introduces the physical concepts needed to understand cosmic rays and the detection of muons. Chapter 3 focusses on how the atmosphere affects muon production. Chapter 4 presents and explains the temperature data used in the analysis. Chapter 5 gives a detailed overview of the KM3NeT experiment along with its various detector configurations. Chapter 6 describes the experimental methods used to analyse the effect of atmospheric temperature on the muon rate. Chapter 7 presents the results of the analysis. Finally, Chapter 8 discusses the findings, draws a conclusion on the findings, and makes recommendations for future research.

2

From Cosmic Rays to Muon Detection

In this chapter, the theoretical background knowledge needed to understand the expected seasonal variation of the atmospheric muon flux is introduced. The creation of muons is explained by starting with primary cosmic rays. The composition, acceleration, and propagation of the primary cosmic rays are discussed, followed by a discussion of how muons come into existence and how they travel through matter.

2.1. Cosmic ray composition

First shown by Hess in the early 20th century, there is constant radiation coming from extraterrestrial sources hitting Earth's atmosphere, which increases with altitude. The atmosphere forms a protective layer that absorbs most of the energy of the cosmic rays before hitting the Earth's surface. However, if the energy of the primary cosmic ray is high enough, some secondary particles can hit the surface or even go underground [15].

Most of the primary cosmic rays are protons, but they can also be other heavier atoms such as helium, oxygen, or iron. When primary cosmic rays hit the Earth atmosphere, they initiate a particle cascade [16]. Most of the primary high-energy cosmic rays are believed to be created by supernovae, active galactic nuclei, or gamma-ray bursts. For the detection of cosmic rays, different instruments can be used, for example, satellites, balloon experiments, ground-based detectors, or underwater detectors such as ORCA and ARCA. For the ground and underwater detectors, the secondary particles have already travelled through the atmosphere and soil or water, which has to be taken into account in the measurements.

The energy of the primary cosmic rays ranges from a couple of GeV to even more than 10^{20}eV. The higher the energy, the lower the flux (φ). The Earth is constantly being hit by cosmic rays at a rate of about 1000 per square metre per second. In Figure 2.1 the flux of cosmic rays is shown per energy of the primary cosmic ray particle [17].

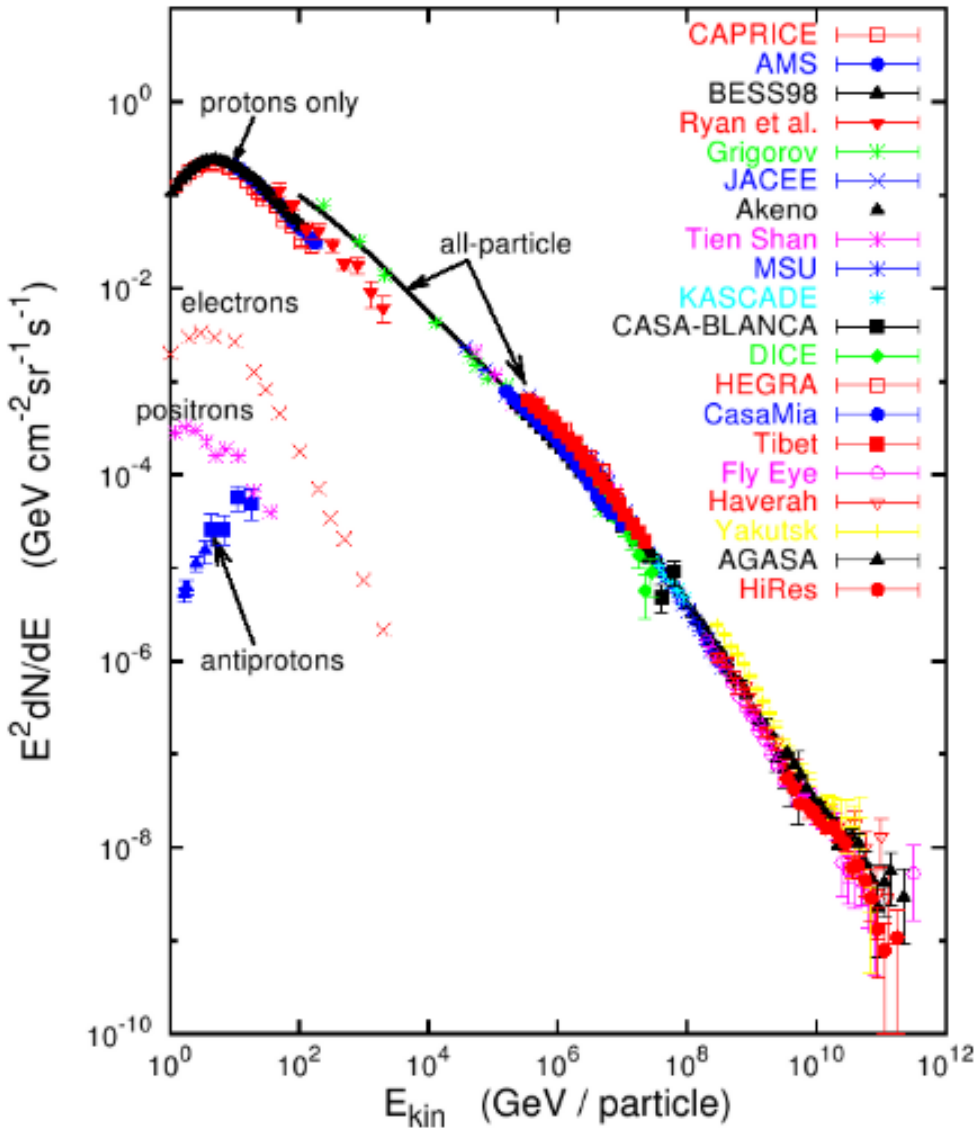

Figure 2.1: Flux of cosmic rays per energy of the primary cosmic ray particle. Different primary particles and experiments are highlighted [17].

The differential flux of cosmic rays can be described by an inverse power law as a function of energy:

$$\frac{dN}{dE} \approx E^{\gamma} \tag{2.1}$$

It should be noted that this is the flux at the top of the atmosphere of the primary cosmic ray. γ is around -2.7 for energies from 10 GeV to around $10^{6.5}$ GeV. Above this energy γ is around -3.1. Above 10^{9} GeV, γ becomes again around -2.7 [17].

Some of the fluxes shown in Figure 2.1 only represent specific particles, such as protons and electrons. These experiments must be conducted outside of the atmosphere of the Earth to capture particles before they interact with the atmosphere. Detectors mounted on balloons or satellites measure both the overall cosmic ray composition and the flux of individual primary particles. For cosmic rays above 10^{5} GeV, the flux is too low for direct measurement of individual particles with such detectors. Instead, ground-based air shower experiments measure the combined flux of all particles. These ground-based detectors capture secondary particles from air showers. Ground-based detectors can distinguish between two main types of air showers: those triggered by photons, electrons, or positrons, and those triggered by heavier particles, such as protons [17].

2.2. Acceleration and propagation of cosmic rays

So far it is not fully understood how the acceleration processes work that give the primary cosmic rays such high energies. It is even not known where the acceleration takes place precisely. However, two possibilities can be considered. The main acceleration of particles occurs either close to the moment of their creation, where they reach maximum energy, or over larger time scales when the particle is travelling through the Galaxy. Solar flares can accelerate particles up to GeV energies, demonstrating acceleration at the point of creation. Planetary shock waves, such as the bow shock of the Earth or the shocks in the solar wind, can also increase the energy of a particle. However, these examples do not explain the higher energies seen in Figure 2.1, suggesting that other sources and mechanisms to accelerate particles also must play a role.
Since local sources, such as the Sun, cannot generate these high energies, higher-energy cosmic rays are thought to come from galactic sources. Cosmic rays with very high energies (above 10^9 Gev) might even be accelerated by active galactic nuclei, gamma-ray bursts, or other powerful astrophysical phenomena [18]. The process that is most likely responsible for the acceleration is the first-order Fermi mechanism. According to this mechanism, strong shock waves, produced by, for example, supernova and active galactic nuclei, create strong magnetic fields. Due to the magnetic field, the particle can be reflected back and forth across the shock front multiple times. In this process, the particle gains a great amount of energy, until it reaches enough energy to escape the shock region [17].

So cosmic rays can be accelerated by a variety of different sources. For particles with energy around MeV and GeV, these sources are relatively nearby, but for higher energy particles (above 10^9 Gev) the sources are believed to be on the scale of the galaxy or an even larger scale. When cosmic rays are detected on Earth the particles have travelled great distances from where they are created and/or accelerated. The direction information we get from the detection on Earth can be used to resolve the processes of the creation and acceleration of the particles. However, this can be difficult if there are material clouds, interstellar magnetic fields, and other obstacles in the path of the cosmic ray that have to be taken into account. When charged particles such as protons and electrons travel through such objects, their path can be altered. The higher the energy, the larger this effect. Neutrinos are created at the same places where cosmic-ray particles are created and/or accelerated. The neutrino, on the other hand, is not affected by such obstacles because it barely interacts with other matter or magnetic fields. However, this makes neutrinos extremely difficult to detect. That is why detectors such as the KM3NeT detectors are built [17].

2.3. Air showers

When cosmic rays hit particles in the atmosphere of the Earth they create air showers. The particles that are created in the air shower can be detected by experiments on Earth. In an air shower, lots of different particles can be created; therefore, detectors need to be specialised for the type of particles they want to detect.

If a primary cosmic-ray particle collides with an atmospheric particle, it creates a cascade of reactions creating secondary particles. This process is called an air shower. There are two different types of air showers. Type one is when a primary cosmic ray particle is a photon, electron, or positron. Type two is when the cosmic ray particle is a proton or a heavier nuclei. If a primary cosmic ray is of type one, the air shower that follows will mainly have an electromagnetic component, electromagnetic showers. If it is a type two primary cosmic ray, the air shower will have three components, electromagnetic, hadronic, and muonic, hadronic showers [18].
The particles that are created in air showers are called secondary particles. These particles can again interact with other particles in the atmosphere or decay. Whether a particle will interact or decay depends on the energy of the particle and the density of the atmosphere. The more interactions away from the initial collision with the cosmic ray, the lower the energy of the particles in the air shower. So, the air shower starts with one cosmic ray particle, then the number of particles quickly increases, and eventually, it will reach a maximum. Then, the number of particles decreases again because the secondary particles have too little energy for further production of particles. The particles then decay further and lose their energy due to radiative and ionisation losses [17]. Figure 2.2 shows how an air shower develops over the depth of the atmosphere. It is clearly shown that first the number of particles

increases and then starts decreasing at some point.

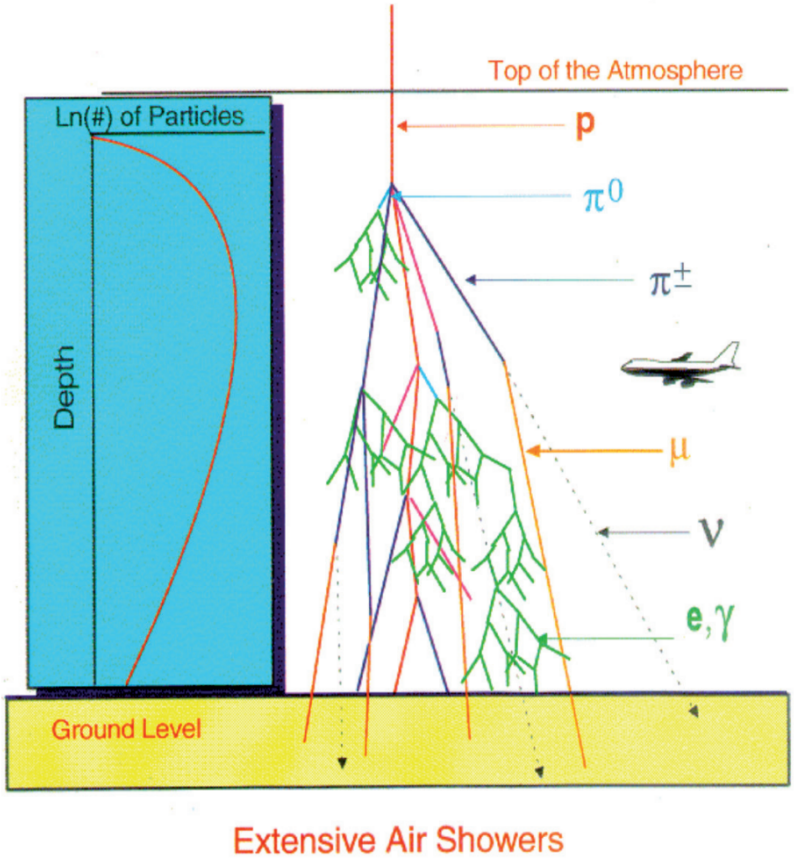

Figure 2.2: Diagram showing the development of air showers [17].

In this study data of the KM3NeT detectors are used which are located at the bottom of the Mediterranean Sea. The muons detected need to travel not only in the atmosphere but also a layer of water and still have enough energy to be detected. Therefore, only high-energy muons can penetrate deep into the water. A consequence of this is that the intensity of the muons decreases the deeper the detector is. This fact is clearly shown in Figure 2.3

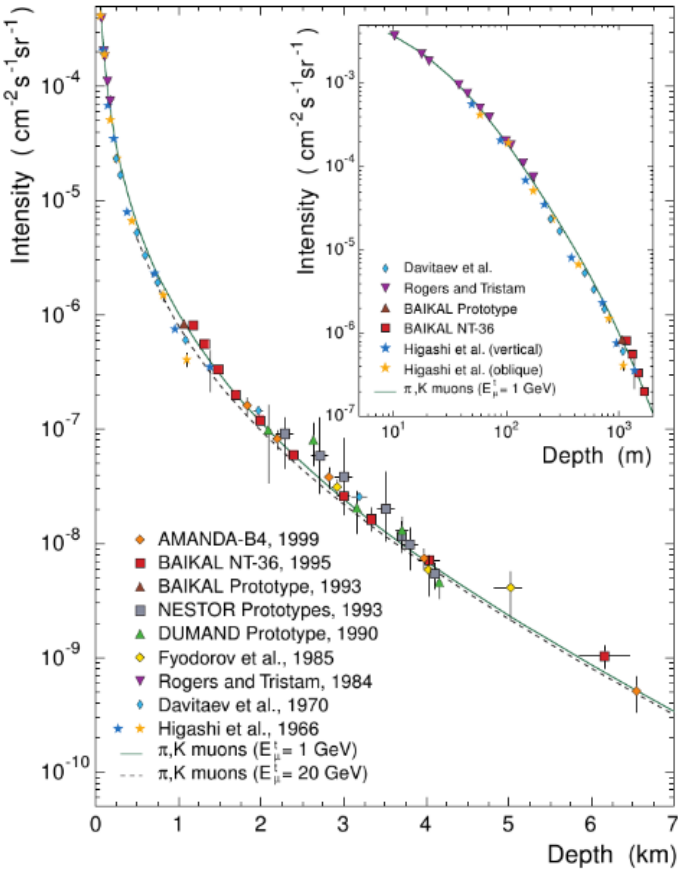

Figure 2.3: Muon intensity vs depth traveled in water for various experiments. [17].

2.3.1. Electromagnetic component

If a high-energy photon interacts with matter in the atmosphere it will create electron and positron pairs, this is called pair production. By a process called Bremsstrahlung, new photons can be created out of these electrons. If these new photons have high enough energy a new pair production will occur. As long as the energy is high enough the number of particles in the electromagnetic component will rapidly grow by the alternating of pair production and bremsstrahlung. If the energies of the electron and positrons fall below the critical energy, they will mainly lose energy through excitation and ionization. At this moment the number of particles will stop growing. When the primary particle of a cosmic ray is a photon, electron, or positron, the electromagnetic is the main component. Air showers from other cosmic ray particles also have this electromagnetic part, however, it is mainly created by high energy hadrons. These hadrons contribute primarily through photons released from the decay of neutral pions (denoted by π). Pions are part of the meson group, which is in itself part of the hadron group. Mesons only consist of one quark and one anti-quark. The neutral pion consist of $u\overline{u}$ or $d\overline{d}$ quarks. This part of the shower ends up holding the largest number of particles overall [18, 17].

2.3.2. Hadronic component

When hadrons such as protons or neutrons interact with molecules in the atmosphere the hadronic component of an air shower is produced. The hadrons produced consist primarily of pions ($\pi^{\pm}, \pi^{0}$) and kaons ($K^{\pm}, K^{0}$), but also protons, neutrons, and other heavier particles. Kaons are also part of the meson group. The charged kaons consist of $u\overline{s}$ quark pair (or $\overline{u}s$ for the anti-kaon). The neutral kaon is made up of either $d\overline{s}$ or $\overline{d}s$. The charged pions consist of $u\overline{d}$ quark pair (or $\overline{u}d$ for the anti-pion). The neutral pions that are formed in the air shower decay again into two photons which will further contribute to the electromagnetic component of the air shower. If the charged pions and kaons decay they will produce muons and neutrinos but they can also interact with other particles in the atmosphere.

The lifetime of a kaon is about $1.238 \cdot 10^8 s$ and the lifetime of a pion is $2.6 \cdot 10^8 s$ [15]. The particles experience time dilation because they travel with high speeds due to their energies. The probability for either interaction or decay depends on the density of the atmosphere and the energy of the pion or kaon. If the density of the atmosphere is higher the particles will encounter more atmospheric particles, thus increasing the change of interaction. If the energy of the particle is lower, they experience less time dilation and thus decay is more probable. If the energy is higher the probability of interaction increases. Because the density of the atmosphere is lower for higher altitudes, more pions, and koans will decay at higher altitudes. At lower altitudes, they are more likely to interact due the the increased density [18, 17]. In Chapter 3 the decay and interaction will be explained in more detail.

2.3.3. Muonic component

When the pions and kaons of the hadronic component decay they will create muons (denoted by μ) which form the muonic component of the air shower. The decay modes of the pions and kaons are shown in Formula 2.2.

$$\begin{aligned} K^{\pm} &\rightarrow \mu^{\pm} + \nu_{\mu} \\ K^{\pm} &\rightarrow \pi^{\pm} + \pi^{0} \\ K^{0} &\rightarrow \pi^{+} + \pi^{-} \\ K^{0} &\rightarrow \pi^{0} + \pi^{0} \\ \pi^{\pm} &\rightarrow \mu^{\pm} + \nu_{\mu} \\ \pi^{0} &\rightarrow \gamma\gamma \end{aligned} \tag{2.2}$$

Muons experience less scattering and energy loss than electrons in the atmosphere because they are heavier, this allows them to penetrate deeper than other components of the air shower and even reach underground detectors [18, 17]. The lifetime of a muon is $2.198 \cdot 10^6 s$, which is significantly longer than both the lifetime of a pion and a koan [15].

2.3.4. Slant depth

The slant depth is an important parameter to understand the air showers in the atmosphere. Slant depth is a measure of the amount of material traversed by a particle along its path. It is such an important parameter because the decay and interaction of particles depend on the amount of material they encounter and not only the distance travelled. In Figure 2.4 a schematic drawing is shown which will be used to explain some definitions related to the slant depth.

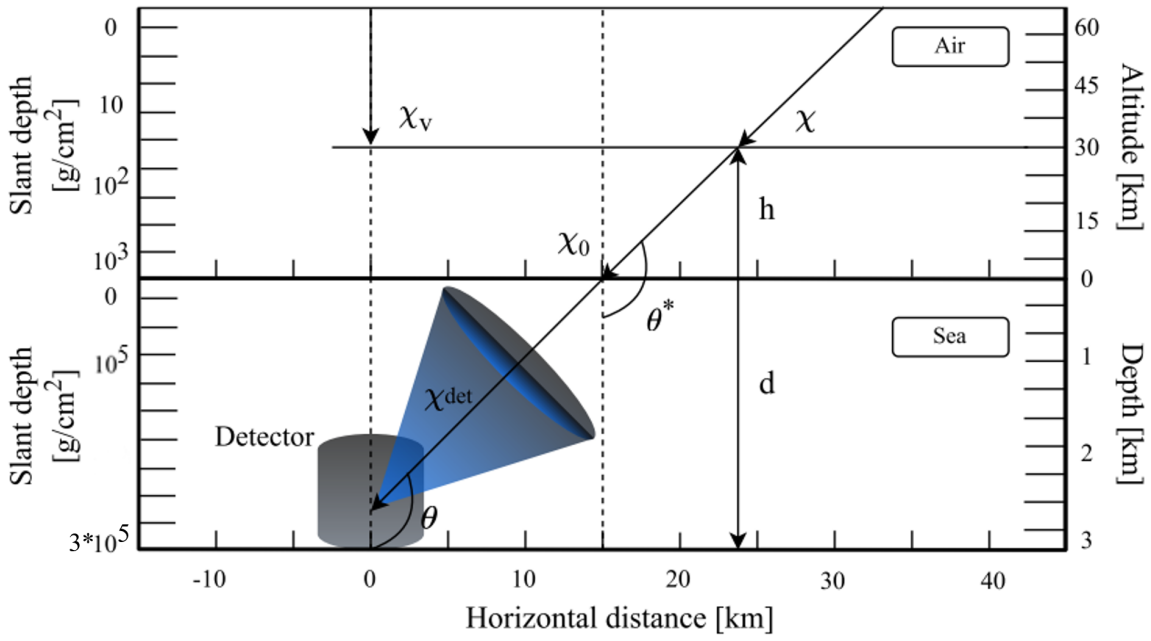

Figure 2.4: Schematic drawing of definitions of slant depth, angles, and distances. $\theta \approx \theta^*$ because the scattering of the water is assumed to be negligible. Slant depth is plotted on the left axis and altitude or depth on the right axis [19].

θ is the zenith angle in the sea. In this study, θ will be defined so that $\theta = 0$ ($\theta = 0°$) is straight up and $\theta = \pi$ ($\theta = 180°$) is straight down. $\theta \approx \theta^*$ because the scattering of the water is assumed to be negligible. Another assumption that will be made is the flat Earth approximation. This means that $0.64\pi \leq \theta < \pi$ ($115° \leq \theta < 180°$) [15]. By doing this we can rewrite the general relation between vertical altitude h as follows:

$$h = -l\cos(\theta) + \frac{1}{2}\frac{l^2}{R_\oplus}\sin^2(\theta) \approx -l\cos(\theta) \tag{2.3}$$

In Equation 2.3 l is the path length and $R_\oplus$ the radius of the Earth. The slant depth for any material can then be written as:

$$X = \int_l^\infty \rho \left[h = -l\cos(\theta) + \frac{1}{2}\frac{l^2}{R_\oplus}\sin^2(\theta)\right] dl \tag{2.4}$$

Using again the flat Earth approximation this can be written as:

$$\rho = \frac{-\chi\cos(\theta)}{h_0} \tag{2.5}$$

h_0 is the scale height defined as $h_0 = \frac{RT}{Mg} = 29.62m/K * T$, where R is the universal gas constant, M is the molar mass and g is the gravitational constant.
The pressure at vertical depth χ_v is $P = g\chi_v$, so at the top of the atmosphere both the pressure and the vertical depth are zero [15].

2.4. Muon production spectrum

The muon production spectrum $P_\mu(E_\mu, \theta, \chi)$ describes the number of muons created per unit of energy E_μ, per zenith angle θ, and per slant depth χ. The muon production spectrum consists of two components, because pions and kaons both have decay modes leading to muons. This is an analytical approximation where the assumed is that only pion and kaon decay leads to muons; in reality there may be other decay modes leading to muons. The total spectrum can be given as:

$$P_\mu(E_\mu, \theta, \chi) = P_\mu^\pi(E_\mu, \theta, \chi) + P_\mu^K(E_\mu, \theta, \chi) \tag{2.6}$$

The high energy approximation can be written as [15]:

$$\begin{aligned} P_\mu(E_\mu,\theta,\chi) \approx N_0(E_\mu) &\frac{\epsilon_\pi}{-\chi\cos\theta\, E_\mu}\frac{1-r_\pi^{\gamma+2}}{(1-r_\pi)(\gamma+2)}\frac{Z_{N\pi}}{1-Z_{NN}}\frac{\Lambda_\pi}{\Lambda_\pi-\Lambda_N}\left(e^{-\chi/\Lambda_\pi}-e^{-\chi/\Lambda_N}\right) \\ &+ 0.635\,\frac{\epsilon_K}{-\chi\cos\theta\, E_\mu}\frac{1-r_K^{\gamma+2}}{(1-r_K)(\gamma+2)}\frac{Z_{NK}}{1-Z_{NN}}\frac{\Lambda_K}{\Lambda_K-\Lambda_N}\left(e^{-\chi/\Lambda_K}-e^{-\chi/\Lambda_N}\right). \end{aligned} \tag{2.7}$$

Equation 2.7 consists of the following components:

1. $N_0(E_\mu)$: the initial flux of cosmic rays at slant depth $\chi = 0$.
2. $\frac{\epsilon_i}{-\chi\cos\theta E_\mu}$ with $i = \pi, K$: this term represents one over the decay length, or $\frac{1}{d_i}$.
3. $\frac{1-r_i^{\gamma+2}}{(1-r_i)(\gamma+2)}$ with $i = \pi, K$; where $r_i = \frac{m_\mu^2}{m_i^2}$ denotes the mass ratios and γ is the spectral index, with $\gamma = 1.7$. This term summarises the meson decay kinematics.
4. $\frac{Z_{N,i}}{1-Z_{N,N}}$ with $i = \pi, K$: describes the probability of creating a particle i when a nucleon N collides with the air. The spectral weighted moments $Z_{N,i}$ and $Z_{N,N}$, describing $N+\text{air} \to i$ and $N+\text{air} \to N$, respectively, depend on the simulated hadronic interaction models.
5. $\frac{\Lambda_i}{\Lambda_i-\Lambda_N}$ with $i = \pi, K$: similar to (4), but this term applies to the decay of pions and kaons. The attenuation length Λ_i depends on the energy and the specific interaction models.
6. $\left(e^{-\chi/\Lambda_i}-e^{-\chi/\Lambda_N}\right)$ with $i = \pi, K$: describes the exponential decrease in production as a function of χ, since most muons are generated in the upper atmosphere.

This high-energy approximation holds when $E\cos\theta > \epsilon_\pi$ and $E\cos\theta > \epsilon_K$, where ϵ is the critical energy at which the decay and interaction probabilities are equal. For pions, $\epsilon_{\pi^\pm} = 115\,\text{GeV}$, and for charged kaons, $\epsilon_{K^\pm} = 850\,\text{GeV}$. Later, it will become evident that muons reaching the detectors (and passing selection criteria) require a higher minimum energy than the critical energy of both pions and kaons at sea level. Therefore, the high-energy approximation is allowed [15].
The high-energy approximation of the total spectrum only gives the number of muons produced. To obtain the flux at sea level, the energy loss, decay, and interaction probabilities need to be taken into account. Using the high energy approximation, it's possible to estimate the flux at sea level for muon energies above 200 GeV [15]:

$$\frac{dN_\mu}{dE_\mu} = \int_0^\infty P_\mu(E_\mu,\theta,\chi)d\chi \approx 0.14E_\mu^{-2.7}\left(\frac{1}{1+\frac{1.11E_\mu\cos(\theta)}{\epsilon_\pi}}+\frac{0.054}{1+\frac{1.11E_\mu\cos(\theta)}{\epsilon_K}}\right) \tag{2.8}$$

The muon intensity can then be written as the integral of the flux [15]:

$$I_\mu = \int_{m_\mu c^2}^\infty \frac{dN_\mu}{dE_\mu}dE_\mu \tag{2.9}$$

2.5. The passage of muons through matter

When particles move through matter such as water or air, they lose energy through different mechanises. For muons, this is not different. However, muons lose relatively small amounts of energy when travelling through matter. This has a couple reasons, but the main two reasons are that muons are leptons, which means they do not interact via strong interactions, which limits their energy loss. The second reason is that the muon has a relatively high mass, which limits radiative losses due to bremsstrahlung. Due to relatively small energy losses, muons can penetrate deep underground and thus reach underground detectors [15].

Muons lose energy through ionisation and radiative processes. The ionisation loss rate is nearly constant. The radiative process can be separated into three parts, bremsstrahlung, pair production, and hadronic interactions. The energy loss for high energy muons can be approximated by [15]:

$$\frac{dE}{d\chi} = -a(E) - E\times\{b_{\text{brem}}(E)+b_{\text{pair}}(E)+b_{\text{hadr}}(E)\} \tag{2.10}$$

In Equation 2.10, $a\ [GeV \cdot cm^2/g]$ is the ionisation energy loss parameter, and the parameters $b\ [cm^2/g]$ are radiative energy loss parameters for bremsstrahlung, pair production and hadronic interactions, respectively. In Figure 2.5 the change in the loss parameters in fresh water and in dry air at 1 atm is shown against the muon energy [20].

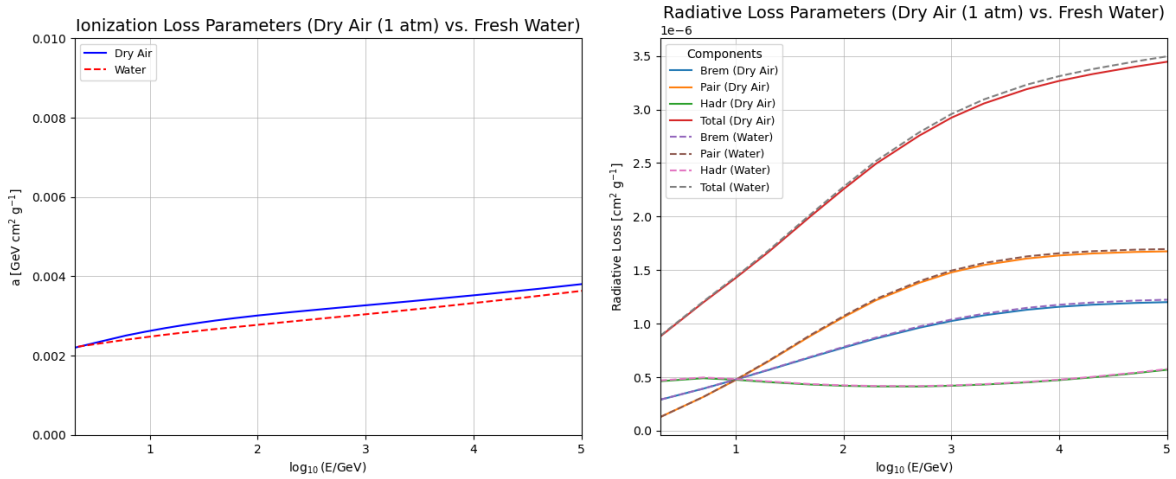

Figure 2.5: Energy loss of a muon in liquid water and dry air due to ionization (left) and radiative processes (right). Values taken from [20].

Equation 2.10 can be solved numerically using the varying loss parameters or analytically if a constant approximation is done for the loss parameters. The analytical solution for constant loss parameters is:

$$\langle E(\chi) \rangle = \left(E_0 + \frac{a}{b} \right) e^{-\chi \cdot b} - \frac{a}{b} \tag{2.11}$$

E_0 is the initial energy of the muon before traversing through the medium so at $\chi = 0$. The minimal energy of a muon in order to reach a slant depth χ can be calculated as followed:

$$\begin{aligned} \langle E(\chi) \rangle &= \left(E_0^{\text{min}} + \frac{a}{b} \right) e^{-\chi \cdot b} - \frac{a}{b} = 0 \\ E_0^{\text{min}} &= \frac{a}{b} \left(e^{\chi \cdot b} - 1 \right) \end{aligned} \tag{2.12}$$

rewriting Equation 2.12 gives the penetrating range equation

$$\chi = \frac{1}{b} \cdot ln \left(1 + \frac{E_0^{\text{min}}}{a/b} \right) \tag{2.13}$$

In order for muons to reach the KM3NeT detectors, they first need to travel through the atmosphere and then the water of the Mediterranean Sea. In Figure 2.6 the maximum reach χ of a muon with energy $E_0(\chi = 0)$ in the air is shown. In Figure 2.7 the same is shown, but now for muons in water. The solid grey line is the numerical solution of Equation 2.10. The dashed lines are the analytical solutions with constant loss parameters (Equation 2.13). On the right y-axis, the average geometric depth is shown. Although the ionisation and radiative loss parameters for water and air are very similar, muons travel much further in the atmosphere than in water for the same slant depth χ. This is because the density of the atmosphere is much lower than the density of water. The conversion from slant depth to average depth is not constant. This is due to changes in the density of the material, for example, caused by changes in temperature or salinity.

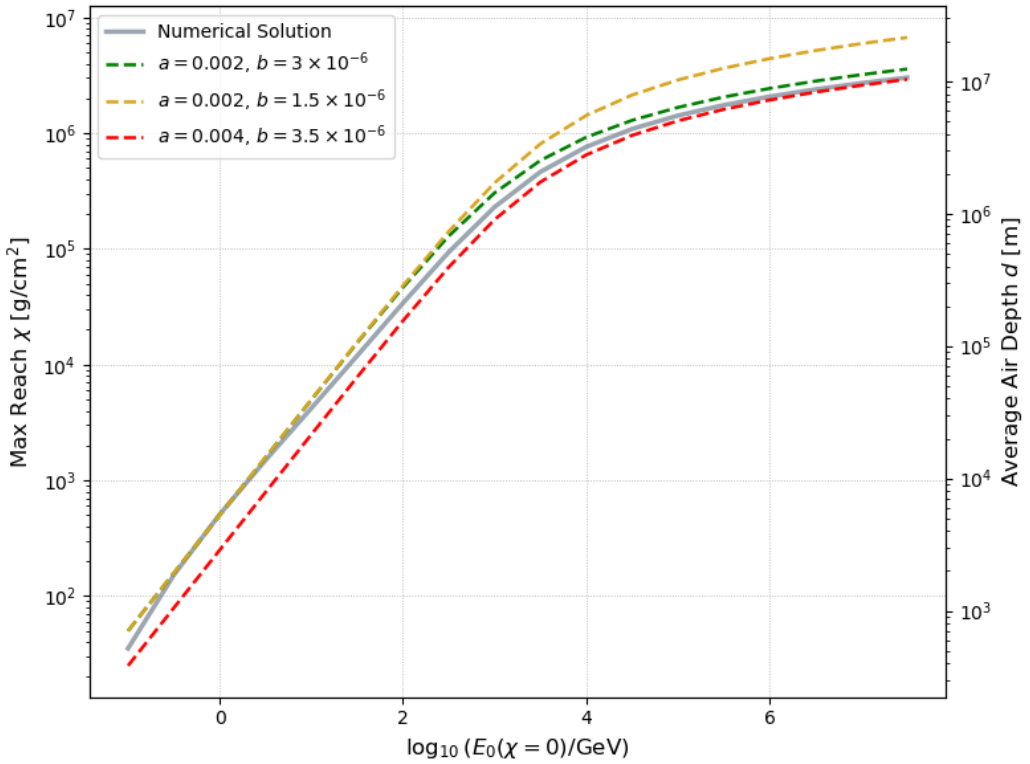

Figure 2.6: Maximum slant depth reach in air by muons with starting energy E_0. The solid grey line is the numerical solution of Equation 2.10. The dashed lines are the analytical solutions with constant loss parameters (Equation 2.13). Changes in density due to temperature changes make the conversion from slant depth to average depth not constant.

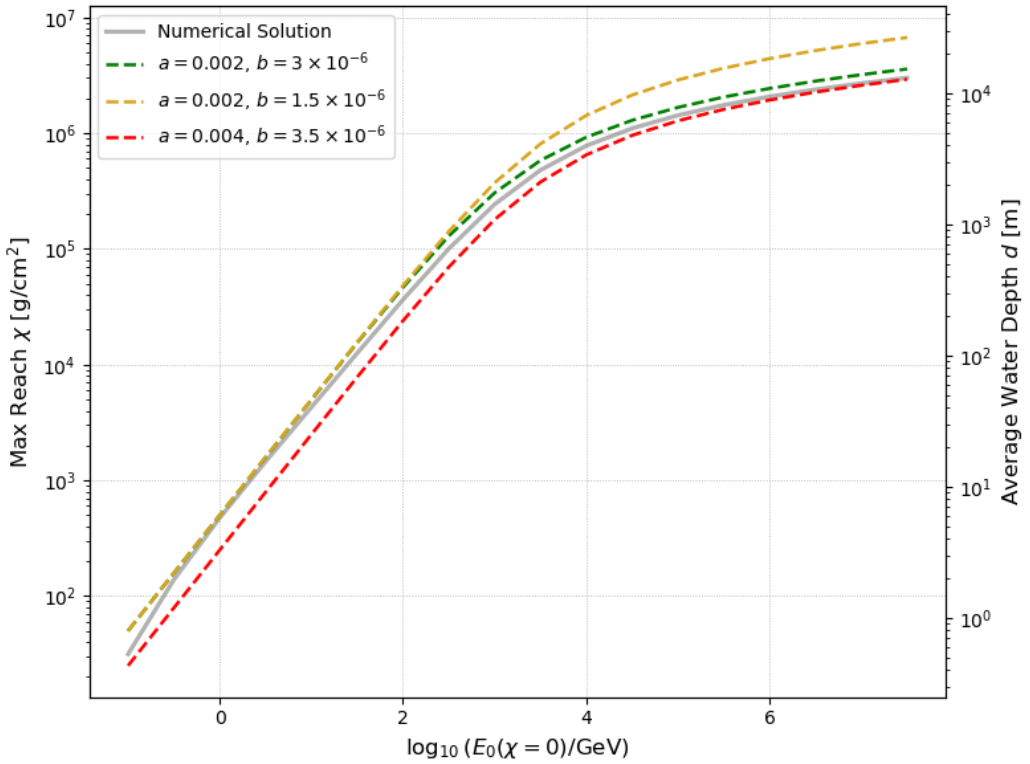

Figure 2.7: Maximum slant depth reach in water by muons with starting energy E_0. The solid grey line is the numerical solution of Equation 2.10. The dashed lines are the analytical solutions with constant loss parameters (Equation 2.13). Changes in density due to temperature and salinity changes make the conversion from slant depth to average depth not constant.

3

Atmospheric effects on the muon rate

As described in the previous chapter, muons are formed when secondary particles from a cosmic ray particle decay. The density of the atmosphere has a large impact on the production, interaction, and decay of secondary particles. The production of muons depends on the energy of the parent particles and the density of the atmosphere. When the energy of a parent particle is higher than the critical energy, it makes it more likely to interact rather than decay. The density and temperature of the atmosphere alter the length of the interaction and the decay length of particles. These are parameters to measure how long a particle travels before it interacts or decays [21].

3.1. Impact of atmospheric temperature on muon production

The interaction length λ_j $[g/cm^2]$ of a particle j, can be written as:

$$\lambda_j = l_j \rho = \frac{\rho}{n_A \sigma_j^{air}} = \frac{A m_p}{\sigma_j^{air}} \tag{3.1}$$

Where ρ is the density of the atmosphere, n_A is the local number density of atoms with an average atomic mass A, and σ_j^{air} is the interaction cross-section of particle j with air. As can be seen in this equation, the interaction length does not depend on the air density. However, the decay length does depend on the air density:

$$d_j = \rho \gamma c \tau_j \tag{3.2}$$

Where γ is the Lorentz factor of particle j which has a rest lifetime of τ_j and c is the speed of light in vacuum. As can be seen, the decay length increases when a particle has a greater energy because of the Lorentz factor. Higher energy means lower changes of decay. This is also true for the density. A higher density means a longer decay length, and therefore fewer decay changes [15].
If the decay length is smaller than the interaction length, the changes in decay are larger than the changes in interaction.

Using Equation 2.5 and some rewriting, the decay length can be written as:

$$d_j = \frac{-\chi E cos\theta}{\epsilon_j} \tag{3.3}$$

Where ϵ_j is the critical energy of a particle j. ϵ_j is defined as:

$$\epsilon_j = \frac{m_j c^2}{c \tau_j} \frac{RT}{Mg} = \epsilon(T_0) \frac{T}{T_0} \tag{3.4}$$

Here R is the universal gas constant, M is the molar mass, g is the acceleration due to gravity, T is the atmospheric temperature, and T_0 is a reference temperature.
When atmospheric temperature increases, so will the critical energy of a particle. The increase in critical energy will result in a shorter decay length, which will cause more particles to decay. Which will

result into more decay to muons [15, 17].

For high-energy muons, this temperature effect dominates. However, when the energy of the muons is small, they will experience this effect themselves. So, if the energy of muons is small, an increase in temperature will cause more muons to decay. This effect is important for muons around its critical energy. Later, it is shown that the muons that reach the KM3NeT detectors are in the high-energy regime, and thus only a positive relation between the temperature and the muon rate is expected. However, for detectors with a lower energy required to reach them, such as the MINOS Near detector [22] and DANSS [23] detectors, a less positive relation is expected.

Looking at Equation 2.8 the temperature dependence comes from the production spectrum $P_\mu(E_\mu, \theta, \chi)$, which can be written as:

$$\begin{aligned} P_\mu(E_\mu, \theta, \chi, T_0 + \Delta T) &= P_\mu(E_\mu, \theta, \chi, T_0) + \left(\frac{\partial P_\mu}{\partial T}\right)_{T_0} \Delta T(\chi) \\ &= P^0_\mu(E_\mu, \theta, \chi) + \eta^0(E_\mu, \theta, \chi)\Delta T(\chi) \end{aligned} \tag{3.5}$$

The parts with a superscript 0 represent the evaluation of the temperature-sensitive functions at $T = T_0$. Using this result and the intensity equation 2.9, the temperature-dependent intensity can be written as:

$$\begin{aligned} I_\mu(T_0 + \Delta T) &= \int_0^\infty dE_\mu \int_0^\infty d\chi \left(P^0_\mu(E_\mu, \theta, \chi) + \eta^0(E_\mu, \theta, \chi)\Delta T(\chi)\right) \\ &= I^0_\mu + \int_0^\infty d\chi \Delta T(\chi) \int_0^\infty dE_\mu \eta^0(E_\mu, \theta, \chi) \end{aligned} \tag{3.6}$$

Writing $I_\mu(T_0 + \Delta T) - I^0_\mu = \Delta I_\mu$, the temperature dependent muon intensity variations can be written as [17]:

$$\frac{\Delta I_\mu}{I^0_\mu} = \int_0^\infty d\chi \alpha(\chi) \frac{\Delta T(\chi)}{T(\chi)} \tag{3.7}$$

$\alpha(\chi)$ is the temperature coefficient defined as:

$$\alpha(\chi) = \frac{T(\chi)}{I^0_\mu} \int_0^\infty dE_\mu \eta^0(E_\mu, \theta, \chi) = \frac{T(\chi)}{I^0_\mu} W(\chi) \tag{3.8}$$

Because the variations of the temperature at different slant depths are unknown, the temperature coefficient is hard to determine experimentally. This is because it is not possible to know at what height a muon is produced. However, by defining an effective temperature T_{eff} the integral can be simplified [17]:

$$T_{eff} = \frac{\int_0^\infty d\chi T(\chi) \int_0^\infty dE_\mu \eta^0(E_\mu, \theta, \chi)}{\int_0^\infty d\chi \int_0^\infty dE_\mu \eta^0(E_\mu, \theta, \chi)} \tag{3.9}$$

The effective temperature coefficient is then defined as follows:

$$\alpha_T = \frac{T_{eff}}{I^0_\mu} \int_0^\infty d\chi \int_0^\infty dE_\mu \eta^0(E_\mu, \theta, \chi) \tag{3.10}$$

Using Equation 3.8 and defining ΔT_{eff} in the same way as T_{eff}, the integral in Equation 3.7 can be rewritten as:

$$\int_0^\infty d\chi \alpha(\chi) \frac{\Delta T(\chi)}{T(\chi)} = \alpha_T \frac{\Delta T_{eff}}{T_{eff}} \tag{3.11}$$

This results in the function to describe the dependence of the muon intensity variations on the variations in the effective temperature:

$$\frac{\Delta I_\mu}{I^0_\mu} = \alpha_T \frac{\Delta T_{eff}}{T_{eff}} \tag{3.12}$$

The muon intensity can be written as [17]:

$$I_\mu = \frac{\frac{N_i}{t_i}}{\epsilon \cdot A_{eff} \cdot \Omega} \tag{3.13}$$

where N_i is the number of muons counted in a time t_i, ϵ the efficiency of the detector, A_{eff} the effective area of the detector and Ω the total solid angle of the detector. From now on it will be assumed that the effective area, the efficiency, and the solid angle are all constant. Equation 3.12 can then be rewritten as follows:

$$\frac{\Delta I_\mu}{I_\mu^0} = \frac{\left(\frac{\Delta N_i/t_i}{\epsilon \cdot A_{eff} \cdot \Omega}\right)}{\left(\frac{N_i/t_i}{\epsilon \cdot A_{eff} \cdot \Omega}\right)} = \frac{\Delta N_i/t_i}{N_i/t_i} = \frac{\Delta R_\mu}{R_\mu(t)} \approx \frac{R_\mu(t) - \langle R_\mu \rangle}{\langle R_\mu \rangle} \tag{3.14}$$

Where $R_\mu(t) = N_i/t_i$ is the muon rate over a time t_i, $\langle R_\mu \rangle$ is the average muon rate over a longer time-taking period.
This gives the final equation that will be used to study the variations in the muon rate due to temperature changes in the atmosphere:

$$\frac{\Delta R_\mu}{\langle R_\mu \rangle} = \alpha_T \frac{\Delta T_{eff}}{\langle T_{eff} \rangle} \tag{3.15}$$

3.2. Effective temperature of the atmosphere

It is not possible to know the exact altitude at which a muon has been produced. That is why the effective temperature is used to approximate the atmospheric temperature.
The pressure and temperature in the atmosphere vary with the altitude. Muon production with energies above the critical energy (ϵ_π, ϵ_K) depends on atmospheric temperature. The production of these muons usually occurs at high altitudes. The effective temperature defined in Equation 3.9 takes into account that muons are more likely to be produced at higher altitudes by the weights defined in Equation 3.8. The weights consist of two parts, one for the pion decay in the air shower and one for the kaon decay. The weights can thus be written as: $W(\chi) = W^\pi + W^K$. A discreet approximation of the effective temperature will be used because the temperature is only known at discreet points [10]:

$$T_{eff} = \frac{\int_0^\infty d\chi T(\chi) W(\chi)}{\int_0^\infty d\chi W(\chi)} \approx \frac{\sum_i \Delta\chi_i T(\chi_i) W(\chi_i)}{\sum_i \Delta\chi_i W(\chi_i)} \tag{3.16}$$

The weights can now be defined as:

$$W^{\pi,K}(\chi) = \frac{\left(1 - \frac{\chi}{\lambda_{\pi,K}}\right)^2 e^{-\frac{\chi}{\Lambda_{\pi,K}}} A_{\pi,K}}{\gamma + (\gamma+1) B_{\pi,K} K(\chi) \left(\frac{\langle E_{\text{thr}} \cos\theta \rangle}{\epsilon_{\pi,K}}\right)^2} \tag{3.17}$$

$$K(\chi) \equiv \frac{\chi \left(1 - \frac{\chi}{\lambda_{\pi,K}}\right)^2}{\left(1 - e^{-\frac{\chi}{\lambda_{\pi,K}}}\right) \lambda_{\pi,K}} \tag{3.18}$$

$$\frac{1}{\lambda_{\pi,K}} = \frac{1}{\Lambda_N} - \frac{1}{\Lambda_{\pi,K}} \tag{3.19}$$

The constant $A_{\pi,K}$ comprises the amount of inclusive meson production in the forward fragmentation region, the masses of mesons and muons, and the muon spectral index. The parameter $B_{\pi,K}$ accounts for the relative atmospheric attenuation of the mesons. The parameter $\Lambda_{N,\pi,K}$ represents the atmospheric attenuation length of cosmic ray particles, pions, and kaons, respectively. The critical energy, $\epsilon_{\pi,K}$, is the energy at which the decay and interaction probabilities are equal. Finally, the parameter γ is the muon spectral index [10]. The values used for these parameters can be seen in Table 3.1. $\langle E_{\text{thr}} \cos\theta \rangle$ describes the average energy that a muon needs at the Earth's surface to reach an underground detector and be detected, and the angle at which it enters the Earth is taken into account for this. The calculation for $\langle E_{\text{thr}} \cos\theta \rangle$ will be explained in more detail in Chapter 6.

Parameter	Value
A_π	1
A_K	$0.38 \cdot r_{K/\pi}$
$r_{K/\pi}$	0.149 ± 0.06
B_π	1.460 ± 0.007
B_K	1.740 ± 0.028
Λ_N	$120\,\mathrm{g/cm^2}$
Λ_π	$180\,\mathrm{g/cm^2}$
Λ_K	$160\,\mathrm{g/cm^2}$
γ	1.7 ± 0.1
ϵ_π	$114 \pm 3\,\mathrm{GeV}$
ϵ_K	$851 \pm 14\,\mathrm{GeV}$

Table 3.1: Values and uncertainties of the parameters needed for the weight calculation of the effective temperature. Values from [10].

3.3. Prediction of temperature coefficient

The theoretical temperature coefficient can be calculated using methods described in [5, 24]:

$$\alpha^{\mathsf{th}} = \frac{1}{D_\pi} \frac{1/\epsilon_K + A_K^1 \left(\frac{D_\pi}{D_K}\right)^2 / \epsilon_\pi}{1/\epsilon_K + A_K^1 \left(\frac{D_\pi}{D_K}\right) / \epsilon_\pi} \tag{3.20}$$

where

$$D_{\pi,K} = \frac{\gamma}{\gamma+1} \frac{\epsilon_{\pi,K}}{1.1 \left\langle E_{\mathsf{thr}} \cos\theta \right\rangle} + 1 \tag{3.21}$$

The values used for these parameters can again be found in Table 3.1. The calculation for $\langle E_{\mathsf{thr}} \cos\theta \rangle$ will be explained in more detail in Chapter 6. The theoretical temperature coefficients are shown in Chapter 7. The theoretical temperature coefficient for only the muon or pion contribution is as follows [24]:

$$\alpha_{\pi,K}^{\mathsf{th}} = \left[\frac{\gamma}{\gamma+1} \frac{\epsilon_{\pi,K}}{1.1 \left\langle E_{\mathsf{thr}} \cos\theta \right\rangle} + 1 \right]^{-1} \tag{3.22}$$

4

The KM3NeT experiment

The Cubic Kilometre Neutrino Telescope, KM3NeT, is a research infrastructure project currently being built on the bottom of the Mediterranean Sea. KM3NeT will consist of a network of neutrino telescopes with two main scientific goals: Discovering and observing high-energy neutrino sources in the universe and determining the neutrino mass hierarchy. The KM3NeT detectors are two large-volume water Cherenkov detectors that can detect cosmic and atmospheric neutrinos and atmospheric muons. KM3NeT uses the water of the Mediterranean Sea as its detection medium, which differs from, for example, IceCube which uses the Antarctic ice sheet as its detection medium [25]. This comes with certain advantages and disadvantages. The two detectors are called ORCA (Oscillations Research with Cosmics in the Abyss) and ARCA (Astroparticle Research with Cosmics in the Abyss). The detectors work according to the same principles but differ in location and size. ORCA has a smaller and denser configuration, which is optimal for detecting atmospheric neutrinos in the GeV range. Therefore, ORCA will be used to study neutrino properties, such as neutrino oscillations. ARCA has a larger and less dense configuration and will therefore be used to study high-energy cosmic neutrinos in the PeV range [26].

4.1. Detector layouts

The two detectors work according to the same principle, but differ in size and location. In addition to this, the detectors are still in construction, so the configuration of the detectors itself is also constantly changing. These changes have to be taken into account for further analysis. Both detectors are built out of several detection units (DU). The DU is a long vertical structure that is built up out of 18 digital optical modules (DOM). The horizontal spacing between the DUs and the vertical spacing of the DOMs on the DU is detector-specific. DOMs are essential for detecting Cherenkov radiation. A DOM is a 17-inch diameter glass sphere that houses 31 photomultiplier tubes (PMTs). When a photon hits a photocathode in a PMT, it releases an electron through the photoelectric effect. The electron is then accelerated towards a series of dynodes, and at each dynode, the number of electros increases. This causes an amplification of the electron current that can eventually create a measurable electrical pulse at the anode in the PMT. The amplitude of the electrical pulse is proportional to the number of photons that hit the photocathode. The PMTs are sensitive enough to detect a single photon. The DOM also contains the necessary equipment needed for timing, calibration, positioning, orientation, and, of course, data readout. The DOMs in an DU are attached to two thin parallel Dyneema ropes with a titanium collar. Along the DU runs an optical cable to the base of the DU providing data transmission and power. The base container functions as an anchor to the seabed and houses power and data components. From the base container, the data will go through some intermediate steps to the shore for further processing. The first DU for ARCA was deployed in December 2015 and for ORCA in September 2017. Every couple of months, sea operations add new DUs or try to recover broken DUs for debugging [25].

Figure 4.1: The detection unit (DU) left and the digital optical module (DOM) on the two thin parallel Dyneema ropes right [25].

4.1.1. ORCA

ORCA is located about 40 kilometres offshore from Toulon, France, at coordinates 42°48'N 06°02'E. The sea has a depth of 2450 metres there. The DUs are 20 metres apart from each other. On each DU there are 18 DOMs with 9 metres spacing between them vertically. The first DOM is around 40 metres above the seafloor, making the total DU 200 metres in height. Because ORCA is relatively dense, it is possible to detect at a lower energy threshold compared to ARCA. When ORCA is completed, it will have 115 DUs in total. The total instrumented volume will be about 7 Mton of sea water when completed. However, ORCA is currently under construction, but is already producing data [25]. Thus, different datasets are available for the constantly growing detector; these datasets are referred to as ORCA-X. The X in this naming scheme stands for the number of DUs in the detector configuration. As of writing this paper, ORCA is currently operating with 24 DUs (ORCA-24). However, as indicated above, the number of DUs is constantly changing and can be found on the website of the KM3NeT organization [27]. It takes some time to process the raw data from a detector before it is available for further analysis. In this study, the detector configurations ORCA-6, ORCA-10, ORCA-11, ORCA-15, and ORCA-18 are studied. The detector configurations have different properties. This makes their average threshold energy, predicted temperature coefficient, and the amount of particles detected per unit of time slightly different. This is because a larger detector can detect more particles in the same amount of time.

4.1.2. ARCA

ARCA is located about 100 kilometres offshore from Porto Palo di Capo Passero, Sicily, Italy at the coordinates 36°16'N 16°06'E. The sea has a depth of 3500 metres there. The DUs are spaced 95 metres apart from each other. On each DU there are 18 DOMs with 36 metres spacing between them vertically. The first DOM is around 80 metres above the seafloor, making the total DU 700 metres in height. Because ARCA is not as dense as ORCA, it has a higher energy threshold compared to ORCA. When ARCA is completed, it will have 230 DUs in total. The total instrumented volume will be about 1045 Mton of sea water when completed, significantly larger than that of ORCA due to the larger distances in the configuration. ARCA is also still under construction, but is also producing data [25].

Thus, different datasets are available for the constantly growing detector; these datasets are referred to as ARCA-X. The X in this naming scheme stands for the number of DUs in the detector configuration. As of writing this paper, ARCA is currently operating with 33 DUs (ARCA-33). Again, the number of DUs is constantly changing and can be found on the website of the KM3NeT organization [28]. In this study, the detector configuration ARCA-21 is studied.

4.2. Detector principle

KM3NeT works, as other neutrino detectors such as ANTARES and IceCube, by detecting Cherenkov radiation. Cherenkov radiation is emitted when a charged particle, like a muon, travels faster than the local speed of light through a medium, such as water or ice. The blue light emitted by a particle in a cone-shaped shape is called Cherenkov radiation. Tamm and Frank calculated the Cherenkov radiation intensity $I(\omega)$, which describes the energy emitted by a particle at a frequency ω per unit of time and per unit frequency interval $d\omega$ [29]:

$$I(\omega)d\omega = v\frac{e^2}{c^2}\left(1 - \frac{c^2}{v^2 n^2(\omega)}\right)\omega d\omega \tag{4.1}$$

Where e is the charge of the particle, $n(\omega)$ the refractive index of the medium at frequency ω, and v the speed of the particle. As can be seen the intensity of the Cherenkov radiation increases for higher frequencies of light such as blue light. A particle, like a muon, also losses energy through radiative processes such as bremsstrahlung, pair-production and hadronic interactions as indicated in Equation 2.10. The particles created in these processes can produce additional Cherenkov radiation. So light can be produced directly by Cherenkov radiation of the main particle but additional light can be produced through secondary radiative processes [25].
Atmospheric muons can be detected directly using Cherenkov radiation and light emitted by secondary processes. For neutrinos to be detected they first need to interact with other particles. This interaction will then create charged particles that, if they have enough energy, can be detected using Cherenkov radiation. The more energy a particle has, the more radiation it emits. Thus, it is also possible that a particle does not travel directly through the detector but still emits enough radiation to be detected. The PMTs detect radiation from all processes and digitises the signal if it exceeds a certain threshold. Each photon that exceeds the threshold is a hit. These data, combined with timing information, are sent to shore for processing. The clocks of the DOMs are synchronised to an order of nanoseconds. The DOMs order the data into 100 ms time slices. In the processing step, an onshore CPU farm looks for correlations between all the hits in the detector within every time slice to see if there are possible particle events. In order to get a time slice of the whole detector, the time slices of the individual DOMs need to be combined. This is only possible if the clocks of the DOMs are running synchronously and aligned to a shared reference time. Multiple trigger algorithms analyse the same data to identify specific types of events, such as muon-like or shower-like events. The requirements for a muon trigger are [25, 30]:

- **Level 0 (L0) Filter**: The pulse of a single photon hit on a PMT has to exceed a certain threshold to be considered an L0 hit. This initial filtering step occurs offshore.
- **Level 1 (L1) Filter**: Two or more L0 hits on the same DOM within 10 nanoseconds. This is an L1 hit.
- **Level 2 (L2) Filter**: The angle between triggered PMTs on the same DOM has to be smaller than 90°, level 2 (L2) filter
- **Directional Filter**: A directional filter scans the entire sky for possible muon tracks by assuming different direction of the muon. The filter considers the intersection of a cylinder with the detector. The centre of the cylinder is the assumed muon track and the radius corresponds to the maximum distance light can travel in water. This limits the number of PMTs to be analysed, thus improving the signal-to-noise ratio.
- **Causality Condition**: A causality condition is applied to every pair of L1 hits. This condition ensures that hits coming from a muon track must happen within a specific time window, which depends on the speed of light in water and the direction of the muon. Every hit must be causal with every other hit.

- **Hit Selection**: A minimum number of L1 hits (typically four or five) is required within the cylinder.

When these requirements are satisfied, the muon trigger is activated. All hits that occur around a specific time window surrounding the trigger are saved as events for further analysis. The muon trigger runs in parallel with other trigger algorithms, such as the shower trigger. A track of a single muon is assumed and fitted to all the hits in an event. The fitting algorithm searches for the track parameters that maximise the likelihood of actually seeing the recorded hits in the event. The track parameters describe characteristics of the particle and the path the particle travelled through the detector. The track parameters are location, direction, velocity, time, energy, and track length. The fit with the highest likelihood is saved along with the track parameters. Now, selections can be made to increase the quality of the data set [25]. Some events could still be badly reconstructed, so it is desirable to remove these from the dataset to obtain a higher purity of the data.
The detector collects data in specific periods, called runs. These runs typically have a lifetime of around 6 hours. These runs are also used for calibration and stability checks to monitor efficiency losses and compensate for them [25].

4.3. Background sources

ORCA's main goal is to study neutrino properties such as neutrino oscillations. To do this, it will look at atmospheric neutrinos that are created in cosmic-rays showers on the opposite side of the Earth. These neutrinos will travel through Earth, enter the detector from below, and travel upward. However, downward neutrinos will also be created in the atmosphere directly above the detector. The problem with the signal from these atmospheric neutrinos is that the neutrinos are accompanied by many atmospheric muons that are created in the same shower. Therefore, the Earth is used as a sort of shield to block unwanted muons. ARCA's main goal is to study higher-energy cosmic neutrinos. However, ARCA also has the same problem with unwanted atmospheric muons. That is why both ORCA and ARCA will use the Earth as a shield for unwanted atmospheric muons. Nevertheless, some downward atmospheric muons are misreconstructed as upward-going events. Since the muon rate will always be significantly higher than the neutrino rate, this is a problem. The atmospheric muons will always be a major source of background signal for neutrino detection at the KM3NeT detectors. Therefore, it is important to understand the atmospheric muon rate and its seasonal variations as well as possible.

Both detectors have several other background sources that are more related to the direct environment of the detectors. It is impossible to perfectly control the environment in which the detectors operate because they are located in the Mediterranean Sea. Several factors could be background sources here, but the main two are Potassium-40 (^{40}K) decay and bioluminescence. Potassium-40, which is naturally present in seawater, decays and causes uncorrelated hits on PMTs. The decay is stable over time and is therefore used for calibrations of the detector. Another factor is bioluminescence, the light produced by living organisms. However, this is not constant over time [31, 32]. When a PMT displays a high rate of activity, the data can be excluded from the analysis. This is called the high-rate veto (HRV). It helps protect DOMs and PMTs against overexposure. When the rate of activity exceeds 20 kHz, the data acquisition will stop for the remainder of the 100 ms time slice. The fraction of time that the DOMs operate in HRV mode is saved per run along with the PMT rates measured in the 100 ms time slices [33].

4.4. Run-By-Run Monte Carlo simulations

The KM3NeT detectors use water as their detection medium. This causes several background sources. Detectors such as IceCube use a more static detection medium which eliminates many of these background sources. For these close-to-ideal detectors, the muon rate in the data is a good approximation of the real muon rate:

$$R_{data}(t) = N(t)/\Delta t \approx R_{true}(t) \tag{4.2}$$

Because of the background sources and the changes in detector efficiency due to the dynamic detection medium in KM3NeT's detectors, the muon rate in the data is better approximated by:

$$R_{data}(t) \approx R_{true}(t) \times C_{data}(t) \tag{4.3}$$

The factor $C_{data}(t)$ accounts here for the changes in efficiency and the background sources.
A run-by-run Monte Carlo simulation simulated a full run of data using the Monte Carlo technique using the same duration and the same mean count rate per PMT. However, due to computer limitations, the amount of simulated muons may differ from the true muon count. To compensate for this, the simulation is scaled with a weight w to match the count rates of the actual data run. Using this technique ensures that the detector response and background sources are taken into account. The simulation assumes a constant muon rate. The Monte Carlo rate should be:

$$R_{MC}(t) = R_{const} \times C_{MC}(t) \tag{4.4}$$

The only thing the Monte Carlo simulation does not account for should be the variation of the muon rate due to atmospheric temperature changes.
Simulations for each neutrino flavour and atmospheric muons are done separately. For atmospheric muons, MUPAGE is used. For these simulations, distributions of parameters of the muon tracks, such as direction, energy, and flux, are known. The track is then simulated to predict the hits on the PMTs they would produce. Using these hits, the track is reconstructed. This is helpful to see how well the reconstruction algorithm performs. In the simulation data, both the ”true” parameters of the simulated track and the reconstructed parameters are available. In the real data only the reconstructed parameters are known.

5

Temperature data

In this chapter, the temperature dataset that will be used for the effective temperature calculation will be introduced and explained. Two datasets will be used, the AIRS data and the ERA5 data. The data sets differ from each other in several ways, and different processing steps are needed to use the data from each of them. Temperature data from 2020, 2021, 2022, and 2023 will be used, since this covers all the live time of the different detector configurations.

5.1. AIRS

The first temperature data set was acquired from NASA's AIRS instrument on board the Aqua satellite. Aqua orbits Earth at an altitude of 705 kilometres in a sun-synchronous polar orbit. The orbit period is about 100 minutes. It takes 2 daily measurements of the atmospheric temperature with an error at 24 pressure levels between 1 hPa and 1000 hPa and has a swath width of 1650 kilometres. The swath width is the width of the Earth's surface measured by the satellite in one pass. The data product is called *Aqua/AIRS L3 Daily Standard Physical Retrieval (AIRS-only) 1 degree x 1 degree V7.0 (AIRS3STD)* and contains temperature measurements of the whole Earth. It divides the Earth into bins of 1°x 1°latitude and longitude [34, 35].

The exact overpass times have to be calculated because the only known information is that the satellite passes the equator twice a day. Once from the south pole to the north pole (ascending pass) at 1:30 pm local time, and once from the north pole to the south pole (descending pass) at 1:30 am local time. The measurements in one pass are all labelled with this general time. So, one pass is during the day and one during the night [34, 35]. To determine a more exact measurement moment, more information is needed about the orbit. This data can be acquired from Two-line element (TLE) data from databases such as CelesTrak [36]. With this data, the position of the satellite can be calculated at every moment. This is done every 30 seconds to get a high resolution. Then, the slant range between the satellite and the detector is calculated. The slant range is the distance in a straight line between the detector and the satellite, taking into account both the vertical and the horizontal distance. Then the passes are determined when the detector is within the visible range of the satellite and if the pass is ascending or descending. Finally, only the overpass time when the slant range was minimised is saved in UTC. In Figure 5.1 the overpass times above the ORCA detector are shown. In orange is the descending overpass time that occurs during the night. In blue are the ascending overpass times that happen during the day. So, the exact moment of measurement is not constant and varies from day to day.

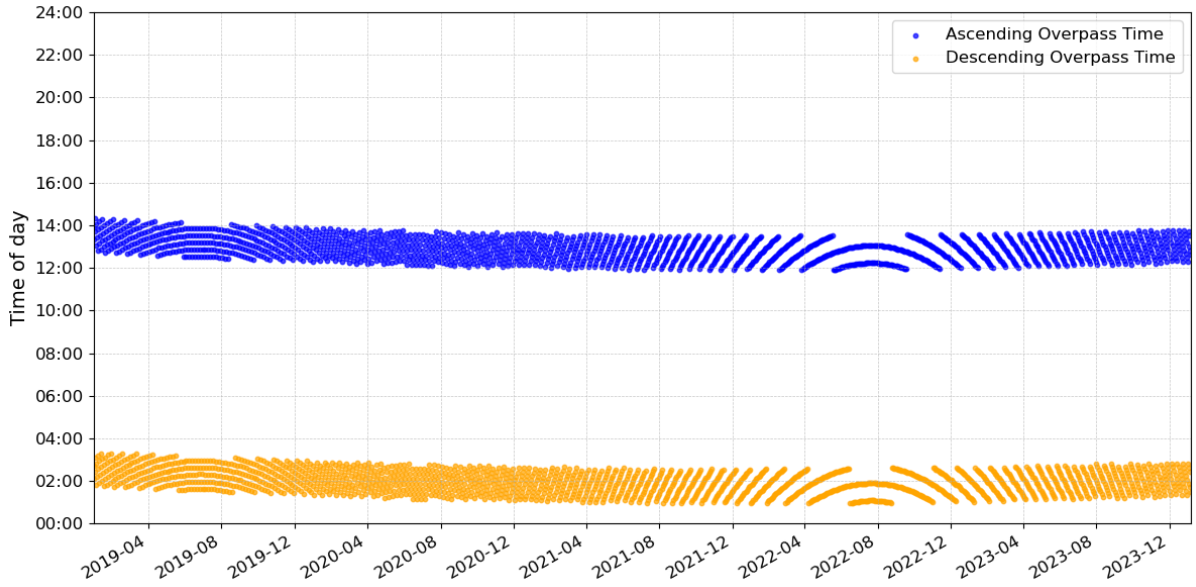

Figure 5.1: Overpass times in UTC of the Aqua satellite above KM3NeT's detector ORCA. In orange is the descending overpass time which happens during nighttime. In blue are the ascending overpass times which happen during the daytime.

5.2. ERA5

The second temperature data set is the ERA5 atmospheric reanalysis acquired from the Copernicus Climate Change Service [37]. ERA5 is a fifth generation of atmospheric reanalysis performed by the European Center for Medium-Range Weather Forecasts (ECMWF) [38]. It covers a period from 1950 to the present day and is updated daily. ERA5 is a reanalysis data set that combines current weather models and historical and current weather observations. This is different from the AIRS data because AIRS uses direct atmospheric measurements.

ERA5 data has a high resolution of 0.25° x 0.25° latitude and longitude bins. For its reanalysis, it uses data from more than 200 satellites and many other metrological measurements, such as radiosondes, drop sondes, and aircraft measurements. AIRS data is also used for the ERA5 reanalysis. The atmospheric temperature data are again given in pressure layers ranging from 1 hPa and 1000 hPa, but now in 37 pressure levels. This gives the possibility to select a temperature profile that better matches the direction of the incoming muons, more about this later in Chapter 6. The other main difference between the ERA5 data and the AIRS data is that ERA5 data is available every hour.

6 Method

6.1. Selection of muon data

In order to get a better purity of the data, it is necessary to apply selections to the data. The purpose of these selections or cuts on the data is to improve the quality of the data for further analysis. The goal is to suppress background noise and remove poorly or incorrect reconstructed events without losing much data. For neutrinos, the count rate is really low, so it is important not to make strict cuts when working with neutrinos. In this case, muons have a much higher count rate, so it is acceptable to have some stronger cuts to reduce the background noise a bit more without losing to much good events.
Each detector and detector configuration are different in sensitivity and build. That is why the cuts on the data for the different detectors and configurations differ from each other. In this section, the process of making the cuts will be explained, and the ORCA-6 detector will be used as an example. The method developed here is applied to all detectors and configurations in the same way.
There are two different types of cuts that can be applied to the data, run cuts and event cuts. Run cuts apply cuts on parameters that are the same for a whole data run, such as the livetime of a run or the time a run spends in HRV mode. These cuts remove a lot of data in one go, so a small change can have a large impact on the final data. Event cuts apply cuts on parameters that differ for each event, such as direction and energy.
Before real cuts are applied, some precuts will filter out some data that are not physical. The precuts make sure that the energy and length of the events are positive, that only events where the muon trigger is activated are included, that the muon is moving downward, and that the likelihood, a parameter reflecting the correctness of the event reconstruction, is positive.

6.1.1. Run cuts

Run cuts will be made to the data because there might be problems with data from a whole run. The run cuts will be the same for both detectors and all of its configurations. One cause of this is that the runs can be cut short for different reasons. For example, runs that follow calibrations run that are needed to calibrate the detector can be cut short to keep up with the schedule of the detector. Other interruptions or disturbances, such as a required restart, can also lead to short runs. These short runs have significantly lower statistics. To have only runs with high enough statistics, the first run cut that is applied is that the livetime of a run needs to be longer than 1200 seconds. An other cause for problems in a whole data run is the amount of time spent in the HRV mode. The longer a run spends in HRV, the less time the detector is actually taking data. This also causes runs with lower statistics. Therefore, a run cut is applied that the time spent in the HRV needs to be lower than 20 % of the total livetime of a run. In Figure 6.1 the livetimes of the runs are shown for ORCA-6. The runs with a livetime shorter than the cut are highlighted in red, the runs that were longer in HRV mode than the cut are highlighted in blue, and the selected runs are highlighted in green. For all other detector configurations the same run cuts are applied of livetime > 1200 seconds and time spend in HRV < 20 % of the total run livetime.

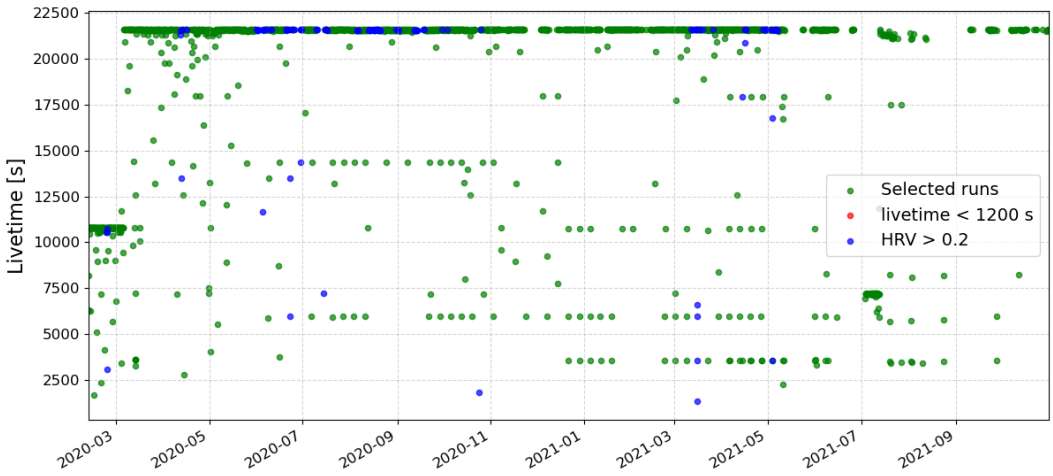

Figure 6.1: Livetimes of the runs for ORCA-6. The runs with a livetime shorter than the cut are highlighted in red, the runs that where longer in HRV mode than the cut are highlighted in blue and the selected runs are highlighted in green.

6.1.2. Event cuts

In order to determine the best cutoff value for a detector, Monte Carlo simulations are used. For the Monte Carlo data, both the ”true” predefined parameters and the reconstructed parameters of the muon tracks are available. Using true and reconstructed muon directions, the opening angle between the directions can be determined. The opening angle is thus the difference between the true and reconstructed direction. In Figure 6.2 the distribution of the opening angle for ORCA-6 is shown before any cuts are applied to the data. As can be seen, the distribution reaches a maximum when the opening angle is 1 degree. Each event is classified as either a good reconstruction when the opening angle is less than 1 degree or as a bad reconstruction when the opening angle is more than 1 degree.

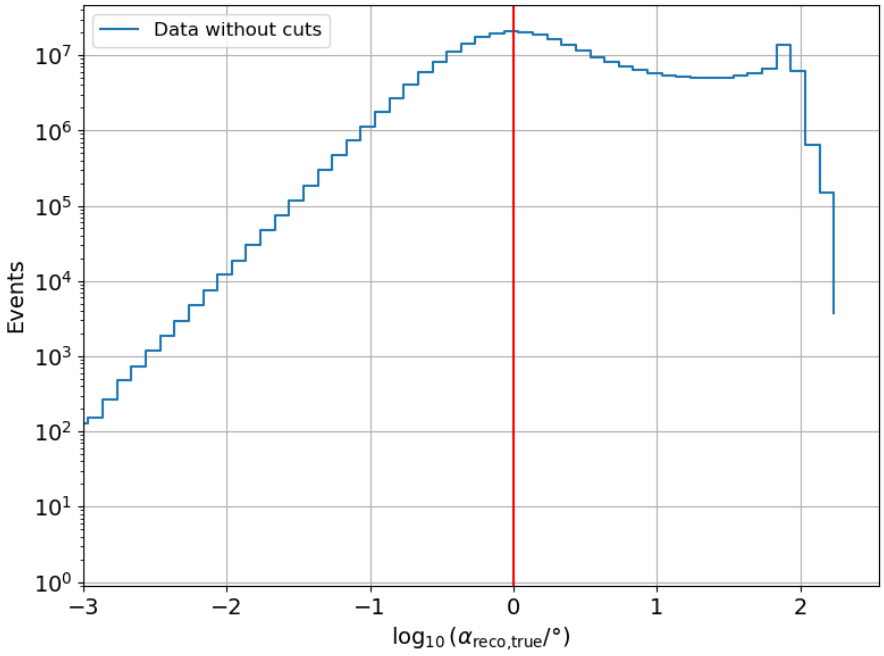

Figure 6.2: Distribution of the opening angle for ORCA-6 before any cuts are applied to the data

Now the goal is to remove as much of the bad reconstructed event without losing too much of the good reconstructed events. In order to do this, a range of cut values for every cut parameter will be tested to see what portion of bad events is removed and what fraction of good events are retained after applying a specific cut. The fraction of good events retained will be called the efficiency. Thus, it is desirable to maximise the removal of bad events while maintaining high efficiency. In order not to lose too much efficiency, a threshold is placed so that the efficiency needs to be at least 97.5%. Having a lower efficiency than this value does not greatly improve the bad removal, so therefore this threshold gives an optimal ratio between efficiency and bad removal. All this is done in a Python script, it loops over a range of cut values for all the cut parameters and outputs the optimal cut values. In Table 6.1 an overview of the cuts can be found with their efficiency and bad removal fraction if they were applied independently on the data set for ORCA-6.

Table 6.1: Cut variable with their efficiency and bad removal fraction if they where applied independent on the dataset for ORCA-6.

Cut variable	Cut value	Efficiency	Bad Removal
Zenith angle ($cos(\theta)$)	< -0.447	0.976	0.078
Energy [GeV]	> 11.323	0.978	0.121
Length [m]	> 37.996	0.976	0.165
Likelihood	> 74.298	0.976	0.217
Number of hits	> 41	0.976	0.166
Likelihood / hits	> 1.144	0.977	0.150

Zenith angle cut

The first cut parameter that is chosen is the reconstructed zenith angle. This is done to improve the angular resolution because events reconstructed near the horizontal plane are more prone to reconstruction problems. Using the optimal cut algorithm, a cut value of $cos(\theta) < -0.447$ is determined. In Figure 6.3 the distribution of the real and simulated zenith angles of ORCA-6 is shown before and after the event cuts. In the lower part of the figure the ratio between the real data and the simulated data can be seen before and after the event cuts. If the simulation worked perfectly, the ratio would always be 1; however, for larger zenith angles the ratio seems to decrease.

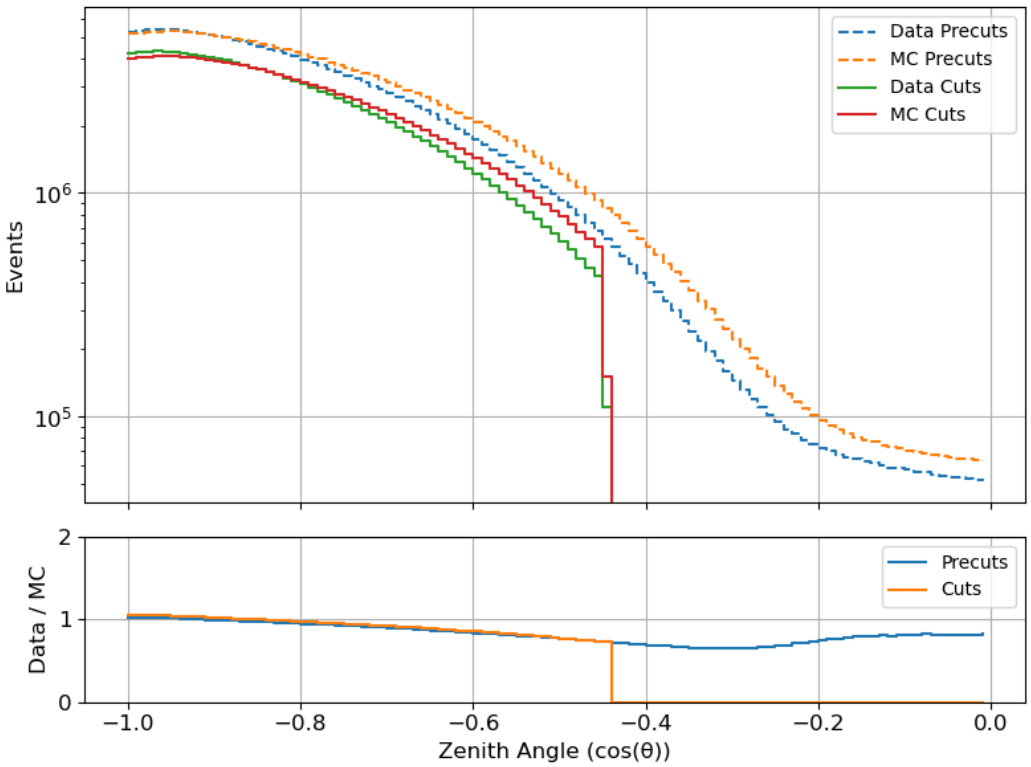

Figure 6.3: Distribution of the real and simulated zenith angles of ORCA-6 before and after the event cuts. In the lower part the ratio between the real data and the simulated data is depicted before and after the event cuts.

Energy cut

The second cut is made on the reconstructed energy of the events. In Figure 6.4 the distribution of the real and simulated reconstructed energies of ORCA-6 is shown before and after the event cuts. In the lower part of the figure the ratio between the real data and the simulated data can be seen before and after the event cuts. For larger energies, it can be seen that the simulation overestimates the number of events detected, both before and after the cuts. Using the optimal cut algorithm, a cut value of the reconstructed energy > 11.323 GeV is determined. The double peak seen in the figure might be caused by the geometrical configuration of the detector. The detector is namely quite tall but also rather narrow. Particles that cross horizontally through the narrow axis might be reconstructed with lower energies than particles that cross the detector vertically through the tall axis. However, this is not yet fully understood. If this is the case, the double peak should disappear as the detector becomes bigger. Another reason to cut lower energies out is that these lower energies are often dominated by background noise. So, by removing, the purity of the data can be improved [10].

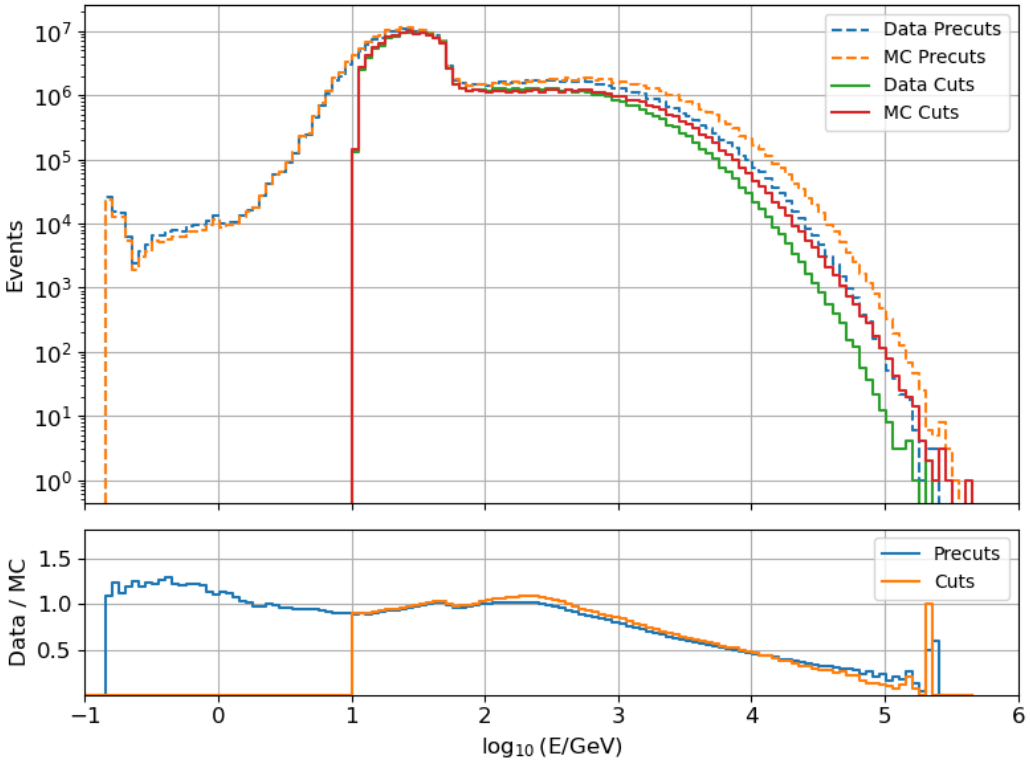

Figure 6.4: Distribution of the real and simulated reconstructed energy's of ORCA-6 before and after the event cuts. In the lower part the ratio between the real data and the simulated data is depicted before and after the event cuts.

Track length cut

The third cut is made on the track length of the events. This is closely related to the reconstructed energy, because more energetic particles produce longer tracks. Cuts on the track length are made because the reliability of track reconstruction algorithms often improves with longer track lengths. This is because longer tracks provide more hit information, which algorithms can use to determine the trajectory and properties of the muon more accurately [23]. In Figure 6.5 the distribution of the real and simulated reconstructed track lengths of ORCA-6 is shown before and after the event cuts. In the lower part of the figure the ratio between the real data and the simulated data can be seen before and after the event cuts. The distribution of the real track lengths closely aligns with the simulations and gets even better after the cuts are applied. Using the optimal cut algorithm, a cut value of the reconstructed track length > 37.996 meter is determined.

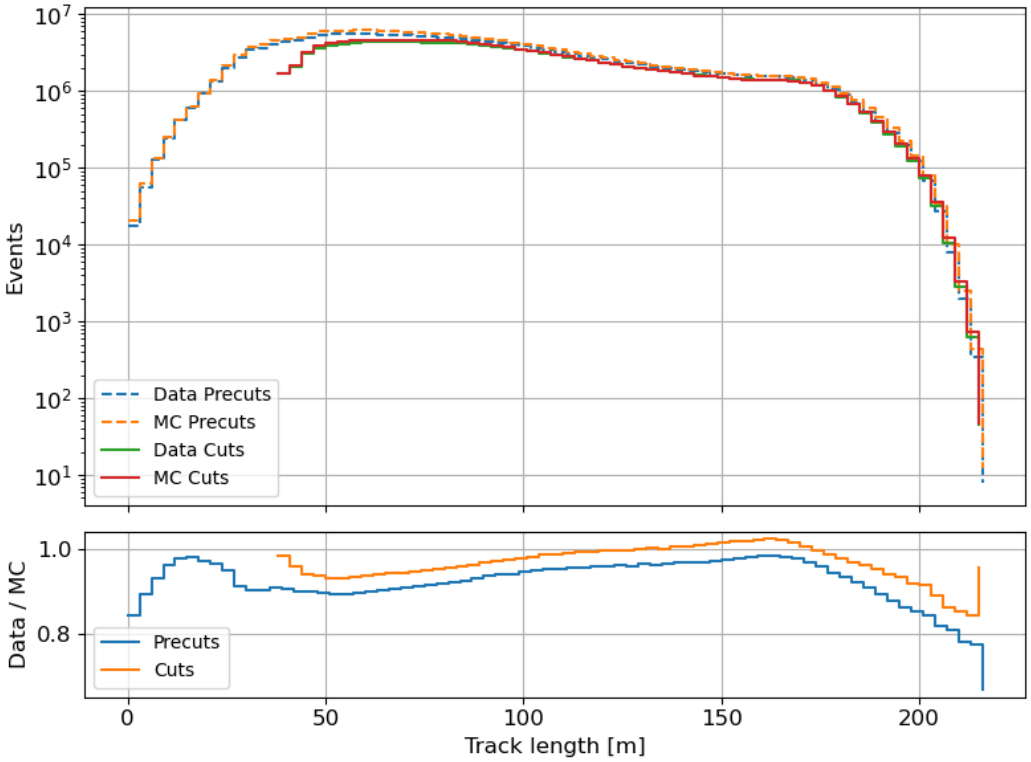

Figure 6.5: Distribution of the real and simulated track lengths of ORCA-6 before and after the event cuts. In the lower part the ratio between the real data and the simulated data is depicted before and after the event cuts.

Likelihood cut

The fourth cut is made on the likelihood of the reconstructed events. The likelihood is a measure of how good the fit of the muon reconstruction is. In Figure 6.6 the distribution of the likelihood of the reconstructed events of the real and simulated ORCA-6 data is shown before and after the event cuts. In the lower part of the figure the ratio between the real data and the simulated data can be seen before and after the event cuts. Using the optimal cut algorithm, a cut value of the likelihood > 74.298 meter is determined.

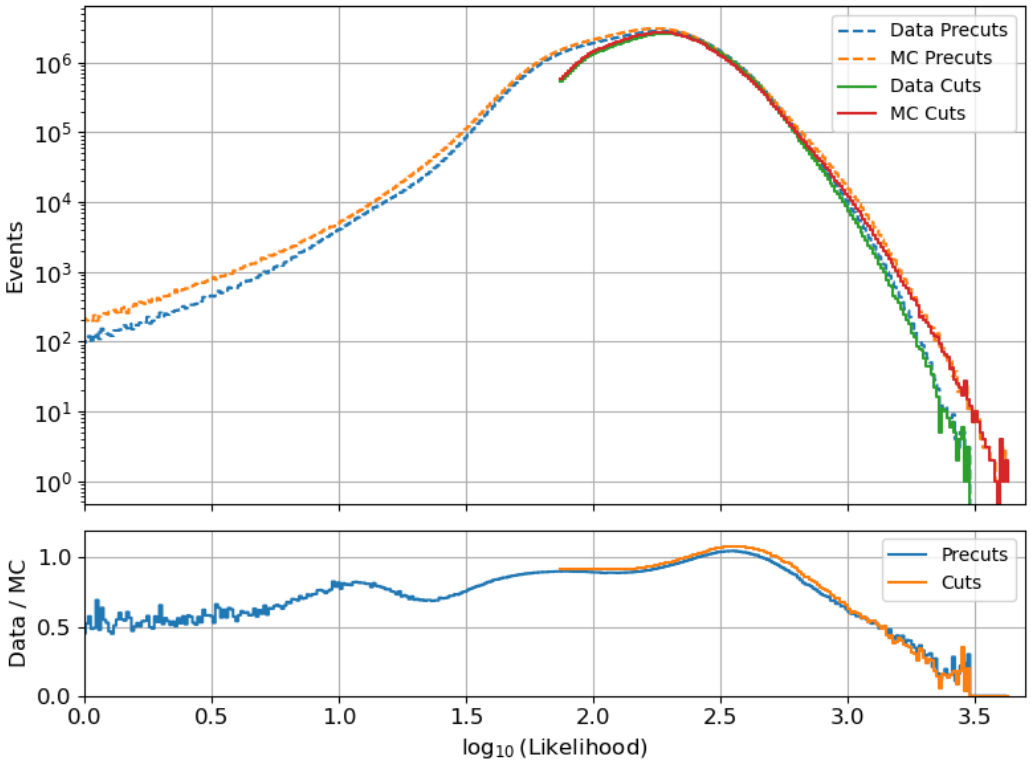

Figure 6.6: Distribution of the likelihood of the reconstructed events of the real and simulated ORCA-6 data before and after the event cuts. In the lower part the ratio between the real data and the simulated data is depicted before and after the event cuts.

Number of hits cut

The fifth cut is made on the number of hits (Nhits) used in the reconstruction of the event. In order to trigger the muon trigger, already 4 hits are necessary. However, it is desirable to have a higher minimum of hits required to reduce noise. Events with a lower number of hits are more likely to have a larger fraction of background sources in the data, making reconstruction more difficult. So, by selecting only events with a higher minimum number of hits, the overall quality of reconstruction of the events can improve. Using the optimal cut algorithm, a cut value of the number of hits (Nhits) > 41 is determined. In Figure 6.7 the distribution of the number of hits of the reconstructed events of the real and simulated ORCA-6 data is shown before and after the event cuts. In the lower part of the figure the ratio between the real data and the simulated data can be seen before and after the event cuts.

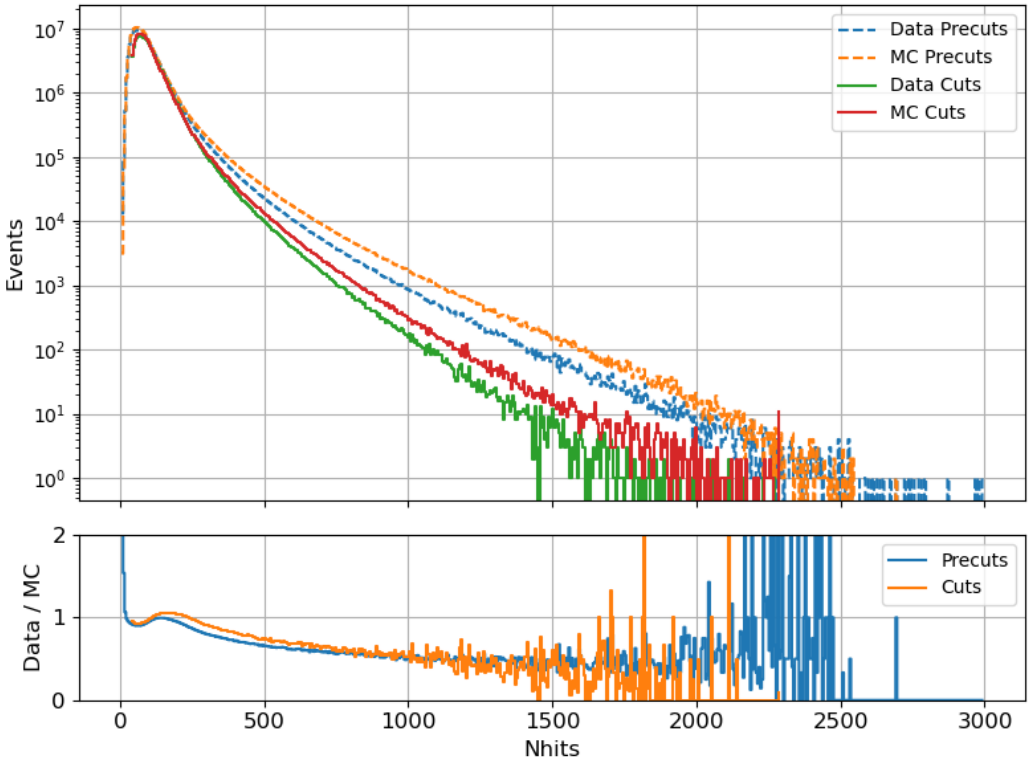

Figure 6.7: Distribution of the number of hits of the reconstructed events of the real and simulated ORCA-6 data before and after the event cuts. In the lower part the ratio between the real data and the simulated data is depicted before and after the event cuts.

Likelihood/Nhits cut

The sixth and final cut is made on the likelihood divided by the number of hits (likelihood/Nhits). This may seem a strange cut. However, events with more hits tend to have a more accurate reconstruction and thus a higher likelihood. On the other hand, events with not that many hits tend to have a lower likelihood. However, a larger likelihood does not necessarily mean a better reconstructed event. Therefore, this new cut parameter is a good measure to quantify the quality of reconstruction per hit. Using the optimal cut algorithm, a cut value of the likelihood/Nhits > 1.144 is determined. In Figure 6.8 the distribution of the likelihood divided by the number of hits of the reconstructed events of the real and simulated ORCA-6 data is shown before and after the event cuts. In the lower part of the figure the ratio between the real data and the simulated data can be seen before and after the event cuts.

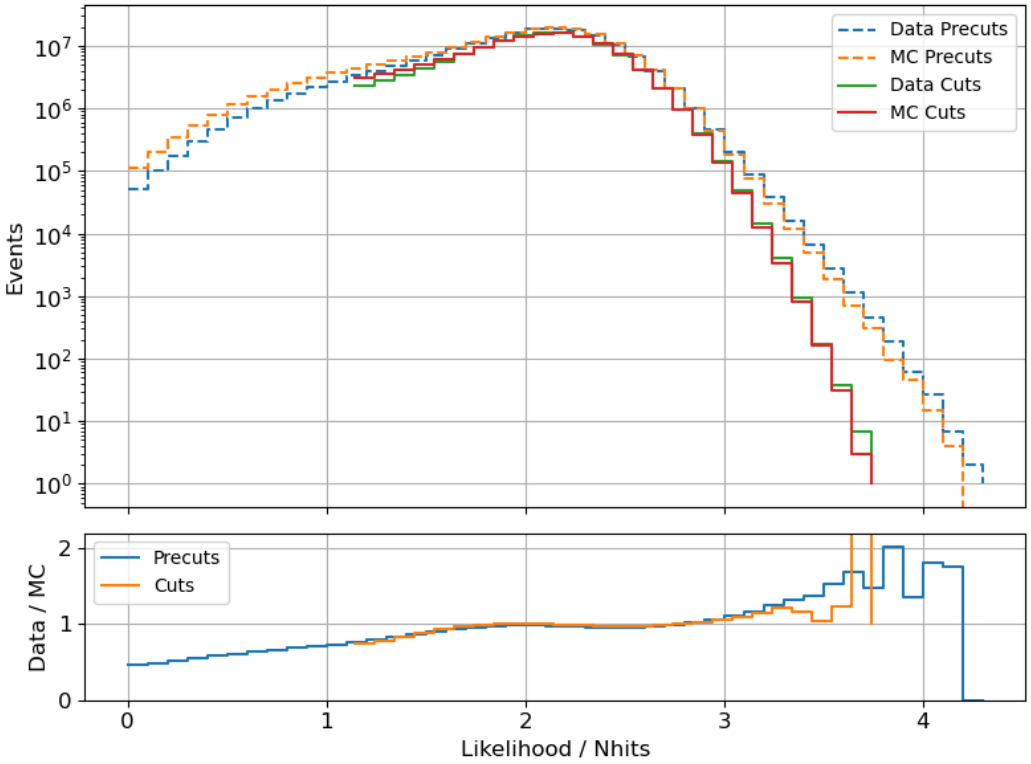

Figure 6.8: Distribution of the likelihood divided by the number of hits of the reconstructed events of the real and simulated ORCA-6 data before and after the event cuts. In the lower part the ratio between the real data and the simulated data is depicted before and after the event cuts.

Opening angle

As discussed above, the optimal cut algorithm calculates the opening angle between the reconstructed direction and the true direction of the simulated data. In Figure 6.9 the three-dimensional opening angle distribution can be seen for the data without cuts, the data with the pre- and the run cuts, and finally for the optimal cuts. Runs with an opening angle larger than $1°$are labelled bad reconstructions. As can be seen, the pre- and run cuts already remove some badly reconstructed events. But the final optimal cuts remove even more badly reconstructed events. The median of the final data set is $0.83°$. In Figure 6.9 a small increase in events around the opening angle of $90°$can be seen; this is likely due to events being reconstructed with the correct zenith angle, but mirrored in the x,y plane.
In Figure 6.10 the distribution of the absolute value of the opening angle of the zenith can be seen for the data without cuts, the data with precuts and run cuts, and finally for the optimal cuts. The final optimal cuts again remove the most badly reconstructed events. The median of the final data set is $0.43°$.

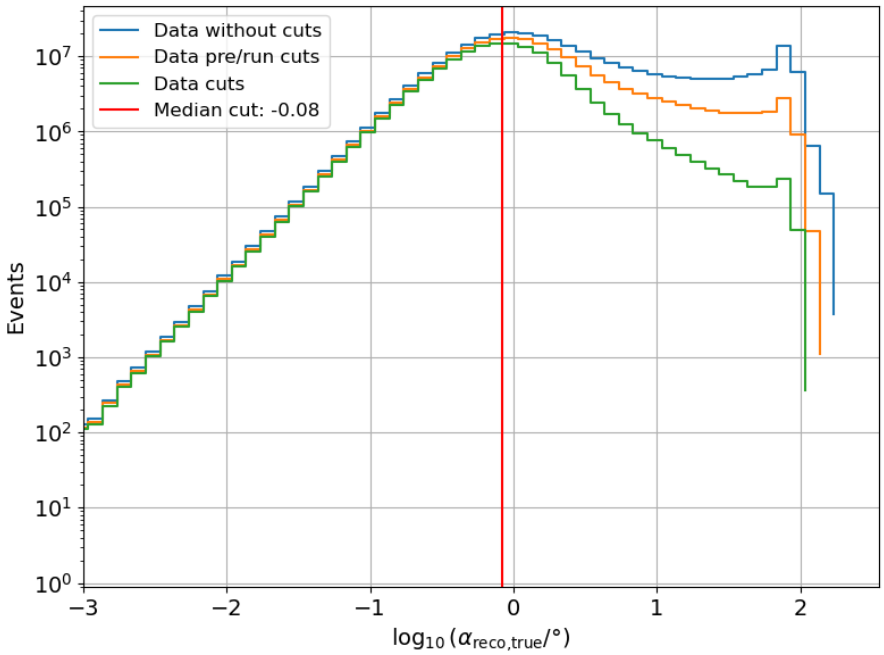

Figure 6.9: Three-dimensional opening angle distribution for the data without cuts in blue, the data with the pre-cuts and the run cuts in orange, and finally for the optimal cuts in green. The median of the data with the optimal cuts is plotted as a vertical line.

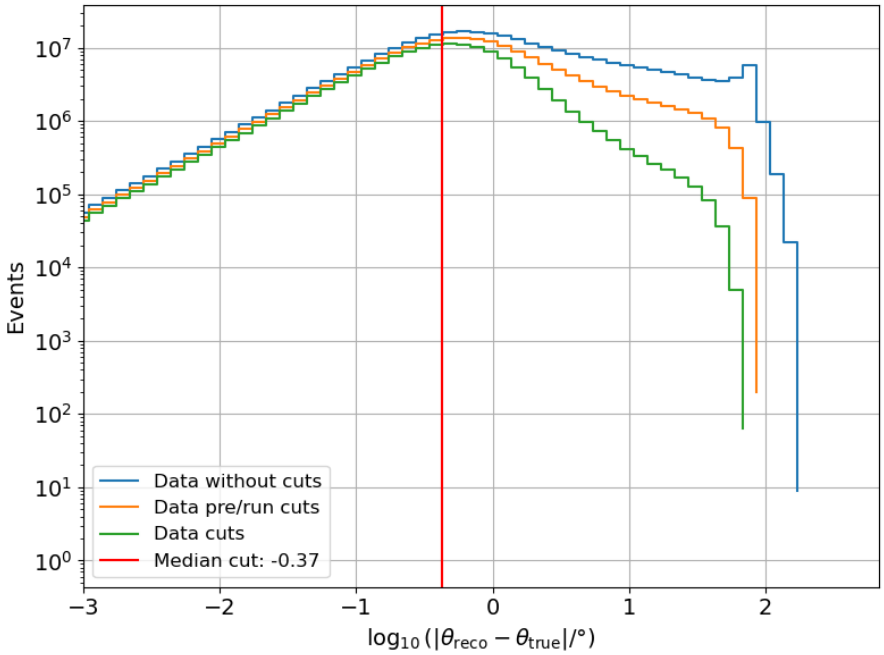

Figure 6.10: Distribution of the absolute value of the opening angle of the zenith for the data without cuts in blue, the data with the pre-cuts and the run cuts in orange, and finally for the optimal cuts in green. The median of the data with the optimal cuts is plotted as a vertical line

Final Cut

For all the different detectors and configurations, the same procedure described above was followed. The cut values found for the detectors are presented in Table 6.2. The cut values for ORCA lie all

relatively close to each other, which makes sense since the detector configuration is similar. The ARCA values are different due to the different configuration and geometry of the detector. For all selected events, the muon trigger must be triggered.

Table 6.2: Data cuts for the different detectors and configurations.

Cut parameter	ORCA-6	ORCA-10	ORCA-11	ORCA-11.1	ORCA-15	ORCA-15.1	ORCA-18	ARCA-21
>Livetime [s]	1200	1200	1200	1200	1200	1200	1200	1200
<HRV	0.2	0.2	0.2	0.2	0.2	0.2	0.2	0.2
<Zenith angle ($\cos(\theta)$)	-0.447	-0.434	-0.434	-0.439	-0.430	-0.432	-0.446	-0.504
>Energy [GeV]	11.323	12.732	12.817	13.603	14.879	14.587	14.960	5.450
>Length [m]	37.996	43.006	43.257	46.080	49.279	48.291	49.132	197.554
>Likelihood	74.298	78.301	76.274	79.029	83.165	83.786	79.840	47.104
>Number of hits	41	41	37	41	47	48	44	30
>Hits / Likelihood	1.144	1.095	1.104	1.022	0.984	0.965	0.917	0.835

In Table 6.3 the statistics of the data sets are shown for the raw data, the data with pre- and run cuts, and the data with the final event cuts applied. As can be seen, the pre- and run cuts remove the biggest part of faulty data, and the event cuts fine-tune it more. The start and end dates of the detector configurations data taking period are also shown in the table. The total amount of days in between de start and end date does not have to be the same as the livetime of the raw data. This is because there can be missing of faulty data already removed from the raw dataset.

Table 6.3: Statistics of the data sets for the raw data, the data with pre- and run cuts, and the data with the final event cuts applied..

Statistic	ORCA-6	ORCA-10	ORCA-11	ORCA-11.1	ORCA-15	ORCA-15.1	ORCA-18	ARCA-21
Start data	26-1-2020	24-11-2021	26-07-2022	14-09-2022	16-12-2022	05-04-2023	01-05-2023	22-09-2022
End data	18-11-2021	10-05-2022	05-09-2022	06-12-2022	05-04-2023	26-04-2023	09-01-2024	11-09-2023
Data without cuts								
Livetime [days]	402.19	105.65	32.79	12.36	62.87	7.50	70.43	98.62
Data events	3.224×10^8	1.112×10^8	3.161×10^7	1.265×10^7	9.104×10^7	1.170×10^7	1.145×10^8	4.287×10^7
MC events	2.904×10^8	8.996×10^7	3.024×10^7	1.186×10^7	6.797×10^7	8.172×10^6	8.560×10^7	4.271×10^7
$\langle R_{data} \rangle$ [Hz]	9.231	12.221	11.147	11.848	16.634	18.063	18.831	5.032
$\langle R_{MC} \rangle$ [Hz]	8.075	9.617	10.273	10.807	12.133	12.120	13.010	4.875
Median HRV	0.044	0.073	0.038	0.025	0.052	0.078	0.064	0.001
Pre and run cuts								
Livetime [days]	367.87	94.62	28.019	12.36	57.56	5.75	66.19	98.50
Data events	1.810×10^8	5.961×10^7	1.947×10^7	8.604×10^6	4.605×10^7	4.689×10^6	6.195×10^7	2.832×10^7
MC events	1.951×10^8	6.213×10^7	2.059×10^7	9.136×10^6	4.906×10^7	4.975×10^6	6.427×10^7	2.820×10^7
$\langle R_{data} \rangle$ [Hz]	5.693	7.297	8.036	8.055	9.256	9.425	10.822	3.329
$\langle R_{MC} \rangle$ [Hz]	5.932	7.424	8.195	8.324	9.643	9.720	10.436	3.219
Median HRV	0.039	0.058	0.032	0.025	0.041	0.073	0.055	0.001
Event cuts								
Livetime [days]	367.87	94.62	28.019	12.36	57.56	5.75	66.19	98.50
Data events	1.328×10^8	4.416×10^7	1.461×10^7	6.581×10^6	3.505×10^7	3.553×10^6	4.493×10^7	2.121×10^7
MC events	1.371×10^8	4.540×10^7	1.489×10^7	6.644×10^6	3.601×10^7	3.651×10^6	4.582×10^7	2.116×10^7
$\langle R_{data} \rangle$ [Hz]	4.176	5.408	6.030	6.161	7.043	7.137	7.848	2.493
$\langle R_{MC} \rangle$ [Hz]	4.167	5.426	5.926	6.054	7.077	7.126	7.440	2.415
Median HRV	0.039	0.057	0.032	0.025	0.041	0.073	0.055	0.001

6.2. Average threshold energy $\langle E_{\text{thr}} \cos\theta \rangle$

$\langle E_{\text{thr}} \cos\theta \rangle$ is the average minimum energy, adjusted for the zenith angle, a muon needs at sea-level in order to reach the detector and be detected. When the zenith angle is larger, the muons need to travel a longer path through the water, and thus need higher energies to reach the detector and be detected. In order to calculate the average threshold energy, the events will be binned based on the zenith angle. The central value of the zenith angle in a bin will then be used to calculate the initial energy at sea level needed for a muon to reach the detector and be detected. The average threshold energy can be calculated as [10]:

$$\langle E_{\text{thr}} \cos\theta \rangle = \sum_i E_{\text{thr}}(cos(\theta_i)) \cdot n(cos(\theta_i)) \cdot |cos(\theta_i)| \tag{6.1}$$

The index i runs through zenith angle $(cos(\theta))$ bins, ranging from -1 to the cutoff value with steps of 0.01. $cos(\theta_i)$ is the value at the centre of the bin, $n(cos(\theta_i))$ is the muon flux normalised to unity in the $cos(\theta_i)$-th bin, and $E_{\text{thr}}(cos(\theta_i))$ is the energy needed at sea level to be detected in the $cos(\theta_i)$-th bin. $E_{\text{thr}}(cos(\theta_i))$ can be calculated analytically using Equation 2.11 and numerically using Equation 2.10. For analytical calculations, constant approximations for the loss parameters have to be chosen. For the numerical approach, the loss parameters acquired from the Particle Data Group [20] are interpolated to get a more accurate result. In order to calculate the energy at sea level, the minimal detected muon energy is needed. This minimal energy will be the minimal reconstructed energy found in the datasets for the specific detectors after cutting. Because the minimal reconstructed energy is different for every detector and configuration, due to different geometries, each detector and configuration will have its own unique average threshold energy.
In order to obtain an error estimate for the average threshold energy, both dependencies of the $cos(\theta)$ bin width (angular resolution) and the minimal reconstructed energy of the detected muon (energy resolution) are taken into account. In order to estimate the uncertainty due to angular resolution, the average threshold energy is calculated for different bin widths. Then the standard deviation of the resulting energies is taken to be the uncertainty due to angular resolution. For the determination of the uncertainty due to the energy resolution, a Gaussian distribution is assumed where the mean is the minimal reconstructed energy and the spread is assumed to have an energy resolution of 10%. The energy resolution is probably significantly larger, but due to the depth of the detector, this will not have a large effect on the end result. A wide range of energies reaches approximately the same depth, especially for the depths of the KM3NeT detectors; see Figure 2.7. Then 4000 Monte Carlo samples are taken from this distribution, and the average threshold energy is calculated for each of them. The standard deviation that follows from this distribution of average threshold energies is taken to be the uncertainty due to the energy resolution. The total error is then the quadratic sum of the uncertainty due to the angular and energy resolution.

6.3. Effective atmospheric temperature

6.3.1. AIRS

The effective atmospheric temperature above the detectors has to be calculated for a volume of atmosphere in order to account for different zenith angles of the incoming muons. The zenith cutoff value for the different detectors is used to determine the size of a cone-like shape in which all the muons travel. For example, ORCA-6 has a cutoff value of the zenith of -0.447. At the highest pressure layer of AIRS at 1 hPa or approximately 60 kilometres altitude, this translates to a radius of 120 kilometres of the cone. To calculate the radius at any point in the altitude, the simple equation $radius = height \cdot tan(\theta)$ can be used. Now, because the AIRS temperature data are binned in 1°x 1°latitude and longitude bins, only the bins where the centre fall in the top radius of the cone are selected. For the ORCA-6 example this corresponds to 42.5 and $43.5°E$ latitude and 5.5 and $7.5°N$ longitude bins. For all of these bins, the average temperature per pressure layer per measurement time is calculated to obtain an average temperature profile above the detector. This temperature profile is then used to calculate the effective temperature above the detector at every measurement moment with Equation 3.16. So, at every overpass time or measurement time, shown in Figure 5.1, which falls within the lifespan of a specific detector, an efficient temperature will be calculated. Every detector configuration spans over a different time period and has a slightly different average threshold energy. Therefore, an effective temperature over time will be calculated specific to every detector.

6.3.2. ERA5

For ERA5 temperature data, the same approach described above for the AIRS data can and will be used. The highest pressure layer measurements of ERA5 are the same as for AIRS but it has more layers than AIRS. ERA5 also has hourly data points compared to the two measurements per day of AIRS. So, it will be interesting to see what the effect is. ERA5 could give a more accurate representation of the effective temperature coefficient because the muon events all have a temperature measurement relatively close. However, the main difference between the ERA5 and AIRS data is that ERA5 has 0.25°x 0.25°latitude and longitude bins. This makes it possible to apply a different approach to the calculation of the effective temperature. Now, no single effective temperature over time is used for all muon tracks in a detector configuration, but multiple effective temperatures over time are calculated for

muons with different directions. In order to do this, muons will be binned using their zenith and azimuth angles, which will be determined later. The mean zenith and azimuth angle of each these bins will be used to calculate a general path through the atmosphere. This general paths will be used to represent the path of all the muon within a bin. The ranges for the bins are shown in Table 6.4. The bin names are formatted as 'Bin_Z_A'. where Z stands for the bin number of the zenith angle, 0 are smaller angles, and 1 are larger angles. A stands for the bin number of the azimuth angle, ranging from 0 to 3.

Table 6.4: Zenith and azimuth angles bins used for different temperature profiles and sorting muon events. The bin names are formatted as 'Bin_Z_A'. where Z stands for the bin number of the zenith angle, 0 are smaller angles, and 1 are larger angles. A stands for the bin number of the azimuth angle, ranging from 0 to 3.

Bin	Zenith Angle Range (°)	Central Zenith Angle (°)	Azimuth Angle Range (°)	Central Azimuth Angle (°)
Bin_0_0	$0 - 32.5$	16.25	$-180 - -90$	-135
Bin_0_1	$0 - 32.5$	16.25	$-90 - 0$	-45
Bin_0_2	$0 - 32.5$	16.25	$0 - 90$	45
Bin_0_3	$0 - 32.5$	16.25	$90 - 180$	135
Bin_1_0	$32.5 - 65$	48.75	$-180 - -90$	-135
Bin_1_1	$32.5 - 65$	48.75	$-90 - 0$	-45
Bin_1_2	$32.5 - 65$	48.75	$0 - 90$	45
Bin_1_3	$32.5 - 65$	48.75	$90 - 180$	135

In order to determine the eight general paths that the muons take for each of the bins, the height of every pressure layer needs to be determined. This is done with the barometric formula. Then for every height, using the central zenith and azimuth angle, the latitude and longitude are calculated with respect to the detector position. First, the horizontal change due to the zenith angle is determined, and then this is decomposed into x and y components using the azimuth angle. Then these x and y change components are translated into the change of latitude and longitude. Now the latitude and longitude coordinates at every height are known. However, the ERA5 data still has only temperature measurements at every 0.25° latitude and longitude. Therefore, the calculated coordinates of the path are matched to the closest grid points. In Figure 6.11 the eight general muon paths in the atmosphere are shown schematically. All the paths start from the detector coordinates, which in this case is ORCA, and then spread out in the atmosphere. With these general paths, it is possible to determine the temperature at each pressure level closest to the true general muon path for every direction bin. At every point in the atmospheric layer it is known to which grid point (latitude, longitude) a general muon path is closest, so the temperature only at that grid point is added to the temperature profile. This creates more accurate temperature profiles for the muons in each of the bins. These temperature profiles are then used to calculate the effective temperature for each of the bins at every measurement moment with Equation 3.16.

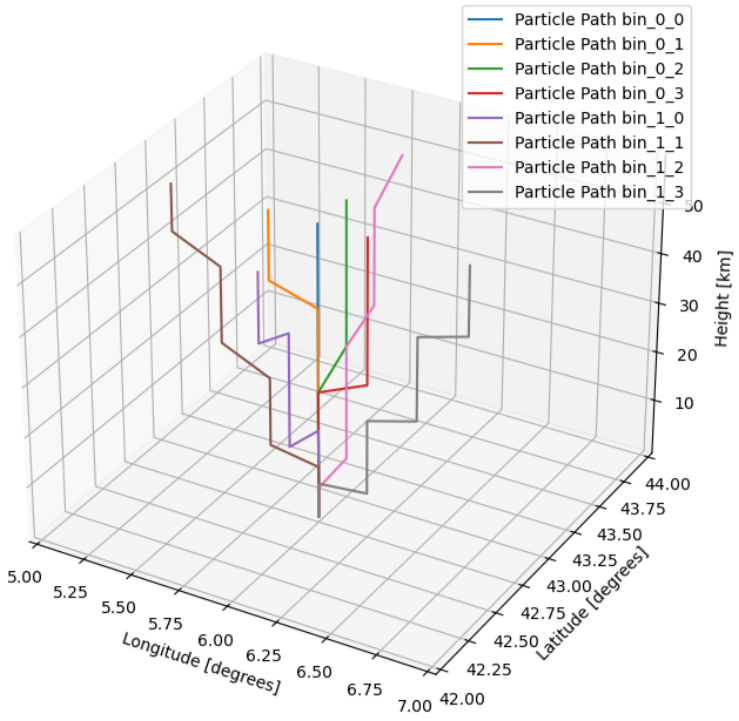

Figure 6.11: General muon paths in the atmosphere for each of the eight bins. All the paths start from the detector coordinates, which in this case is ORCA, and then spread out in the atmosphere.

6.3.3. Error effective temperature

In order to get an estimate of the error in the effective temperature, a toy Monte Carlo simulation is performed. For 400 days, the effective temperature was calculated 3000 times by sampling from Gaussian distributions based on AIRS and ERA5 data. Distributions are defined by the mean temperature and standard deviation of each pressure layer over a detector configuration period. Similarly, the weights for the calculation are sampled from a Gaussian, using the mean and standard deviation of the weights in each pressure layer. For each day, a distribution of effective temperatures follows with a standard deviation. The mean of all standard deviations for all days will be the error of the effective temperature. This approach will be used for the AIRS data and for both ERA5 effective temperature calculations.

6.4. Ratio of data and simulation

In Section 4.4, the run-by-run Monte Carlo simulations were introduced and explained. The simulation should follow the real detector conditions as closely as possible except for the seasonal variation of the muon rate. It was also shown that the rate in the real data was affected by environmental conditions, in particular bioluminescence, and detector conditions, such as changing PMT efficiencies. The ratio of the real data rate and the Monte Carlo rate can now be given by:

$$\begin{aligned} R_{\frac{data}{mc}}(t) &= \frac{R_{data}(t)}{R_{MC}(t)} \\ &= \frac{R_{true}(t) \times C_{data}(t)}{R_{const} \times C_{MC}(t)} \end{aligned} \tag{6.2}$$

C represents here all the factors that have an influence on the detected muon rate expect the seasonal variation. Now, the assumption that is made for the simulation is that it accurately models all influences on the rate except the influence of the atmospheric temperature. So, $C_{data}(t) = C_{MC}(t)$. The ratio will then become:

$$R_{\frac{data}{mc}}(t) = \frac{R_{true}(t)}{R_{const}} \tag{6.3}$$

In the ideal case $R_{\frac{data}{mc}} = 1$, all the influences are correctly simulated. So by studying this ratio as defined in Equation 6.2, the changing behaviour of the true ratio $R_{true}(t)$ due to the atmospheric temperature changes can be probed. This approach will only work if the simulations are accurate. If some factors are not (fully) taken into account, deviations from the expected correlation will occur when the ratio is correlated with the effective temperature.
Substituting the newly defined ratio, which only describes the influence of atmosphere temperature on the rate, into Equation 3.15 gives a more accurate representation of the true muon rate. Rewrite Equation 6.3 as $R_\mu(t) = R_{true}(t) = R_{\frac{data}{mc}}(t) \cdot R_{const}$, and substituting it into the left part of Equation 3.15, so that:

$$\begin{aligned} \frac{R_\mu(t) - \langle R_\mu \rangle}{\langle R_\mu \rangle} &= \frac{R_{\frac{data}{mc}}(t) \cdot R_{\text{const}} - \langle R_{\frac{data}{mc}}(t) \cdot R_{\text{const}} \rangle}{\langle R_{\frac{data}{mc}} \cdot R_{\text{const}} \rangle} \\ &= \frac{R_{\frac{data}{mc}}(t) \cdot R_{\text{const}} - \langle R_{\frac{data}{mc}}(t) \rangle \cdot \langle R_{\text{const}} \rangle}{\langle R_{\frac{data}{mc}}(t) \rangle \cdot \langle R_{\text{const}} \rangle} \end{aligned} \tag{6.4}$$

Since R_{const} is constant over time ($R_{const} = \langle R_{\text{const}} \rangle$), it can be divided out. Giving the final relation between the ratio of the real data and the Monte Carlo simulation and the effective temperature:

$$\begin{aligned} \frac{R_{\frac{data}{mc}}(t) - \langle R_{\frac{data}{mc}}(t) \rangle}{\langle R_{\frac{data}{mc}}(t) \rangle} &= \alpha_T \frac{T_{eff}(t) - \langle T_{eff} \rangle}{\langle T_{eff} \rangle} \\ \frac{\Delta R_{\frac{data}{mc}}}{\langle R_{\frac{data}{mc}} \rangle} &= \alpha_T \frac{\Delta T_{eff}}{\langle T_{eff} \rangle} \end{aligned} \tag{6.5}$$

It is important to note that for this derivation, R_{const} is assumed to be constant for the whole data set for which the ratio is computed. If this is not the case, for example, between different detectors and configurations, the ratio and its mean value should be calculated separately for each data set. Therefore, in this study, an effective temperature coefficient will be determined for all different detectors and configurations.
In order to check this for every detector and configuration, the mean values of the ratio and the effective temperatures can be calculated for different timespans. In principle, one would expect the effective temperature coefficient to be constant over time. However, if some factors are not correctly simulated, the effective temperature coefficient might differ from what would be expected theoretically.

6.4.1. Ratio decrease over time

The assumption made for using the ratio to determine the effective temperature coefficient was that the simulation accurately models all influences on the rate except the influence of the atmospheric temperature. However, this might not be true. An effect that will be tested is a linear decrease in the ratio over time. This could hint that the efficiency losses in the detector are not fully accounted for in the simulation. In order to do this, a cosine model with a linear trend will be fitted through the temperature data and the ratio data. The assumption here is that a sinusoidal function with a period of one year is the dominant mode. First, a fit with a period of one year will be done through the four years of temperature data. Using this fit, a new fit can be made through the ratio data. In order to line up the fits of the temperature and the ratio, the same period of one year and the phase found in the temperature fit will be used for the ratio fit. The following fit model will be used:

$$ratio = A \times cos(\frac{2\pi}{period} \times t + phase) + B \times t + offset \tag{6.6}$$

where A the amplitude of the oscillations is, t the time and B the linear trend coefficient. For the temperature fit, phase, offset, and amplitude are free parameters, and the period will be set to one year and the linear trend coefficient to 0. For the fit of the ratio, the linear trend coefficient, the offset, and the amplitude are free parameters. The period is again fixed to one year and the phase is fixed on the phase found for the temperature fit. For the fit of the ratio, a linear trend coefficient of 0 and an offset of 1 would be expected if the simulations were perfect, assuming only the temperature behaves as a sinusoidal function and the ratio is perfectly correlated with the temperature.

6.4.2. Ratio calculation AIRS

The data rate, the number of muons per second ($R_{data}(t) = N(t)/\Delta t$), can be calculated for different times and time intervals. For AIRS temperature data, the temperature is known for two overpasses a day. So, the rate will be calculated for a data run when one of these overpass times falls within the duration of the run. However, the rate within a run or within any other time period could still vary, causing some scattering. Therefore, the rate will also be calculated for events that occur ± 30 minutes around these overpass times to try to minimise this scattering. It could happen that a temperature measurement happens at the beginning or end of a run, so, for example, only 40 minutes of the 60 minute time window falls within one run. Therefore, only events that occur in a run in which a temperature measurement occurs can be selected in this way. Extra attention should be paid to the rate calculation because Δt is therefore not a constant, but should be calculated every time to obtain an accurate rate. If the overlap time is shorter than 40 minutes, the rate will not be calculated due to a lack of statistics, and this data point will no longer be used in future calculations.
The rate calculation for the Monte Carlo simulations is slightly different. The timestamps within a run in the Monte Carlo simulation have no physical meaning, so they cannot be used to select only events close to a temperature measurement. Therefore, the rate will always be constant in a run. Because the number of events of a simulation run is not exactly the same as the number of events of a real run, the Monte Carlo data needs to be scaled to be able to compare them to the real data. The rate of will be calculated using a weight w that differs for every run but is close to 1. The Monte Carlo rate will be calculated by counting the events in a run, scaling this by the weight w and dividing this by the livetime of the real run.
The data rate can thus vary in the same run, but the Monte Carlo rate is always constant in a run. The data rate will thus be calculated in two different ways, and the Monte Carlo rate will only be calculated in this one way.
The ratio $R_{\frac{data}{mc}}$, can now simply be calculated by dividing the data rate by the Monte Carlo rate. Note that the ratio can only be calculated when the data rate and the Monte Carlo rate are from the same run.

6.4.3. Ratio calculation ERA5

For the second effective temperature calculation approach discussed for the ERA5 data, different temperature profiles were calculated for the different bins presented in Table 6.4. Now, for each of the bins, a muon rate and ratio need to be determined. In order to do this, the zenith and azimuth angles of the muons need to be determined. For every muon event, a direction vector is known. However, this direction vector is calculated using a UTM coordinate system that is slightly different from the coordinate system that uses the geographical north used by ERA5. Therefore, the direction vector must be rotated to align with the temperature data coordinate system according to:

$$\begin{aligned} x_{\text{rot}} &= x\cos(\gamma) - y\sin(\gamma), \\ y_{\text{rot}} &= x\sin(\gamma) + y\cos(\gamma), \\ z_{\text{rot}} &= z \end{aligned} \tag{6.7}$$

As can be seen the z direction component is not affected by this rotation. The rotation angle γ for ORCA is $-2.02°$and for ARCA $0.65°$. Now the zenith and the azimuth angle can be calculated with:

$$\begin{aligned} zenith &= \arccos(z) \\ azimuth &= \arctan 2(x_{\text{rot}}, y_{\text{rot}}) \end{aligned} \tag{6.8}$$

For reconstructed directions in both the real data and the Monte Carlo data the zenith and azimuth will be calculated and used to bin the events into the bins presented in Table 6.4. Then the data rate and the Monte Carlo rate can be calculated in the same way as described in Section 6.4.2. However, because ERA5 data have hourly data points, the rate will only be calculated in 60 minute time windows. Again, the same thing can happen that a time window is cut short by the start of end of a run, so extra care is needed here. Also, when the time window is shorter than 40 minutes, the data will not be used to have sufficient statistics. The Monte Carlo rate calculation will be exactly the same as described before, which is a constant rate for a whole run.
Because there is more than one temperature measurement in one run for ERA5 data, there are more

than one data rate for one run. However, there is still only one Monte Carlo rate for one run. So when calculating the ratio, the data rate will change, but the Monte Carlo rate will remain the same within a run.

In order to compare the ERA5 data and the AIRS data more directly, the ratio will also be calculated without the binning but with the 60 minute time windows.

6.4.4. Uncertainty of the ratio

The uncertainty of the ratio is made up of two parts, the statistical and the systematic error. The statistical error of the ratio is a Poisson error due to the event counts in the real data N_{data} and the Monte Carlo data N_{MC}, added quadratic [19]:

$$\left[\frac{\sigma\left(R_{\frac{data}{mc}}\right)}{R_{\frac{data}{mc}}}\right]^2_{\text{stat}} = \left(\frac{\sqrt{N_{\text{data}}}}{N_{\text{data}}}\right)^2 + \left(w\frac{\sqrt{N_{\text{MC}}/w}}{N_{\text{MC}}}\right)^2 = \frac{1}{N_{\text{data}}} + \frac{w}{N_{\text{MC}}} \tag{6.9}$$

where w is the weight used for scaling the Monte Carlo simulations.
The systematic uncertainty will be estimated using the standard deviation ($std(\Delta R_{data})$) of the change in rate between consecutive rate calculations for a detector configuration. This is because the rate could change during a time window corresponding to a temperature measurement. This could cause some scattering of the effective temperature coefficient. To account for this account for this the systematic uncertainty will be added in quadrature to the statistical uncertainty, resulting in the total uncertainty [19]:

$$\left[\frac{\sigma\left(R_{\frac{data}{mc}}\right)}{R_{\frac{data}{mc}}}\right]^2_{\text{tot}} = \frac{1}{N_{\text{data}}} + \frac{w}{N_{\text{MC}}} + \left(\frac{std(\Delta R_{data})}{\langle R_{data}\rangle}\right)^2 \tag{6.10}$$

6.5. Fit model

The ratio and effective temperature in Equation 6.5 are now known. To determine the effective temperature coefficient, α_T, a model must be fitted to the data. In this study the following model will be used:

$$\frac{\Delta R_{\frac{data}{mc}}(t)}{\langle R_{\frac{data}{mc}}\rangle} \times 100\% = \alpha_T \frac{\Delta T_{eff}(t)}{\langle T_{eff}\rangle} \times 100\% + \beta \tag{6.11}$$

where both α_T and β are free parameters. β is added to account for possible systematic shifts in muon rate or temperature. The addition of the percentages is not necessary but makes the interpretation of the results easier. To utilise the errors in the ratio and effective temperature, the errors are scaled by $100\%/\langle R_{\frac{data}{mc}}\rangle$ and $100\%/\langle T_{eff}\rangle$, respectively. In order to fit a line through the data and account for the errors in both the x and y values, a regular least-square fitting cannot be used. Therefore, the orthogonal distance regression fit is used, taking into account the errors in both dimensions [39].

7

Results

7.1. Average threshold energy $\langle E_{\text{thr}} \cos\theta \rangle$

ORCA-6 will be used to illustrate a general result. The calculations for all detectors and configurations are based on the same calculations and steps. In Figure 7.1 the results of the calculation for $E_{\text{thr}}(cos(\theta_i))$ are shown for both the analytical approach in blue using Equation 2.11 and the numerical approach in orange using Equation 2.10. Because the numerical approach gives more accurate results, the calculations proceed with these results.

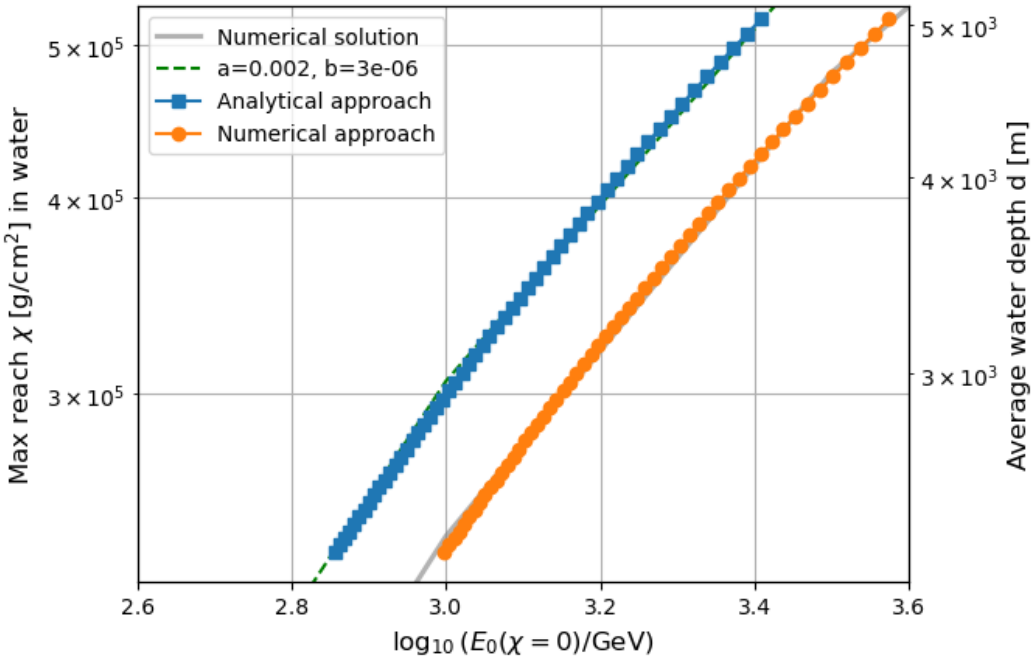

Figure 7.1: Maximum slant depth reach in water by muons with starting energy E_0. The solid grey line is the numerical solution of Equation 2.10. The dashed lines are the analytical solutions with constant loss parameters (Equation 2.13). Changes in density due to temperature and salinity changes make the conversion from slant depth to average depth not constant. The blue data points are the result of calculating the energy needed for different zenith angles to reach the detector with an analytical approach. The orange data points are the result of calculating the energy needed for different zenith angles to reach the detector with an numerical approach.

The results of the uncertainty analysis due to the angular resolution for ORCA-6 are shown in Figure 7.2. The standard deviation and thus the uncertainty due to the angular resolution is 3 GeV.

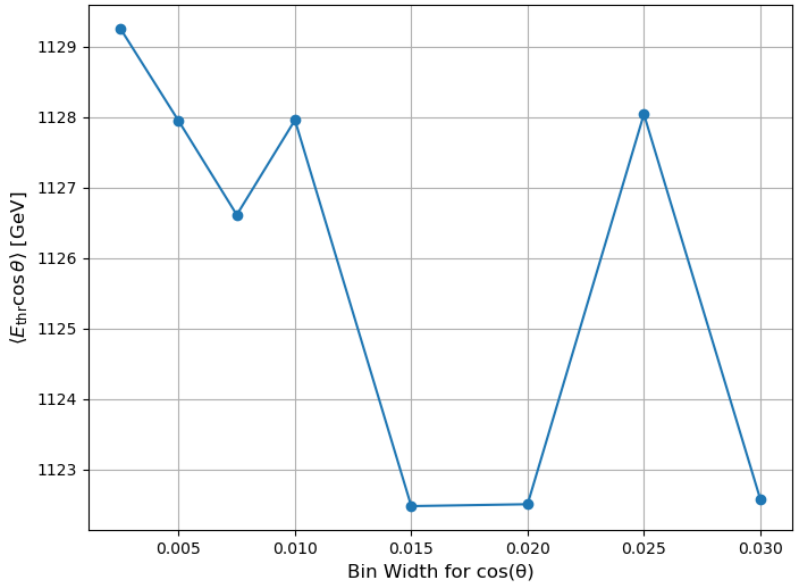

Figure 7.2: Distribution of average threshold energy due to varying the bin width of the zenith angle bins. The standard deviation of this distribution is assumed to be the uncertainty due to the angular resolution.

The results of the uncertainty analysis due to the energy resolution of ORCA-6 are shown in Figure 7.2. The standard deviation and thus the uncertainty due to the energy resolution is 17 GeV. This is significantly larger than the uncertainty because of the angular resolution. As mentioned above, the energy resolution probably has been underestimated and could be significantly larger than 10%. However, the impact of this is expected to be minimal because of the depth of the detector. If the detector was closer to the surface, the impacts could have been greater.

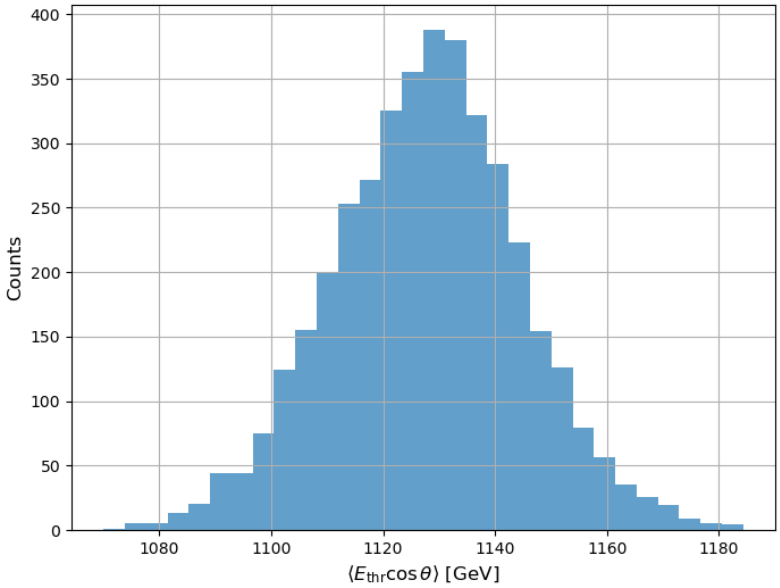

Figure 7.3: Distribution of average threshold energy due to random sampling of the minimal reconstructed muon energy from a Gaussian distribution. The standard deviation of this distribution is assumed to be the uncertainty due to the energy resolution.

In the table below the average threshold energies with uncertainties for all detectors and configurations are show. ARCA-21 has a significantly higher average threshold energy than ORCA detectors because the detector is much deeper in the water. Therefore, muons that reach the detector need to have more energy to be able to penetrate the additional water layers compared to ORCA.

Table 7.1: Average threshold energies with uncertainties for all detectors and configurations.

Detector	$\langle E_{\mathbf{thr}} \cos\theta \rangle$ [GeV]	σ [GeV]
ORCA-6	1128	17
ORCA-10	1134	17
ORCA-11	1132	17
ORCA-11.1	1136	17
ORCA-15	1136	17
ORCA-15.1	1136	18
ORCA-18	1135	17
ARCA-21	1933	35

7.2. Theoretical temperature coefficient

Using the average threshold energies, the theoretical temperature coefficients can be calculated using Equations 3.20 and 3.22. In Figure 7.4 the theoretical values of the temperature coefficient are plotted versus the average energy threshold. In yellow, green, and blue are the pion, kaon, and total contributions, respectively. On the left side is a complete overview of the spectrum and on the right a more zoomed-in picture. The detectors are highlighted by the coloured dots.

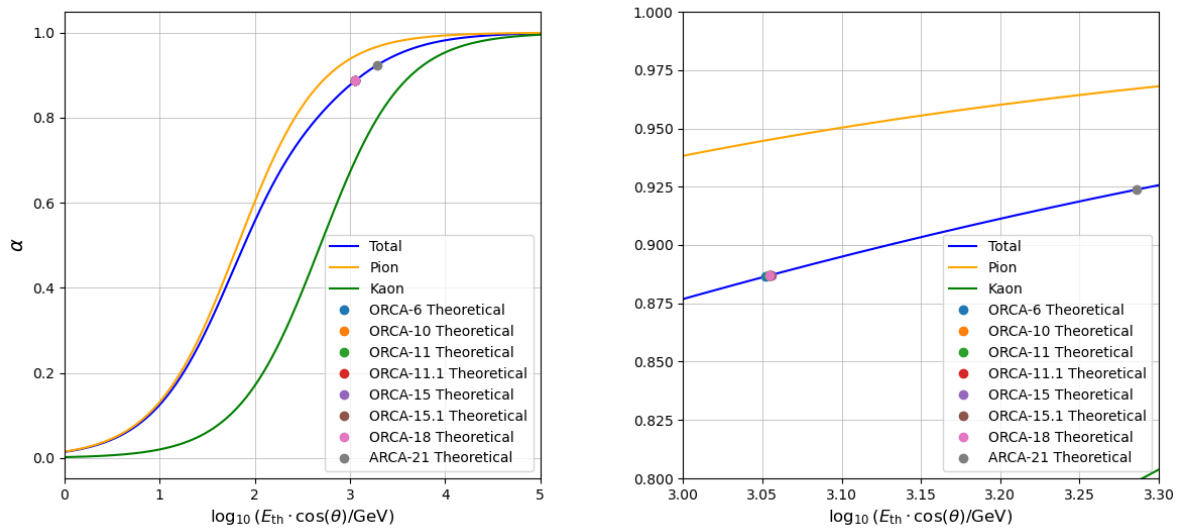

Figure 7.4: Theoretical values of the temperature coefficient plotted versus the average energy threshold. In yellow, green, and blue are the pion, kaon, and total contributions, respectively. On the left complete overview of the spectrum and on the right a more zoomed-in picture. The detectors are highlighted by the coloured dots.

In Table 7.2 the theoretical values for the overall theoretical temperature coefficient as well as the contributions of the pions and kaons can be seen for all detectors and configurations.

Table 7.2: The theoretical values for the overall temperature coefficient as well as the contributions of the pions and kaons can be seen for all detectors and configurations.

Detector	$\langle E_{\mathbf{thr}} \cos\theta \rangle$ [GeV]	α^{th}	α_{π}^{th}	α_{K}^{th}
ORCA-6	1128	0.8865	0.9449	0.6984
ORCA-10	1134	0.8870	0.9451	0.6994
ORCA-11	1132	0.8870	0.9450	0.6992
ORCA-11.1	1136	0.8871	0.9452	0.6999
ORCA-15	1136	0.8872	0.9452	0.7000
ORCA-15.1	1136	0.8871	0.9452	0.6999
ORCA-18	1135	0.8870	0.9452	0.6996
ARCA-21	1932	0.9238	0.9671	0.7987

As can be seen from both the graph and the table, the temperature coefficient becomes higher as the average energy threshold becomes larger. This makes sense because, as discussed before, high-energy muons are mainly produced in the upper part of the atmosphere where their parent mesons decay chances are directly impacted by the temperature variations. The lower-energy muons that are formed in these upper parts of the atmosphere are more susceptible to decay themselves before they can reach a detector and be detected, thus reducing the correlation seen between the muon rate and atmospheric temperature at lower energies. In addition to this, lower-energy muons that are formed by decay from mesons below their critical energy are less effective by temperature variations because the lower-energy mesons have higher decay changes regardless of temperature variations.

7.3. Atmospheric temperature profile

The atmospheric profiles were acquired through two data sets, AIRS and ERA5, see Section 6.3.

7.3.1. AIRS

In Figure 7.5 the atmospheric temperature profile above ORCA is shown for the AIRS data. The left y-axis shows the pressure on a logarithmic scale and the right y-axis shows the average geometrical height above sea level. Changes in density due to changes in temperature make the conversion from pressure to geometric height not constant. During the summer, relatively smooth temperature changes are observed. In winter, more sudden spikes in temperature occur. In Figure 7.6 the atmospheric temperature profile above ARCA is shown in the same way.

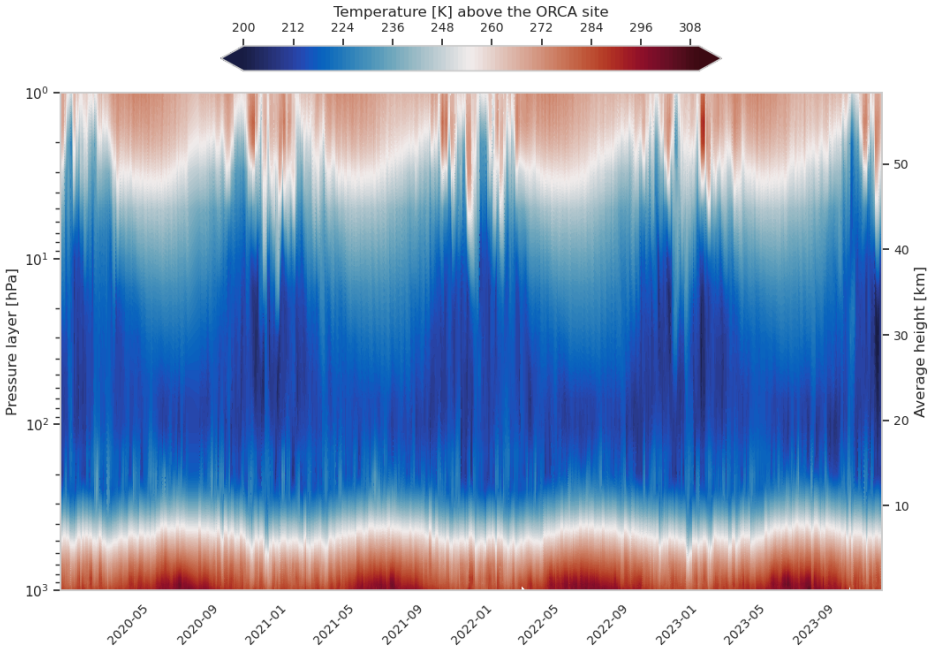

Figure 7.5: Contour plot of the average atmospheric temperature over the selected region per pressure layer above the ORCA detector for the AIRS data. The left y-axis shows the pressure on a logarithmic scale and the right y-axis shows the average geometrical height above sea level. Changes in density due to changes in temperature make the conversion from pressure to geometric height not constant.

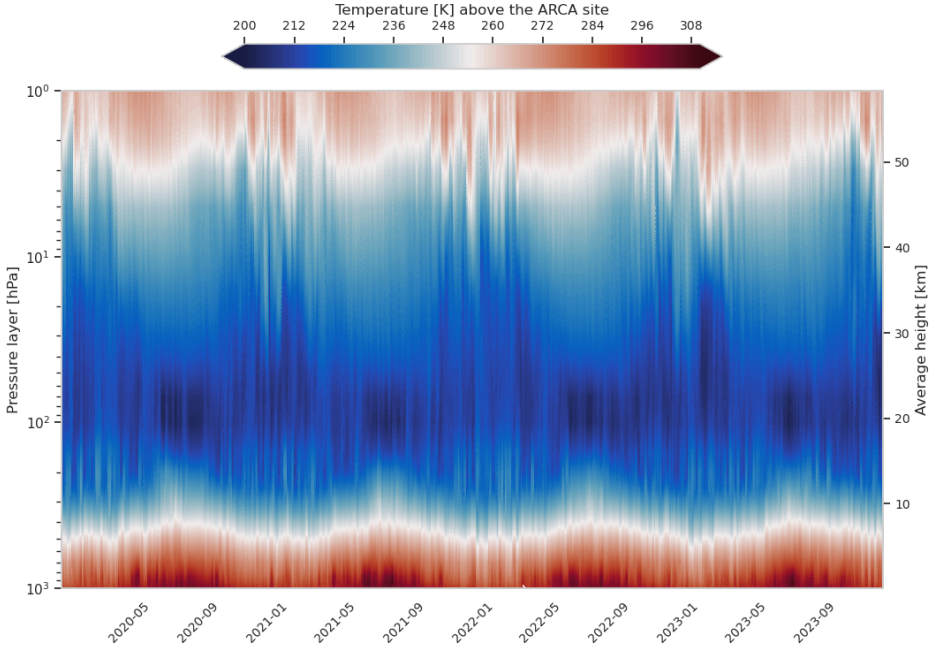

Figure 7.6: Contour plot of the average atmospheric temperature over the selected region per pressure layer above the ARCA detector for the AIRS data. The left y-axis shows the pressure on a logarithmic scale and the right y-axis shows the average geometrical height above sea level. Changes in density due to changes in temperature make the conversion from pressure to average geometric height not constant.

The differences between two consecutive measurements, ΔT, also called the rolling difference, provide a measure of the short-term variations and their differences between the pressure layers. The density of the distribution of ΔT for every pressure layer has been plotted in a violin plot for ORCA in Figure 7.7 and for ARCA in Figure 7.8. The 1 hPa pressure layer for ORCA has two maximums at ± 2.5 K. It can also be seen that the distribution ΔT is more narrow for pressure layers between 10 and 100 hPa. For ARCA, the pressure layers between 10 and 100 hPa are also the most narrow, but the clearly visible dual peak of the 1 hPa pressure layer of ORCA is no longer visible. However, it can still be seen that the 1 hPa distribution of ARCA is noticeably wider than that of other layers.

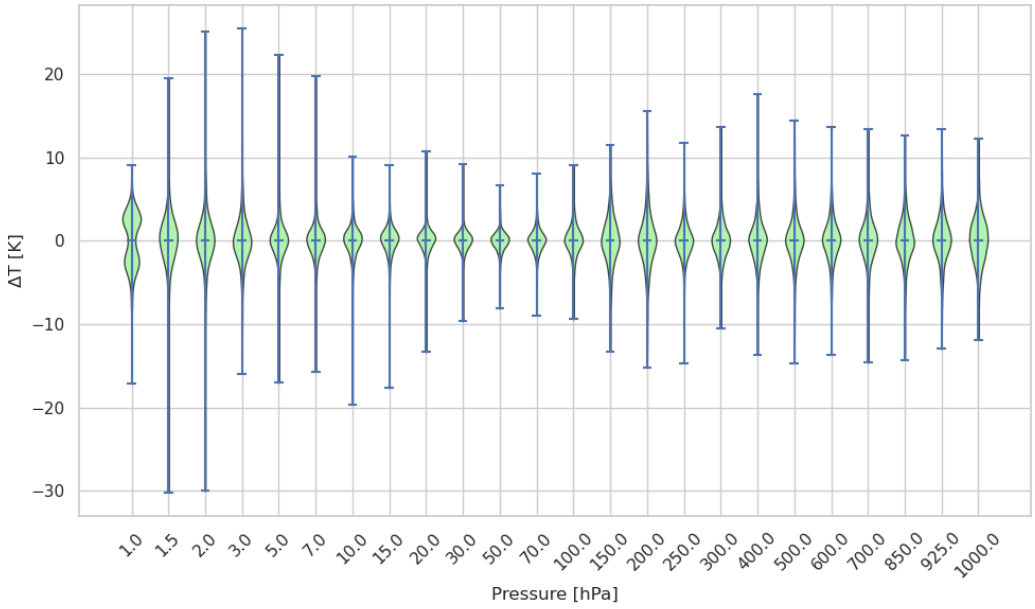

Figure 7.7: Violin plot of the distribution densities of the difference between two consecutive measurements of AIRS, ΔT, for the pressure layers above ORCA.

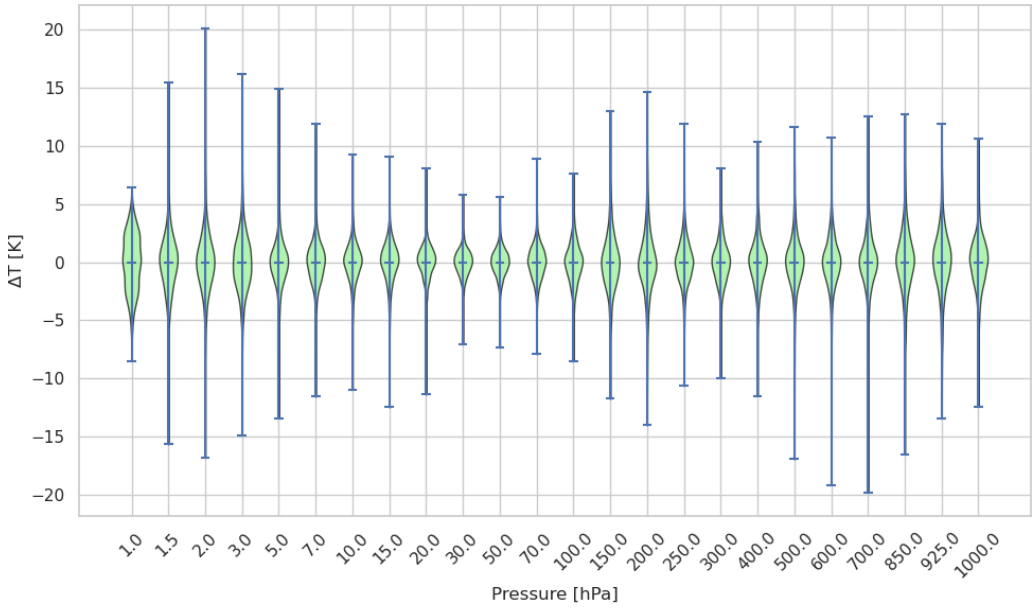

Figure 7.8: Violin plot of the distribution densities of the difference between two consecutive measurements of AIRS, ΔT, for the pressure layers above ARCA.

7.3.2. ERA5

In Figure 7.9 the average atmospheric temperature profile above ORCA is shown for the ERA5 data. The left y-axis shows the pressure on a logarithmic scale and the right y-axis shows the average geometrical height above sea level. The temperature profile looks very similar to that acquired through the AIRS data. During the summer, relatively smooth temperature changes are again observed. In winter, sudden spikes in temperature also occur. In Figure 7.10 the average atmospheric temperature profile above ARCA is shown in the same way.

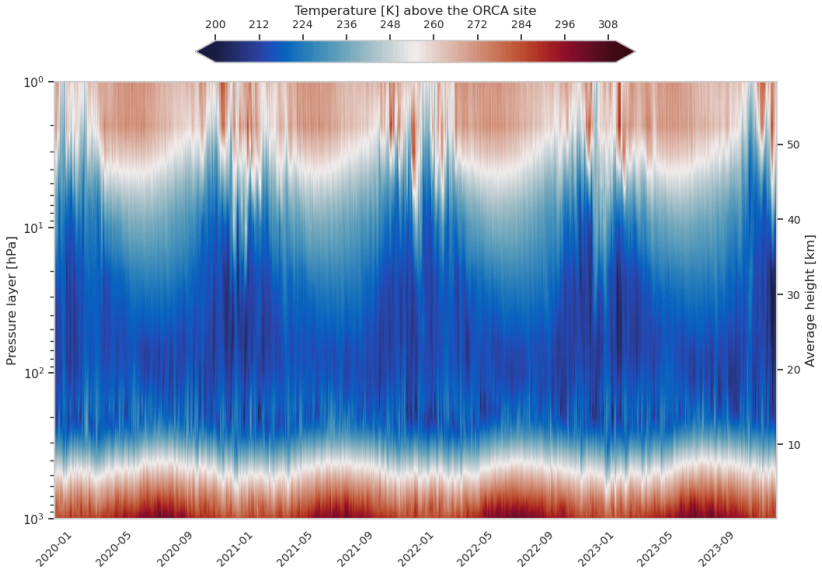

Figure 7.9: Contour plot of the average atmospheric temperature per pressure layer above the ORCA detector for the ERA5 data. The left y-axis shows the pressure on a logarithmic scale and the right y-axis shows the average geometrical height above sea level.

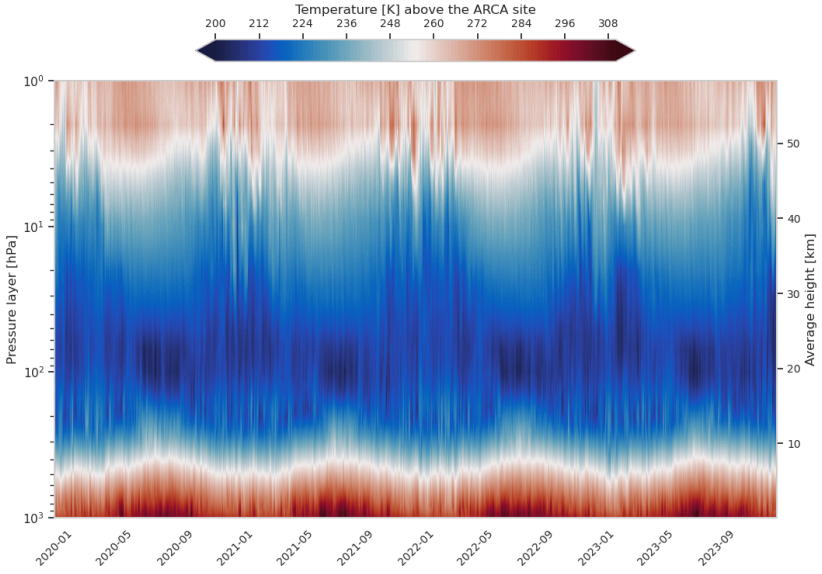

Figure 7.10: Contour plot of the average atmospheric temperature per pressure layer above the ARCA detector for the ERA5 data. The left y-axis shows the pressure on a logarithmic scale and the right y-axis shows the average geometrical height above sea level.

The differences between two consecutive measurements, ΔT, is again calculated for ERA5 data. The density of the distribution of ΔT for every pressure layer has been plotted in a violin plot for ORCA in Figure 7.11 and for ARCA in Figure 7.12. ERA5 has hourly measurements making ΔT much smaller than for the AIRS data. In addition, the increased number of pressure layers in the ERA5 data is visible compared to the AIRS data.

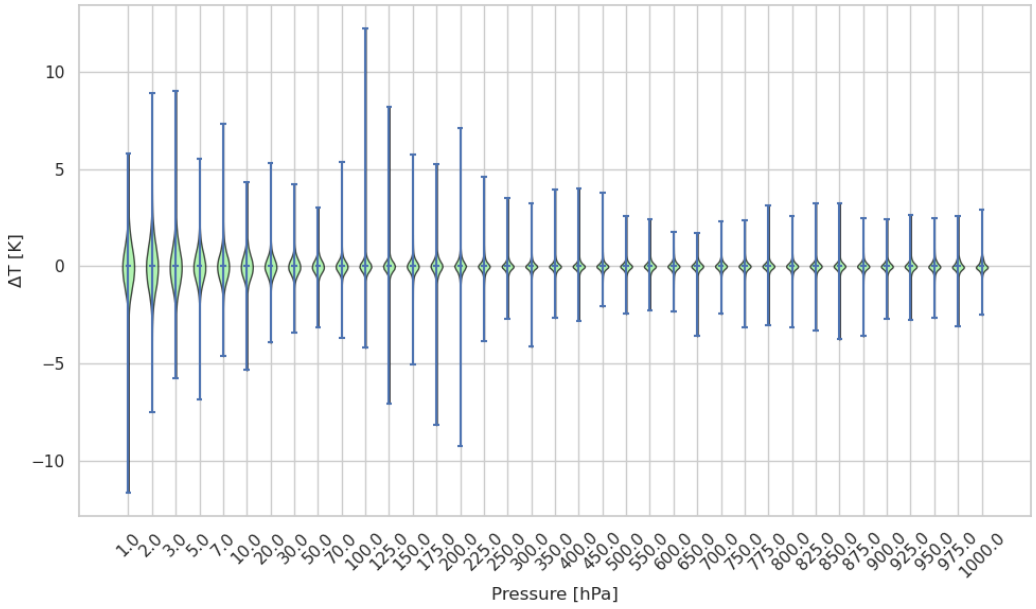

Figure 7.11: Violin plot of the distribution densities of the difference between two consecutive measurements of ERA5, ΔT, for the pressure layers above ORCA.

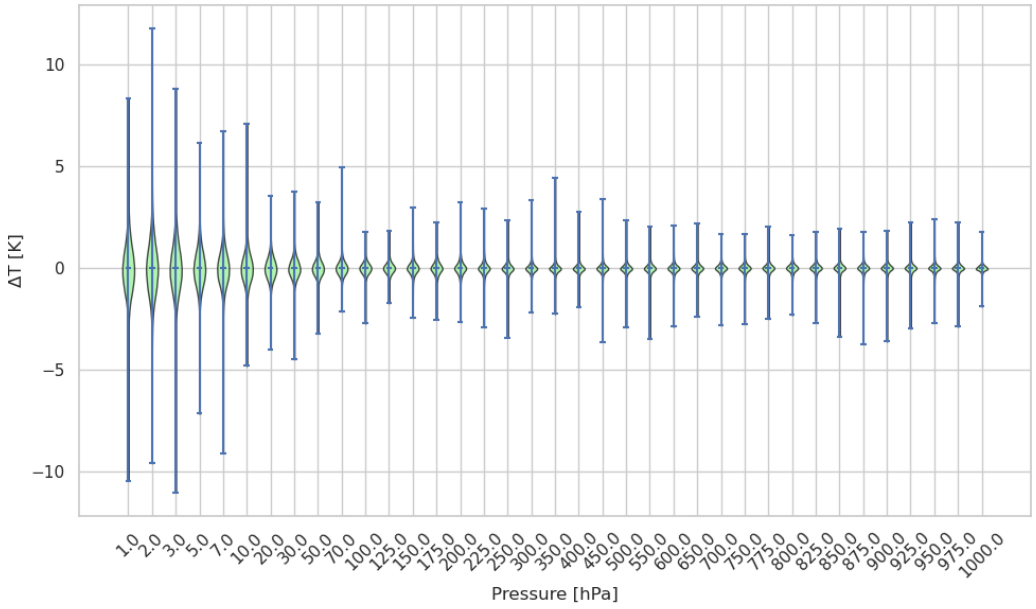

Figure 7.12: Violin plot of the distribution densities of the difference between two consecutive measurements of ERA5, ΔT, for the pressure layers above ARCA.

In Figures 7.13 and 7.14 the temperature difference between the AIRS data and the ERA5 data has been plotted for the atmosphere above ORCA and ARCA, respectively. The temperature difference is calculated by subtracting the ERA5 data from the AIRS data. Because not all pressure levels overlap between the two datasets, the difference has been calculated only for the layers that match. The same is done for the measuring times; only the measuring times that are within an hour of each other are used to calculate the differences in temperature. The absolute mean temperature difference between AIRS and ERA5 above ORCA is 0.643 K and above ARCA 0.563 K.

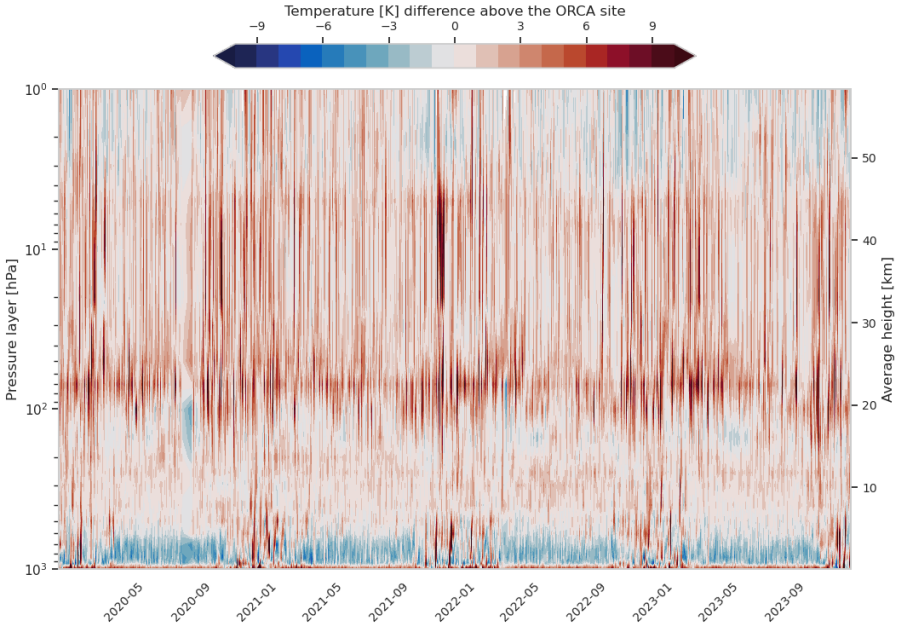

Figure 7.13: Contour plot of the difference in average atmospheric temperature per pressure layer above the ORCA detector between AIRS and ERA5 data. The left y-axis shows the pressure on a logarithmic scale and the right y-axis shows the average geometrical height above sea level.

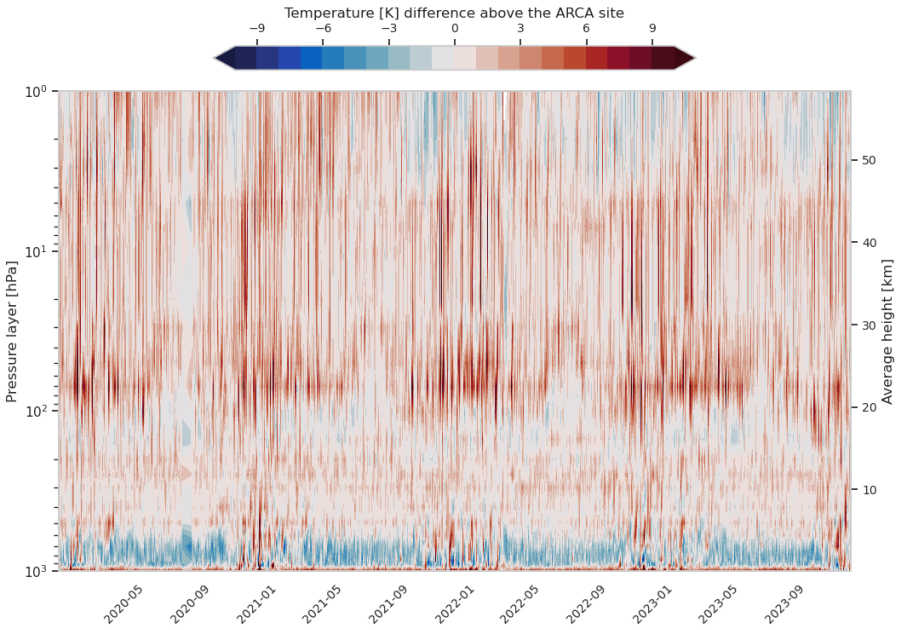

Figure 7.14: Contour plot of the difference in average atmospheric temperature per pressure layer above the ARCA detector between AIRS and ERA5 data. The left y-axis shows the pressure on a logarithmic scale and the right y-axis shows the average geometrical height above sea level.

For the ERA5 data analysis, temperature profiles for the direction binned muon events are used. The atmospheric temperature per pressure layer for the average path a muon takes in each bin above ORCA is shown in Figure 7.15. The differences in the pressure layers are subtle and most noticeable in the lower pressure layers.

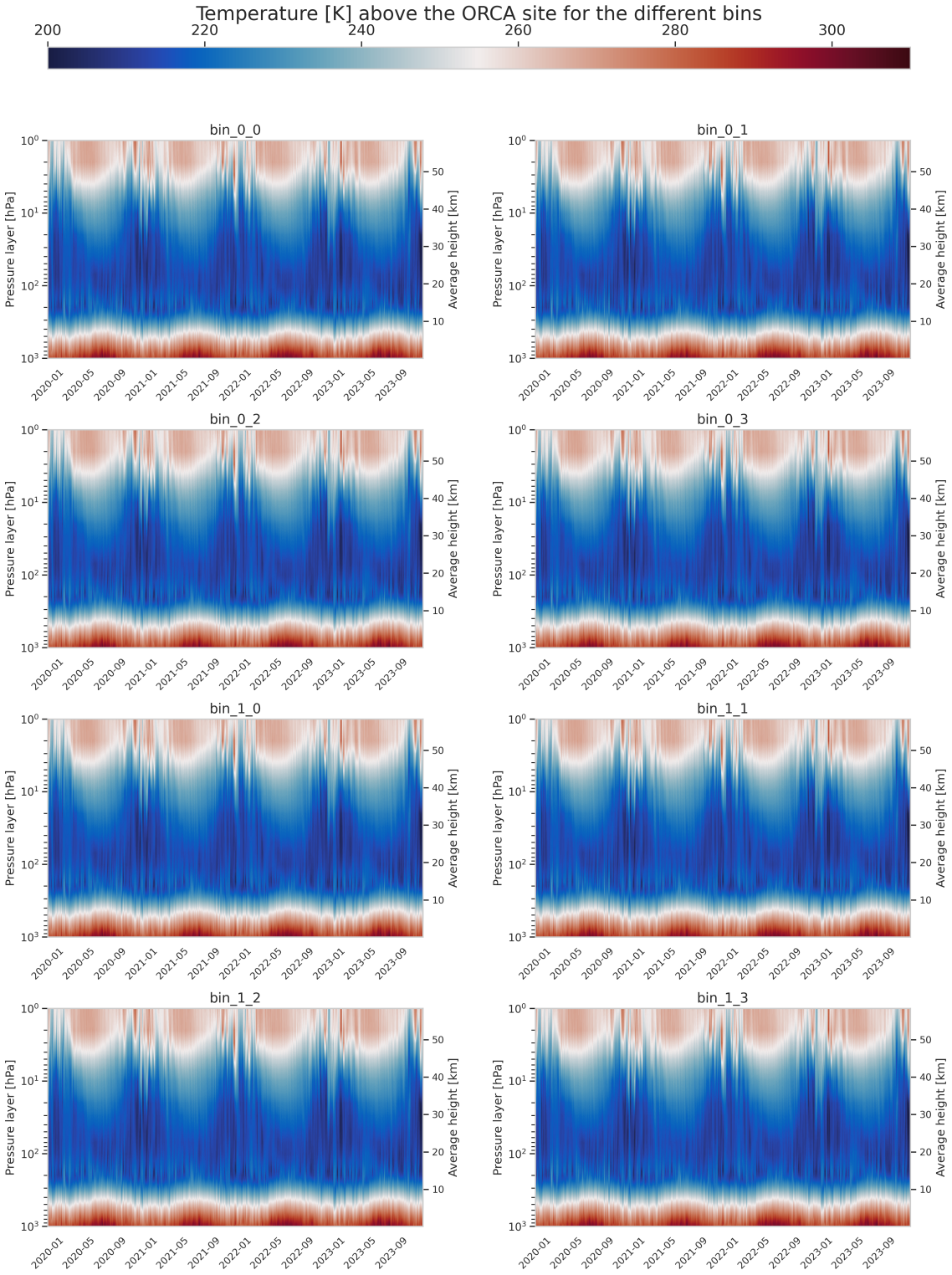

Figure 7.15: Contour plot of the the atmospheric temperature per pressure layer for the average path a muon takes in each bin above ORCA. The left y-axis shows the pressure on a logarithmic scale and the right y-axis shows the average geometrical height above sea level.

7.3.3. Weights

To calculate the effective temperature, the weights defined in Equation 3.17 must be determined. The weights differ slightly from detector configurations, because they are dependent on the average thresh-

old energy. In Figure 7.16, the pion (W_π), kaon (W_K), and total (W_{tot}) weights as functions of atmospheric pressure are shown. The primary x-axis shows the average temperature derived from the AIRS and ERA5 datasets, plotted against pressure on a logarithmic scale. The secondary x-axis shows the corresponding normalized weights of the pion, kaon, and total contributions. These weights are calculated for ORCA-6 but other detectors deviate only slightly and follow the same pattern. The average temperature is calculated over 2020 but other years show similar profiles. As can be seen in the figure, pressure levels near the top of the atmosphere have weights higher than those at lower levels. This is because the high-energy parent particles of the muon have a much higher chance to interact instead of decay in the lower-altitude high-density layers due to the increased number of particles they come across. Another reason is that only a small number of high-energy parent particles actually reach lower altitudes because most of them have already decayed or interacted before, so particles at lower altitudes have lower average energies [10].

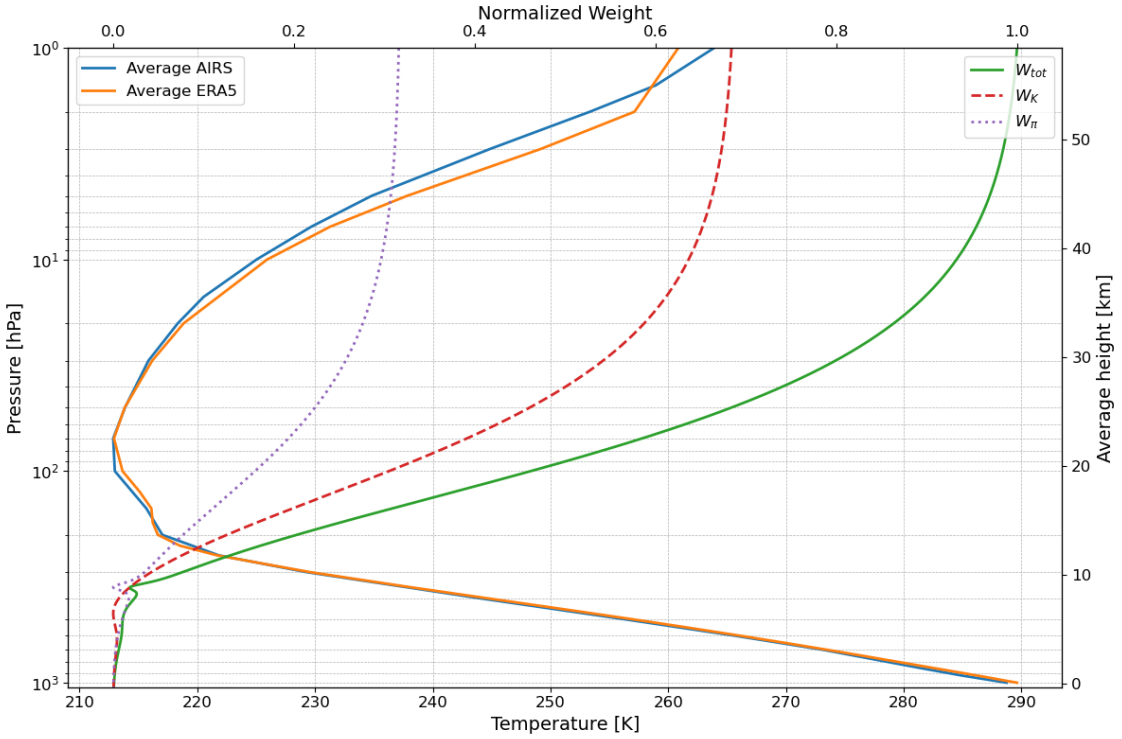

Figure 7.16: Distribution of the pion (W_π), kaon (W_K), and total (W_{tot}) weights as functions of atmospheric pressure. The primary x-axis shows the average temperature derived from the AIRS and ERA5 datasets, plotted against pressure on a logarithmic scale. The secondary x-axis shows the corresponding normalized weights of the pion, kaon, and total contributions. These weights are calculated for ORCA-6 but other detectors deviate only slightly and follow the same pattern.

7.4. Effective temperature

7.4.1. AIRS

The effective temperature is calculated independently for every detector using Equation 3.16. In Figure 7.17 the effective temperature of AIRS for all ORCA-X detectors is shown together with its errors. The maxima take place during the summer months, and the minima during the winter months. Throughout the range, short-term fluctuations are visible, but the biggest spikes occur during the winter months. This is because these spikes in winter were already present in the atmospheric temperature profile. In Figure 7.18 the effective temperature of AIRS for ARCA-21 is shown together with its errors. Again, a maximum can be seen in the summer and a minimum in the winter.

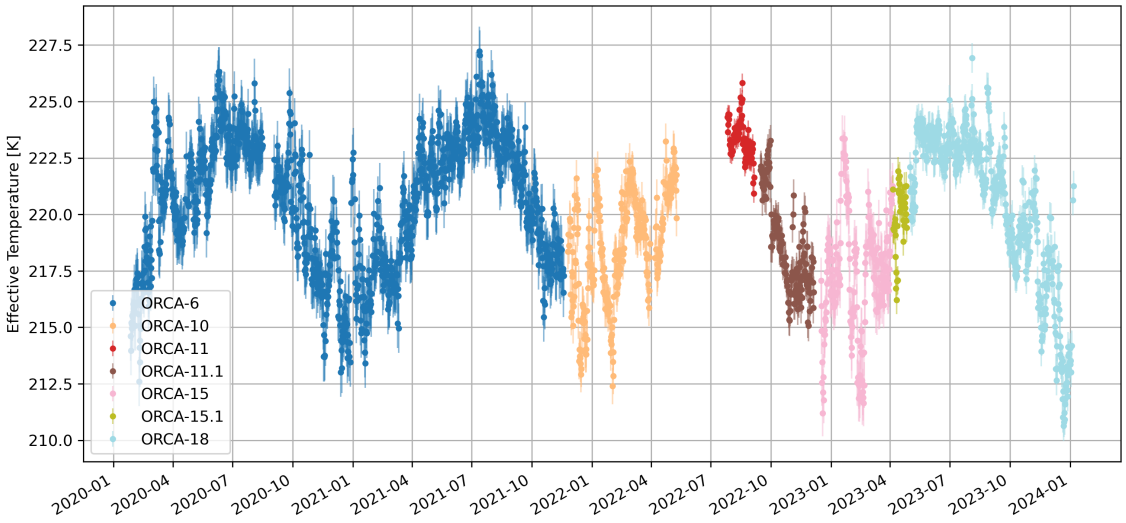

Figure 7.17: Effective temperature over time calculated with AIRS data for all ORCA-X detectors together with the errors.

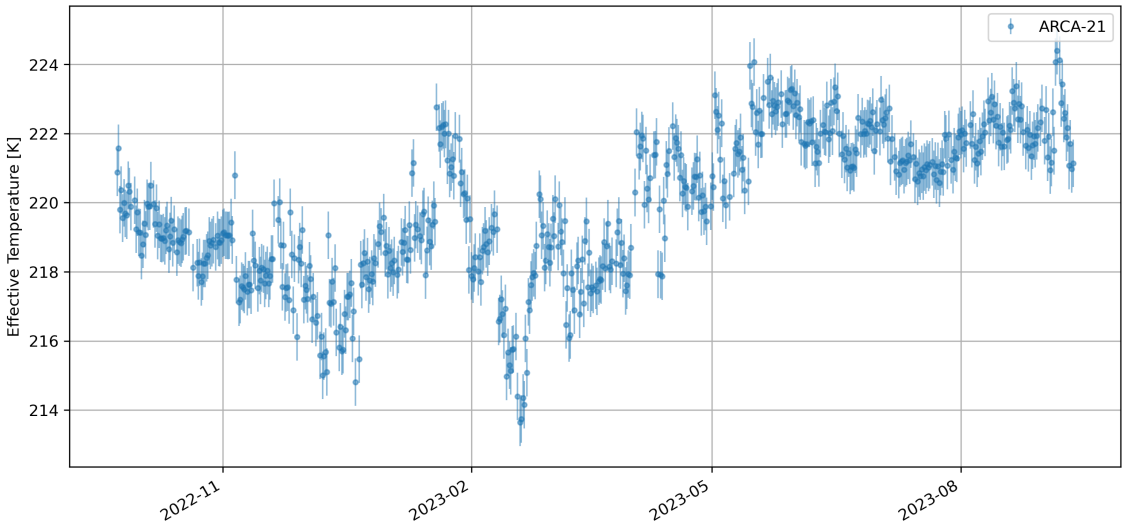

Figure 7.18: Effective temperature over time calculated with the AIRS data for ARCA-21 together with the errors.

The errors in the effective temperatures are determined with the help of the toy Monte Carlo introduced in section 6.3.3. In Figure 7.19, the result of the toy Monte Carlo calculation for ORCA-6 is shown. As can be seen, the distribution follows a normal distribution centred on a mean of 1.095. This mean will be used for the error in the effective temperature for all ORCA-6 data.

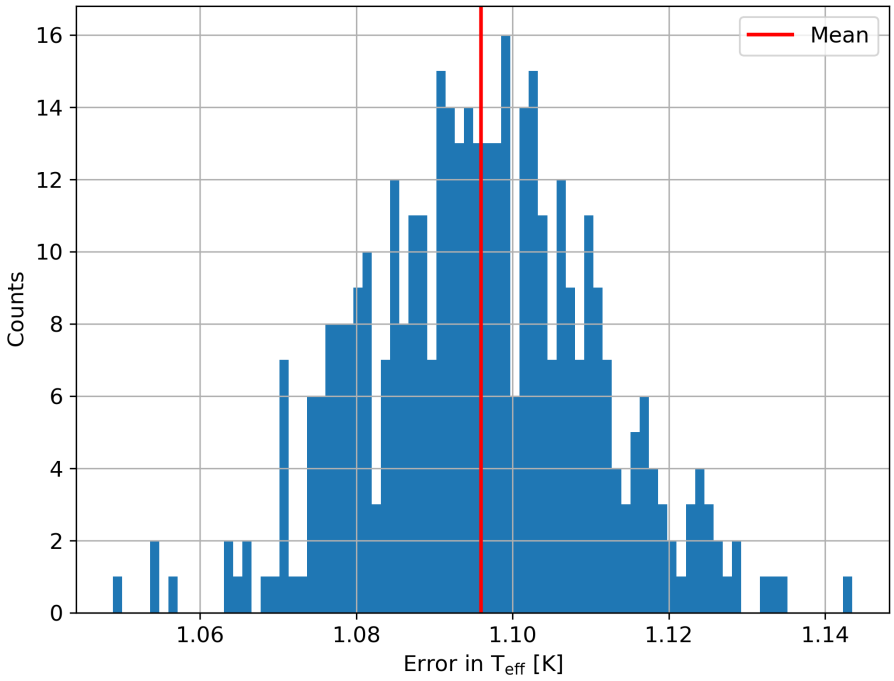

Figure 7.19: Normal distribution resulting from toy Monte Carlo calculation for the effective temperature error of ORCA-6 data.

In Table 7.3 the results of the toy Monte Carlo for the calculation of the errors of the effective temperature for all detector configurations are shown. The main cause of the difference is due to the sample distribution of the temperature. Distributions are defined by the mean temperature and standard deviation of each pressure layer over a detector configuration period. When the standard deviation of the sample distribution increases, the error on the effective temperature increases.

Table 7.3: Errors in the effective temperature for the specific detectors. These results are acquired using a toy Monte Carlo and the AIRS temperature data.

Detector	Error in T_{eff} [K]
ORCA-6	1.095
ORCA-10	0.803
ORCA-11	0.416
ORCA-11.1	0.698
ORCA-15	1.020
ORCA-15.1	0.627
ORCA-18	0.664
ARCA-21	0.687

7.4.2. ERA5

The effective temperature is calculated independently for every detector using Equation 3.16. For the ERA5 data set, the effective temperature is first calculated for the approach without bins. This will thus give a general effective temperature that will be used in all directions. In Figure 7.20 the general effective temperature of ERA5 for all ORCA-X detectors is shown together with its errors. The same general pattern as in Figure 7.17 is visible, but there are many more data points because ERA5 has more measurement times. In Figure 7.21 the general effective temperature of ERA5 for ARCA-21 is shown together with its errors.

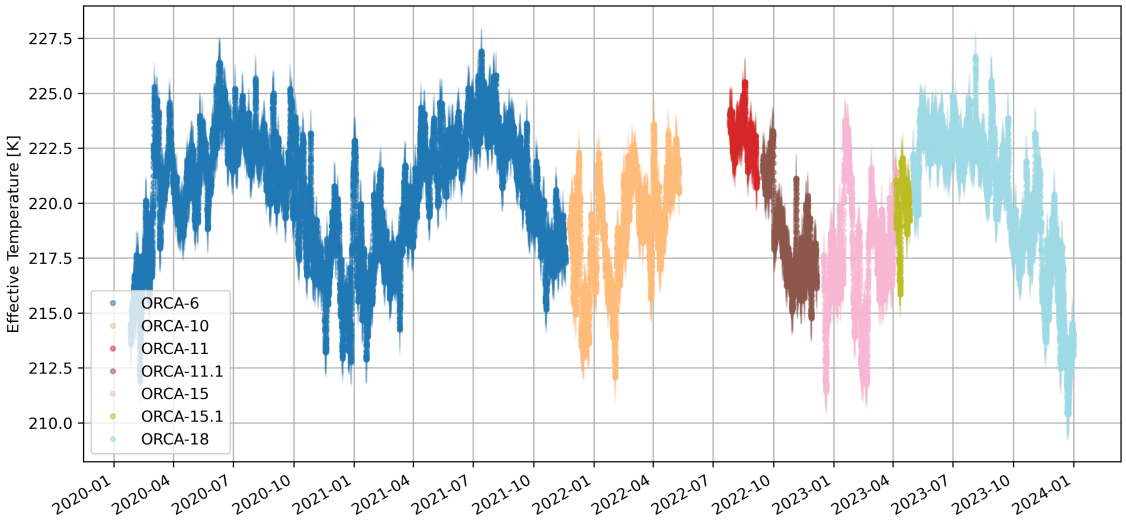

Figure 7.20: General effective temperature of ERA5 over time for all ORCA-X detectors together with its errors.

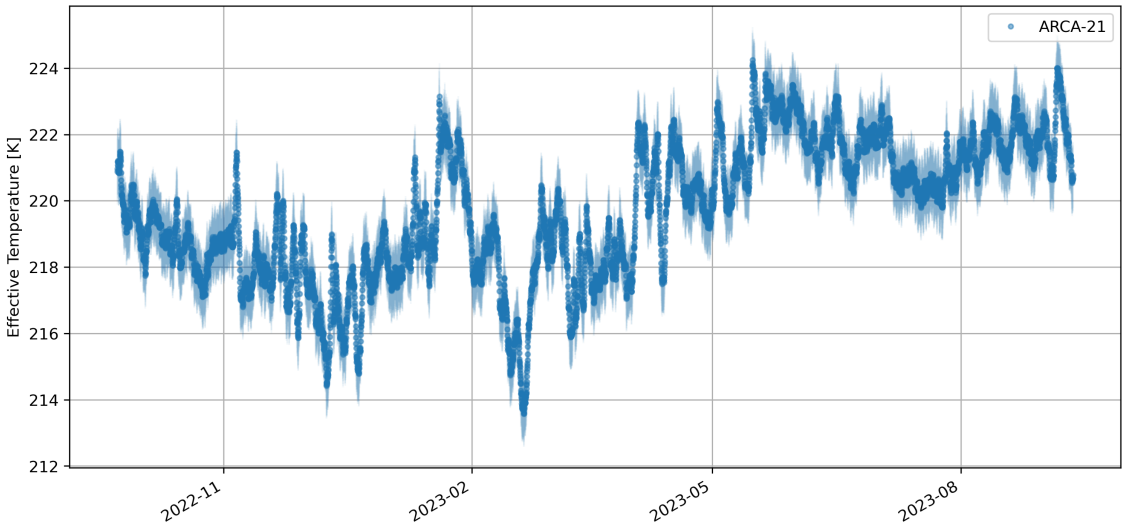

Figure 7.21: General effective temperature of ERA5 over time for ARCA-21 together with its errors.

The error in the effective temperature is calculated in the same way as before with the toy Monte Carlo. In Table 7.4 the results of the calculation of the effective temperature errors are shown for all detector configurations.

Table 7.4: Errors in the effective temperature for the specific detectors. These results are acquired using a toy Monte Carlo and the ERA5 temperature data.

Detector	Error in T_{eff} [K]
ORCA-6	1.073
ORCA-10	1.030
ORCA-11	0.506
ORCA-11.1	0.933
ORCA-15	1.192
ORCA-15.1	0.665
ORCA-18	1.211
ARCA-21	1.004

The effective temperatures of the specific bins for the ORCA-X detectors are plotted in Figure 7.22. The errors are not plotted because this would create too much clutter; however, they only slightly deviate from the errors indicated in Table 7.4. As can be seen, the effective temperature of each bin only slightly deviates from the general effective temperature plotted in Figures 7.20. However, it should be noted that there are small differences. The effective temperatures of the specific bins for ARCA-21 are plotted in Figure 7.23. Again, the errors are not plotted to avoid too much clutter; however, they only slightly deviate from the errors indicated in Table 7.4.

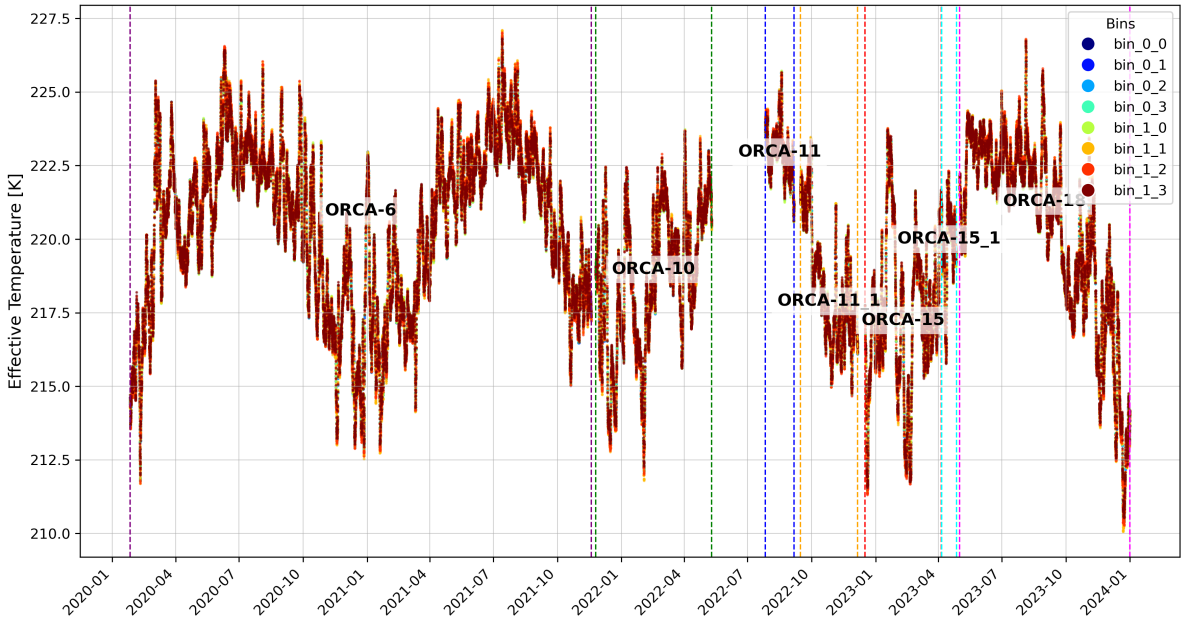

Figure 7.22: ERA5 effective temperature of each bin over time for all ORCA-X detectors. Each bins effective temperature is highlighted with a different colour. Due to only slight changes form bin to bin, the profiles overlap.

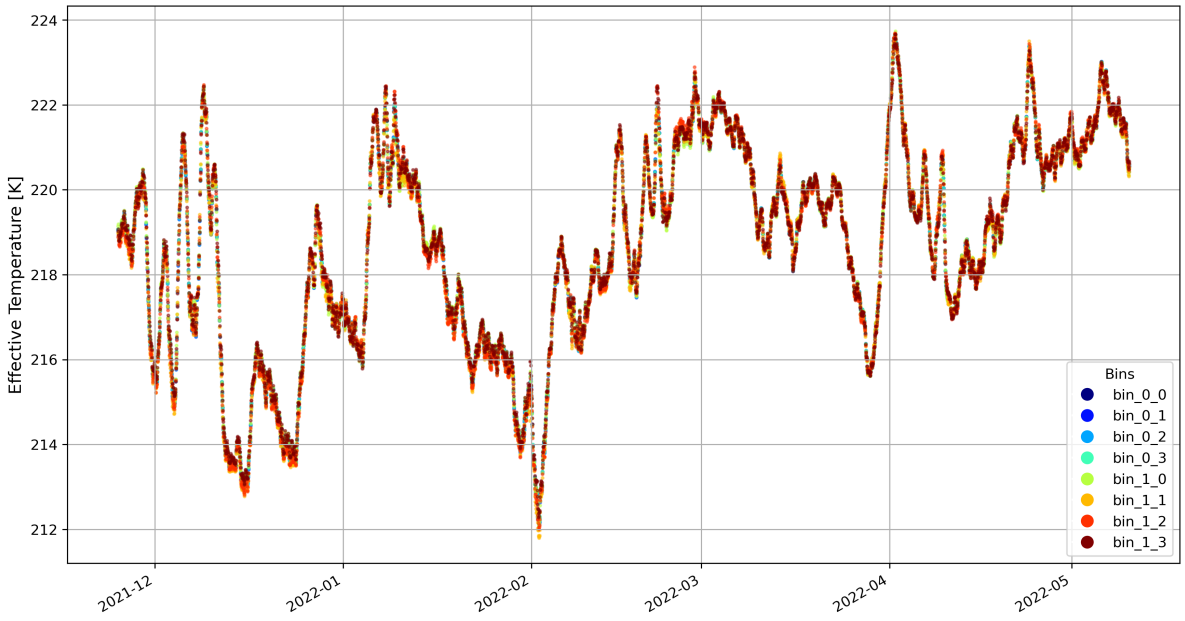

Figure 7.23: ERA5 effective temperature of each bin over time for ARCA-21. Each bins effective temperature is highlighted with a different colour. Due to only slight changes form bin to bin, the profiles overlap.

7.5. Muon rate and ratio

In this section the results of the calculation of the rate and ratio of ORCA-6 will be presented. The results of the other detectors can be found in the tables in this section. More detailed figures for the other detectors will be given in the appendix.

7.5.1. AIRS

For the calculation of the AIRS rate and ratio, the rate was calculated in two ways. First, the rate was calculated for the entire duration of a run. Secondly, the rate and the ratio are calculated for the 60-minute time window around a temperature measurement.

Full Run Analysis

In Figure 7.24 the rate and ratio of ORCA-6 can be seen before cuts, and in Figure 7.25 the rate and ratio of ORCA-6 after cuts can be seen. In the rate plot, the errors are left out to avoid clutter.

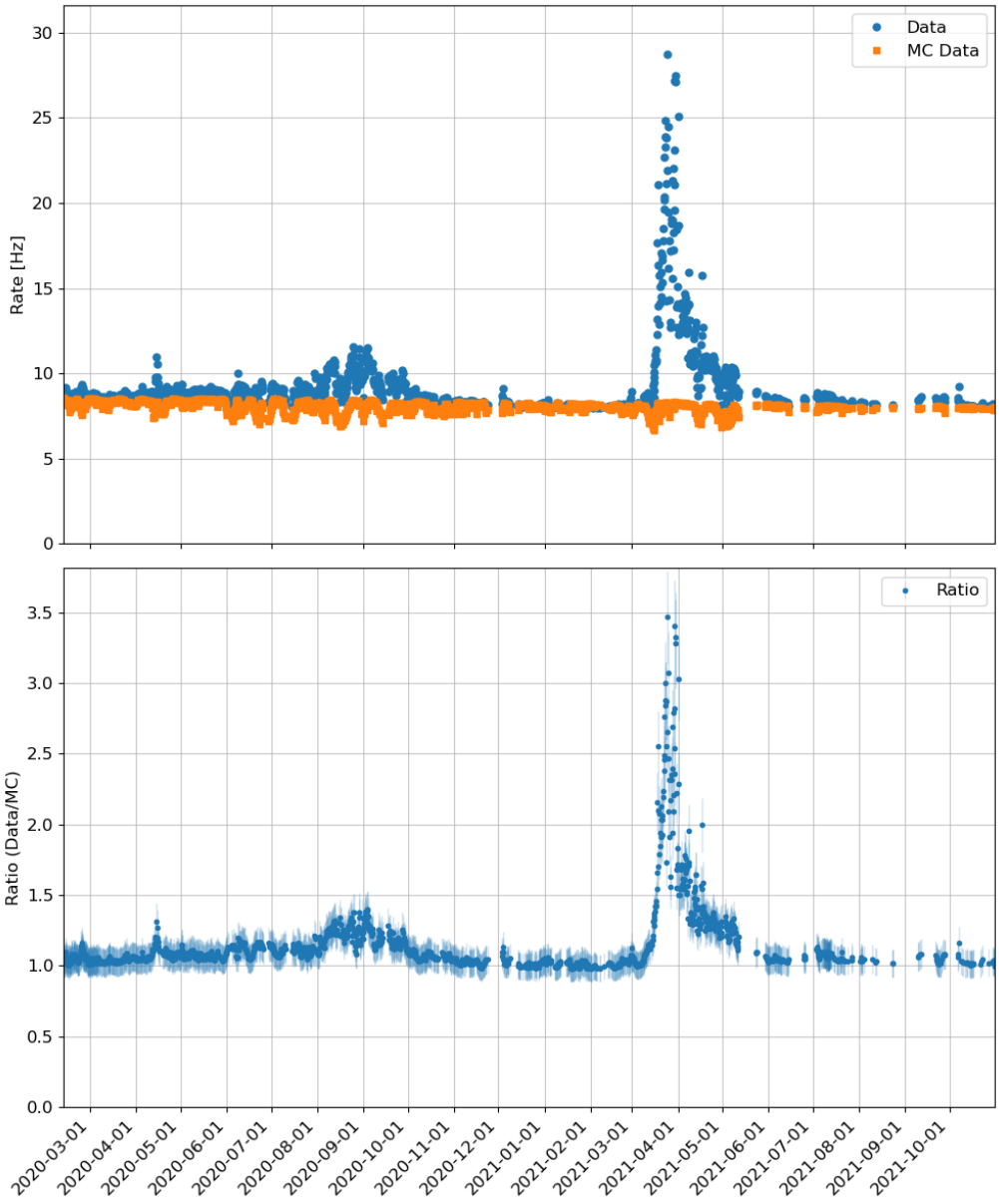

Figure 7.24: Rate and ratio of data and the Monte Carlo simulation for ORCA-6 before cuts are applied. In the top part the count rates without error of the data and the Monte Carlo simulation are shown. In the bottom part the ratio of the two is shown with error.

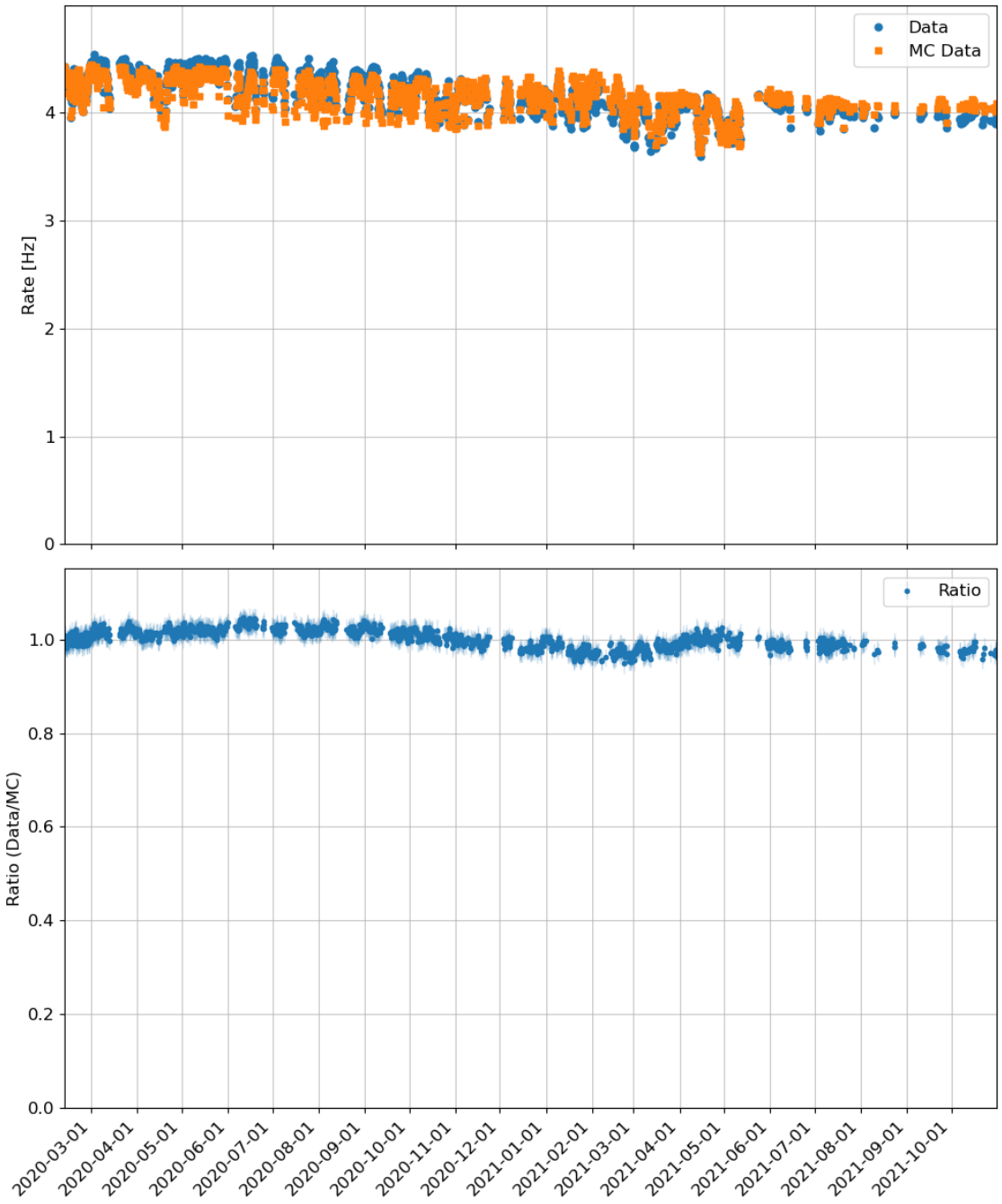

Figure 7.25: Rate and ratio of data and the Monte Carlo simulation for ORCA-6 after cuts are applied. In the top part the count rates without error of the data and the Monte Carlo simulation are shown. In the bottom part the ratio of the two is shown with error.

The cuts significantly reduce the mean rate of both the data and the Monte Carlo simulation. Before the cuts a big peak in the data rate can be seen, which is likely due to a problem related to data acquisition. The cuts remove this problem for a large part, but it can still be seen that data around and following this peak are corrupted; therefore, data after this peak will not be used in analysis. The Monte Carlo rate follows the rate even on short time scales because of the run-by-run simulations. The rate decreases over the whole period of the data taking; this could be due to efficiency losses in the detector. The Monte Carlo simulation should account for these efficiencies losses completely. So in the ratio, there should no longer be a downward trend. Looking at the ratio, the first signs of an oscillating pattern are revealed.

In the left graph of Figure 7.26 the distribution of the data rate and the Monte Carlo simulation rate are shown. On the right-hand side the distribution of the difference between consecutive runs is shown. A Gaussian distribution is fitted to this with a standard deviation of 0.081 Hz. This means that most runs differ with 0.081 Hz from the previous run. This will create a systematic uncertainty on the rate because the runs are on average 6 hours long and there is only a temperature measurement every 12 hours. Therefore, the systematic uncertainty will be set to $0.08\ 1Hz/\langle Rate\rangle$ when calculating the rate for a whole run. For the other cases, when the rate and ratio are calculated only over a maximum time span of 60 minutes, this systematic uncertainty will be calculated using the standard deviation of the distribution of the difference between two consecutive rate calculation periods.

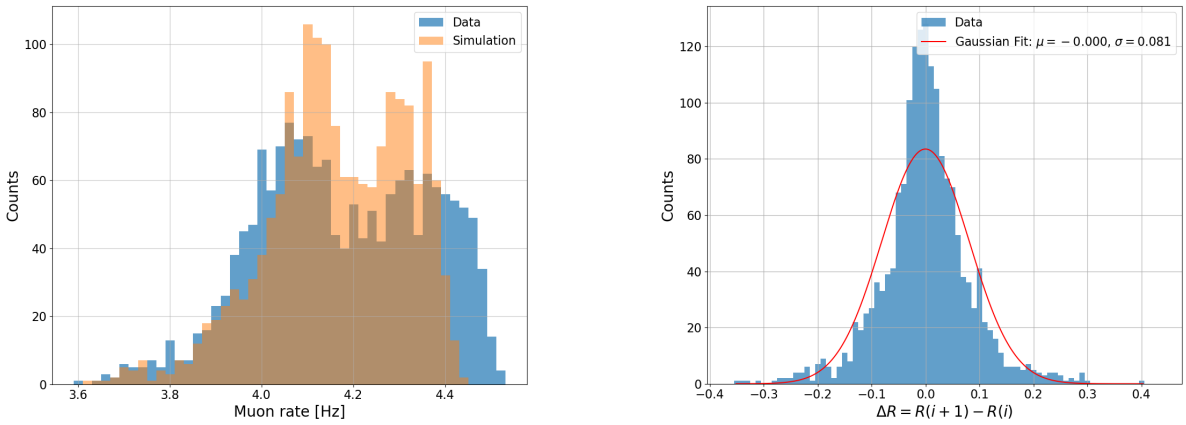

Figure 7.26: Left graph shows the distribution of the data rate and the Monte Carlo simulation rate. Right plot shows the rate distribution of the difference between consecutive runs with a Gaussian fit. The standard deviation of this Gaussian is used as the systematic uncertainty.

The distribution of the ratio between the data and the Monte Carlo simulation is shown on the left side of Figure 7.27. As can be seen, the cuts improve the ratio, they remove events that are not or not correctly simulated. Before the cuts the distribution is not centred around 1 and has a long tail, after cuts it is much more centred and the tail has disappeared. The plot on the right shows the difference in the ratio between two consecutive runs.

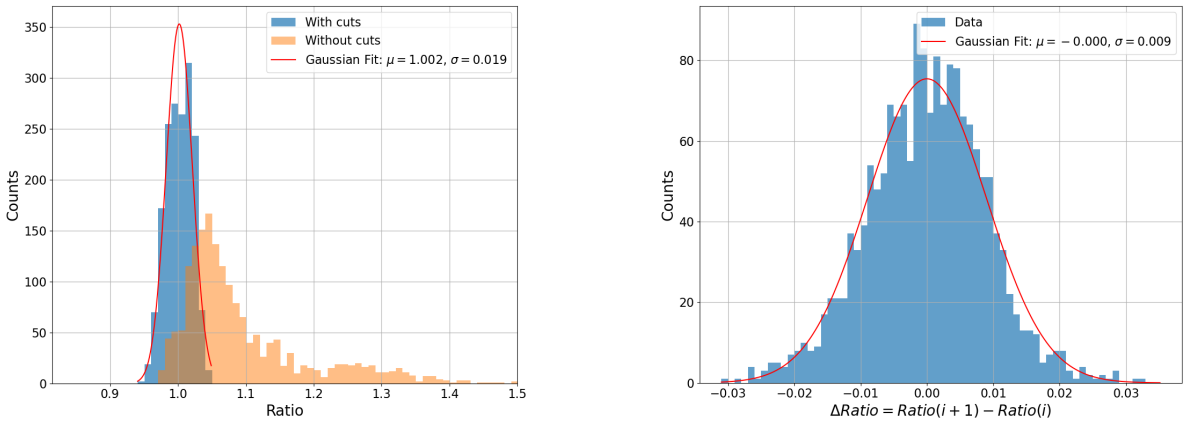

Figure 7.27: Left graph shows the distribution of the ratio between the data rate and the Monte Carlo simulation rate. Right plot shows the distribution of the ratio difference between consecutive runs with a Gaussian fit.

In Figure 7.25 the last section of the ratio data seems to deviate a bit from the pattern seen before. If the ratio data are plotted on top of the effective temperature, as is done in Figure 7.28, the deviation becomes even more visible. The deviations start at the third of May 2021; here, a dotted red line is plotted. It is not fully understood why the ratio starts deviating at this date; however, it is known that some detector changes are implemented at this date. This deviation is caused by the same problem

that causes the peak in the rate before the cuts seen in Figure 7.24. In further analysis, the ORCA-6 data after this date will not be used.

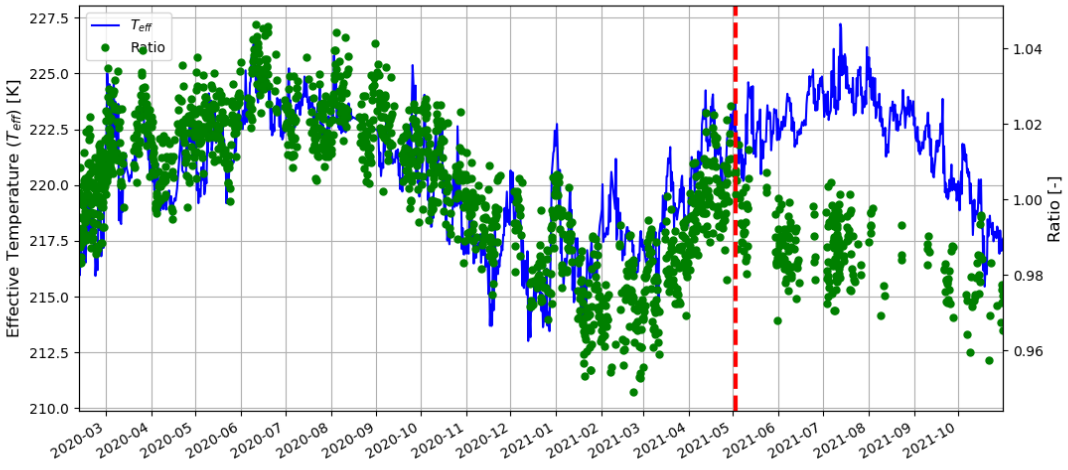

Figure 7.28: ORCA-6 ratio data plotted on top of the effective temperature data. At the third of May 2021 some detector changes are implemented which likely causes the deviation of the expected pattern of the ratio from this date onward.

To verify the presumption made for the use of the ratio to determine the effective temperature coefficient, the model in Equation 6.11 was fitted to the data of the ratio. In Figure 7.29 the fit can be seen with the linear trend. The results of the fit are an amplitude of $A = 0.0187$, an offset of 1.0423, and a linear trend coefficient of $B = -5.9520 \times 10^{-5}$ $[day^{-1}]$. By subtracting the linear part of the fit, a detrended ratio can be determined which can be centred around 1, as shown in Figure 7.30. The time span of other detector configurations is too short to determine an accurate amplitude of the ratio; therefore, the amplitude found for ORCA-6 will be used for all detector configurations. Only for ARCA-21 an amplitude will be determined because the detector is too different from ORCA-6 and data over a longer time span are available. The other fit parameters will be determined for each detector independently. From now on, both the trend ratio and the detrended ratio will be analysed.

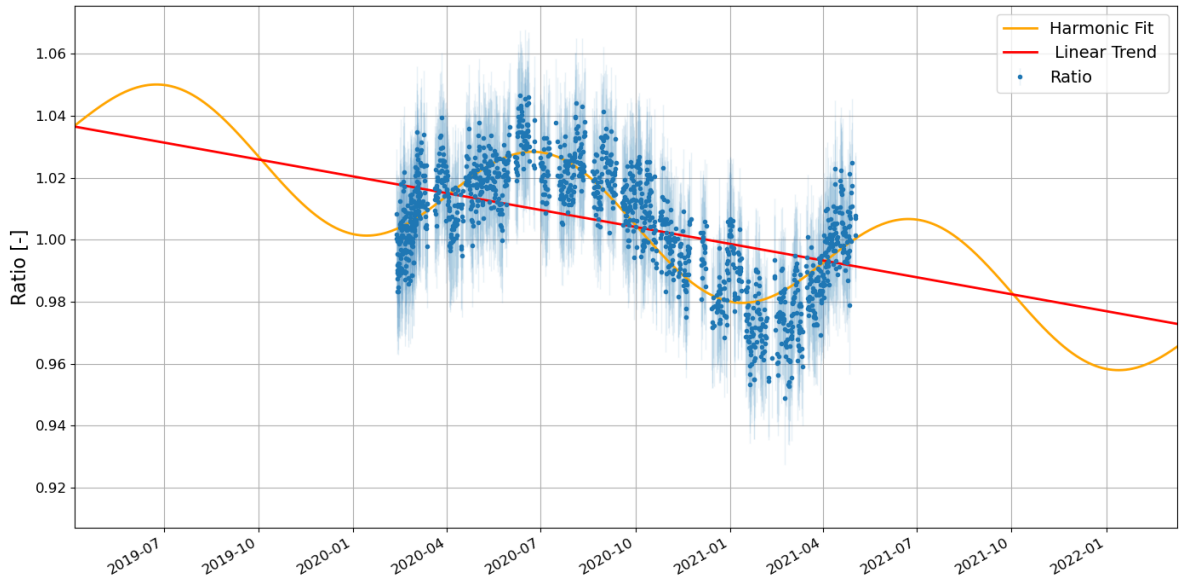

Figure 7.29: Fit of the model in Equation 6.11 to the ratio data of ORCA-6. The parameters fit are an amplitude of $A = 0.0187$, an offset of 1.0423, and a linear trend coefficient of $B = -5.9520 \times 10^{-5}$ $[day^{-1}]$.

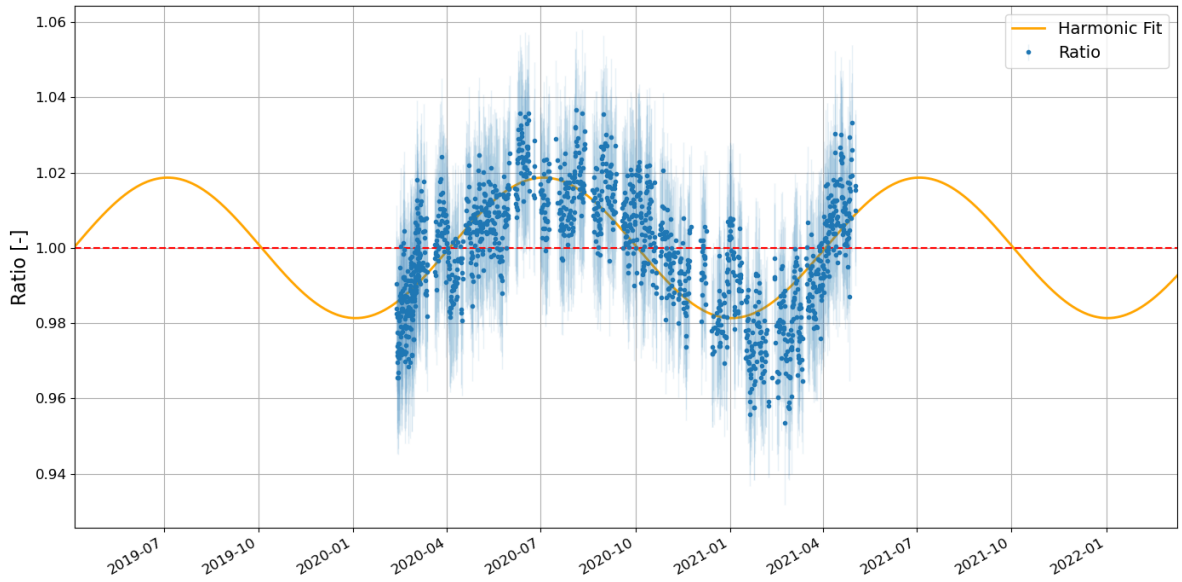

Figure 7.30: Detrended ratio of ORCA-6 by subtracting the linear part of the fit from the ratio and centring it around 1.

The fit parameters for all detector configurations are shown in Table 7.5. These parameters will be used to calculate the detrended ratio for each of the detector configurations.

Table 7.5: Fit parameters found by fitting the model of Equation 6.11 to the ratio data of each detector.

Detector	Amplitude	Linear trend coefficient $[day^{-1}]$	Offset
ORCA-6	0.0187	-5.962×10^{-5}	1.042
ORCA-10	0.0187	-2.458×10^{-4}	1.288
ORCA-11	0.0187	-6.855×10^{-5}	1.095
ORCA-11.1	0.0187	-3.790×10^{-6}	1.017
ORCA-15	0.0187	-3.197×10^{-5}	1.489
ORCA-15.1	0.0187	-2.839×10^{-6}	1.002
ORCA-18	0.0187	-1.199×10^{-4}	1.238
ARCA-21	0.0191	-1.004×10^{-4}	1.188

Due to the detrending all the ratios of the ORCA detector are fitted to a cosine that is centred around 1 and has a fixed amplitude. This makes it possible to plot the ratios in the same figure to get a better idea of how the ratio varies over time. If detrending is not done, the ratios are more difficult to compare with each other. In Figure 7.31 the ratios of the different ORCA detectors are plotted without the detrending. In Figure 7.32 the ratios of the different ORCA detectors are plotted with the detrending.

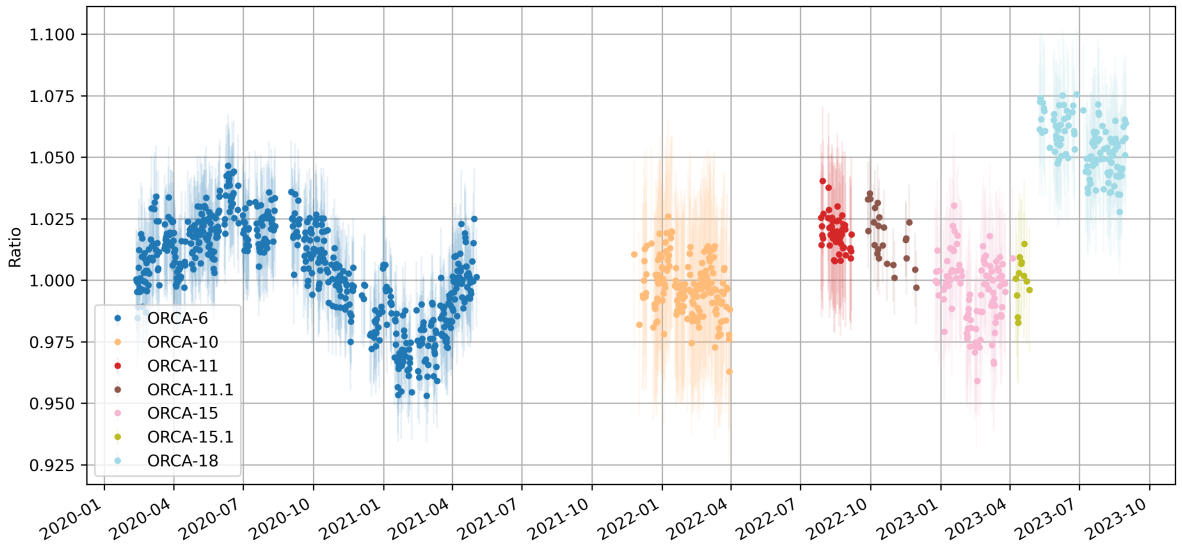

Figure 7.31: Ratios of the different ORCA detectors without the detrending

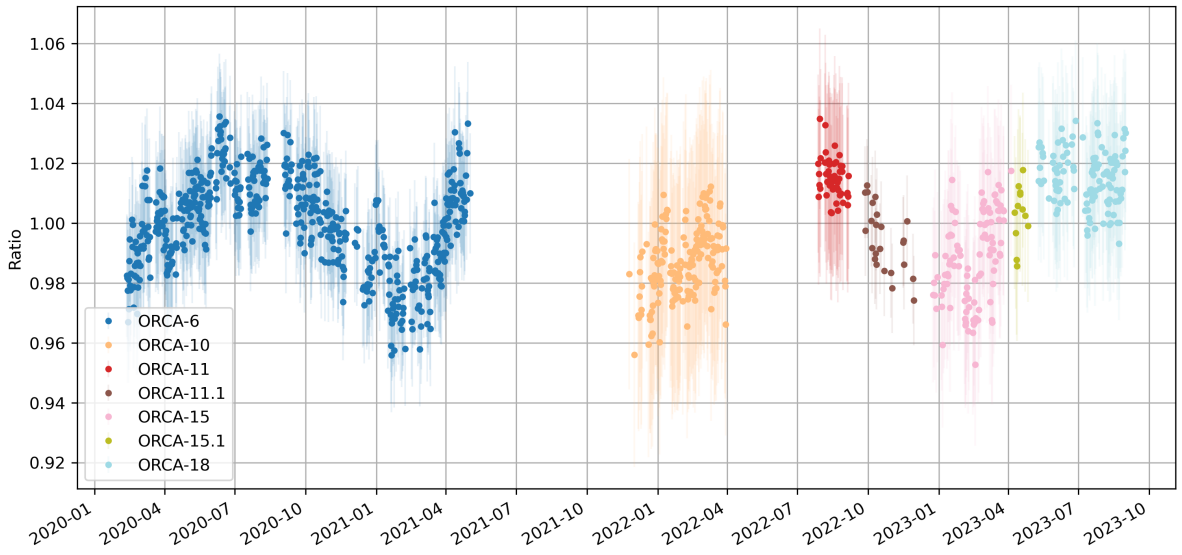

Figure 7.32: Ratios of the different ORCA detectors with the detrending

60-Minute Window Around Temperature Measurements

In Figure 7.33 the rate and ratio of ORCA-6 in 60-minute window around a temperature measurement can be seen after the cuts are applied to the data. Again, the errors are left out in the rate plot to avoid clutter. The same pattern can be seen in the rate and ratio can be seen as before.

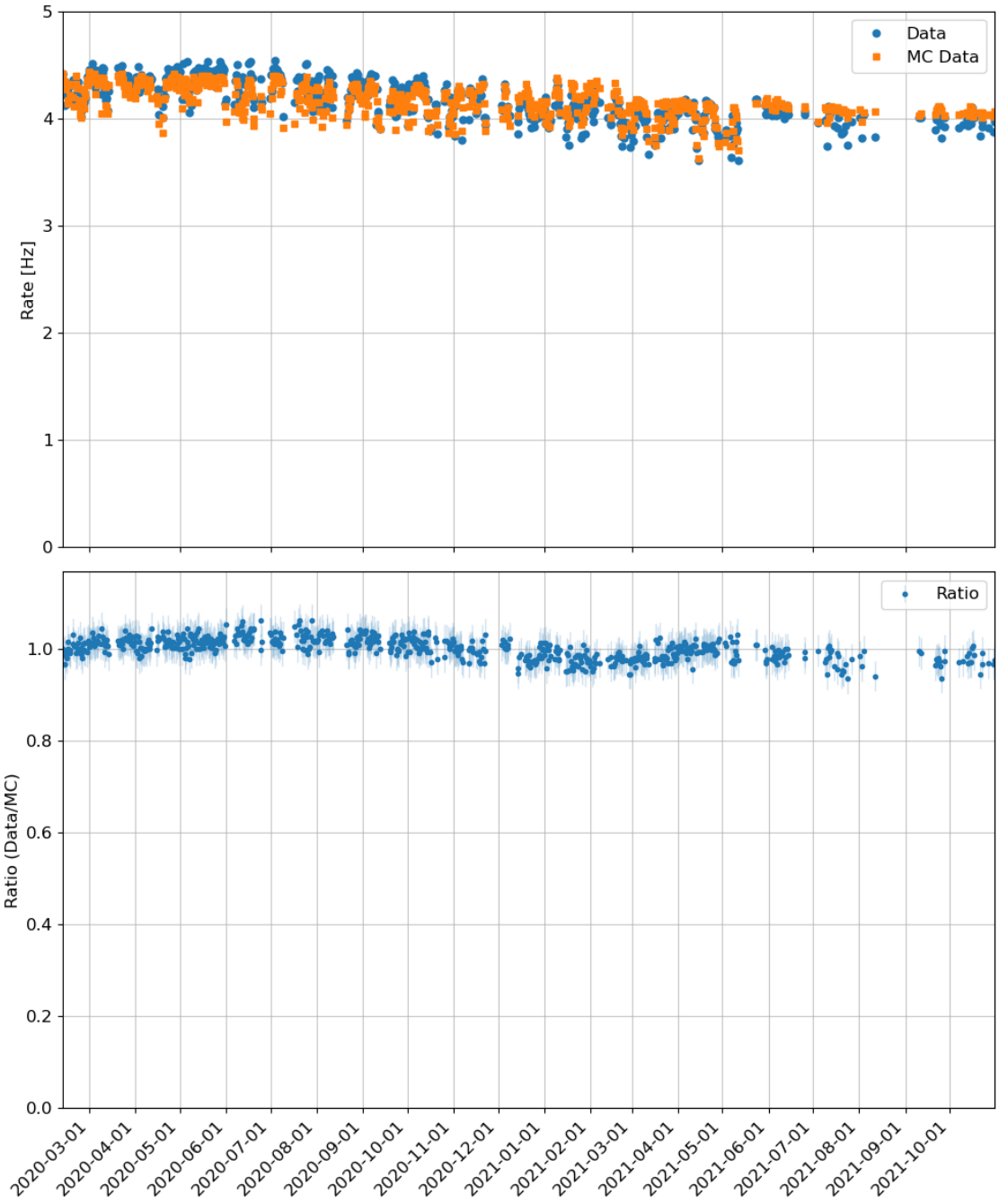

Figure 7.33: Rate and ratio per 60-minute window around temperature measurements for ORCA-6 after cuts are applied. In the top part the count rates of the data and the Monte Carlo simulation are shown. In the bottom part the ratio of the two is shown.

The fit parameters resulting from the fitting of the model of Equation 6.11 to the ratio around a temperature measurement can be found in table 7.6.

Table 7.6: Fit parameters found by fitting the model of Equation 6.11 to the ratio calculated around a temperature measurement of each detector.

Detector	Amplitude	Linear trend coefficient $[day^{-1}]$	Offset
ORCA-6	0.0187	-5.138×10^{-5}	1.037
ORCA-10	0.0187	-2.182×10^{-4}	1.258
ORCA-11	0.0187	-1.016×10^{-5}	1.021
ORCA-11.1	0.0187	-3.025×10^{-4}	1.447
ORCA-15	0.0187	-3.415×10^{-5}	1.523
ORCA-15.1	0.0187	-2.669×10^{-6}	1.002
ORCA-18	0.0187	-1.351×10^{-4}	1.264
ARCA-21	0.0191	-9.262×10^{-5}	1.177

7.5.2. ERA5

For the calculation of the ERA5 rate and ratio, the rate was again calculated in two ways. First, the rate and ratio were calculated in 60-minute windows around the temperature measurements. Secondly, the rate and ratio per direction bin were calculated in 60-minute windows around the temperature measurements.

60-Minute Window Around Temperature Measurement

In Figure 7.34 the rate and ratio of ORCA-6 after cuts can be seen. In the rate plot, the errors are left out to avoid clutter. Compared to previous rate and ratio calculations, there are many more data points available because the ERA5 data have hourly temperature measurements. This means that there will be more than one temperature measurement within a data run, and thus more than one window for calculating the rate within a data run.

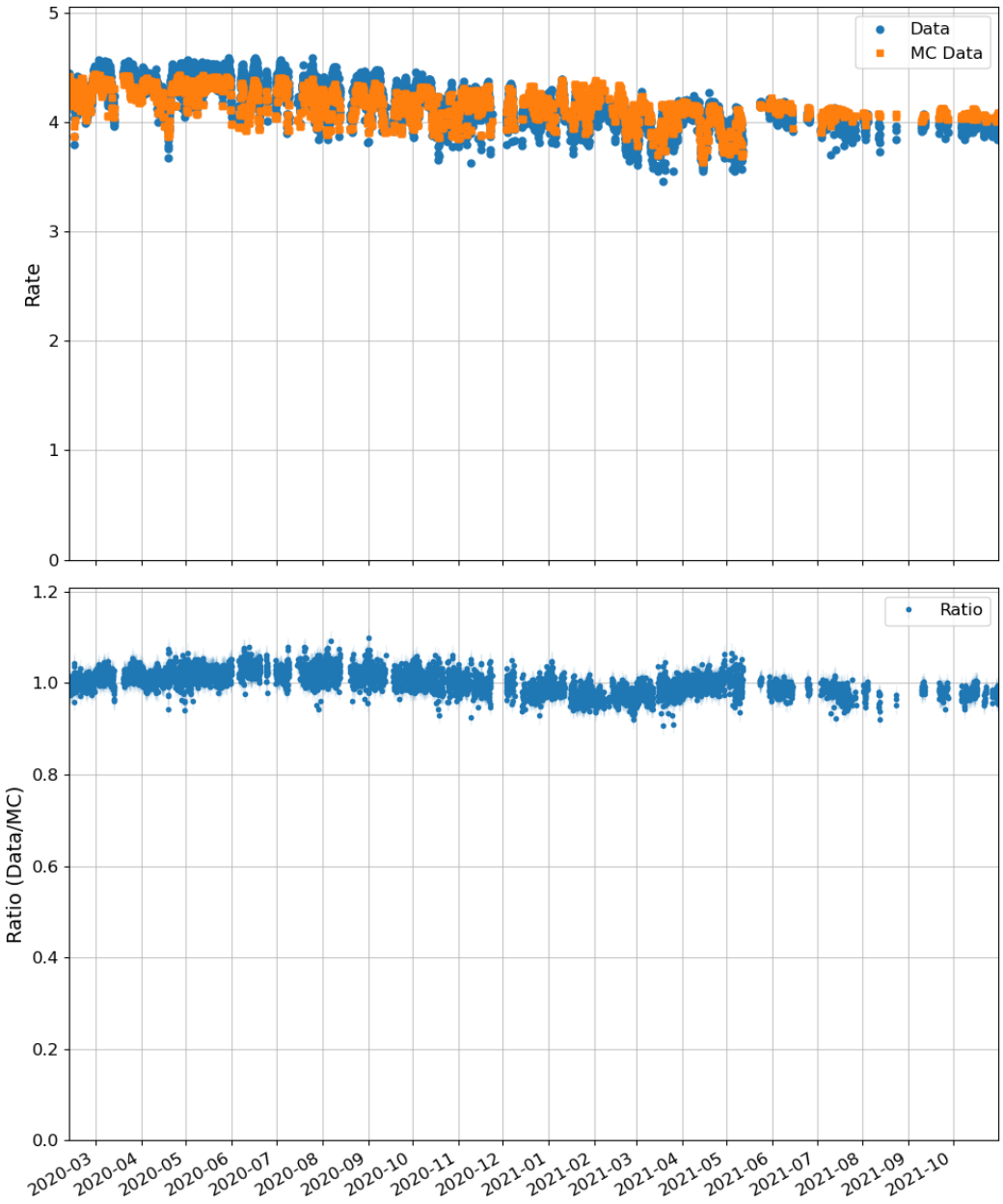

Figure 7.34: Rate and ratio per 60-minute window around temperature measurements for ORCA-6 after cuts are applied. In the top part the count rates of the data and the Monte Carlo simulation are shown. In the bottom part the ratio of the two is shown.

Fitting the equation model 6.11 happens in the same way as before for all detectors. In Table 7.7 the results can be found.

Table 7.7: Fit parameters found by fitting the model of Equation 6.11 to the ratio calculated around a temperature measurement of each detector.

Detector	Amplitude	Linear trend coefficient $[day^{-1}]$	Offset
ORCA-6	0.0179	-6.086×10^{-5}	1.021
ORCA-10	0.0179	-2.326×10^{-4}	1.188
ORCA-11	0.0179	-2.552×10^{-4}	1.253
ORCA-11.1	0.0179	-6.549×10^{-5}	1.092
ORCA-15	0.0179	-3.450×10^{-4}	1.401
ORCA-15.1	0.0179	-6.182×10^{-4}	1.744
ORCA-18	0.0179	-1.171×10^{-4}	1.057
ARCA-21	0.0197	-9.588×10^{-5}	1.148

Binned analysis

In Figure 7.35 the rate and ratio of ORCA-6 after cuts can be seen for the binned analysis. In the rate plot, the errors are left out to avoid clutter. Now there are even more data points available because not only there is a temperature measurement every hour, but for every hour there are eight bins for which the rate and ratio are calculated.

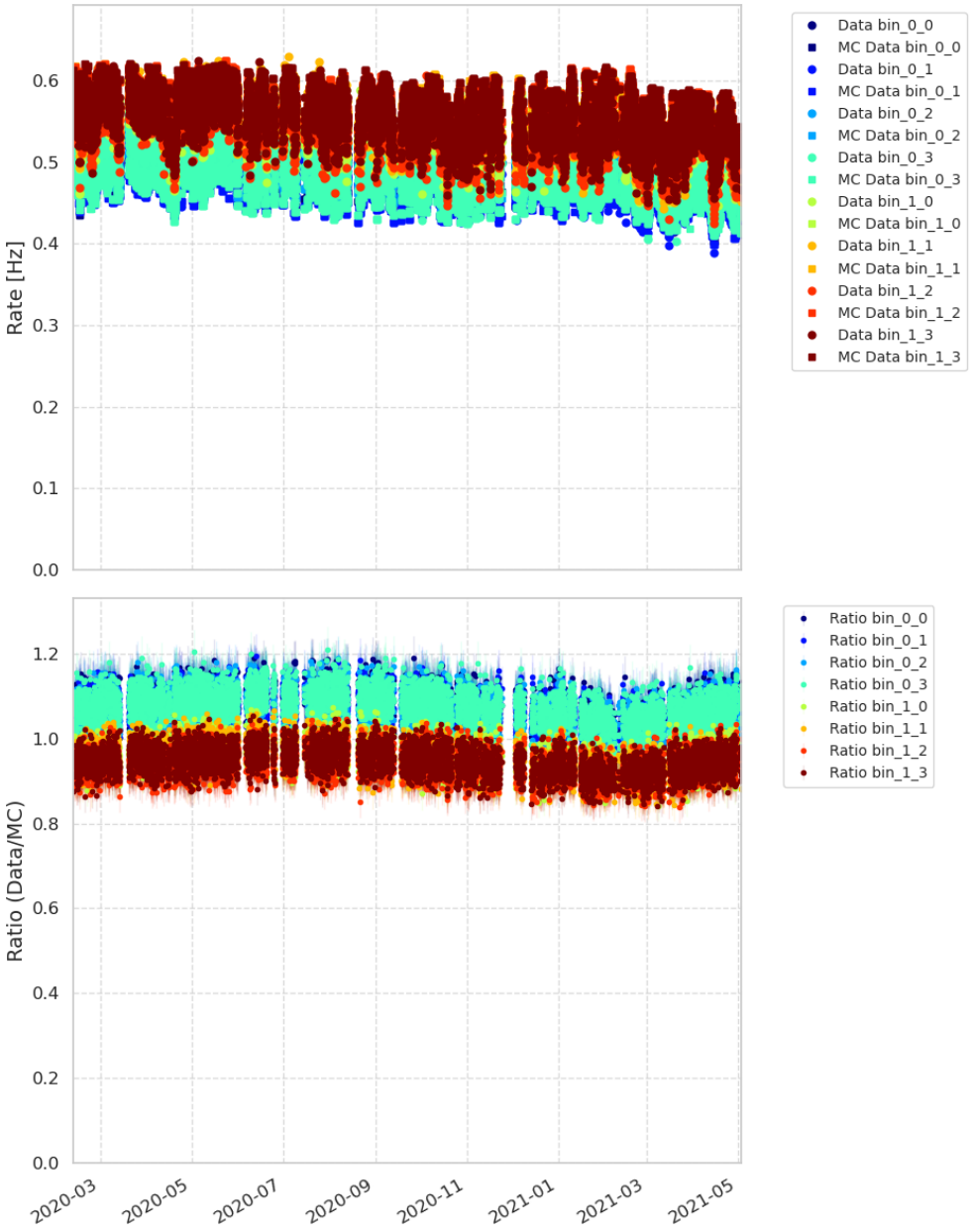

Figure 7.35: Rate and ratio per bin per 60-minute window around temperature measurements for ORCA-6 after cuts are applied. In the top part the count rates of the data and the Monte Carlo simulation are shown. In the bottom part the ratio of the two is shown.

In the upper part of Figure 7.35 the rates are plotted. The rates of the bins with a smaller zenith angle are lower than the rates of the bins with a larger zenith angle. In the lower part, the ratio of the data and the Monte Carlo simulation is plotted. As can be seen, there is again a clear difference between bins with a smaller zenith angle and bins with a larger zenith angle. This is an interesting result, because all the ratios are expected to be centred around 1 regardless of the zenith angle. The simulations underestimate the rates for bins with a smaller zenith angle and overestimate the bins with a larger zenith angle. Other studies such as the one done by Aiello et al. have also found indications that the rate is not correctly simulated [40].
The fitting of Model 6.11 now takes place in a slightly different way. To obtain an accurate fit, the fit is done for every bin independently. The results of the fitting are not shown, but the fit of each bin only slightly deviates from the fitting without the bins. By doing the fit and detrending the ratio for each bin,

the ratio's will all be centred around 1. In Figure 7.36 the detrended ratio for all bins is shown. As can be seen, all of the bins follow the same pattern.

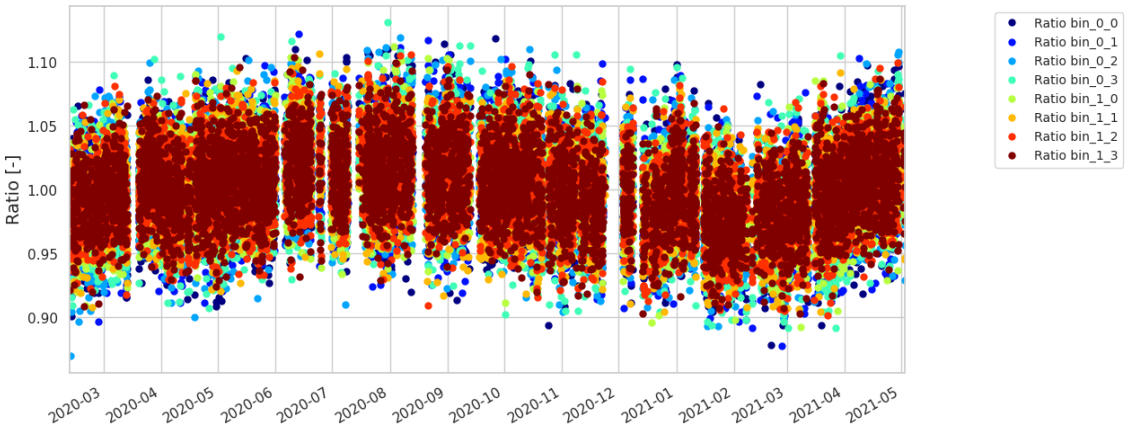

Figure 7.36: Detrended ratio without errors for each bin of ORCA-6 data.

7.6. Fitting the temperature coefficient

In this section the results of the fitting of the effective temperature coefficient of ORCA-6 will be shown. In order to do the fit, the ratio and effective temperate must first be normalised, as shown in Equation 6.11. The normalised temperature is calculated as $\frac{T_{eff}(t)-\langle T_{eff}\rangle}{\langle T_{eff}\rangle} \times 100\% = \frac{\Delta T_{eff}(t)}{\langle T_{eff}\rangle} \times 100\%$ and the normalised ratio as $\frac{R_{\frac{data}{mc}}(t)-\langle R_{\frac{data}{mc}}\rangle}{\langle R_{\frac{data}{mc}}\rangle} \times 100\% = \frac{\Delta R_{\frac{data}{mc}}(t)}{\langle R_{\frac{data}{mc}}\rangle} \times 100\%$. First, the results of the AIRS calculations will be presented, followed by the results of the ERA5 calculations. This will be done for the normal data and the detrended data. The results of the other detectors can be found in the tables in this section. More detailed figures for the other detectors will be given in the appendix.

7.6.1. AIRS

For the calculation of the AIRS rate and ratio, the rate was calculated in two ways. First, the rate was calculated for the entire duration of a run. Secondly, the rate and the ratio are calculated for the 60-minute time window around a temperature measurement.

Full Run Analysis

Before the effective temperature coefficient can be determined, the ratio and the effective temperature must be normalised as shown in Equation 6.5. In Figure 7.37 the normalised effective temperature and ratio without detrending are plotted. In Figure 7.38 the normalised effective temperature and ratio with detrending are plotted. At dates closer to the end of the range, the effects of the detrending become more visible. There should be a constant factor between the effective temperature and the ratio, the effective temperature coefficient. Before detrending this factor seems to become bigger over time, after detrending this becomes more constant. This could be because at the end of a detector configuration, the efficiency losses of a detector could become more noticeable as they build up over time.

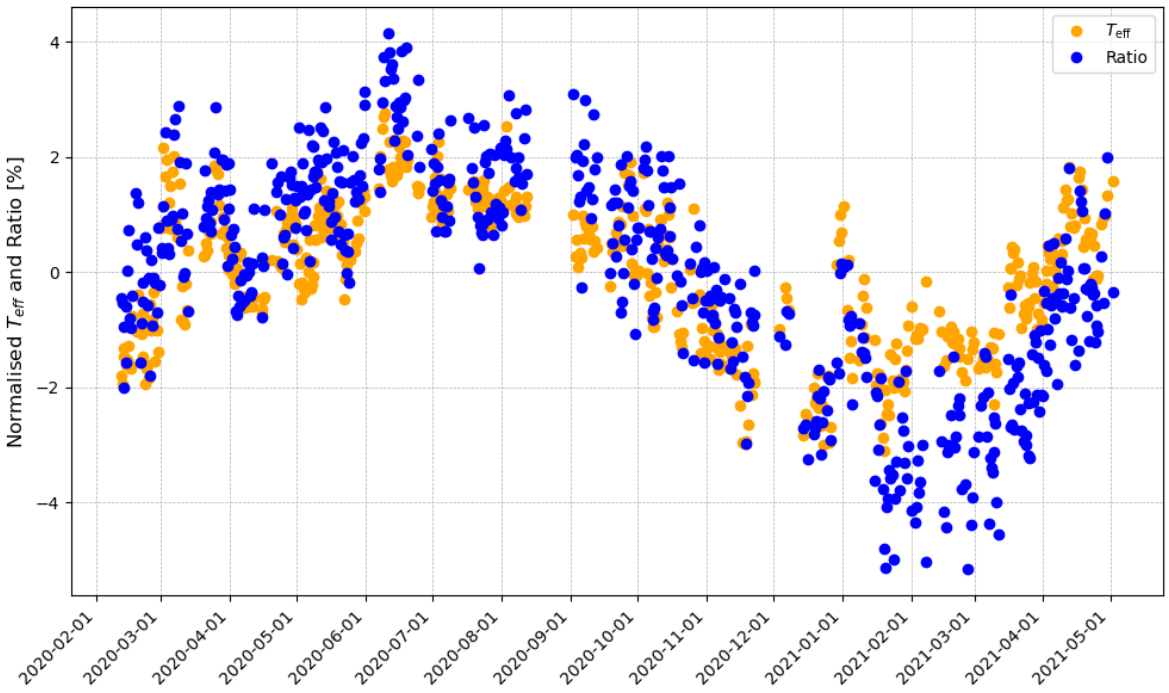

Figure 7.37: Normalised effective temperature and ratio without detrending over time for ORCA-6

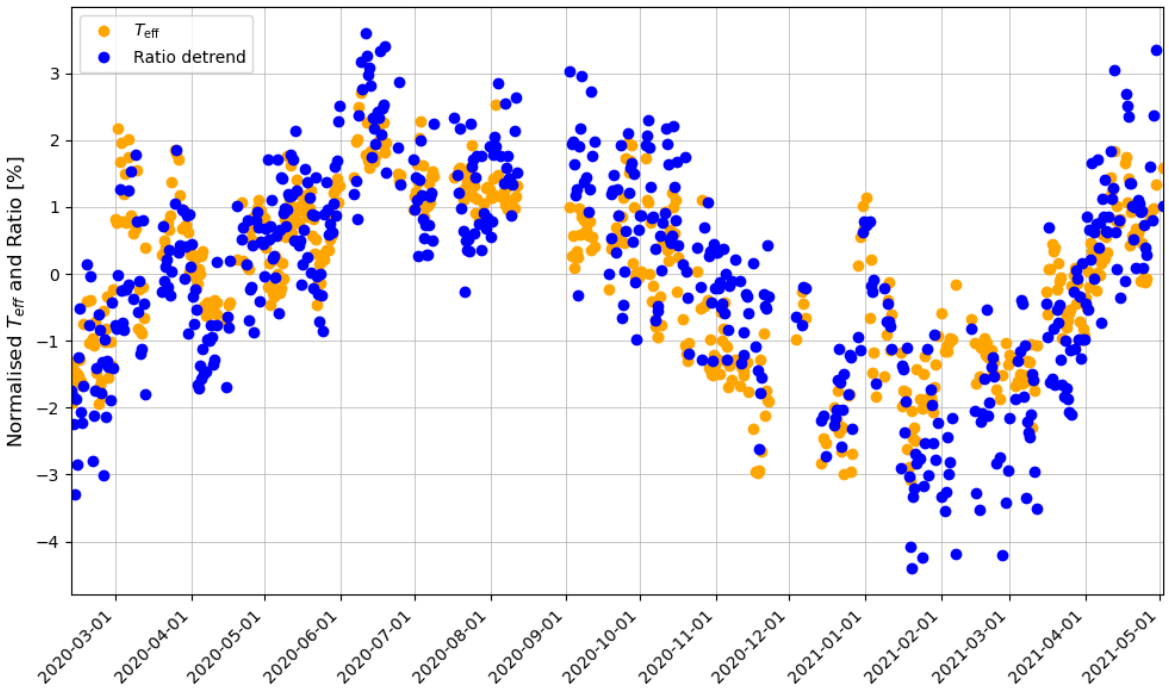

Figure 7.38: Normalised effective temperature and ratio with detrending over time for ORCA-6

In Figure 7.39 the normalised effective temperature and ratio without detrending are plotted in a scatter plot with the errors. Through these data points, the model of Equation 6.11 is fitted, giving an effective temperature coefficient of $\alpha = 1.25 \pm 0.04$ and a goodness of fit $\chi^2/dof = 0.39$. In Figure 7.40 the same is done but now with the detrended ratio, giving an effective temperature coefficient of $\alpha = 1.00 \pm 0.03$ and a goodness of fit $\chi^2/dof = 0.25$.

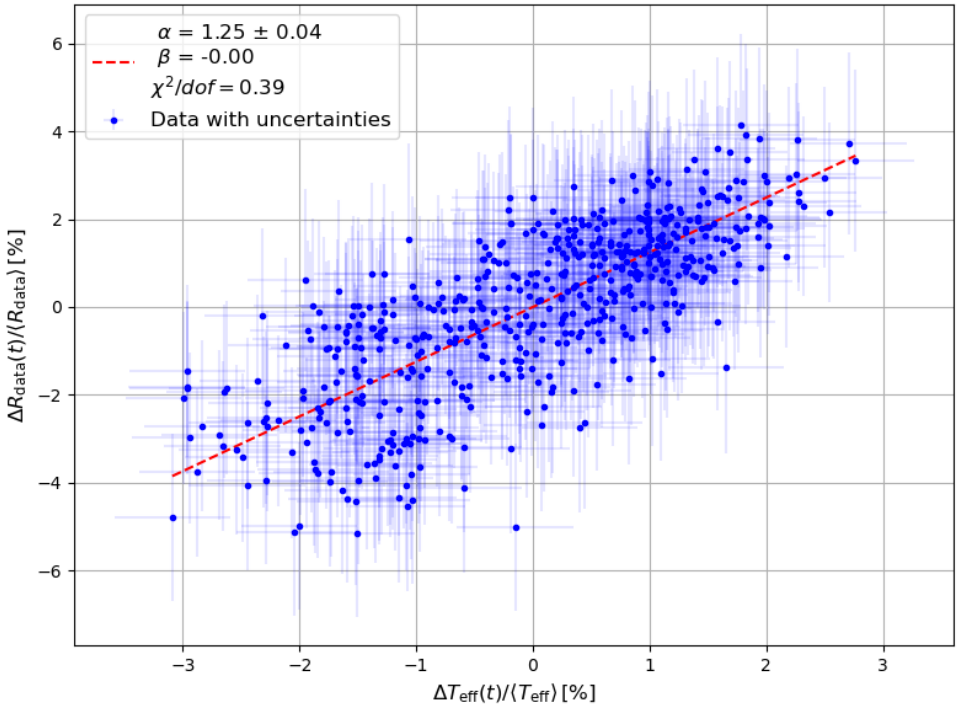

Figure 7.39: Normalised effective temperature T_{eff} and ratio without detrending R_{data} of ORCA-6 showing the relative variation in percentage. The red line is a fit of the model in Equation 6.11. The errors are taken into account in the fit.

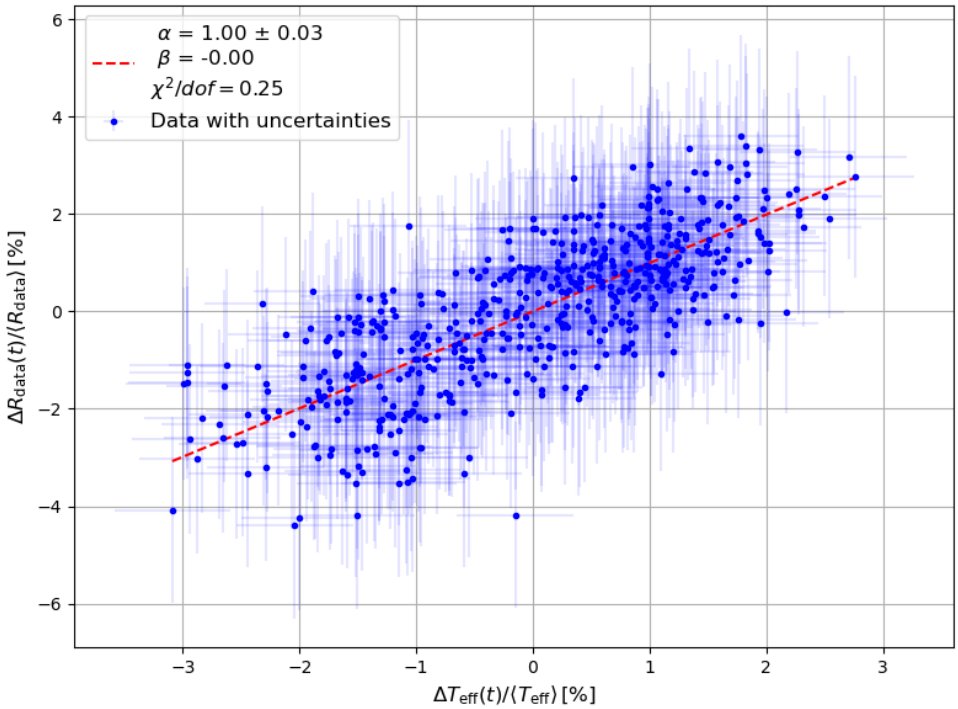

Figure 7.40: Normalised effective temperature T_{eff} and ratio with detrending R_{data} of ORCA-6 showing the relative variation in percentage. The red line is a fit of the model in Equation 6.11. The errors are taken into account in the fit.

In Figure 7.4 the theoretically expected total, pion, and kaon effective temperature coefficient (α) is plotted over a range of average threshold energy. The theoretical expected α for ORCA-6 is highlighted

by the red triangle. The experimentally determined α for ORCA-6 without detrending is plotted as a black circle, and with detrending is plotted as a brown circle.

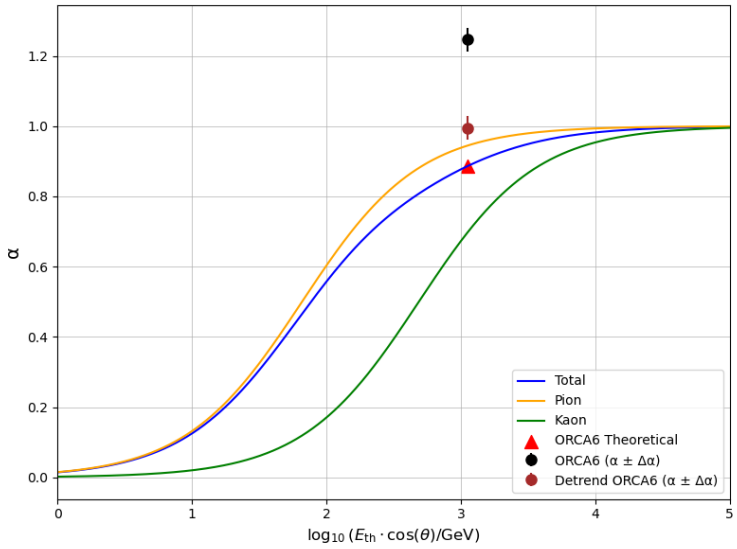

Figure 7.41: The theoretically expected total, pion, and kaon effective temperature coefficient (α) is plotted over a range of average threshold energy. The theoretical expected α for ORCA-6 is highlighted by the red triangle. The experimentally determined α for ORCA-6 without detrending is plotted as a black circle, and with detrending is plotted as a brown circle.

Full Run Time Analysis

Now, every temperature, regardless of when this temperature occurs over time, is expected to cause the same ratio in the data. This is illustrated in Figure 7.42. The normalised ratio without detrending is plotted over time; the colour of each ratio point shows what the effective temperature is at that ratio point. In the ideal case, horizontal bands of points with the same ratio would have the same colour, indicating that the ratio is caused by the same effective temperature. In general, this can be seen in the figure but not perfectly. In the months leading up to the lowest ratio in 2021, ratios can be seen that have a lower temperature than similar ratios.

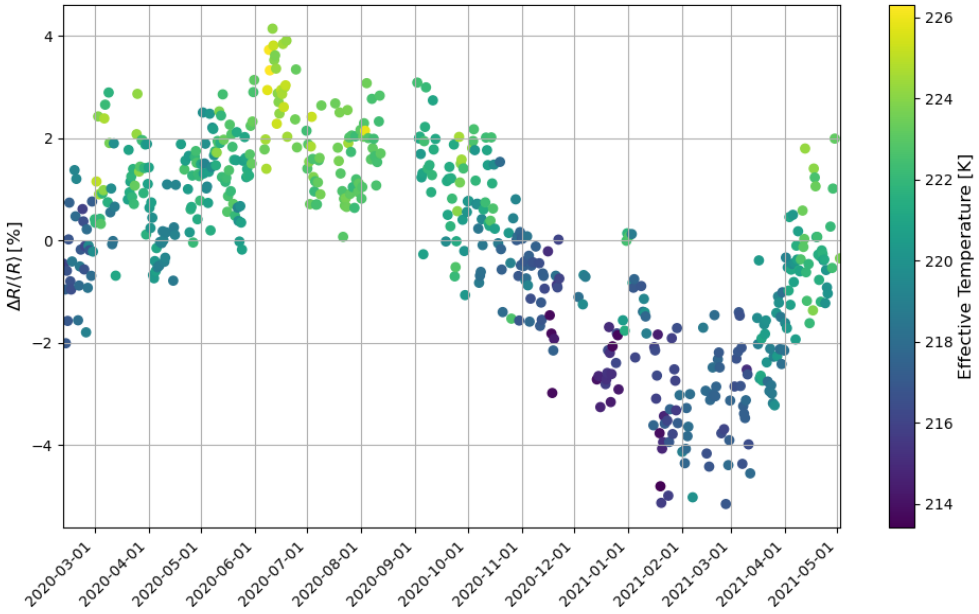

Figure 7.42: The normalised ratio without detrending is plotted over time; the colour of each ratio point shows what the effective temperature is at that ratio point.

Until now, the effective temperate coefficient has been calculated over the whole range of time of a detector configuration. However, it can also be calculated over shorter windows of time. This is done by normalising the data in a specific window and then fitting the model of Equation 6.11 only through the data points in this window. This, of course, can be done for a range of window sizes. In Figure 7.43 this is done for the data without detrending and in Figure 7.44 for the data with detrending. On the y-axis the effective temperature coefficient α is plotted and on the x-axis the central date of the window used to calculate the effective temperature is plotted. The green dotted line indicates the effective temperature coefficient expected theoretically. For both detrended and non-detrended data sets, the coefficients seem to move around the theoretical value over time with slight deviations; expect some outliers. The points in both plots are very similar, but especially for the larger windows some differences are visible.

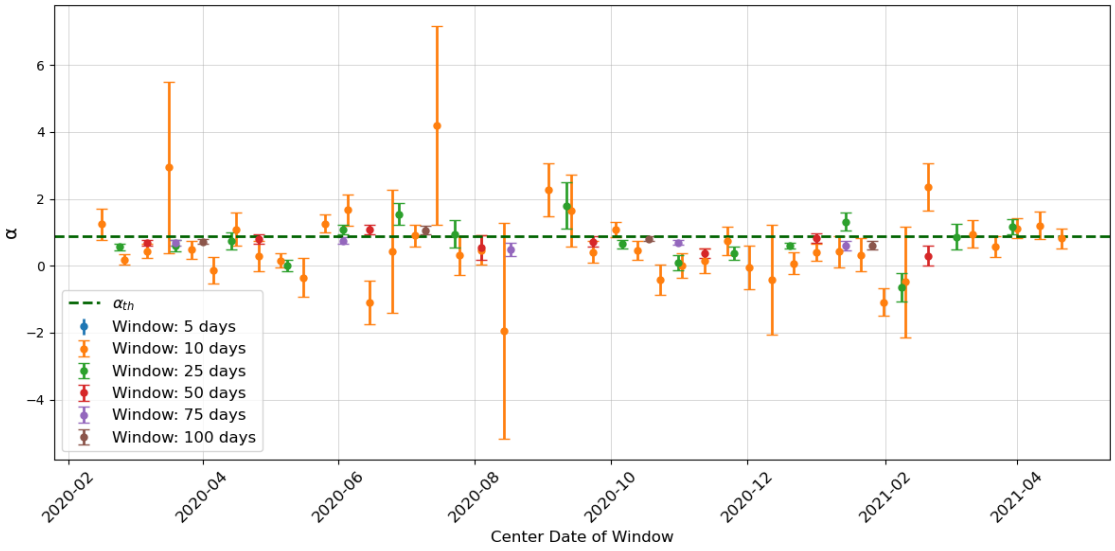

Figure 7.43: Effective temperature coefficient calculated over different time windows. This is done by normalising the ORCA-6 data without detrending in a specific window and the fitting the model of Equation 6.11 only through the data points in this window. On the y-axis the effective temperature coefficient α is plotted and on the x-axis the central date of the window used to calculate the effective temperature is plotted.

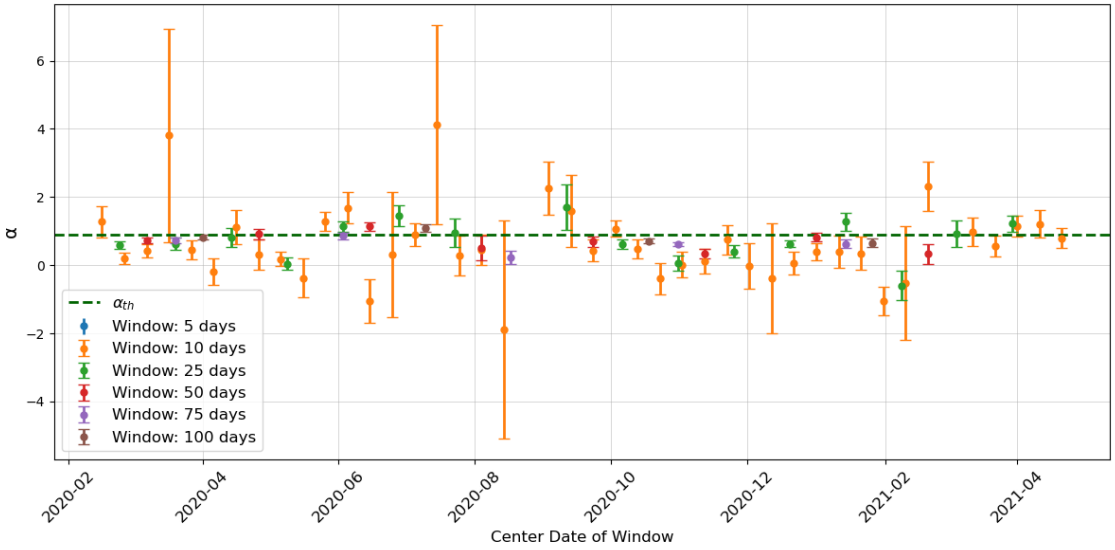

Figure 7.44: Effective temperature coefficient calculated over different time windows. This is done by normalising the ORCA-6 data with detrending in a specific window and the fitting the model of Equation 6.11 only through the data points in this window. On the y-axis the effective temperature coefficient α is plotted and on the x-axis the central date of the window used to calculate the effective temperature is plotted.

A window of five days fits of course many more times in the total range of time than a window of one hundred days. Therefore, to compare the effective temperature coefficient of each window size with each other, the average of window with the same size will be determined. It should be noted that the windows are strongly correlated with each other, a window of six days shares most of its data with a window of five days. In Figure 7.45 the average effective temperature coefficient over a specific window or period is plotted for the data without detrending. In Figure 7.46 this is done for the data with detrending. The red points show for which periods the coefficient is larger than 1 and the green dotted line shows what the coefficient theoretically should be.

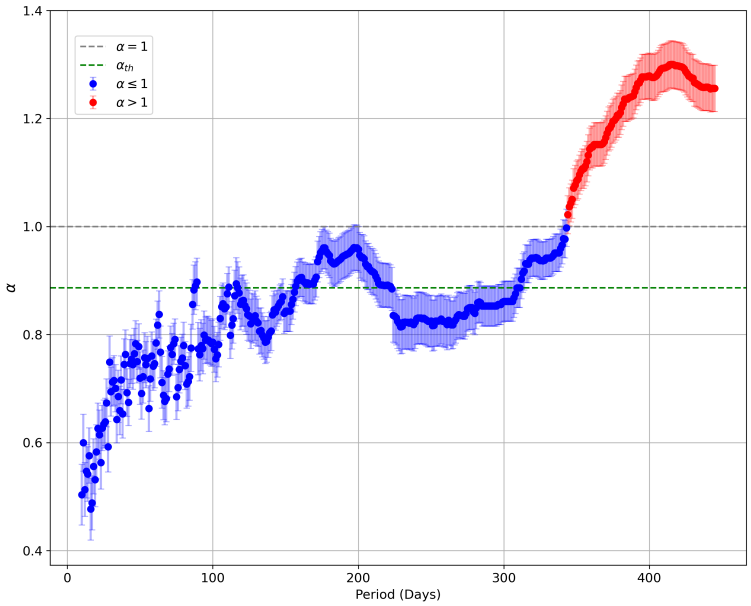

Figure 7.45: The average effective temperature coefficient over a specific window or period is plotted for the data without detrending. The red points show for which periods the coefficient is larger than 1 and the green dotted line shows what the coefficient theoretically should be.

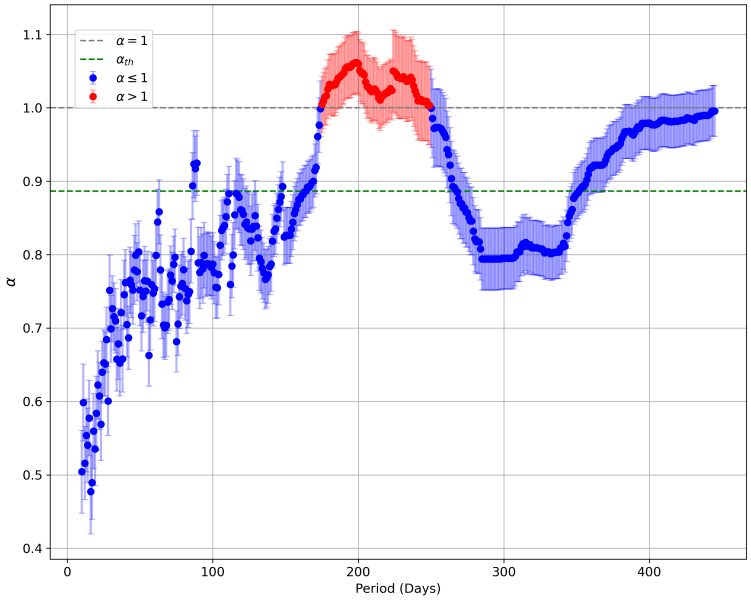

Figure 7.46: The average effective temperature coefficient over a specific window or period is plotted for the data with detrending. The red points show for which periods the coefficient is larger than 1 and the green dotted line shows what the coefficient theoretically should be.

For the average effective temperature coefficient for the data without detrending, a gradual increase with some oscillations can be seen, but in general the larger the window or period, the larger the coefficient. For the average effective temperature coefficient for the data with detrending, this increasing trend is somewhat removed. Now, mainly an oscillation around the theoretical value is seen.
These average effective temperature coefficients can be plotted as histograms. This is done in Figure 7.47 for the data without detrending and in Figure 7.48 for the data with detrending. The colour of the bin indicates the mean window size of that bin. For each histogram, two Gaussian distributions are fitted to the data to get a better view of the data. For data without detrending, the Gaussians have a

mean of 0.84 and 1.24. For data with detrending the Gaussians have a mean of 0.82 and 1.00.

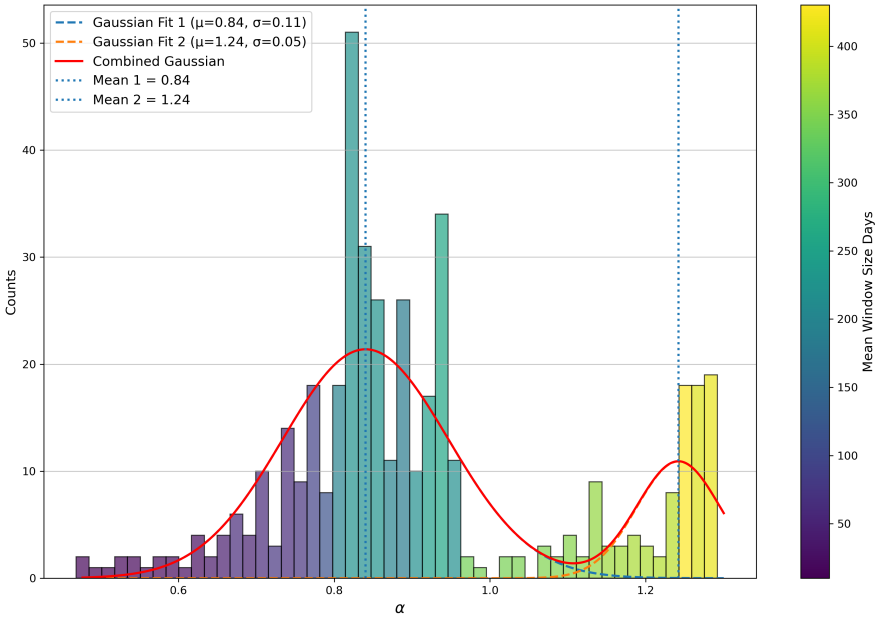

Figure 7.47: Histogram of the average effective temperate coefficients of the data without detrending. The colour of the bin indicates the mean window size of that bin. Two Gaussian distributions are fitted to the data.

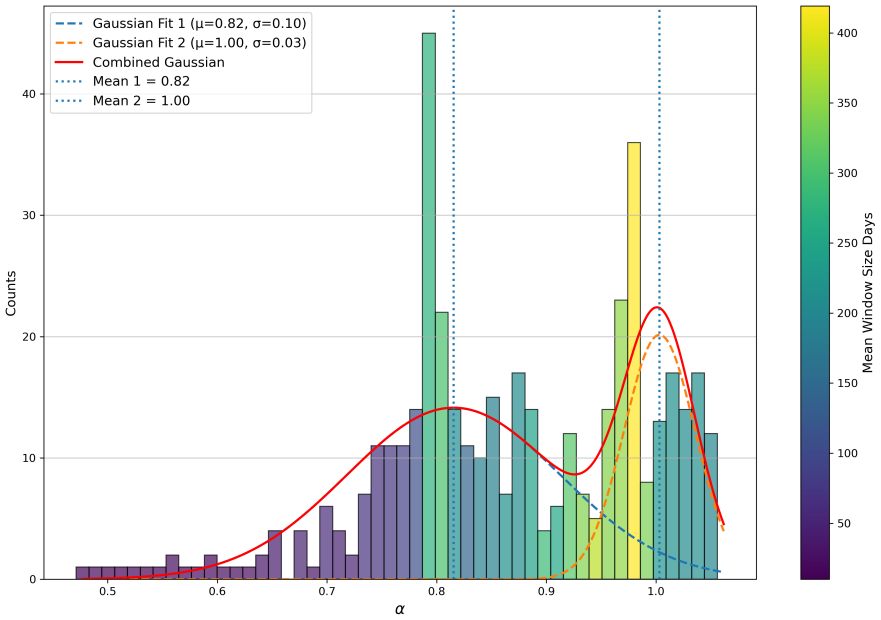

Figure 7.48: Histogram of the average effective temperate coefficients of the data without detrending. The colour of the bin indicates the mean window size of that bin. Two Gaussian distributions are fitted to the data.

In Table 7.8 the resulting effective temperature coefficient of all detector configurations is shown for data with and without detrending.

Table 7.8: Resulting effective temperature coefficient α for all detector configurations while doing the full run analysis. The theoretical α is shown to compare it with the α for data with and without detrending.

Detector	Theoretical α	α	α with detrending
ORCA-6	0.8865	1.25 ± 0.04	1.00 ± 0.03
ORCA-10	0.8870	0.40 ± 0.08	0.71 ± 0.07
ORCA-11	0.8870	0.45 ± 0.23	0.34 ± 0.22
ORCA-11.1	0.8871	0.83 ± 0.21	0.86 ± 0.22
ORCA-15	0.8872	0.90 ± 0.10	0.81 ± 0.12
ORCA-15.1	0.8871	0.91 ± 0.33	0.91 ± 0.32
ORCA-18	0.8870	1.06 ± 0.19	0.87 ± 0.18
ARCA-21	0.9238	0.93 ± 0.17	1.28 ± 0.18

60-Minute Window Around Temperature Measurement

In Figure 7.49 the normalised effective temperature and ratio without detrending are plotted in a scatter plot with the errors. The ratios are calculated in 60-minute windows around temperature measurements. Through these data points, the model of Equation 6.11 is fitted, giving an effective temperature coefficient of $\alpha = 1.19 \pm 0.06$ and a goodness of fit $\chi^2/dof = 0.23$. In Figure 7.50 the same is done but now with the detrended ratio, giving an effective temperature coefficient of $\alpha = 0.99 \pm 0.05$ and a goodness of fit $\chi^2/dof = 0.20$.

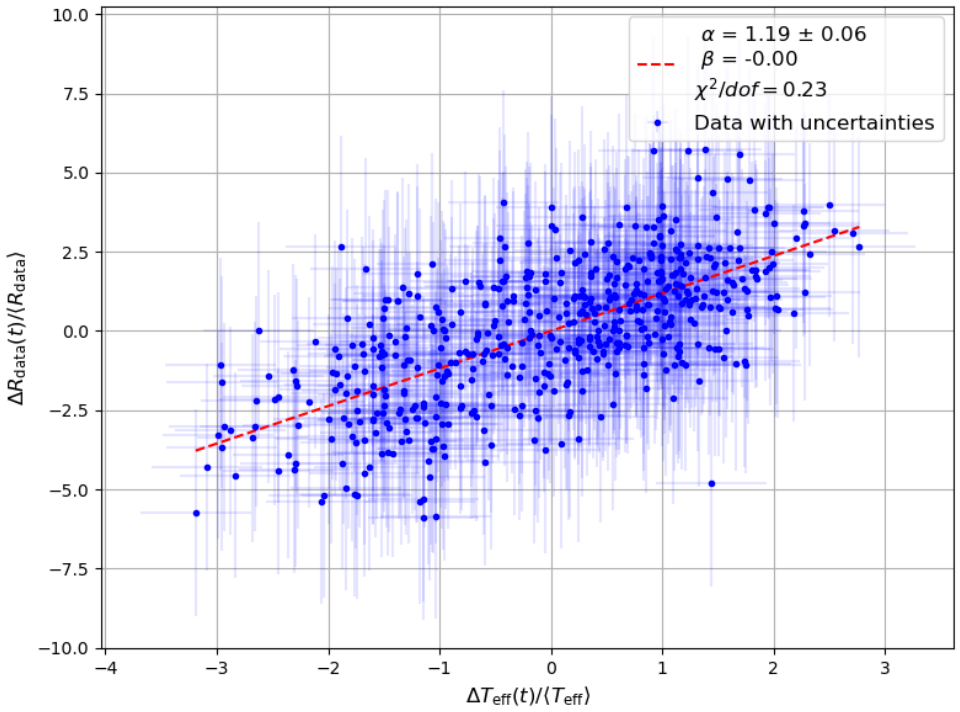

Figure 7.49: Normalised effective temperature T_{eff} and ratio without detrending R_{data} of ORCA-6 showing the relative variation in percentage. The ratios are calculated in 60-minute windows around temperature measurements. The red line is a fit of the model in Equation 6.11. The errors are taken into account in the fit.

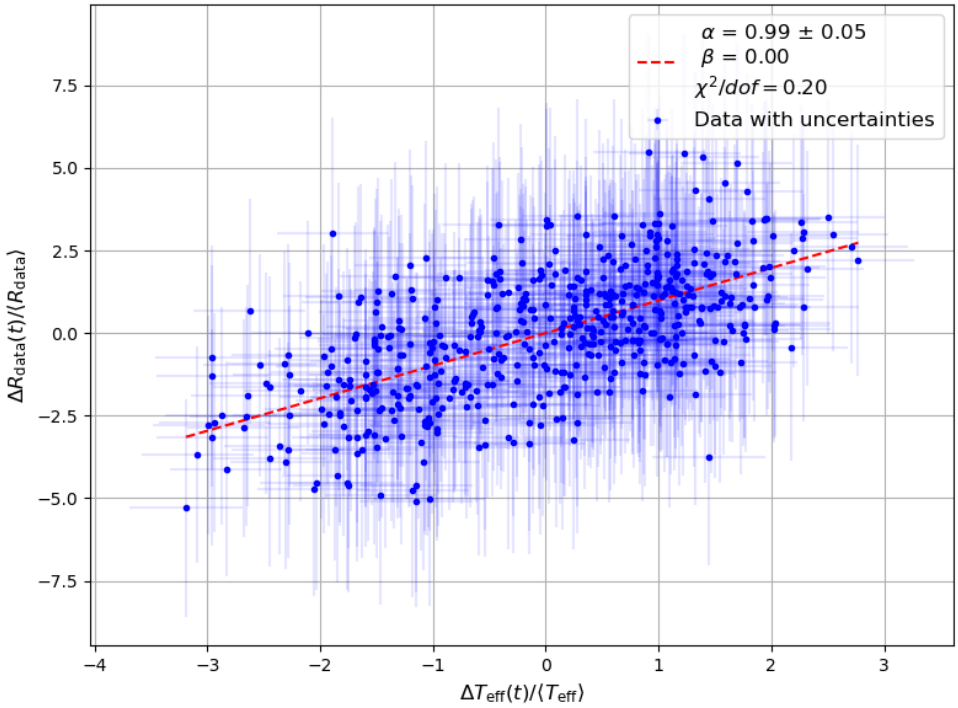

Figure 7.50: Normalised effective temperature T_{eff} and ratio with detrending R_{data} of ORCA-6 showing the relative variation in percentage. The ratios are calculated in 60-minute windows around temperature measurements.The red line is a fit of the model in Equation 6.11. The errors are taken into account in the fit.

The plots of other detector configurations can be found in the appendix. In Table 7.9 the resulting effective temperature coefficient of all detector configurations is shown for data with and without detrending.

Table 7.9: Resulting effective temperature coefficient α for all detector configurations while doing the 60-minute window analysis. The theoretical α is shown to compare it with the α for data with and without detrending.

Detector	**Theoretical α**	α	**α with detrending**
ORCA-6	0.8865	1.19 ± 0.06	0.99 ± 0.05
ORCA-10	0.8870	0.32 ± 0.10	0.61 ± 0.10
ORCA-11	0.8870	-0.02 ± 0.40	-0.04 ± 0.41
ORCA-11.1	0.8871	1.48 ± 0.28	0.84 ± 0.28
ORCA-15	0.8872	0.95 ± 0.13	0.81 ± 0.15
ORCA-15.1	0.8871	0.87 ± 0.48	0.87 ± 0.47
ORCA-18	0.8870	0.99 ± 0.22	0.79 ± 0.21
ARCA-21	0.9238	0.85 ± 0.22	1.15 ± 0.22

7.6.2. ERA5

For the calculation of the ERA5 rate and ratio, the rate was again calculated in two ways. First, the rate and ratio were calculated in 60-minute windows around the temperature measurements. Secondly, the rate and ratio per bin were calculated in 60-minute windows around the temperature measurements.

60-Minute Window Around Temperature Measurement

In Figure 7.51 the normalised effective temperature and ratio without detrending are plotted in a scatter plot with the errors. The ratios are calculated in 60-minute windows around temperature measurements. Through these data points, the model of Equation 6.11 is fitted, giving an effective temperature coefficient of $\alpha = 1.40 \pm 0.02$ and a goodness of fit $\chi^2/dof = 0.81$. In Figure 7.52 the same is done but now with the detrended ratio, giving an effective temperature coefficient of $\alpha = 1.11 \pm 0.02$ and a goodness of fit $\chi^2/dof = 0.66$.

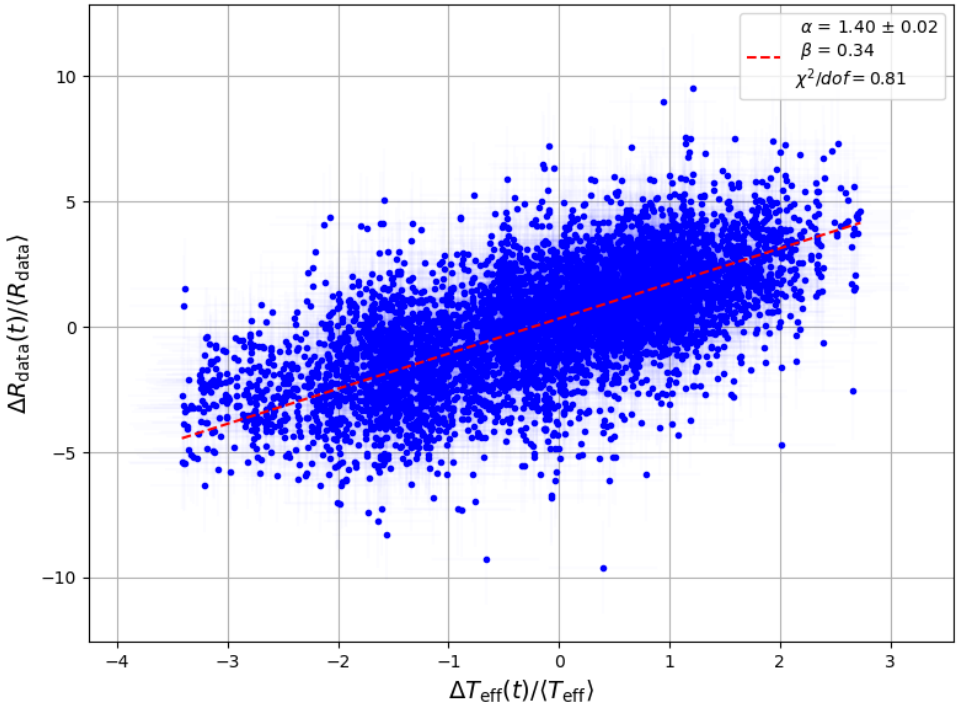

Figure 7.51: Normalised effective temperature T_{eff} and ratio without detrending R_{data} of ORCA-6 showing the relative variation in percentage. The ratios are calculated in 60-minute windows around temperature measurements. The red line is a fit of the model in Equation 6.11. The errors are taken into account in the fit.

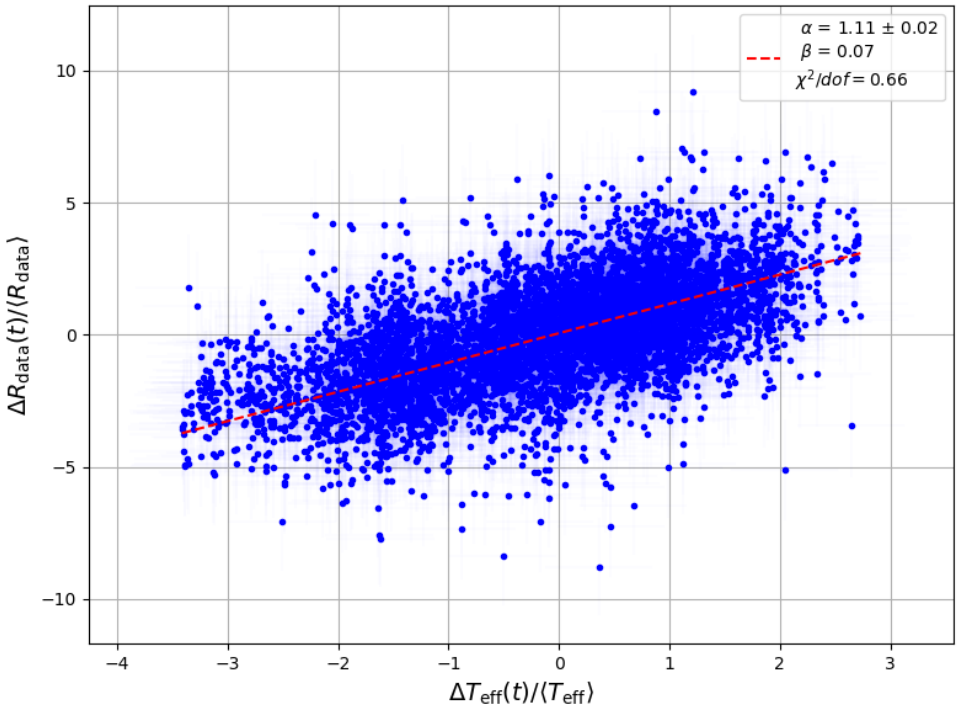

Figure 7.52: Normalised effective temperature T_{eff} and ratio with detrending R_{data} of ORCA-6 showing the relative variation in percentage. The ratios are calculated in 60-minute windows around temperature measurements.The red line is a fit of the model in Equation 6.11. The errors are taken into account in the fit.

The plots of the other detector configurations can be found in the appendix. In Table 7.10 the resulting effective temperature coefficient of all detector configurations is shown for data with and without detrending.

Table 7.10: Resulting effective temperature coefficient α for all detector configurations while doing the 60-minute window analysis. The theoretical α is shown to compare it with the α for data with and without detrending.

Detector	**Theoretical α**	α	**α with detrending**
ORCA-6	0.8865	1.40 ± 0.02	1.11 ± 0.02
ORCA-10	0.8870	0.41 ± 0.03	0.75 ± 0.03
ORCA-11	0.8870	1.07 ± 0.13	1.05 ± 0.13
ORCA-11.1	0.8871	0.94 ± 0.07	0.84 ± 0.07
ORCA-15	0.8872	1.13 ± 0.04	1.01 ± 0.04
ORCA-15.1	0.8871	1.17 ± 0.15	1.25 ± 0.15
ORCA-18	0.8870	1.13 ± 0.07	0.96 ± 0.07
ARCA-21	0.9238	1.23 ± 0.07	1.61 ± 0.07

Binned analysis

For the binned analysis, all bins can be added together to calculate one effective temperature coefficient. This is done in Figures 7.53 and 7.54 for ORCA-6 data without detrending and with detrending, respectively. Each data point in these figures is still plotted with respect to the binned effective temperature and ratio. So, the ratio and temperature of each bin get normalised separately, and the plotted. Then the fit is made through all the data points together.

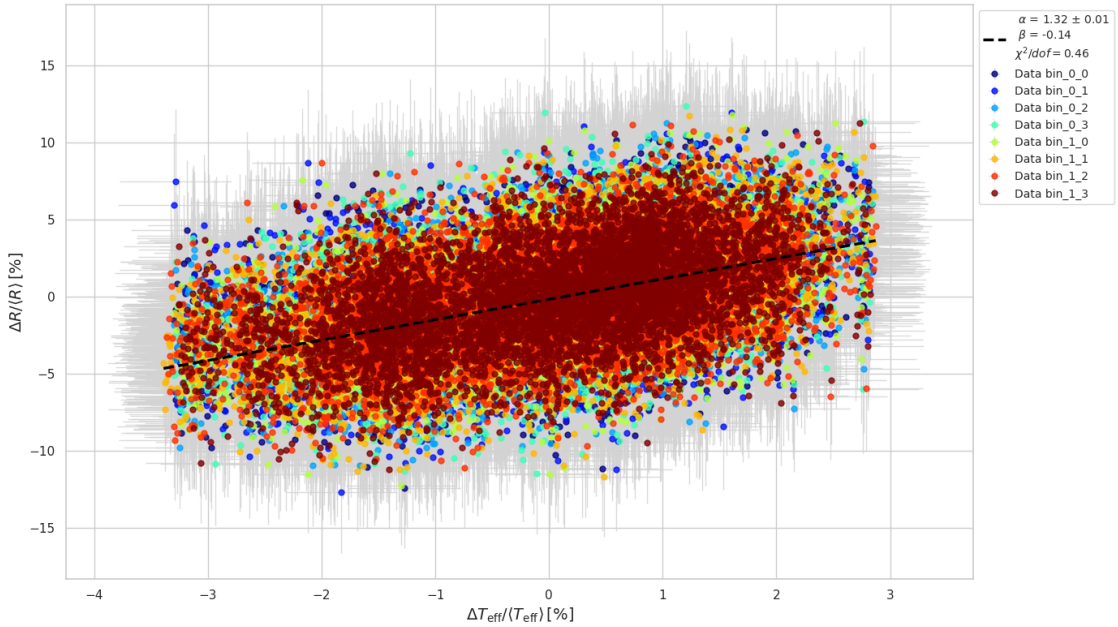

Figure 7.53: Normalised effective temperature T_{eff} and ratio without detrending R_{data} of ORCA-6 showing the relative variation in percentage for each bin plotted together. The black line is a fit of the model in Equation 6.11 though all the data points combined. The errors are taken into account in the fit.

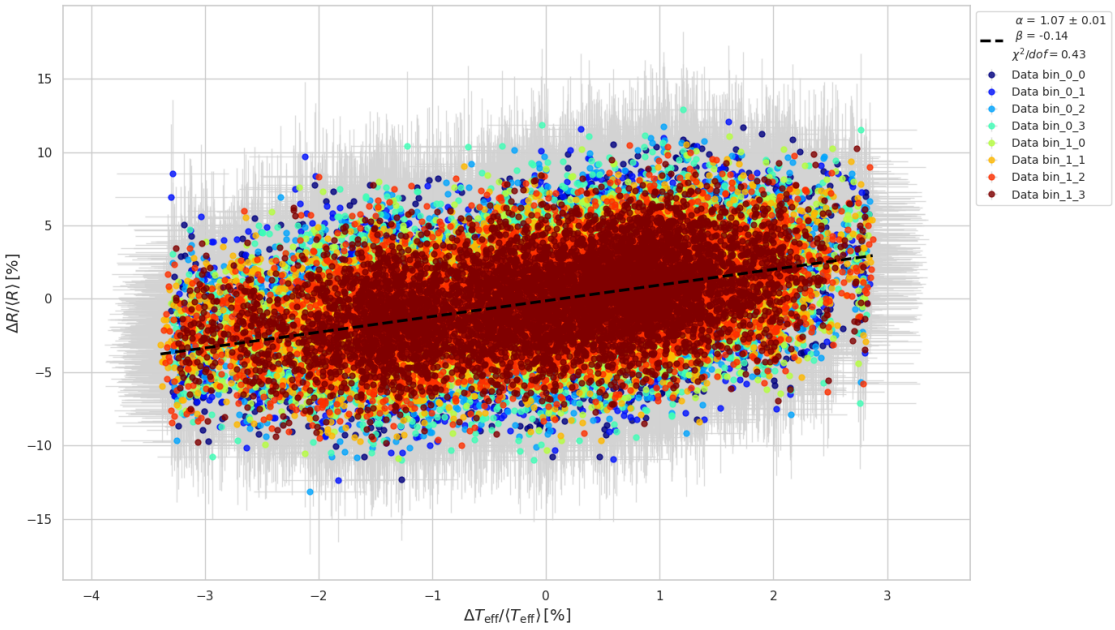

Figure 7.54: Normalised effective temperature T_{eff} and ratio with detrending R_{data} of ORCA-6 showing the relative variation in percentage for each bin plotted together. The black line is a fit of the model in Equation 6.11 though all the data points combined. The errors are taken into account in the fit.

However, an effective temperate coefficient can also be calculated for each separate bin of ORCA-6 data. The fits of each bin can be seen in Figures 7.55 and 7.56 for the data without detrending and with detrending, respectively.

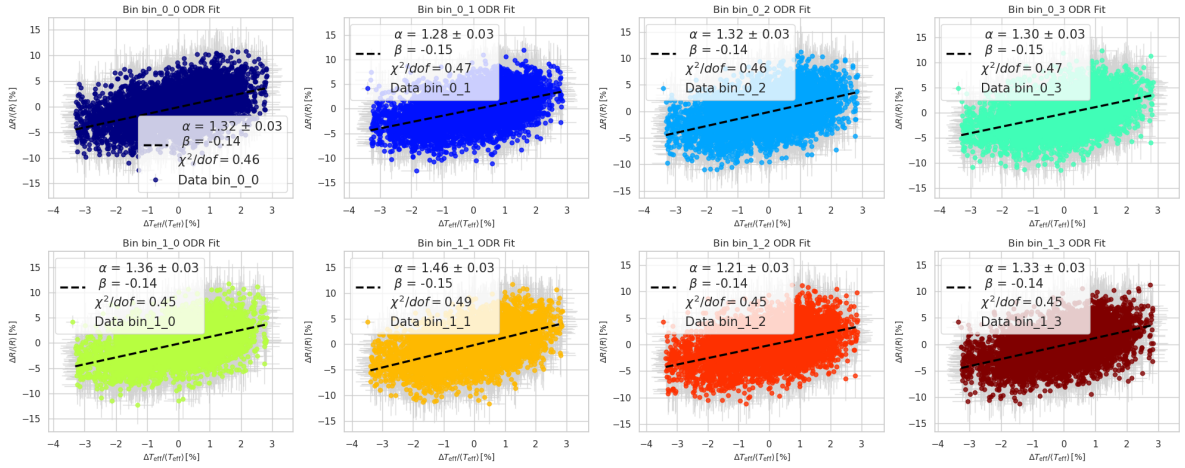

Figure 7.55: Normalised effective temperature T_{eff} and ratio without detrending R_{data} of ORCA-6 showing the relative variation in percentage for each separate bin. The black line in each plot is a fit of the model in Equation 6.11 though the data of each bin separate. The errors are taken into account in the fit.

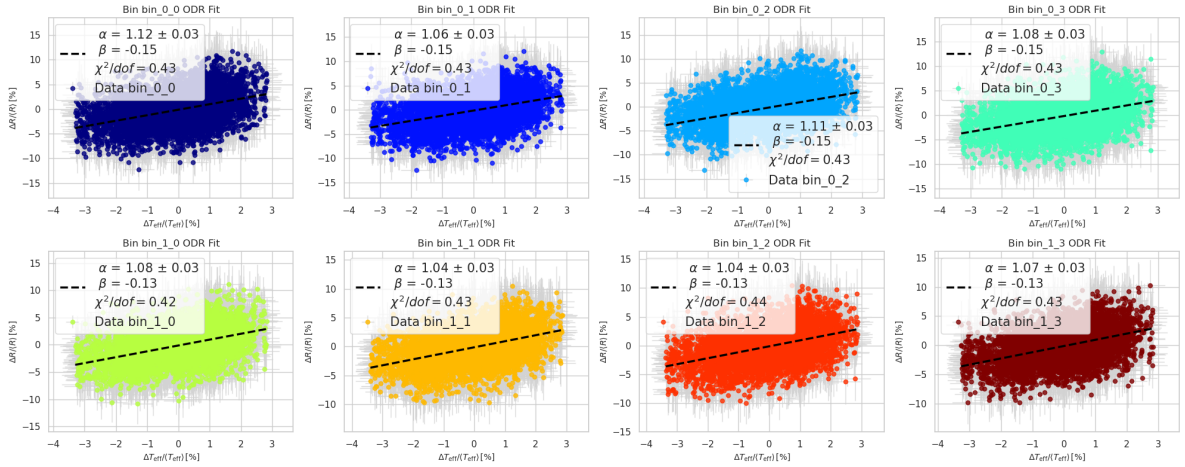

Figure 7.56: Normalised effective temperature T_{eff} and ratio with detrending R_{data} of ORCA-6 showing the relative variation in percentage for each separate bin. The black line in each plot is a fit of the model in Equation 6.11 though the data of each bin separate. The errors are taken into account in the fit.

Without detrending, bins with a larger zenith angle have a larger effective temperature coefficient. This is expected because the larger the zenith angle, the longer the path of the muon through the sea, which causes a higher average threshold energy for these bins. However, after detrending this is no longer the case, the larger zenith angle bins have a lower effective temperature coefficient. In Figure 7.57 the effective temperature coefficient of the bins is plotted with respect to the theoretical effective temperature coefficient for ORCA-6. On the left side for the data without detrending and on the right side with detrending.

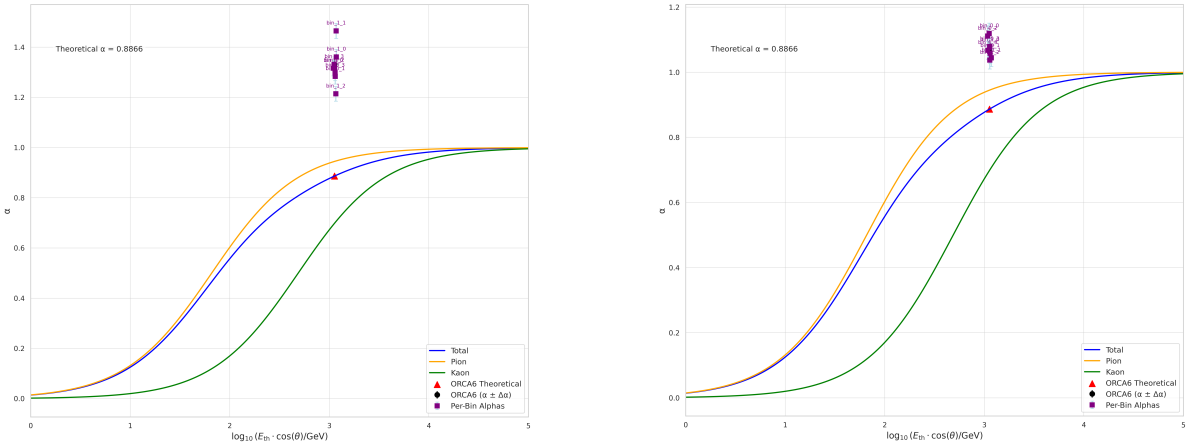

Figure 7.57: The theoretically expected total, pion, and kaon effective temperature coefficient (α) is plotted over a range of average threshold energy. The theoretical expected α for ORCA-6 is highlighted by the red triangle. The experimentally determined α for ORCA-6 for each bin without detrending is plotted in the left figure and with detrending in the right figure.

Table 7.11: Resulting effective temperature coefficient α for all detector configurations while doing the binned analysis. The theoretical α is shown to compare it with the α for data with and without detrending.

Detector	**Theoretical α**	α	**α with detrending**
ORCA-6	0.8865	1.32 ± 0.01	1.07 ± 0.01
ORCA-10	0.8870	0.42 ± 0.02	0.79 ± 0.02
ORCA-11	0.8870	1.12 ± 0.10	0.99 ± 0.10
ORCA-11.1	0.8871	0.93 ± 0.06	0.84 ± 0.06
ORCA-15	0.8872	1.11 ± 0.02	0.98 ± 0.02
ORCA-15.1	0.8871	1.14 ± 0.12	1.22 ± 0.12
ORCA-18	0.8870	1.31 ± 0.05	1.32 ± 0.05
ARCA-21	0.9238	1.03 ± 0.05	1.25 ± 0.05

8

Discussion and Conclusion

In this study, the seasonal variation of the atmospheric muon rate detected by the KM3NeT ORCA and ARCA detectors was studied, focussing on the impact of atmospheric temperature on the detected muon rate. Using atmospheric temperature profile data from the AIRS satellite and the ERA5 reanalysis, the effective temperature coefficient (α) was derived in several ways. Since both ORCA and ARCA are still in construction, only limited data lifetimes are available. Only ORCA-6 has enough data to see seasonal variation over a time period of one year. This limits the accuracy of the analysis that can be done on the other detector configurations, as it becomes harder to distinguish between seasonal temperature changes and other effects. To correct for possible other effects on the detected rate, the ratio between the detected rate and a simulated rate is used. The simulated rate should account for all effects on the rate except for the atmospheric temperature influence. By studying the ratio, the effect of the atmospheric temperature should thus become isolated.

8.1. Discussion

Full Run Analysis with AIRS Data

The first analysis done on the data is done with AIRS temperature data, the muon rate during a run is calculated if there happens to be a temperature measurement of AIRS in that run. The resulting effective temperature coefficients show a number of interesting points. The α of ORCA-6 is found to be 1.25 ± 0.04, which is significantly higher than the theoretically expected value of 0.8865. A reason of this could be that the Monte Carlo simulations, used to correct for detector and other effects besides the impact of atmospheric temperature, do not accurately simulate all factors of influence, such as efficiency losses, on the detected muon rate. This means that the ratio between the data and the simulation could give an inaccurate view of the true muon rate. To test this, a harmonic fit with a period of one year (due to the seasonal nature) and a linear trend were fitted to the ratio data. In the ORCA-6 data, a harmonic with an amplitude of 0.0187 and a linear trend of -5.9520×10^{-5} $[day^{-1}]$ and offset 1.0423 was fitted. The linear trend could point to the fact that the Monte Carlo simulation does not accurately account for all efficiency losses in the detector. Similar fits have been performed for the other detector configurations. However, fitting becomes more difficult because of the limited duration of stable data taking of the other detectors. Therefore, the amplitude found for the ORCA-6 data was used for the other detector configuration except ARCA-21. The amplitude in ratio of each detector configuration could differ in reality, but since no whole data period is available, it is hard to find this amplitude using this method. For all detectors, a downward linear trend can be found, but due to the limited lifetimes of some fit, this could be inaccurate. The fit could find a downward linear trend but on small timescales the harmonic variation can also be fitted with a linear trend. However, this linear trend can still be removed from the data and the effective temperature coefficient of ORCA-6 becomes 1.00 ± 0.03. This is already closer to the theoretically expected value. A similar change can be seen for ORCA-10 and ORCA-18. For ORCA-10 without detrending α was found to be significantly smaller than expected, after detrending it becomes closer to what is expected. For ORCA-18 without detrending α was found to be significantly larger than expected, after detrending it becomes closer to what is expected. This

improvement could be due to accurate fits to the data from these three detectors because they span the longest time of the detector configurations studied. For ORCA-11 and ARCA-21, the opposite is found, and α after the detrending deviates more from the expected value than before. For ORCA-11 this could be due to the limited data available, causing an inaccurate fit. For ARCA-21 it could be that the Monte Carlo simulations better account for the efficiency losses in the detector, causing a fit of a downward linear trend where there is actually no linear trend.
A goodness of fit was determined for all α calculations; in all cases this was found to be less than 1. This means that the uncertainties of the data might be overestimated.
Next, α was calculated in different windows over time. If no other factors would influence the ratio, α should be constant in every window over time. However, this is not the case; fluctuations over time can be seen in α. This could hint at other factors not being accurately simulated in the Monte Carlo simulation. For ORCA-6, a gradual increase in α can be seen when the window becomes larger. This could again be a hint that the efficiency is not accurately simulated, and thus being in line with the downward trend seen before. After detrending this gradual increase is gone but some oscillations in α over window size remain. This could be due to the fact that some other factors that are not (accurately) simulated influence the rate periodical that aligns with these window. For detectors with a shorter time span α remains more constant over time, this could be because on these shorter time scales the efficiency losses have less impact. ORCA-6, ORCA-10, and ORCA-18 are again good examples in which detrending makes α more stable over time.

Detector efficiency

The atmospheric muons studied in this paper are mostly detected by the PMTs in the upper part of the DOMs. These PMTs are more affected by sedimentation, which reduces the efficiency compared to PMTs in the lower part of the DOMs. The detector efficiencies are estimated using the correlation rates of neighbouring PMTs. Since efficiency is direction-dependent, this method averages efficiency over the directions of neighbouring PMTs. However, there are no PMTs orientated directly upward, which could potentially cause a systematic overestimation of the efficiency of the upper PMTs. This effect increases with higher levels of sedimentation. This overestimation of the efficiency of the detector in the upward direction could be the cause of the downward trend that is found in the ratio data. If the efficiency is overestimated, the muon rate for the simulation will be higher that in reality causing the ratio to decrease. This could become especially noticeable in the data of the detector configurations with a longer life time because more sedimentation will form during a longer period.
It would be interesting to see what would happen if in the future there was a detector configuration with a lifetime longer than that of ORCA-6. In Figure 7.46 an oscillating pattern of the average effective temperature coefficient can be seen over time with a frequency of approximately half a year. It could be that this oscillating pattern continues for larger windows. This could point to a new influence on the rate of the detected muons.

60-Minute Window Around Temperature Measurements with AIRS Data

The second analysis is performed again using the AIRS temperature data. However, now instead of calculating the rate over a whole run, the rate is calculated in a 60 minute time window around a temperature measurement. This is done to reduce some potential scattering caused by the fact that the rate in a data run is not constant. However, the Monte Carlo simulation of a run uses a distribution of rates that is the same as the distribution of the rates in the real run. Because the simulations are performed for a whole run, the changing of the rate over time in a run gets lost, and the rate for a Monte Carlo simulation run will become constant. This forces the use of the constant rate of the simulation for the calculation of the ratio for the 60-minute time window. This could cause some error. Therefore, in order to improve this, a Monte Carlo simulation could be performed for smaller time intervals instead of a whole run. This would create more computer load for the stimulations, so a Monte Carlo simulation run could, for example, be scaled into blocks to somewhat limit the computational load.
Looking at the fitting of the harmonic model with a linear trend to the ratio data, the results are similar to the fit made before to the whole run ratio. Now comparing the resulting effective temperature coefficients α with the α found before for the whole run ratio. It can be seen that α of ORCA-6, ORCA-10, ORCA-15, ORCA-15.1, ORCA-18, and ARCA-21 remain very similar before and after detrending. α of ORCA-11 becomes almost 0 indicating no correlation. α of ORCA-11.1 increases significantly before detrending but after detrending it becomes very similar to the α found before. It is difficult to say

whether the shorter time window improves the result and possible removes some additional factors that correlate over longer time scales. For future research, it is recommended to test more time windows around a temperature measurement to better understand the impact of the window on the effective temperature correlation. Additionally, it would be recommended to have a Monte Carlo simulation that is performed on smaller time intervals so that the ratio would more accurately reflect the true muon rate that is only affected by the atmospheric temperature.

60-Minute Window Around Temperature Measurements with ERA5 Data

The third analysis performed uses the ERA5 temperature data. ERA5 has hourly temperature measurements, so the rates were again calculated in 60-minute windows around a temperature measurement. Because there are less events in the 60 minute windows, some statistics get lost and the errors on the rate increase. Many more ratio points are available now with a wider spread, making the fitting process to the ratio and the determination of the effective temperature coefficient less accurate. The resulting effective temperature coefficients are higher for every detector configuration before and after detrending. After detrending, the values seem to improve a bit, but they still deviate significantly from the expected value. In order to test whether this change comes from the use of the ERA5 temperature data or that it has some other cause, it is recommended to do the analysis for a varying window duration in future research.

Binned analysis with ERA5 Data

The fourth and final analysis performed uses again the ERA5 temperature data. Now, the rates are calculated in the 60-minute window around a temperature measurement and in bins based on the direction. The rates form the bins with a larger zenith angle, which is closer to the horizontal plane, have a higher rate than the bins with a smaller zenith angle. No clear difference between the azimuth bins can be seen. When looking at the ratio of the data and the Monte Carlo simulation in these bins, it can be seen that the ratio of the bins with a smaller zenith angle is larger than the ratio of the bins with a bigger zenith angle. This is an interesting result, because all the ratios are expected to be centred around 1 regardless of the zenith angle. The simulations underestimate the rates for bins with a smaller zenith angle and overestimate the bins with a larger zenith angle. The effective temperate coefficient has now been calculated in two ways. First, with all the data combined, this gives as expected a result very similar to the third analysis. Secondly, the effective temperate coefficient was calculated for the separate bins. Before detrending, it is found that, in general, the coefficient is larger for larger zenith angles. This is expected because the muons reaching the detector with a larger zenith angle need higher energies to travel the longer path through the water. Higher energy muons are expected to have a stronger temperature correlation. However, after detrending this is no longer that clear; the larger zenith angles are more similar to the smaller zenith angles and sometimes even smaller. In general, the effective temperature coefficients of the bins do not differ more than one or two standard deviations from each other, indicating that the detector does not have a directional bias for atmospheric muons.

Relationship analysis's

The AIRS and ERA5 analysis's have been done to see if different temperature data has a effect on the resulting effective temperature coefficients. In order to directly compare the different temperature datasets, the analysis was done in 60-minute windows around a temperature measurement. In general, the analysis performed with the ERA5 temperature data results in higher effective temperature coefficients; this could be due to the fact that ERA5 has hourly temperature measurements. For the AIRS 60-minute window analysis, only two temperature measurements per day are made, and only the events that fall within a 60-minute window around this temperature measurement are selected. The binned analysis is performed to see if the effective temperature coefficient is directional dependent, which turn out not to be the case.

General discussion

The rate and ratio have only been determined in windows that equal the duration of a run and in windows of 60 minutes around a temperature measurement. For future research, it would be interesting to see how the effective temperature coefficient would behave for different window sizes, such as the analysis done by Abbasi et al. [41], on IceCube atmospheric neutrino data. In addition to this, a different approach to the Monte Carlo simulations would make it possible to have a varying rate in the

simulation runs and thus would make it possible to calculate a more accurate ratio. The limited lifetime of the different detector configurations also makes the analysis more difficult, because the fitting procedure could find a linear trend on a short time scale that is actually part of the harmonic seasonal variation. The only detector configuration that spans at least one seasonal variation period of one year is ORCA-6. However, this is still limited. To make a reliable fit and minimise the bias to any time of the year, a multi-year stable dataset needs to be available. A stable data set means that not only is the period of data collection constant but also the detector configuration stable and the efficiency of the detector is well understood. For now, this is difficult as the detector is constantly growing because of the construction. As the detector grows, it could be that the detector has some systematic differences in how it collects data as a result of changing geometries and the varying number of DUs. In addition, the detector efficiency constantly varies over time. The Monte Carlo simulations try to compensate for this, but the suspicion is that the efficiencies of the detector in the upward direction are overestimated. This raises the question whether the Monte Carlo simulations factor in all influences on the detected muon rate except for the seasonal variation. In the calculations of the effective temperature coefficient over time, some fluctuations could be seen, hinting that not all factors are accounted for. Factors in the sea that could have an indirect influence on the detected rate, such as the inflow of water from rivers, changing the composition of the seawater, or other atmospheric processes, could not be fully accounted for in the Monte Carlo simulation.
In addition to this, the reconstruction algorithm assumes that only one muon is responsible for an observed event. However, this is not always the case; multiple-muon events are also created in air showers and can also be detected by detectors such as KM3NeT's. Due to the design of the KM3NeT detectors, it is currently very complicated to distinguish between a single or multiple muon event. Although machine learning applications are in development [42]. The strange thing now is that multiple studies have found a winter peak in the multiple-muon rate compared to the summer peak of the single-muon rate [7, 9, 43, 44]. The anticorrelation of multiple-muon event rates is not yet fully understood. It would be interesting to see what the effects would be on the effective temperature coefficient if, in the future, it is possible to distinguish between single-muon and multiple-muon events.
Finally, a linear fit is used to determine the effective temperature coefficient. However, other papers, such as one about IceCube, find indications for a nonlinear relationship. They also found that the coefficient depends on the data range chosen for the fit [45]. This would cause a non-constant effective coefficient over time. In order to do this analysis, data from a multi-year stable dataset is needed and a better understanding of possible biases the Monte Carlo simulation has.

Comparison to other experiments

In Figure 8.1 the effective temperature coefficients of other experiments are reported together with the results of the full run analysis done in this study. In dashed black, dotted black, and red, the pion, kaon, and total contributions are plotted, respectively. The green line is a fit where the kaon-to-pion ratio ($r_{K/\pi}$) is fitted through the data points. The figure was acquired from Ambrosio et al. [46] and modified to include KM3NeT results. As can be seen, mainly ORCA-6 and ORCA-10 deviate from the theory; after they are detrended, they already come closer to the theoretical value. For ARCA-21 the opposite seems to happen.

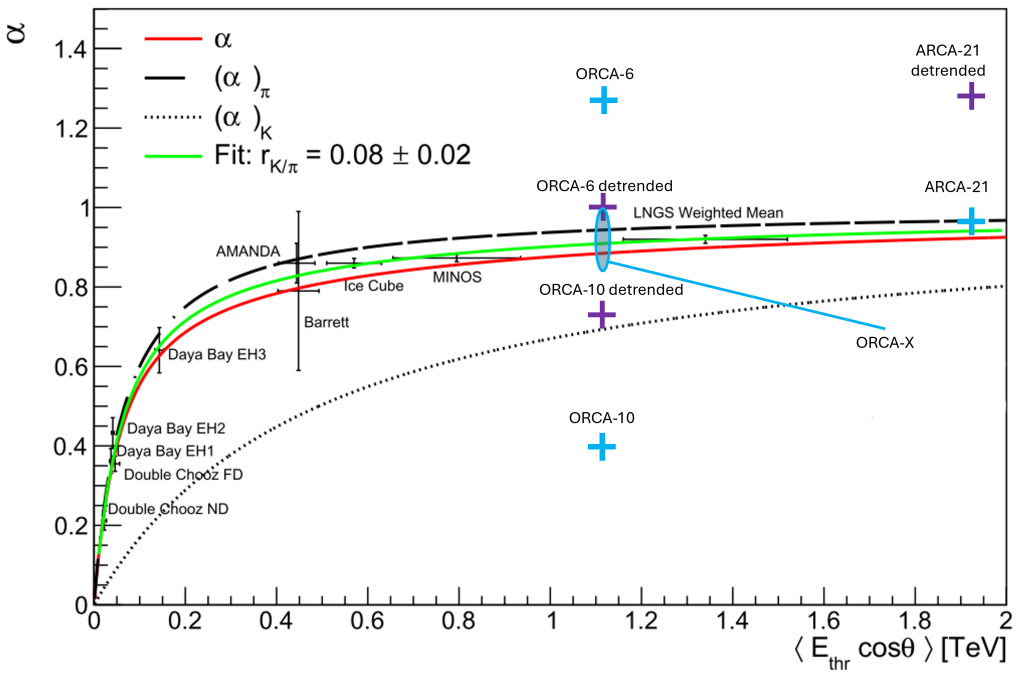

Figure 8.1: The effective temperature coefficients of other experiments together with the results of the full run analysis done in this study. In dashed black, dotted black, and red, the pion, kaon, and total contributions are plotted, respectively. The green line is a fit where the kaon-to-pion ratio ($r_{K/\pi}$) is fitted through the data points. acquired from Ambrosio et al. [46] and modified to include KM3NeT results.

The kaon-to-pion ratio is a measure of how many kaons are produced in an air-shower compared to pions. The kaon-to-pion ratio is important because it affects the properties of the muons that reach a detector, such as the energy of a muon and how much they are affected by atmospheric temperature variations. If the kaon-to-pion ratio decreases, the effective temperature coefficient increases. This is because pions have a lower critical energy and thus experience a greater correlation with temperature variations in the atmosphere. The kaon-to-pion ratio is measured indirectly by measuring the effective temperature coefficient and can be determined as [24]:

$$r_{K/\pi} = \frac{\alpha_\pi^{th}/\alpha^{exp} - 1}{1 - \alpha_K^{th}/\alpha^{exp}} \tag{8.1}$$

where $\alpha_{K,\pi}^{th}$ are the theoretical kaon and pion contributions determined according to Equation 3.22. α^{exp} are the experimental determinate effective temperature coefficients.

8.2. Conclusion

During this study, the seasonal variation of atmospheric muons detected by the KM3NeT ORCA and ARCA detectors was investigated. The main focus was on the impact of atmospheric temperatures on the detected muon rate. The muon rates were correlated with the effective atmospheric temperature above the KM3NeT detectors to calculate an effective temperature coefficient (α). The effective temperature is a weighted average over all pressure levels in the raw temperature data sets. In this study, the AIRS and ERA5 temperature datasets are used to calculate two effective temperatures over time. An effective temperature analysis is needed to account for the fact that most muons are produced in the upper parts of the atmosphere. The KM3NeT detectors experience a high degree of background rate. Therefore, not the muon rate gets correlated with the effective temperature but the ratio of the muon rate with the muon rate out of run-by-run Monte Carlo simulation. This simulation should account for all the factors that impact the true muon rate, except for the temperature variation. The effective temperature coefficient was calculated in four ways. First, the ratio was calculated for entire data runs and correlated to a AIRS temperature measurement that coincided with this run. Second, the ratio was calculated in 60-minute windows around an AIRS temperature measurement and then correlated with it. Third, the ratio was calculated in 60-minute windows around an ERA5 temperature measurement and then correlated with it. Fourth, the muons were binned according to their directions, and the ratio was calculated in 60-minute windows around an ERA5 temperature measurement and then correlated with it. The effective temperature coefficients found for these analyses are presented in Table 8.1. A positive correlation between muon rate and atmospheric temperature has been found, but for most detector configurations studied, the correlation is stronger than expected.

Table 8.1: Comparison of α values across different detectors and analyses.

Analysis	ORCA-6	ORCA-10	ORCA-11	ORCA-11.1	ORCA-15	ORCA-15.1	ORCA-18	ARCA-21
Theoretical α	0.8865	0.8870	0.8870	0.8871	0.8872	0.8871	0.8870	0.9238
Full Run α	1.25 ± 0.04	0.40 ± 0.08	0.45 ± 0.23	0.83 ± 0.21	0.90 ± 0.10	0.91 ± 0.33	1.06 ± 0.19	0.93 ± 0.17
Full Run α (Detrended)	1.00 ± 0.03	0.71 ± 0.07	0.34 ± 0.22	0.86 ± 0.22	0.81 ± 0.12	0.91 ± 0.32	0.87 ± 0.18	1.28 ± 0.18
60-min AIRS Window α	1.19 ± 0.06	0.32 ± 0.10	-0.02 ± 0.40	1.48 ± 0.28	0.95 ± 0.13	0.87 ± 0.48	0.99 ± 0.22	0.85 ± 0.22
60-min AIRS Window α (Detrended)	0.99 ± 0.05	0.61 ± 0.10	-0.04 ± 0.41	0.84 ± 0.28	0.81 ± 0.15	0.87 ± 0.47	0.79 ± 0.21	1.15 ± 0.22
60-min ERA5 Window α	1.40 ± 0.02	0.41 ± 0.03	1.07 ± 0.13	0.94 ± 0.07	1.13 ± 0.04	1.17 ± 0.15	1.13 ± 0.07	1.23 ± 0.07
60-min ERA5 Window α (Detrended)	1.11 ± 0.02	0.75 ± 0.03	1.05 ± 0.13	0.84 ± 0.07	1.01 ± 0.04	1.25 ± 0.15	0.96 ± 0.07	1.61 ± 0.07
Binned Analysis α	1.32 ± 0.01	0.42 ± 0.02	1.12 ± 0.10	0.93 ± 0.06	1.11 ± 0.02	1.14 ± 0.12	1.31 ± 0.05	1.03 ± 0.05
Binned Analysis α (Detrended)	1.07 ± 0.01	0.79 ± 0.02	0.99 ± 0.10	0.84 ± 0.06	0.98 ± 0.02	1.22 ± 0.12	1.32 ± 0.05	1.25 ± 0.05

The analysis remains difficult because of the lack of a multi-year stable dataset. Not only does the data taking period need to be done over a longer period with a constant detector setup, but all factor influencing the detected rate need to be well understood, such as the detector efficiency. The only data set that spans at least one year is the ORCA-6 data set, and in this data set a decrease in the mean ratio can be seen, pointing to some problems with the Monte Carlo simulations. The Monte Carlo simulations probably do not accurately account for all influences on the detected rate such as efficiency losses of the detector and other periodic variations in the rata. In all data sets used in this study, a linear downward trend was found in the ratio data. This trend can be removed, and the effective temperature coefficient can then be recalculated. The results of this are shown in Table 8.1. After detrending, the correlation between the muon rate and atmospheric temperature moves closer to the expected value for most detector configurations, but it still deviates significantly. The linear downward trend can be caused by a time-dependent overestimation of detector efficiency in the upward direction by Monte Carlo simulations. In addition to this, in the binned analysis it is found that the Monte Carlo simulation underestimates the rates for smaller zenith angles and overestimates the rates for larger zenith angles. This could be caused by flaws in the muon simulation.

In order to improve the analysis for future studies, the Monte Carlo simulation could be done differently. Currently, the rate in a simulation run is constant, but this is not the case for the real rate in a run. By varying the rate in the simulations more accurate ratios of smaller time windows could be calculated giving new insights. Future research should focus on using multi-year stable datasets, improving the overall accuracy of the Monte Carlo simulations, exploring different time window analyses, and further studying the impact of multiple-muon events.

References

[1] Thomas Bergauer. *Cosmic ray air showers*. Ars Electronica, Aug. 2011. URL: https://www.flickr.com/photos/arselectronica/6069688893.

[2] Dieter Fick and Dieter Hoffmann. "Werner Kolhörster (1887-1945): The German pioneer of cosmic ray physics". In: *Astroparticle Physics* 53.C (Jan. 2014), pp. 50–54. ISSN: 09276505. DOI: 10.1016/j.astropartphys.2013.09.007.

[3] VIKTOR F. HESS. "Observations of the Penetrating Radiation on Seven Balloon Flights". In: *Cosmic Rays*. July 1972, pp. 139–147. DOI: 10.1016/b978-0-08-016724-4.50013-6. arXiv: 1808.02927. URL: https://arxiv.org/abs/1808.02927v2.

[4] Pierre Auger et al. "Extensive cosmic-ray showers". In: *Reviews of Modern Physics* 11.3-4 (July 1939), pp. 288–291. ISSN: 00346861. DOI: 10.1103/RevModPhys.11.288. URL: https://journals.aps.org/rmp/abstract/10.1103/RevModPhys.11.288.

[5] Paul H. Barrett et al. "Interpretation of cosmic-ray measurements far underground". In: *Reviews of Modern Physics* 24.3 (July 1952), pp. 133–178. ISSN: 00346861. DOI: 10.1103/RevModPhys.24.133. URL: https://journals.aps.org/rmp/abstract/10.1103/RevModPhys.24.133.

[6] M. Ambrosio et al. "Seasonal variations in the underground muon intensity as seen by MACRO". In: *Astroparticle Physics* 7.1-2 (1997), pp. 109–124. ISSN: 09276505. DOI: 10.1016/S0927-6505(97)00011-X.

[7] P. Adamson et al. "Observation of seasonal variation of atmospheric multiple-muon events in the MINOS Near and Far Detectors". In: *Physical Review D - Particles, Fields, Gravitation and Cosmology* 91.11 (2015), pp. 1–9. ISSN: 15502368. DOI: 10.1103/PhysRevD.91.112006. arXiv: 1503.09104.

[8] Serap Tilav et al. "Seasonal variation of atmospheric muons in IceCube". In: *Proceedings of Science*. Vol. 358. Sissa Medialab Srl, Sept. 2019. DOI: 10.22323/1.358.0894. arXiv: 1909.01406. URL: https://arxiv.org/abs/1909.01406v1.

[9] M. A. Acero et al. "Observation of seasonal variation of atmospheric multiple-muon events in the NOvA Near Detector". In: *Physical Review D* 99.12 (June 2019), p. 122004. ISSN: 24700029. DOI: 10.1103/PhysRevD.99.122004. arXiv: 1904.12975. URL: https://journals.aps.org/prd/abstract/10.1103/PhysRevD.99.122004.

[10] F. P. An et al. "Seasonal variation of the underground cosmic muon flux observed at Daya Bay". In: *Journal of Cosmology and Astroparticle Physics* 2018.1 (Jan. 2018), p. 001. ISSN: 14757516. DOI: 10.1088/1475-7516/2018/01/001. arXiv: 1708.01265. URL: https://iopscience.iop.org/article/10.1088/1475-7516/2018/01/001%20https://iopscience.iop.org/article/10.1088/1475-7516/2018/01/001/meta.

[11] N. Yu. Agafonova et al. "Characterization of the varying flux of atmospheric muons measured with the Large Volume Detector for 24 years CHARACTERIZATION of the VARYING FLUX of ATMOSPHERIC ... N. YU. AGAFONOVA et al." In: *Physical Review D* 100.6 (Sept. 2019). ISSN: 24700029. DOI: 10.1103/PhysRevD.100.062002. arXiv: 1909.04579v2. URL: http://arxiv.org/abs/1909.04579%20http://dx.doi.org/10.1103/PhysRevD.100.062002.

[12] *De aardse toepassingen van muonen | EOS Wetenschap*. URL: https://www.eoswetenschap.eu/ruimte/de-aardse-toepassingen-van-muonen (visited on 11/04/2024).

[13] Valeri Tioukov et al. "Hidden chamber discovery in the underground Hellenistic necropolis of Neapolis by muography". In: *Scientific Reports* 13.1 (Apr. 2023), pp. 1–10. ISSN: 20452322. DOI: 10.1038/s41598-023-32626-0. URL: https://www.nature.com/articles/s41598-023-32626-0.

[14] G. Bonomi et al. *Applications of cosmic-ray muons*. May 2020. DOI: 10.1016/j.ppnp.2020.103768.

[15] Thomas K. Gaisser, Ralph Engel, and Elisa Resconi. *Cosmic rays and particle physics*. Cambridge University Press, June 2016, pp. 1–444. ISBN: 9781139192194. DOI: 10.1017/CBO9781139192194. URL: https://www.cambridge.org/core/books/cosmic-rays-and-particle-physics/C81BA71195ADFC89EFCC2C565B617702.

[16] N. Mauri. "Annual modulation of the atmospheric muon flux measured by the OPERA experiment". In: *Journal of Physics: Conference Series*. Vol. 1342. 1. IOP Publishing, Jan. 2020, p. 012013. DOI: 10.1088/1742-6596/1342/1/012013. URL: https://iopscience.iop.org/article/10.1088/1742-6596/1342/1/012013%20https://iopscience.iop.org/article/10.1088/1742-6596/1342/1/012013/meta.

[17] K Geyer. "Measurements of the atmospheric muon rate with the ANTARES neutrino telescope". In: (2015). URL: https://ecap.nat.fau.de/wp-content/uploads/2021/03/KlausGeyerDissertation.pdf.

[18] Spurio. *Particles and astrophysics*. Astronomy and Astrophysics Library. Cham: Springer International Publishing, 2016. ISBN: 9783319080505. DOI: 10.1007/978-3-319-08051-2. URL: https://link.springer.com/10.1007/978-3-319-08051-2.

[19] Jelmer Mulder and Ronald Bruijn. "Seasonal variation of the atmopsheric muon flux in the KM3NeT detectors". In: *Proceedings of 38th International Cosmic Ray Conference — PoS(ICRC2023)*. 2021. Trieste, Italy: Sissa Medialab, Aug. 2023, p. 355. DOI: 10.22323/1.444.0355. URL: https://pos.sissa.it/444/355.

[20] Particle Data Group. 2024. URL: https://pdg.lbl.gov/2024/AtomicNuclearProperties/HTML/air_dry_1_atm.html.

[21] G. Bellini et al. "Cosmic-muon flux and annual modulation in Borexino at 3800 m water-equivalent depth". In: *Journal of Cosmology and Astroparticle Physics* 2012.5 (2012), p. 015. ISSN: 14757516. DOI: 10.1088/1475-7516/2012/05/015. arXiv: 1202.6403. URL: http://dx.doi.org/10.1088/1475-7516/2012/05/015.

[22] P. Adamson et al. "Observation of muon intensity variations by season with the MINOS near detector". In: *Physical Review D - Particles, Fields, Gravitation and Cosmology* 90.1 (June 2014). ISSN: 15502368. DOI: 10.1103/PhysRevD.90.012010. arXiv: 1406.7019. URL: http://arxiv.org/abs/1406.7019%20http://dx.doi.org/10.1103/PhysRevD.90.012010.

[23] I. Alekseev et al. "Observation of the temperature and barometric effects on the cosmic muon flux by the DANSS detector". In: *European Physical Journal C* 82.6 (Dec. 2022). ISSN: 14346052. DOI: 10.1140/epjc/s10052-022-10471-1. arXiv: 2112.03702. URL: https://arxiv.org/abs/2112.03702v2.

[24] E. W. Grashorn et al. "The atmospheric charged kaon/pion ratio using seasonal variation methods". In: *Astroparticle Physics* 33.3 (Apr. 2010), pp. 140–145. ISSN: 09276505. DOI: 10.1016/j.astropartphys.2009.12.006. arXiv: 0909.5382.

[25] S. Adrián-Martínez et al. "Letter of intent for KM3NeT 2.0". In: *Journal of Physics G: Nuclear and Particle Physics* 43.8 (June 2016), p. 084001. ISSN: 13616471. DOI: 10.1088/0954-3899/43/8/084001. arXiv: 1601.07459. URL: https://iopscience.iop.org/article/10.1088/0954-3899/43/8/084001%20https://iopscience.iop.org/article/10.1088/0954-3899/43/8/084001/meta.

[26] Brían Fearraigh et al. "Tuning parametric models of the atmospheric muon flux in MUPAGE to data from the KM3NeT detector". In: *Proceedings of Science*. Vol. 395. SISSA Medialab, Mar. 2022, p. 1176. DOI: 10.22323/1.395.1176.

[27] KM3NeT collaboration. Oct. 2024. URL: https://www.km3net.org/research/physics/particle-physics-with-orca/.

[28] KM3NeT collaboration. Oct. 2024. URL: https://www.km3net.org/research/physics/astronomy-with-arca/.

[29] Boris M Bolotovskii. "Vavilov–Cherenkov radiation: its discovery and application". In: *Physics-Uspekhi* 52.11 (2009), p. 1099.

[30] Brían Ó Fearraigh and Printed by: Gildeprint. “Following the light : novel event reconstruction techniques for neutrino oscillation analyses in KM3NeT/ORCA”. PhD thesis. University of Amsterdam, 2024, p. 250. ISBN: 9789464960198.

[31] S. Adrián-Martínez et al. “Deep sea tests of a prototype of the KM3NeT digital optical module: KM3NeT Collaboration”. In: *European Physical Journal C* 74.9 (Sept. 2014), pp. 1–8. ISSN: 14346052. DOI: 10.1140/epjc/s10052-014-3056-3. URL: https://link.springer.com/article/10.1140/epjc/s10052-014-3056-3.

[32] S. Adrián-Martínez et al. “The prototype detection unit of the KM3NeT detector: KM3NeT Collaboration”. In: *European Physical Journal C* 76.2 (Jan. 2016), pp. 1–12. ISSN: 14346052. DOI: 10.1140/epjc/s10052-015-3868-9. URL: https://link.springer.com/article/10.1140/epjc/s10052-015-3868-9.

[33] M. Ageron et al. “Dependence of atmospheric muon flux on seawater depth measured with the first KM3NeT detection units: The KM3NeT Collaboration”. In: *European Physical Journal C* 80.2 (Feb. 2020), pp. 1–11. ISSN: 14346052. DOI: 10.1140/epjc/s10052-020-7629-z. URL: https://link.springer.com/article/10.1140/epjc/s10052-020-7629-z.

[34] NASA. May 2021. URL: https://airs.jpl.nasa.gov/data/about-the-data/earth-coverage/.

[35] Baijun Tian et al. “AIRS V7 L3 Product User Guide”. In: (2020), pp. 1–34.

[36] CelesTrak. URL: https://celestrak.org/.

[37] Copernicus Climate Change Service (C3S). *ERA5 hourly data on single levels from 1940 to present*. 2024. DOI: https://doi.org/10.24381/cds.adbb2d47. (Visited on 10/20/2024).

[38] H. Hersbach et al. “ERA5 hourly data on single levels from 1940 to present”. In: *Copernicus Climate Change Service (C3S) Climate Data Store (CDS)* (2018). DOI: 10.24381/cds.adbb2d47. (Visited on 10/20/2024).

[39] Paul T. Boggs and Janet E. Rogers. “Orthogonal distance regression”. In: 1989 (1990), pp. 183–194. DOI: 10.1090/conm/112/1087109.

[40] S. Aiello et al. “Atmospheric muons measured with the KM3NeT detectors in comparison with updated numeric predictions”. In: *European Physical Journal C* 84.7 (July 2024), p. 696. ISSN: 14346052. DOI: 10.1140/epjc/s10052-024-13018-8. arXiv: 2403.11946. URL: https://doi.org/10.1140/epjc/s10052-024-13018-8.

[41] R. Abbasi et al. “Observation of seasonal variations of the flux of high-energy atmospheric neutrinos with IceCube”. In: *European Physical Journal C* 83.9 (Mar. 2023). ISSN: 14346052. DOI: 10.1140/epjc/s10052-023-11679-5. arXiv: 2303.04682. URL: http://arxiv.org/abs/2303.04682%20http://dx.doi.org/10.1140/epjc/s10052-023-11679-5.

[42] Marco Circella and Thomas Eberl. “Machine learning techniques deep underwater in km3net”. In: *Europhysics News* 53.2 (2022), pp. 26–29. ISSN: 14321092. DOI: 10.1051/epn/2022206. URL: https://www.europhysicsnews.org/articles/epn/abs/2022/02/epn2022532p26/epn2022532p26.html.

[43] Jordi Tuneu, Eva Santos, and Peter Filip. “Unveiling the seasonal variation of multi-muon events at the NOνA Detector”. In: *Proceedings of Science*. Vol. 441. SISSA Medialab, Sept. 2024, p. 347. DOI: 10.22323/1.444.0347.

[44] M. A. Acero et al. “Seasonal variation of multiple-muon cosmic ray air showers observed in the NOvA detector on the surface”. In: *Physical Review D* 104.1 (July 2021), p. 012014. ISSN: 24700029. DOI: 10.1103/PhysRevD.104.012014. arXiv: 2105.03848. URL: https://journals.aps.org/prd/abstract/10.1103/PhysRevD.104.012014.

[45] Serap Tilav et al. “Seasonal variation of atmospheric muons in IceCube”. In: *Proceedings of Science* 358 (2019). ISSN: 18248039. DOI: 10.22323/1.358.0894. arXiv: 1909.01406.

[46] M. Ambrosio et al. “Seasonal variations in the underground muon intensity as seen by MACRO”. In: *Astroparticle Physics* 7.1-2 (1997), pp. 109–124. ISSN: 09276505. DOI: 10.1016/S0927-6505(97)00011-X.

A Appendix

A.1. AIRS

A.1.1. Full Run Analysis

Figure A.1: Rate and ratio of data and the Monte Carlo simulation for ORCA-10 after cuts are applied. In the top part the count rates without error of the data and the Monte Carlo simulation are shown. In the bottom part the ratio of the two is shown with error.

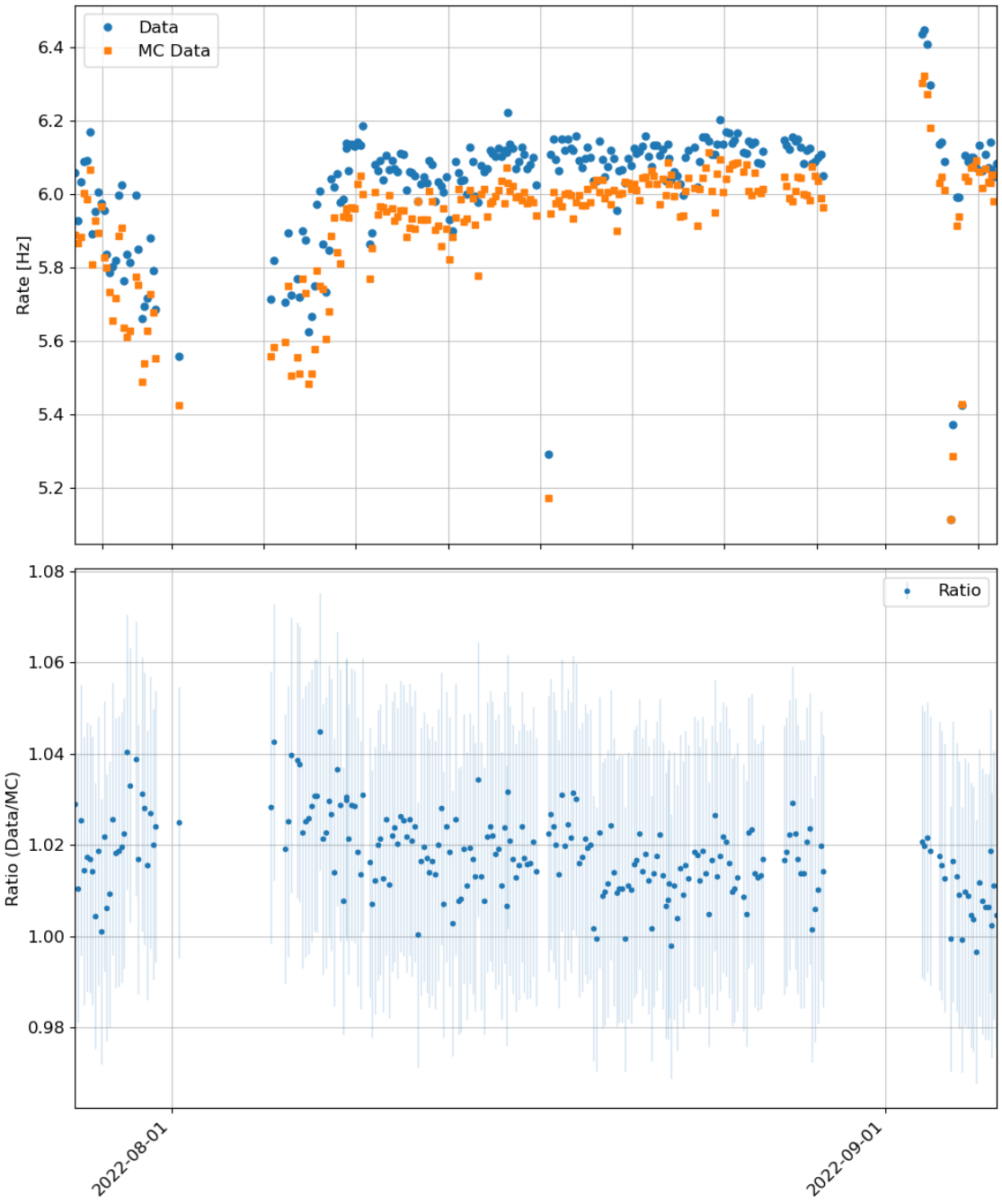

Figure A.2: Rate and ratio of data and the Monte Carlo simulation for ORCA-11 after cuts are applied. In the top part the count rates without error of the data and the Monte Carlo simulation are shown. In the bottom part the ratio of the two is shown with error.

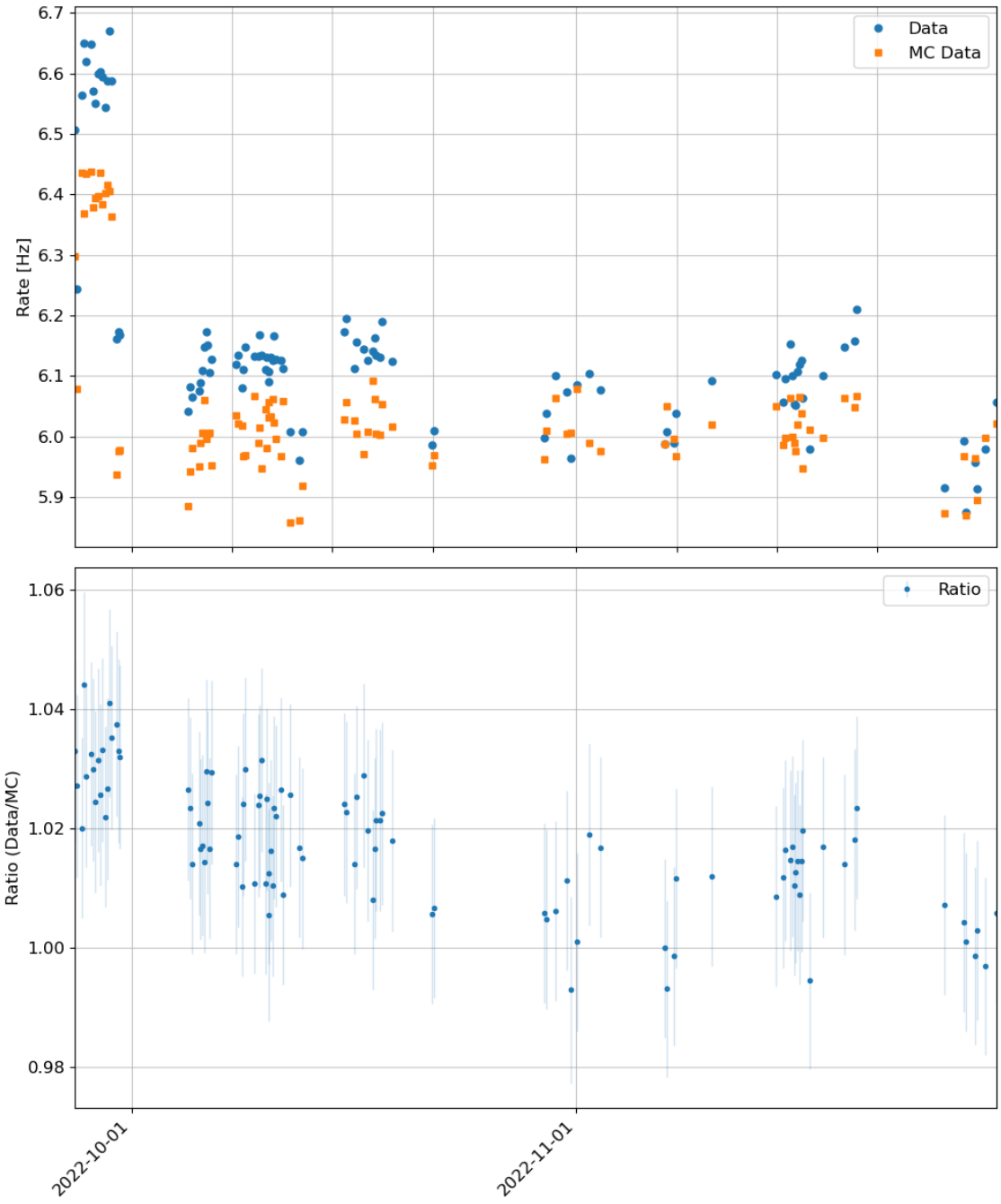

Figure A.3: Rate and ratio of data and the Monte Carlo simulation for ORCA-11.1 after cuts are applied. In the top part the count rates without error of the data and the Monte Carlo simulation are shown. In the bottom part the ratio of the two is shown with error.

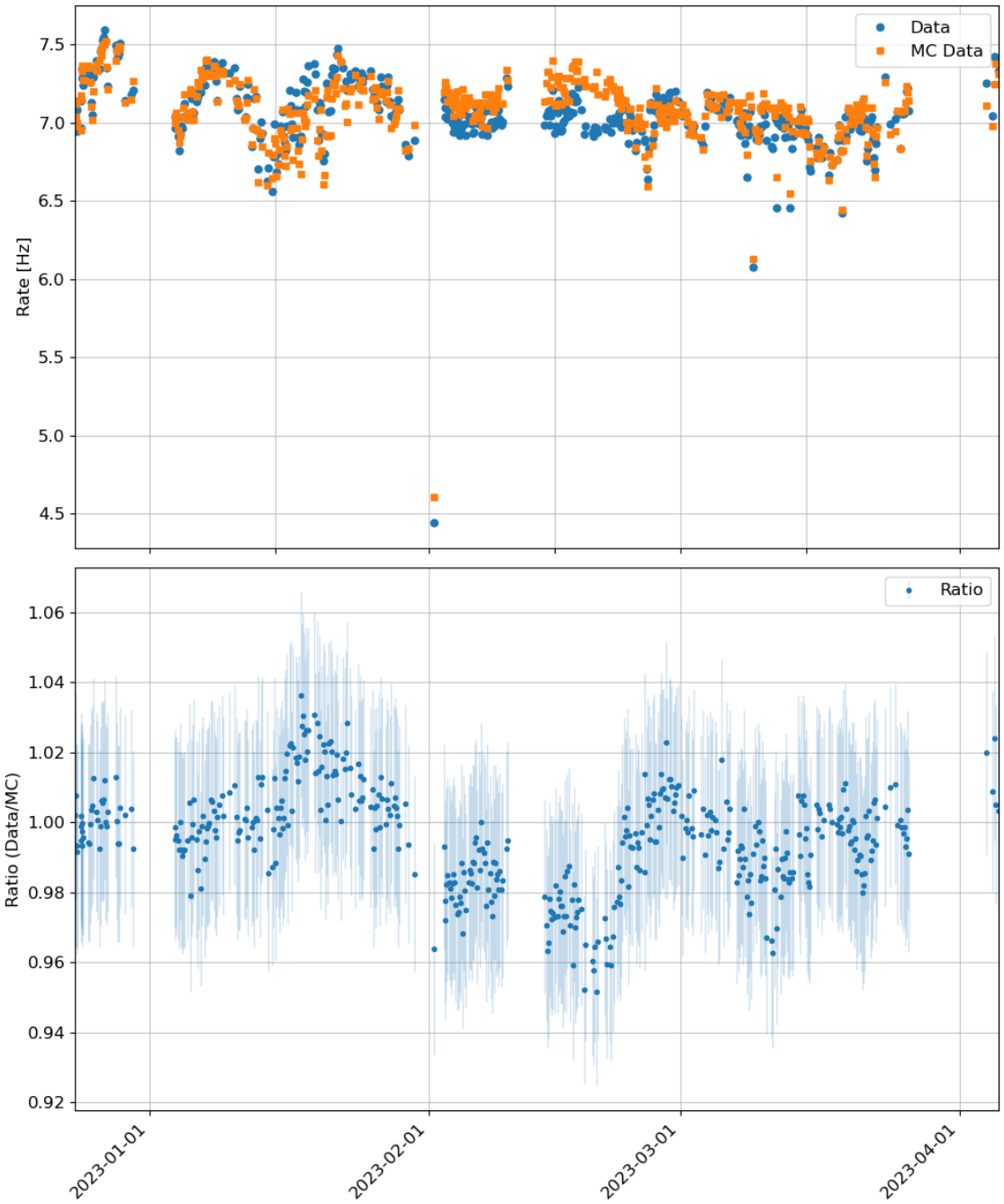

Figure A.4: Rate and ratio of data and the Monte Carlo simulation for ORCA-15 after cuts are applied. In the top part the count rates without error of the data and the Monte Carlo simulation are shown. In the bottom part the ratio of the two is shown with error.

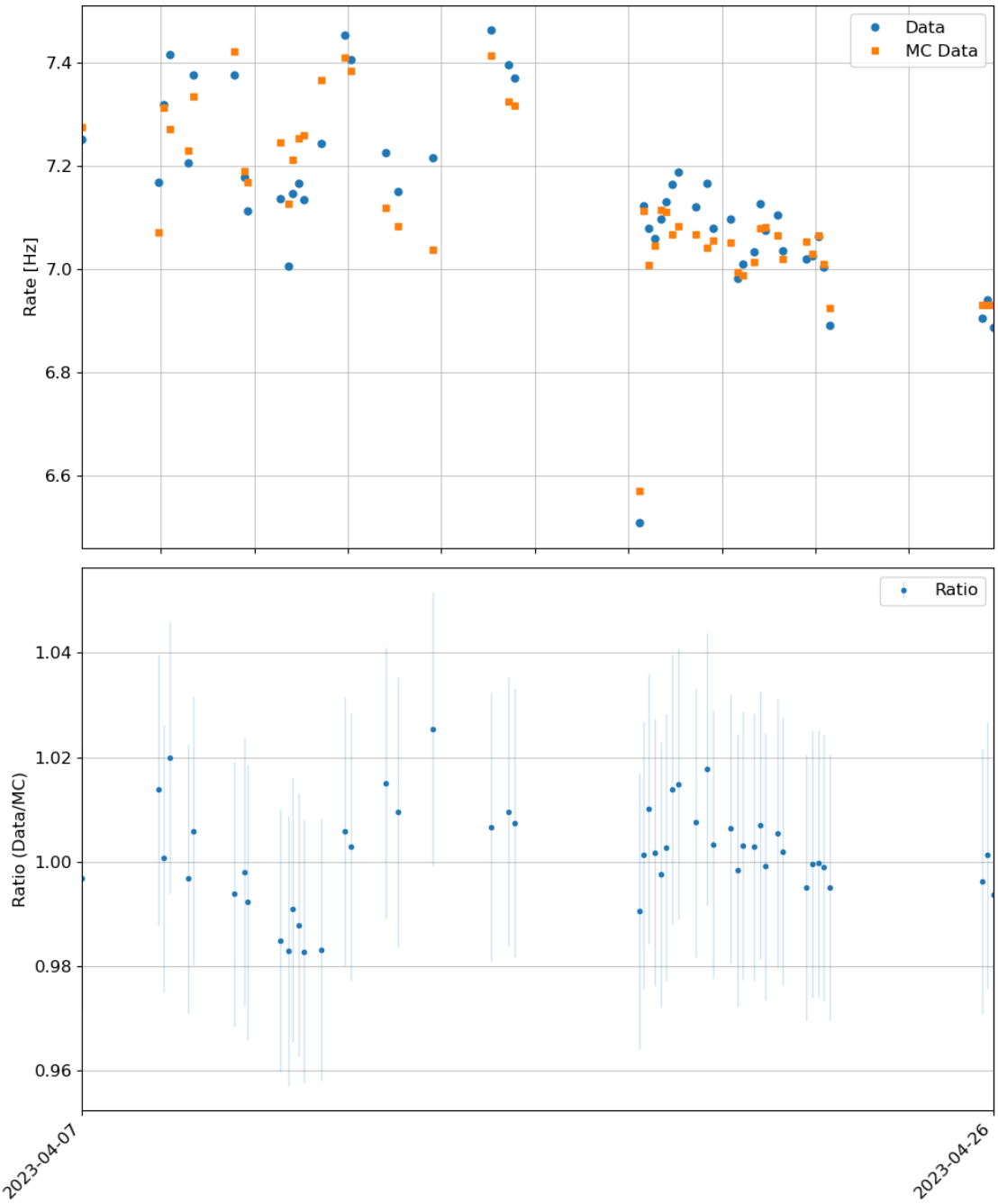

Figure A.5: Rate and ratio of data and the Monte Carlo simulation for ORCA-15.1 after cuts are applied. In the top part the count rates without error of the data and the Monte Carlo simulation are shown. In the bottom part the ratio of the two is shown with error.

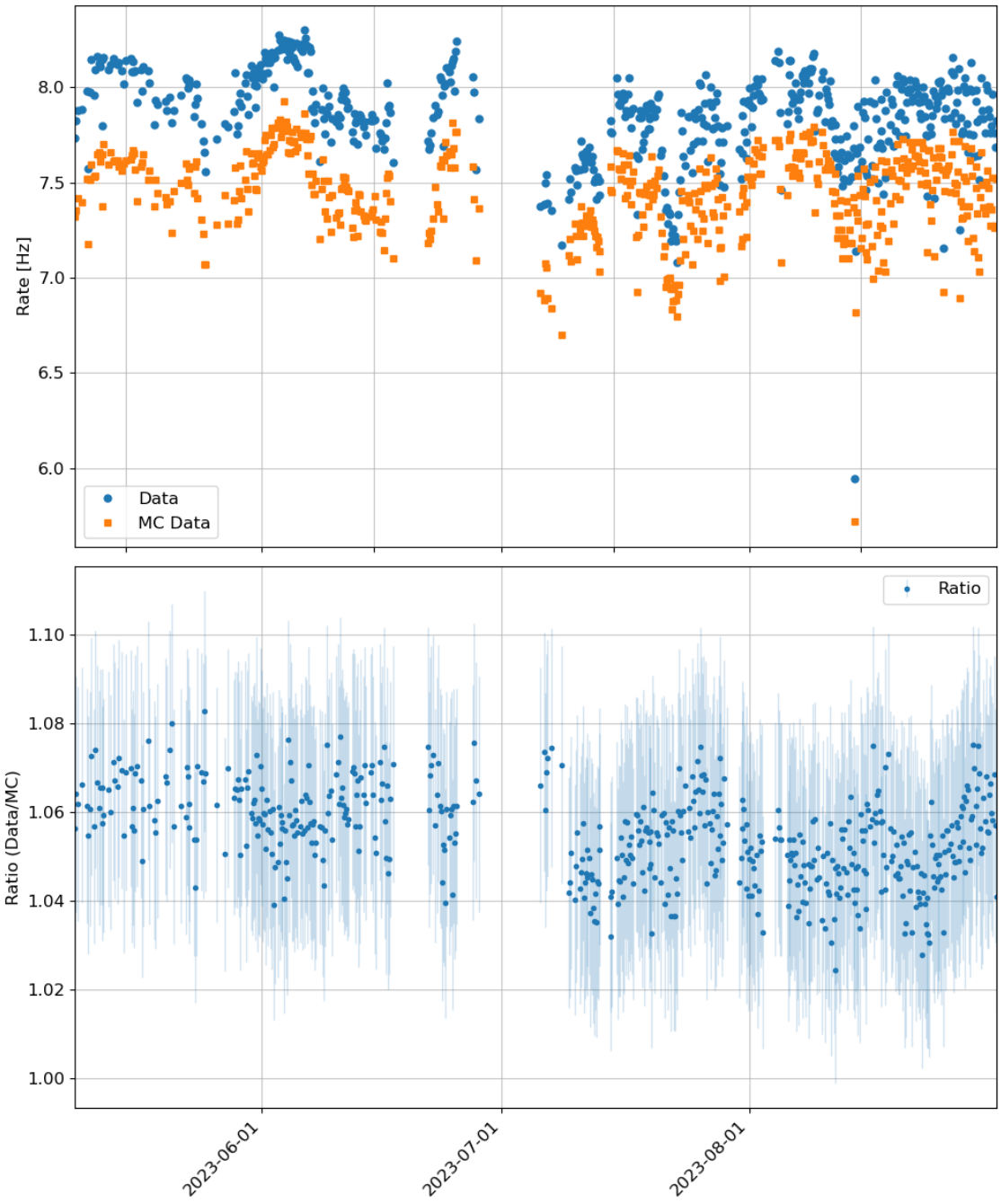

Figure A.6: Rate and ratio of data and the Monte Carlo simulation for ORCA-18 after cuts are applied. In the top part the count rates without error of the data and the Monte Carlo simulation are shown. In the bottom part the ratio of the two is shown with error.

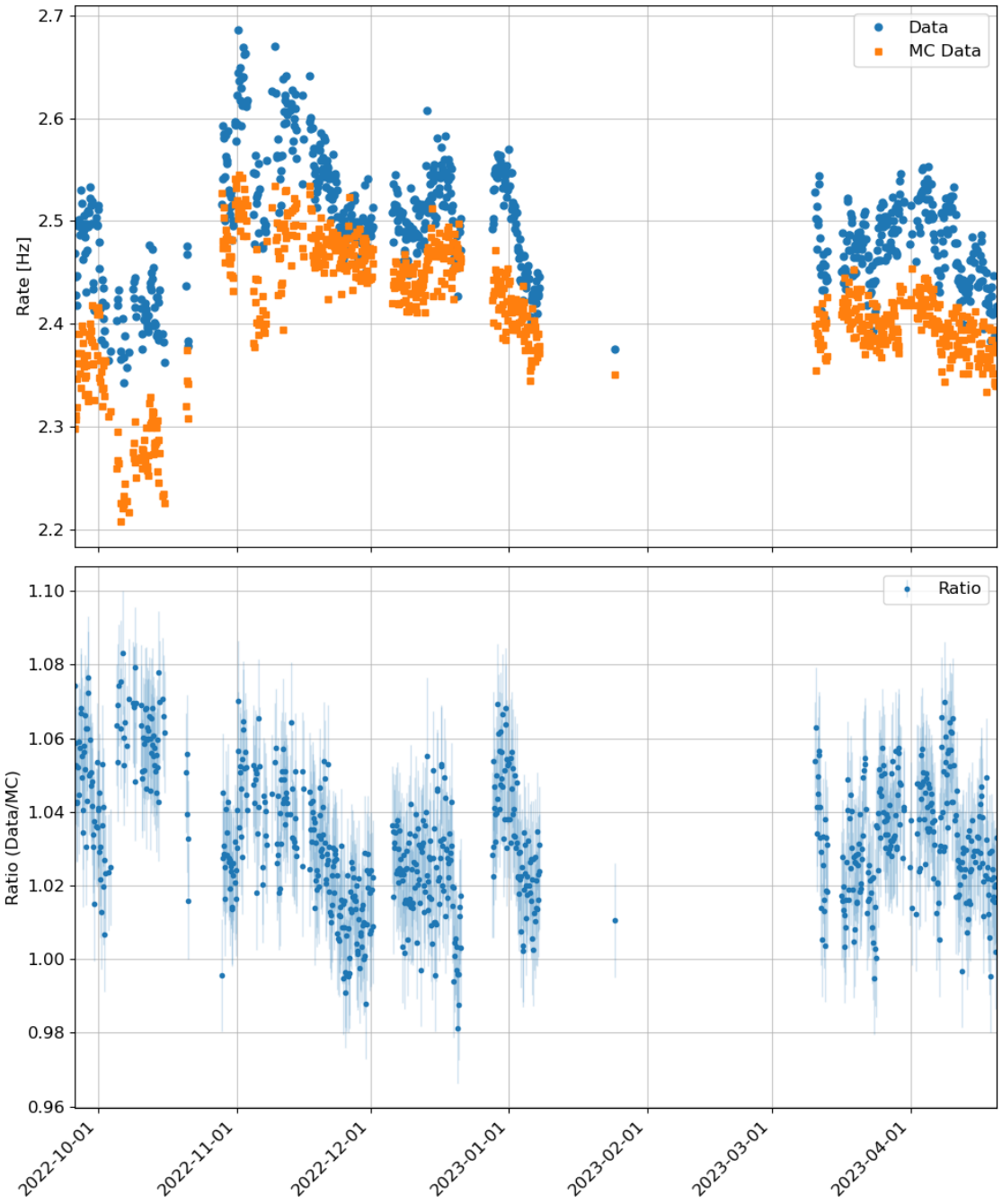

Figure A.7: Rate and ratio of data and the Monte Carlo simulation for ARCA-21 after cuts are applied. In the top part the count rates without error of the data and the Monte Carlo simulation are shown. In the bottom part the ratio of the two is shown with error.

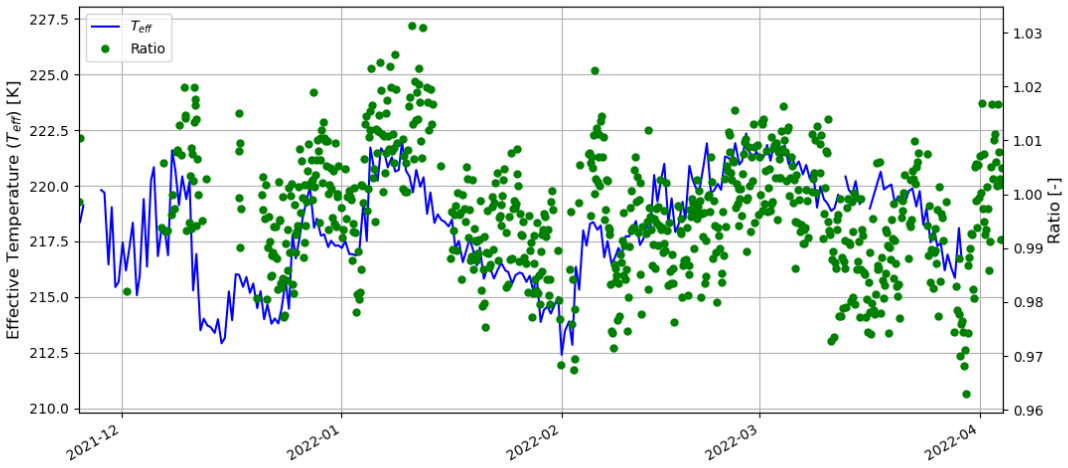

Figure A.8: ORCA-10 ratio data plotted on top of the effective temperature data.

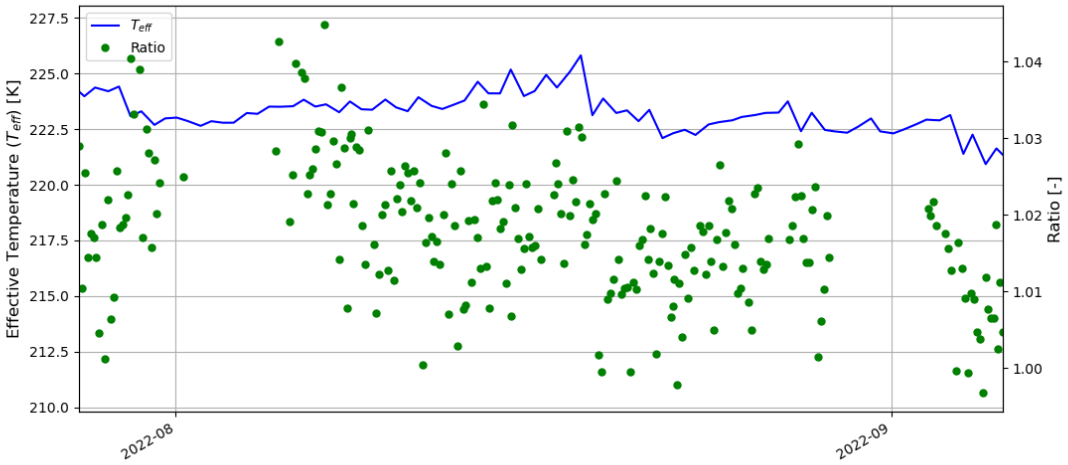

Figure A.9: ORCA-11 ratio data plotted on top of the effective temperature data.

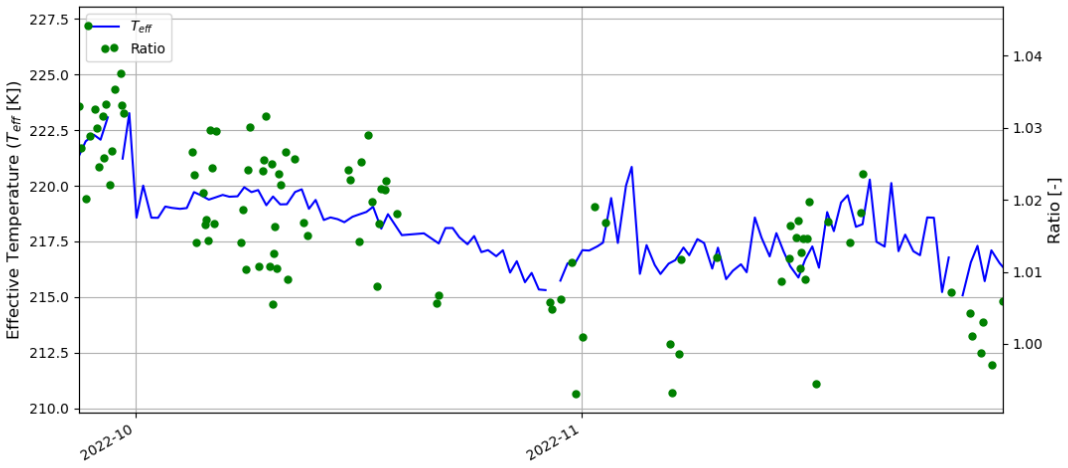

Figure A.10: ORCA-11.1 ratio data plotted on top of the effective temperature data.

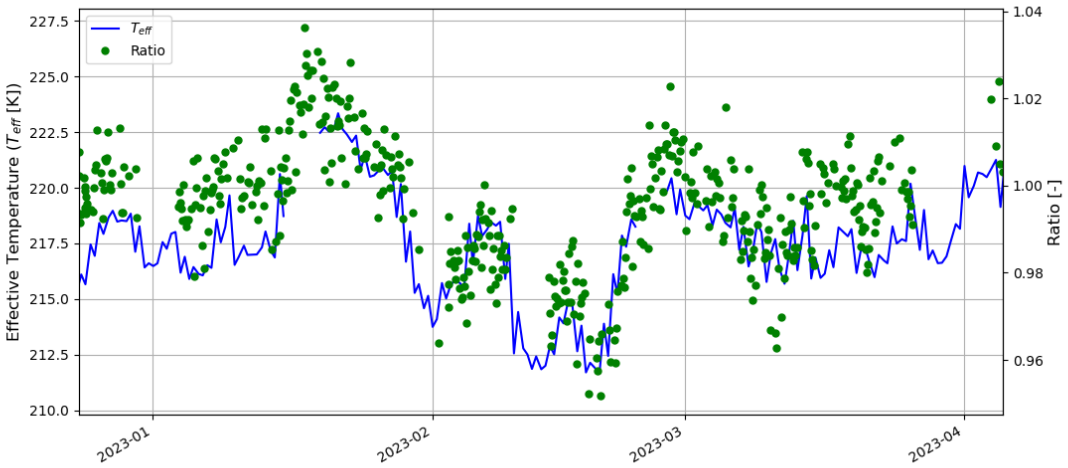

Figure A.11: ORCA-15 ratio data plotted on top of the effective temperature data.

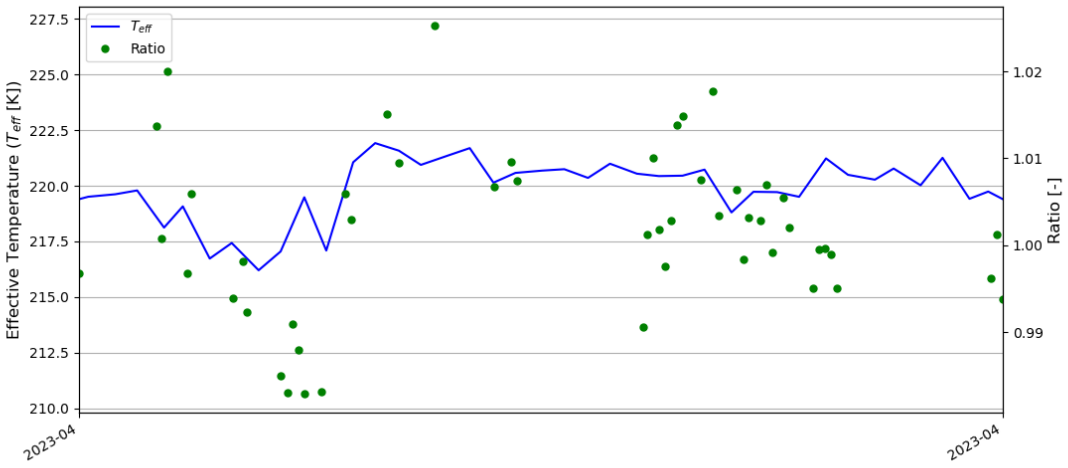

Figure A.12: ORCA-15.1 ratio data plotted on top of the effective temperature data.

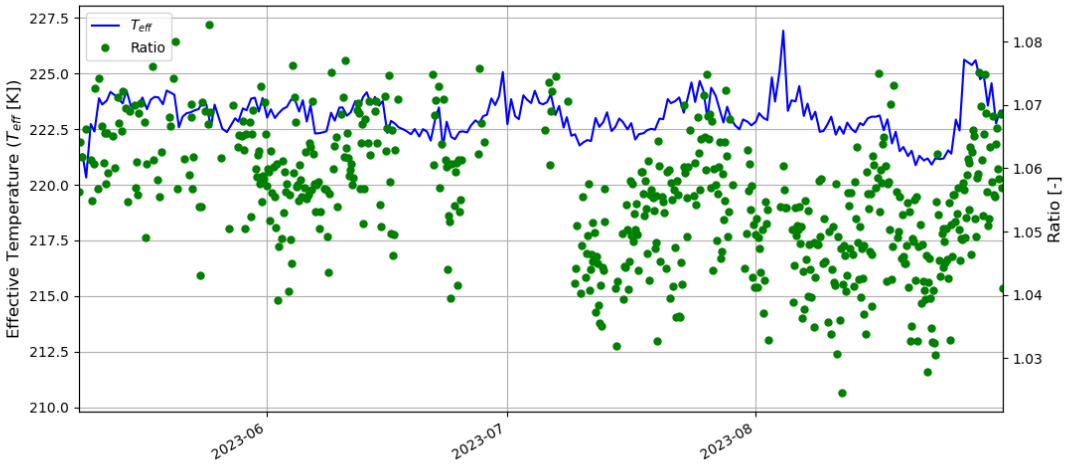

Figure A.13: ORCA-18 ratio data plotted on top of the effective temperature data.

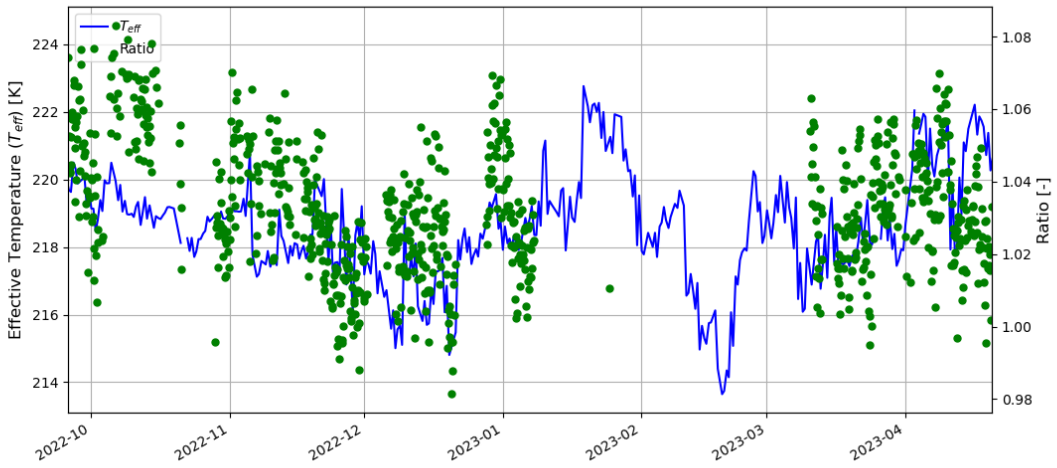

Figure A.14: ARCA-21 ratio data plotted on top of the effective temperature data.

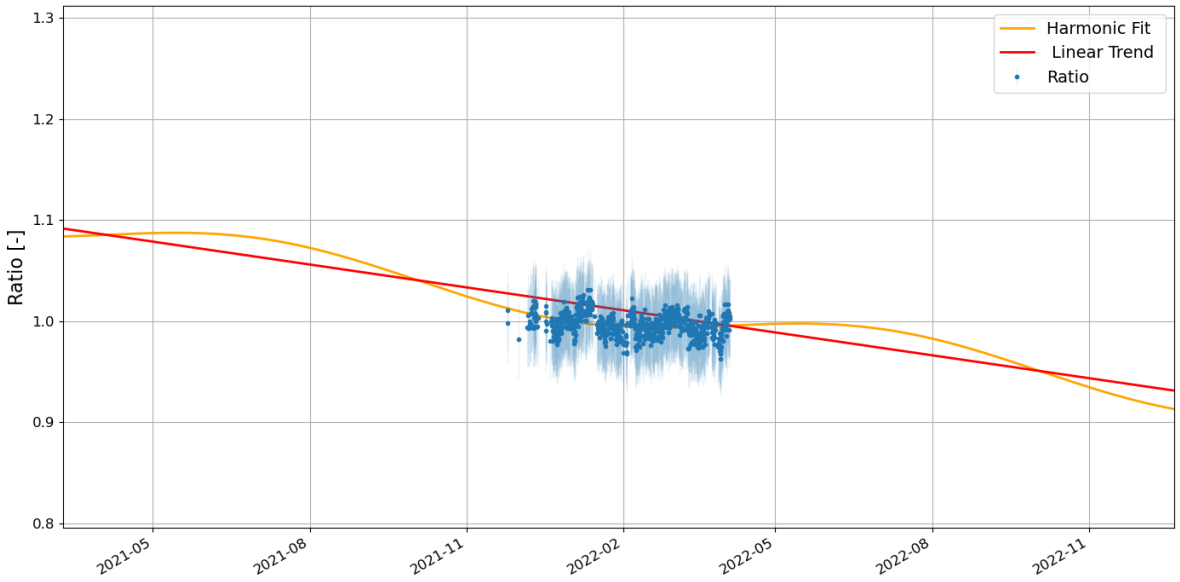

Figure A.15: Fit of the model in Equation 6.11 to the ratio data of ORCA-10. The parameters fit are an amplitude of $A = 0.0187$, an offset of 1.288, and a linear trend coefficient of $B = -2.458 \times 10^{-4}$ $[day^{-1}]$.

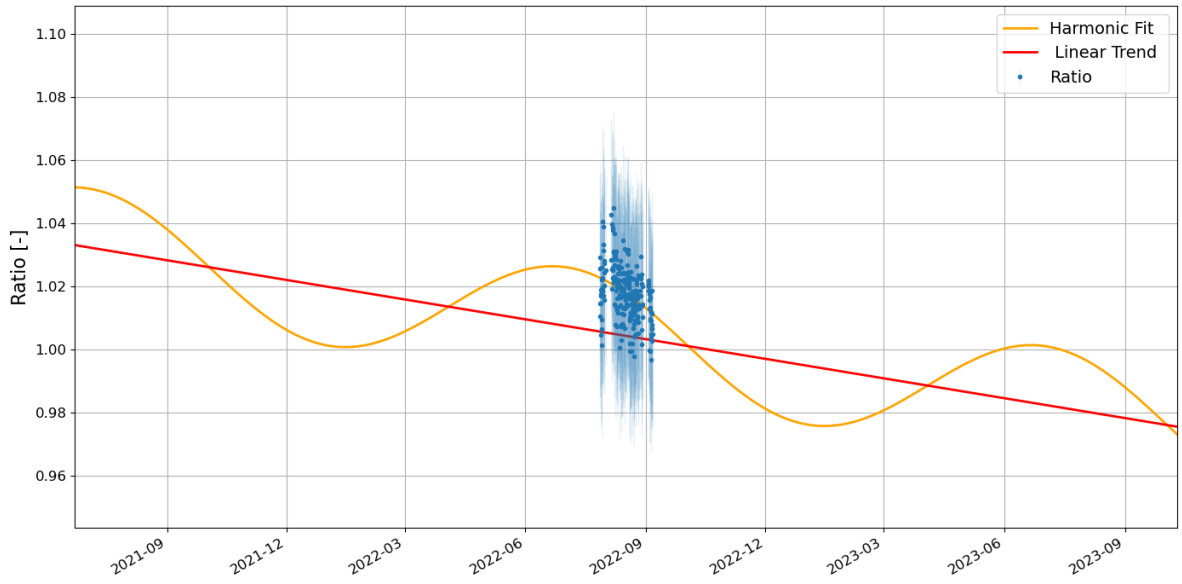

Figure A.16: Fit of the model in Equation 6.11 to the ratio data of ORCA-11. The parameters fit are an amplitude of $A = 0.0187$, an offset of 1.095, and a linear trend coefficient of $B = -6.855 \times 10^{-5}$ $[day^{-1}]$.

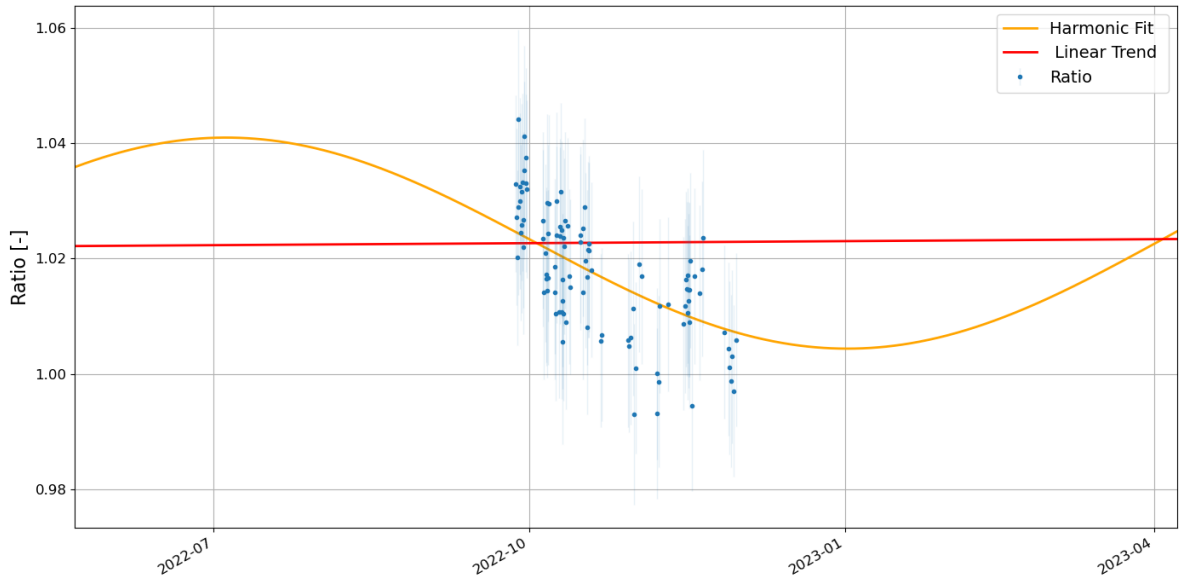

Figure A.17: Fit of the model in Equation 6.11 to the ratio data of ORCA-11.1. The parameters fit are an amplitude of $A = 0.0187$, an offset of 1.017, and a linear trend coefficient of $B = -3.790 \times 10^{-6}$ $[day^{-1}]$.

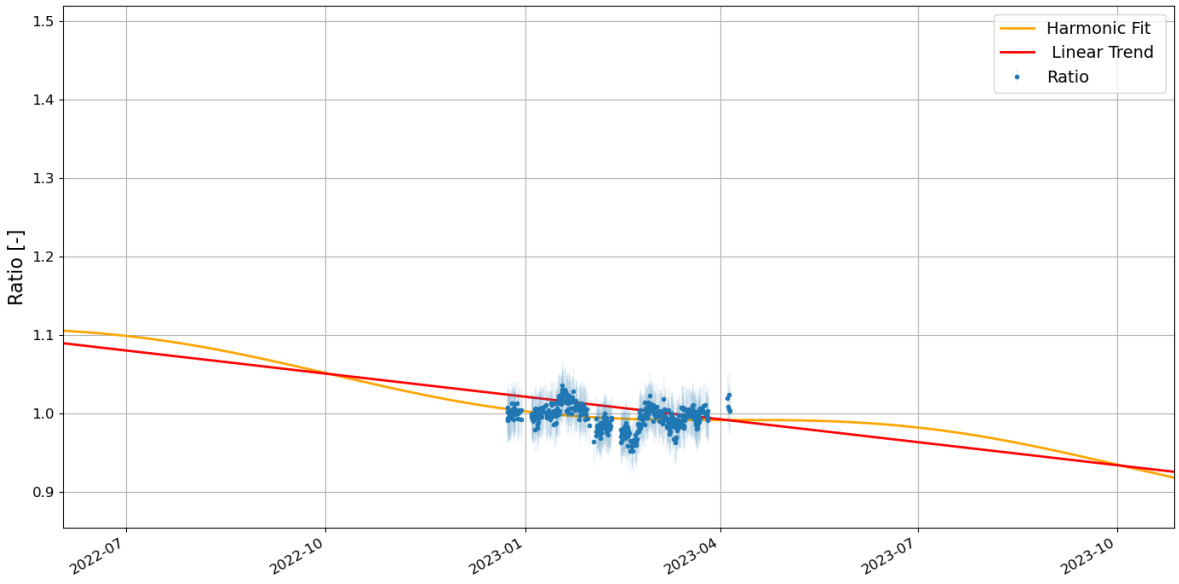

Figure A.18: Fit of the model in Equation 6.11 to the ratio data of ORCA-15. The parameters fit are an amplitude of $A = 0.0187$, an offset of 1.489, and a linear trend coefficient of $B = -3.197 \times 10^{-5}$ $[day^{-1}]$.

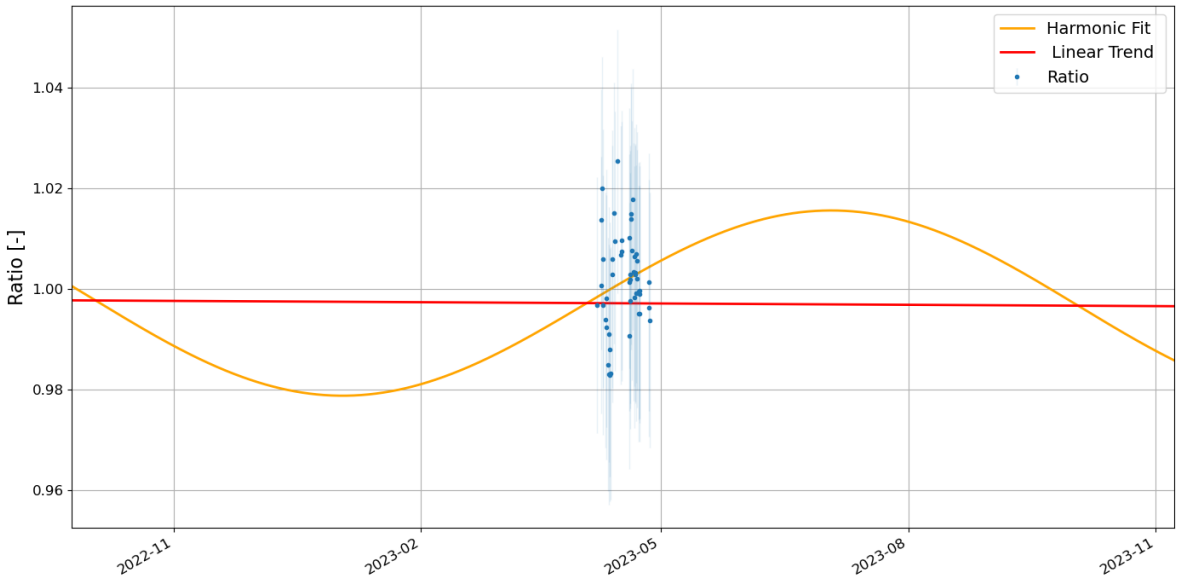

Figure A.19: Fit of the model in Equation 6.11 to the ratio data of ORCA-15.1. The parameters fit are an amplitude of $A = 0.0187$, an offset of 1.002, and a linear trend coefficient of $B = -2.839 \times 10^{-6}$ $[day^{-1}]$.

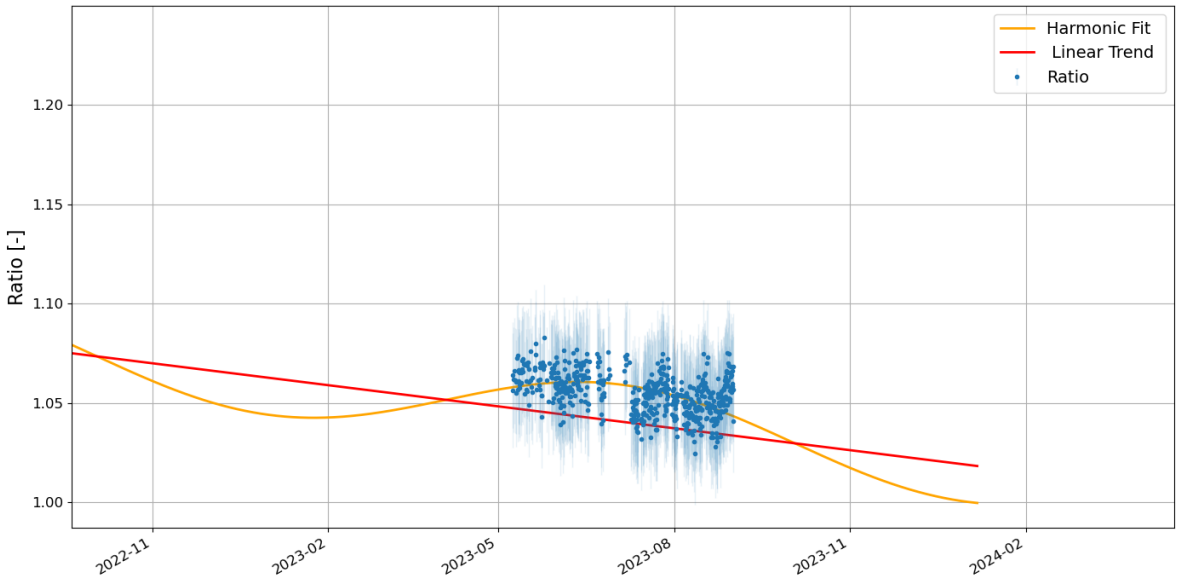

Figure A.20: Fit of the model in Equation 6.11 to the ratio data of ORCA-18. The parameters fit are an amplitude of $A = 0.0187$, an offset of 1.238, and a linear trend coefficient of $B = -1.119 \times 10^{-4}$ $[day^{-1}]$.

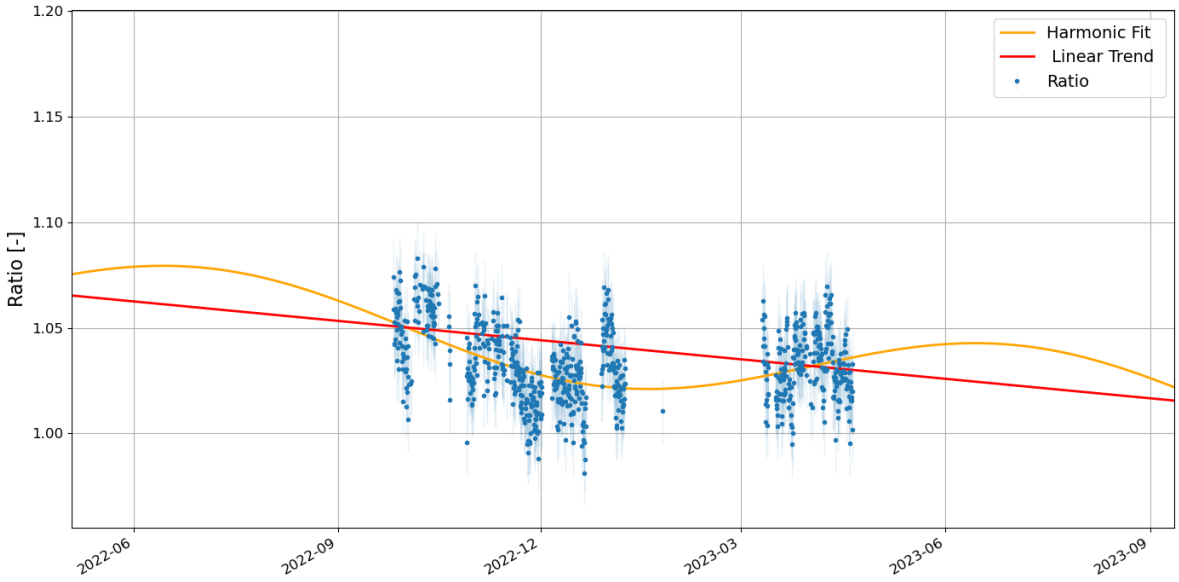

Figure A.21: Fit of the model in Equation 6.11 to the ratio data of ARCA-21. The parameters fit are an amplitude of $A = 0.0191$, an offset of 1.188, and a linear trend coefficient of $B = -1.004 \times 10^{-4}$ $[day^{-1}]$.

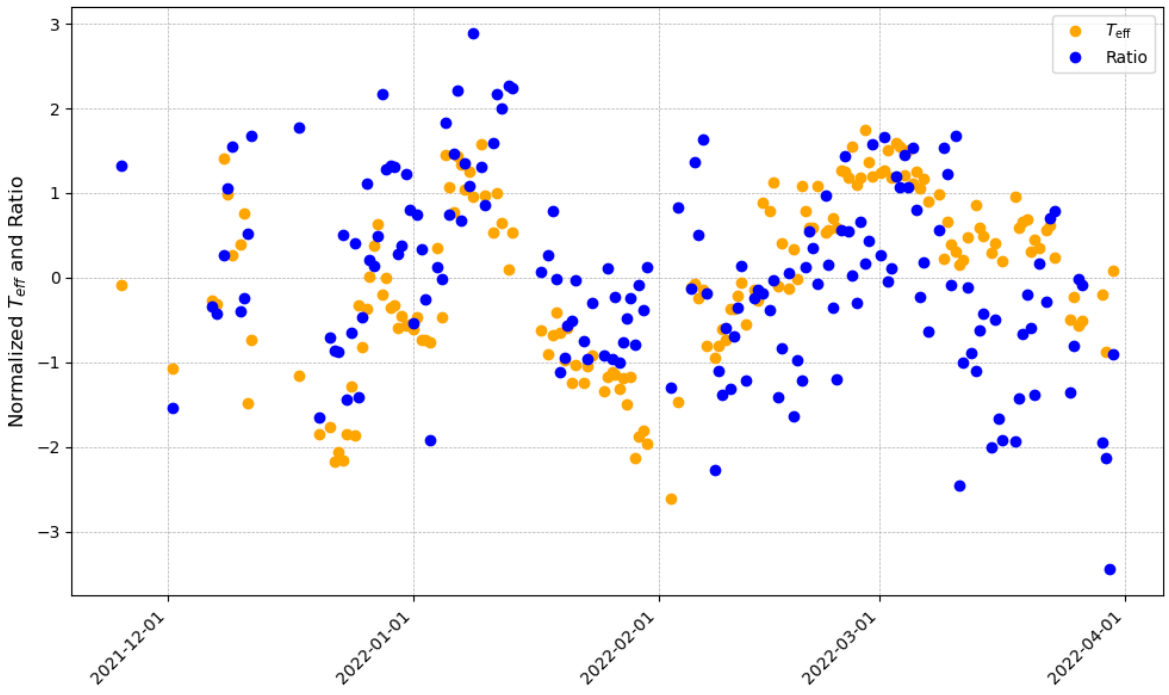

Figure A.22: Normalised effective temperature and ratio without detrending over time for ORCA-10

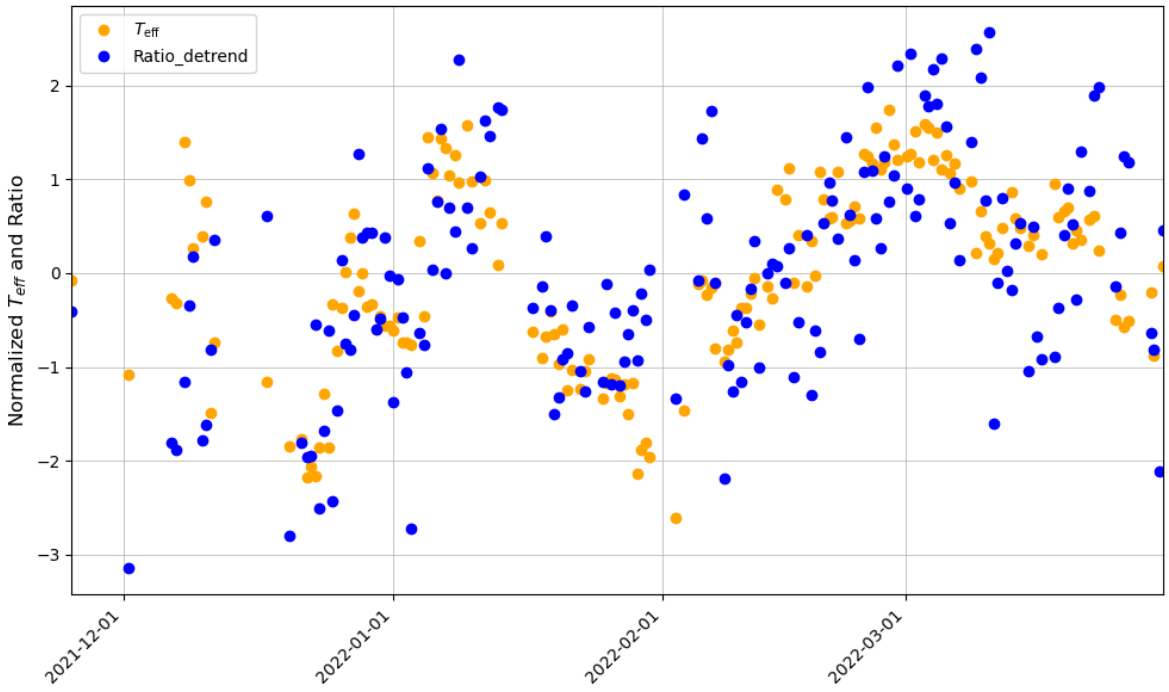

Figure A.23: Normalised effective temperature and ratio with detrending over time for ORCA-10

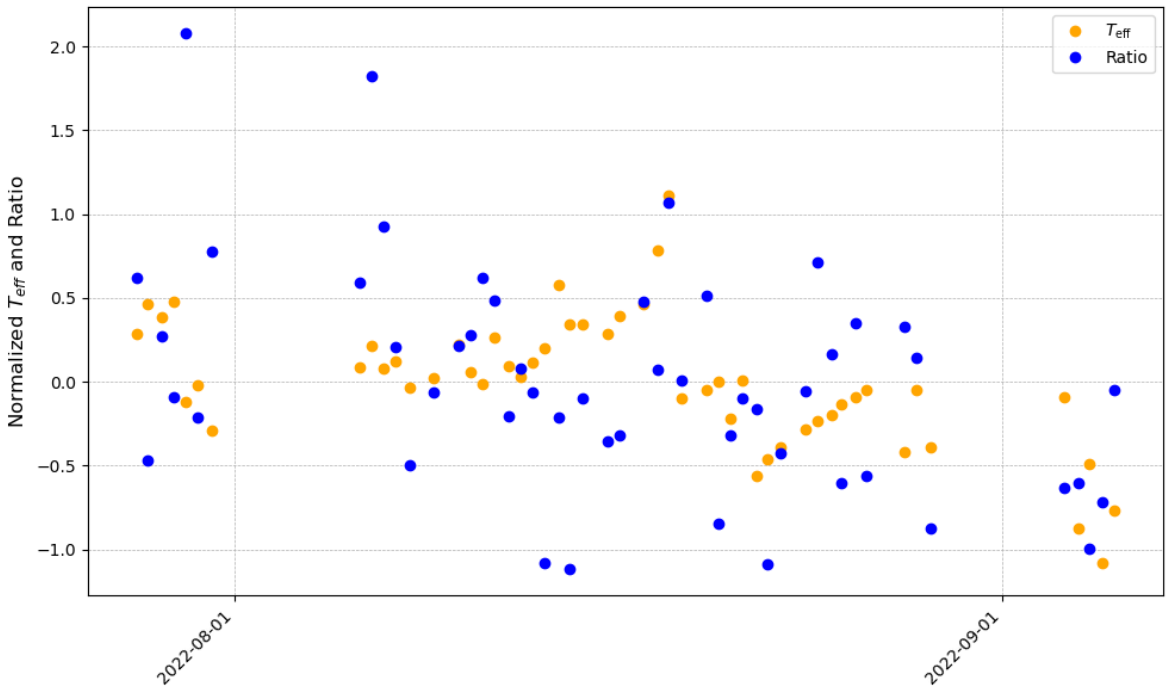

Figure A.24: Normalised effective temperature and ratio without detrending over time for ORCA-11

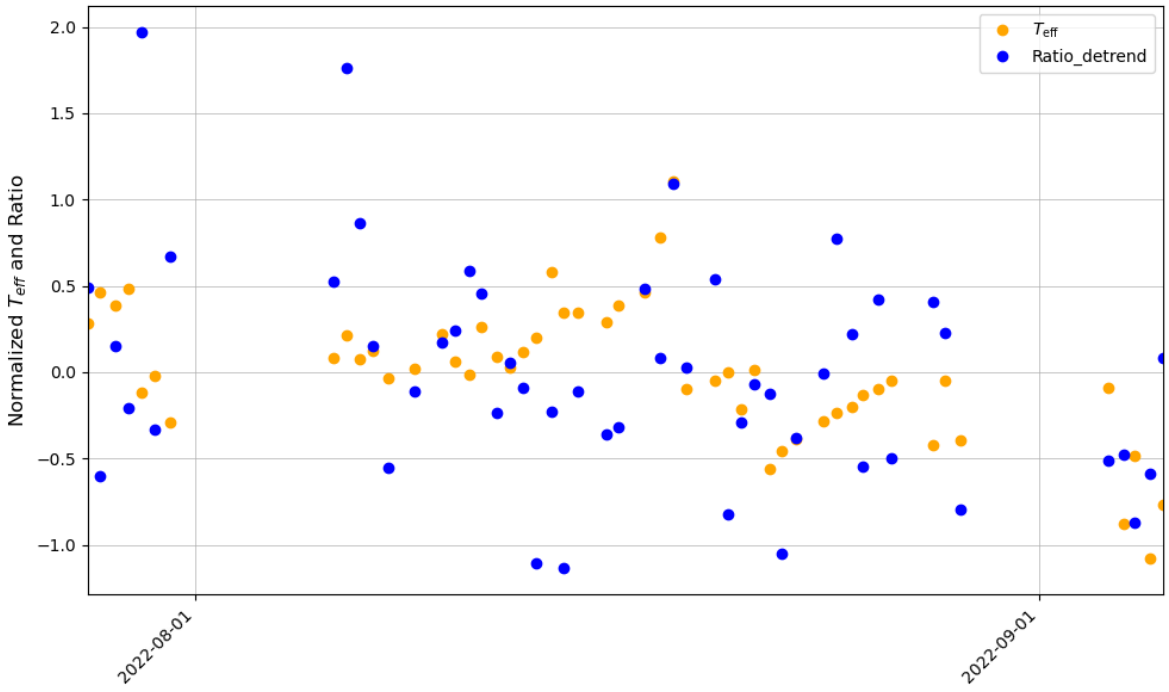

Figure A.25: Normalised effective temperature and ratio with detrending over time for ORCA-11

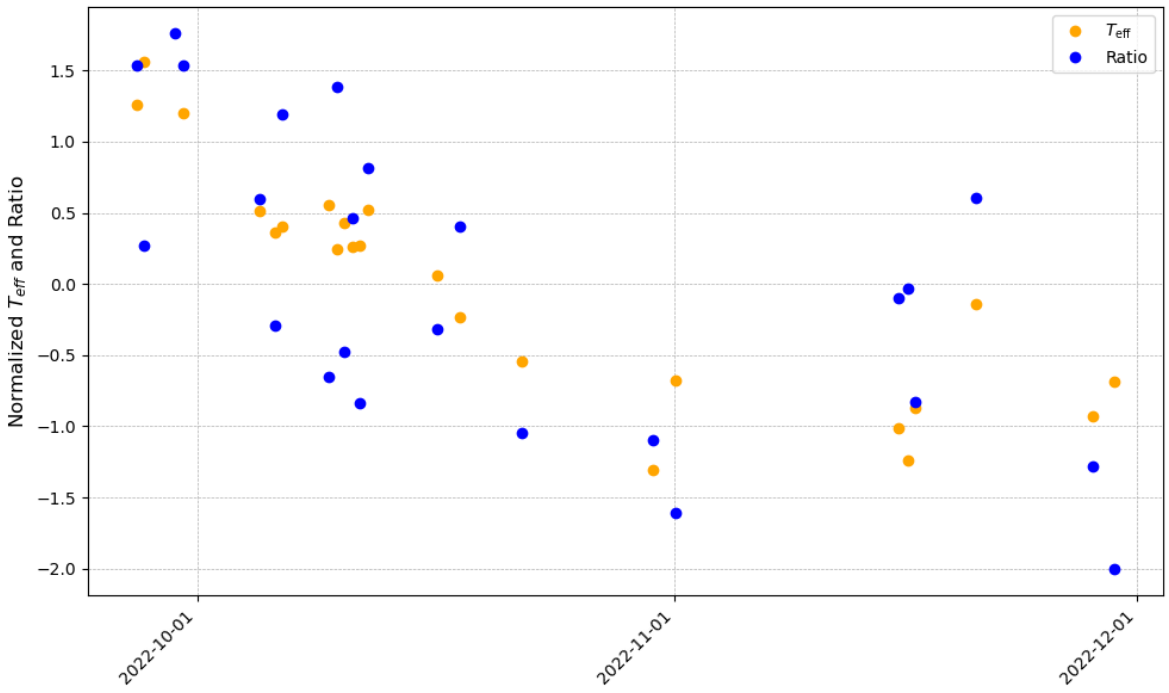

Figure A.26: Normalised effective temperature and ratio without detrending over time for ORCA-11.1

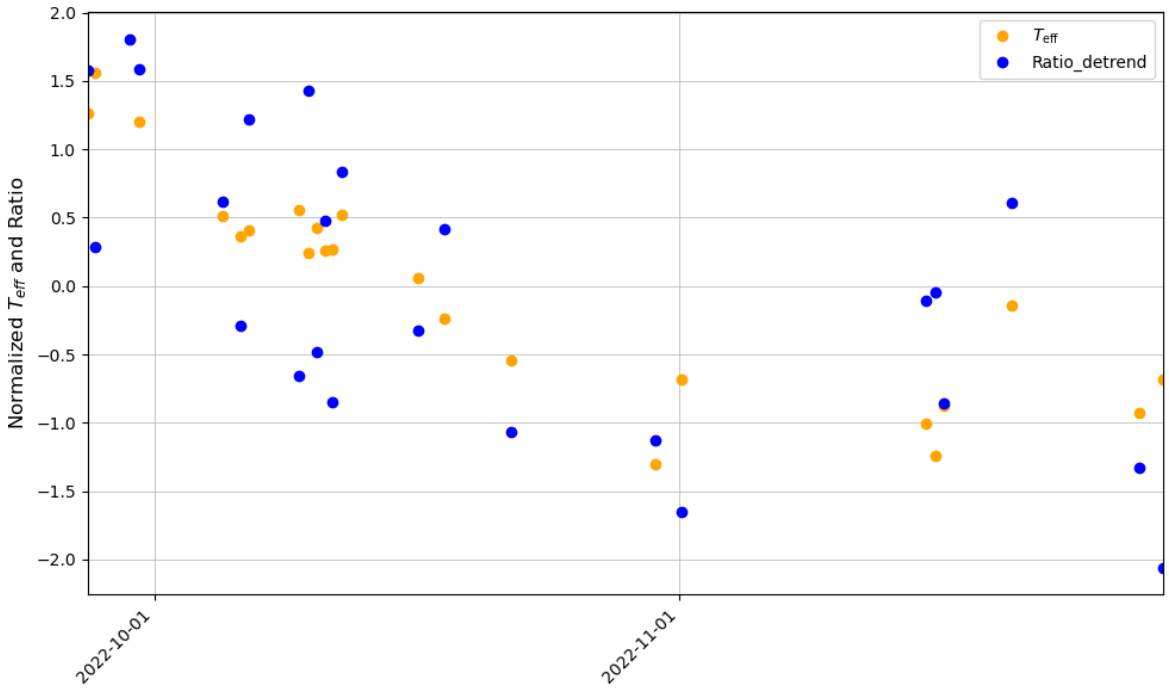

Figure A.27: Normalised effective temperature and ratio with detrending over time for ORCA-11.1

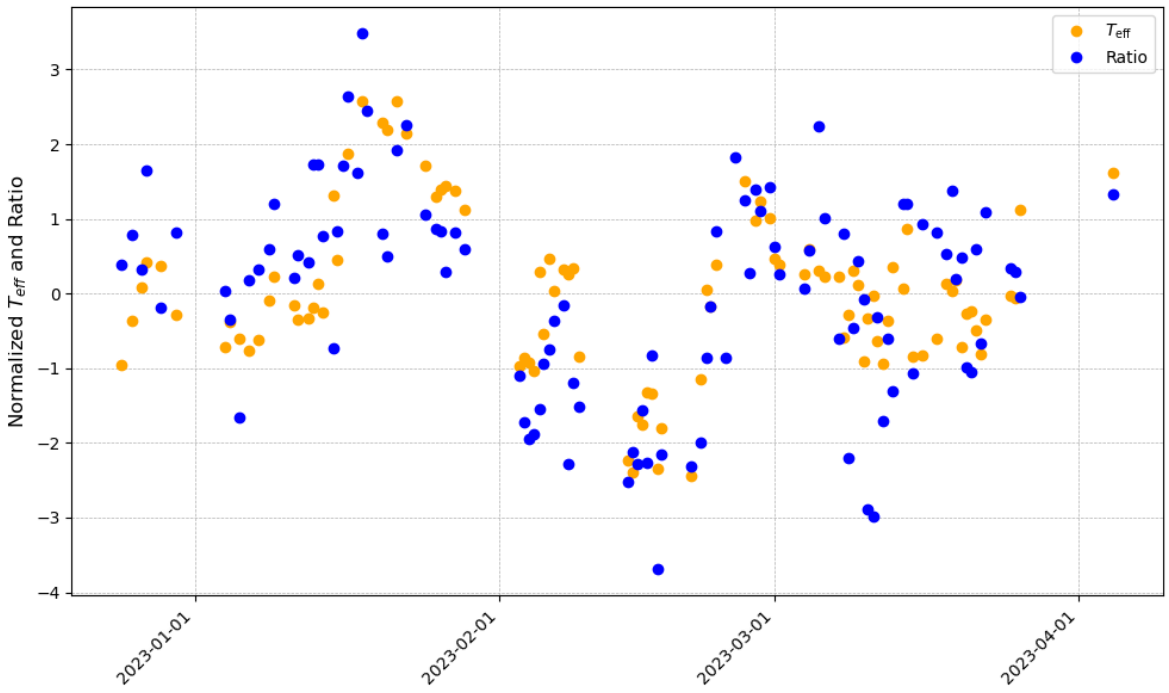

Figure A.28: Normalised effective temperature and ratio without detrending over time for ORCA-15

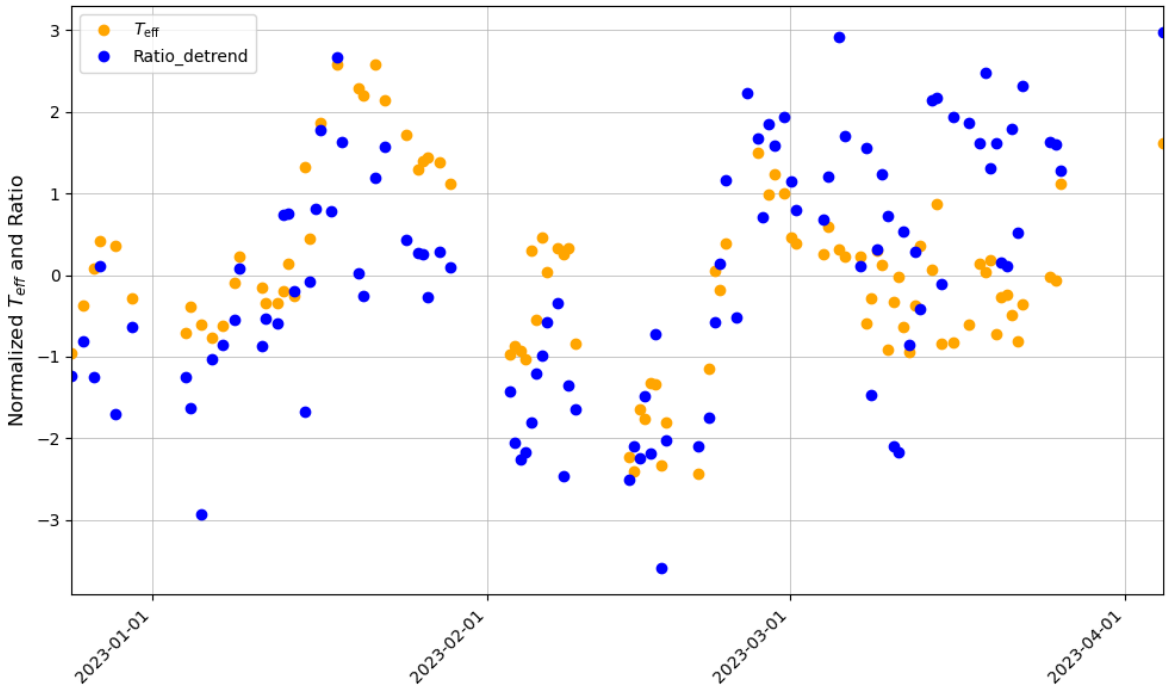

Figure A.29: Normalised effective temperature and ratio with detrending over time for ORCA-15

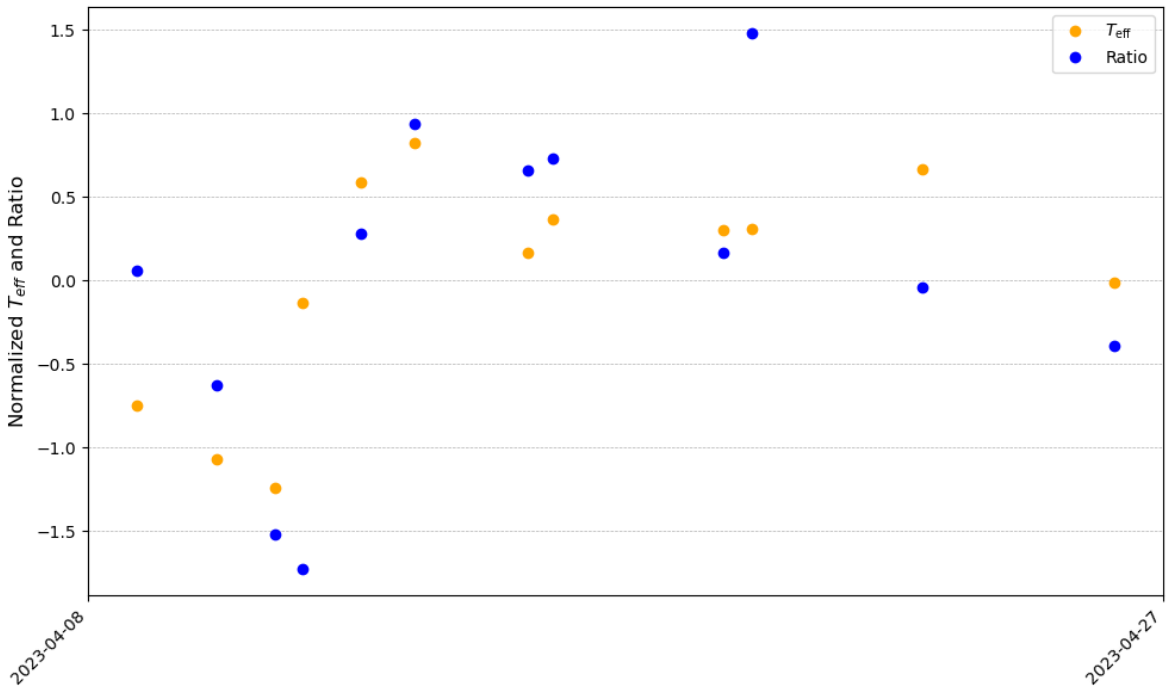

Figure A.30: Normalised effective temperature and ratio without detrending over time for ORCA-15.1

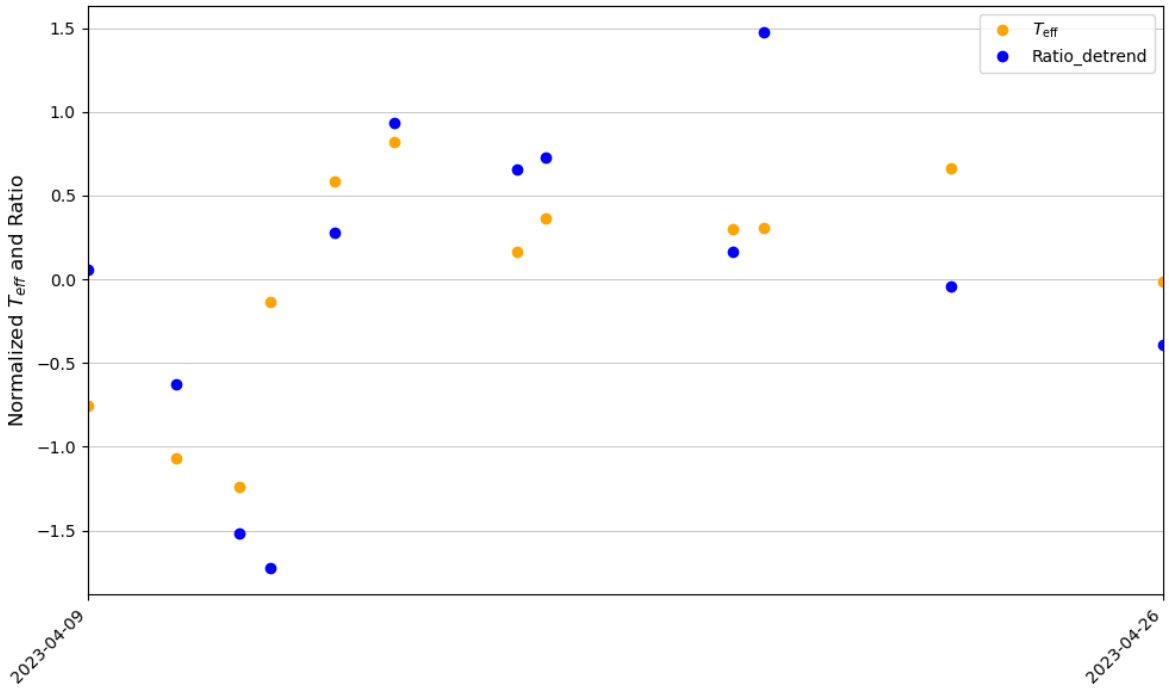

Figure A.31: Normalised effective temperature and ratio with detrending over time for ORCA-15.1

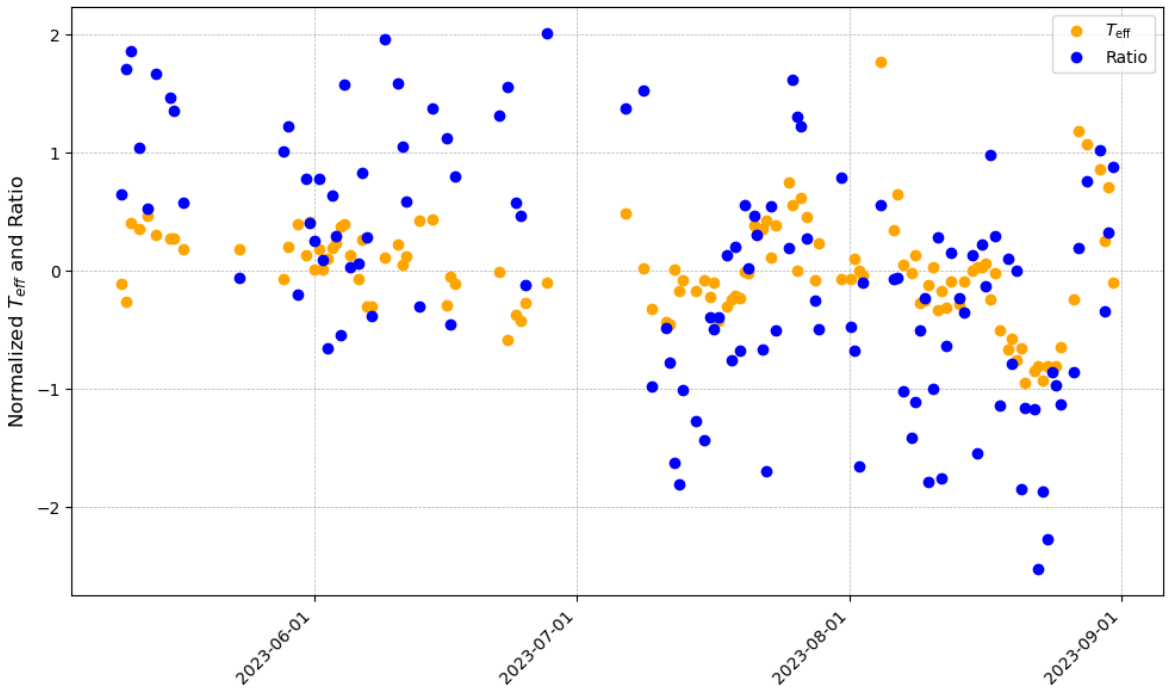

Figure A.32: Normalised effective temperature and ratio without detrending over time for ORCA-18

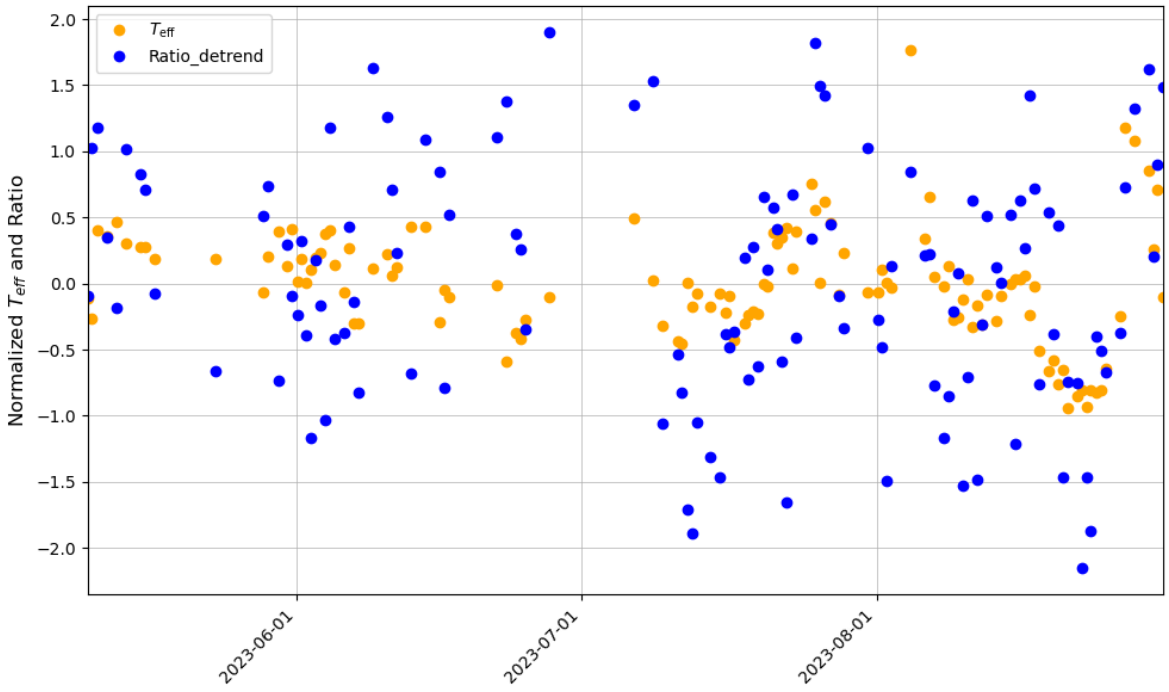

Figure A.33: Normalised effective temperature and ratio with detrending over time for ORCA-18

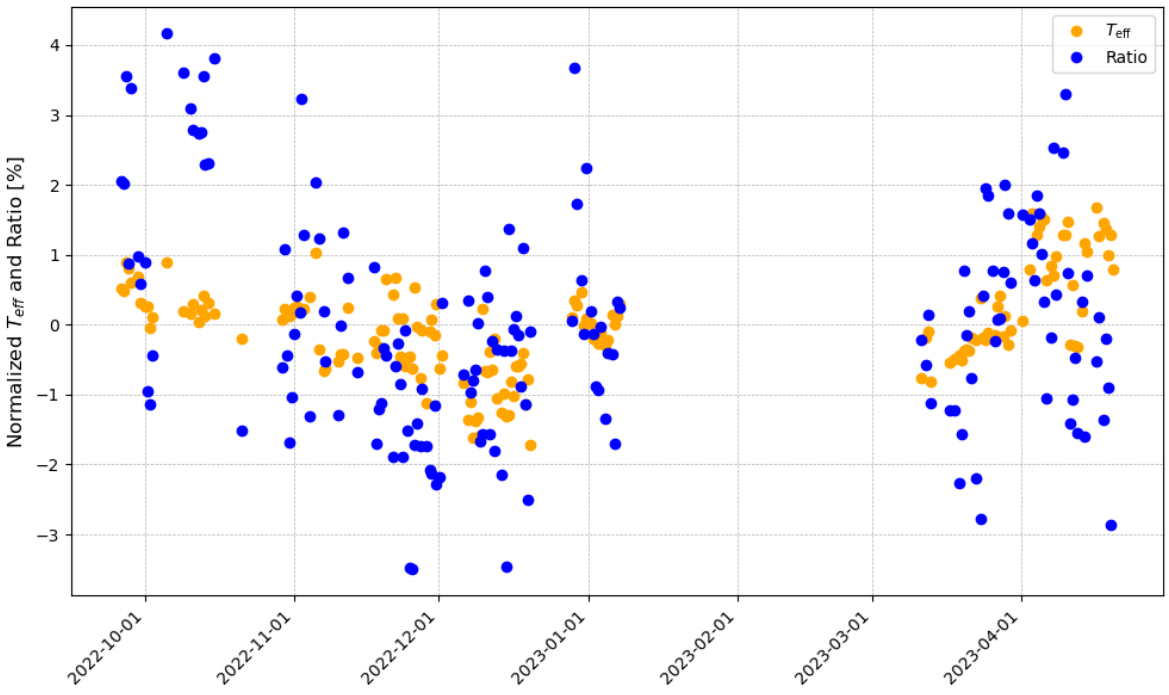

Figure A.34: Normalised effective temperature and ratio without detrending over time for ARCA-21

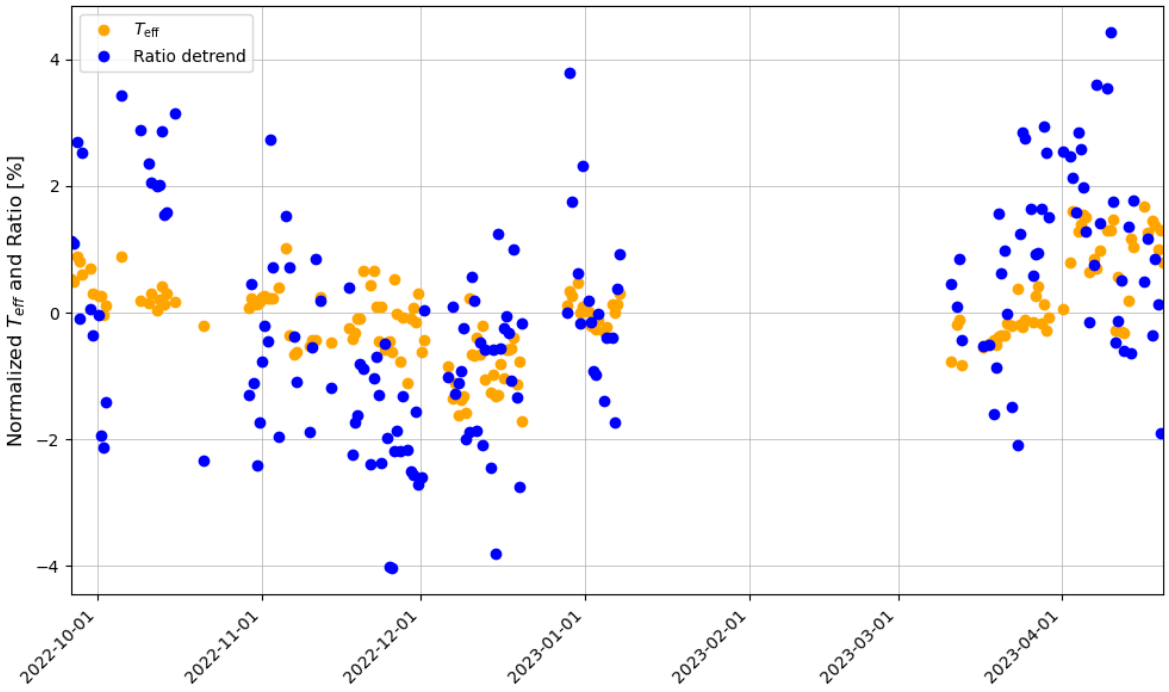

Figure A.35: Normalised effective temperature and ratio with detrending over time for ARCA-21

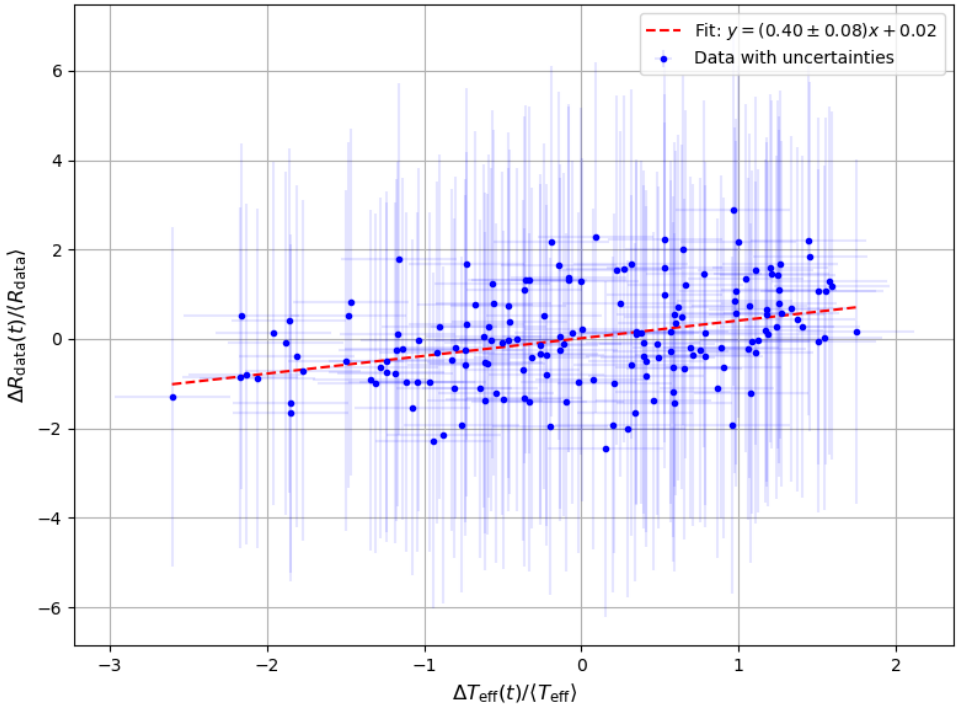

Figure A.36: Normalised effective temperature T_{eff} and ratio without detrending R_{data} of ORCA-10 showing the relative variation in percentage. The red line is a fit of the model in Equation 6.11. The errors are taken into account in the fit.

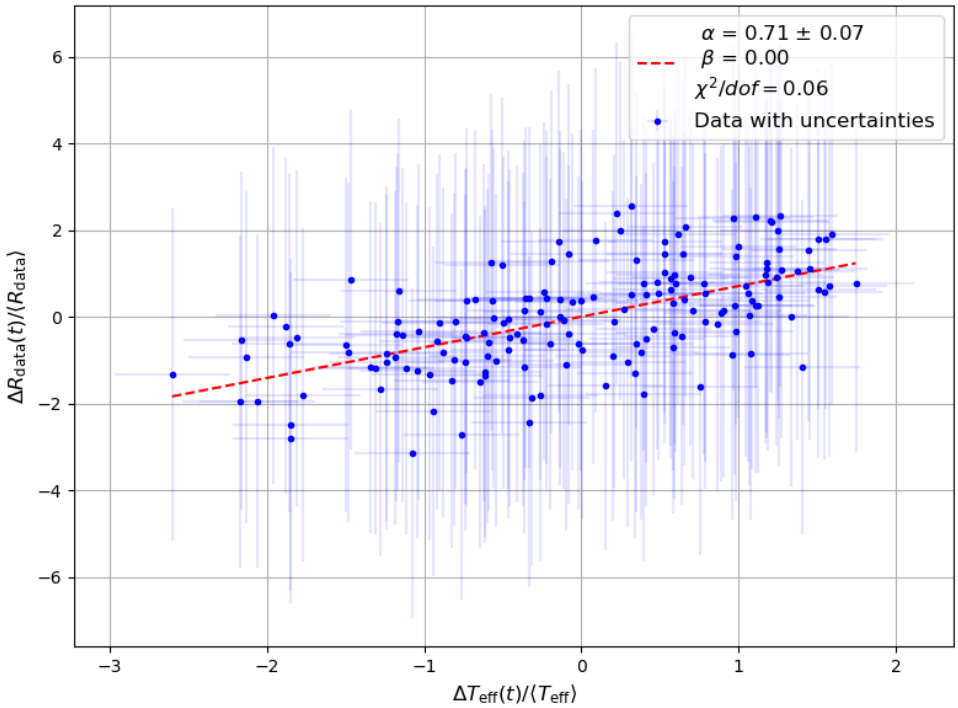

Figure A.37: Normalised effective temperature T_{eff} and ratio with detrending R_{data} of ORCA-10 showing the relative variation in percentage. The red line is a fit of the model in Equation 6.11. The errors are taken into account in the fit.

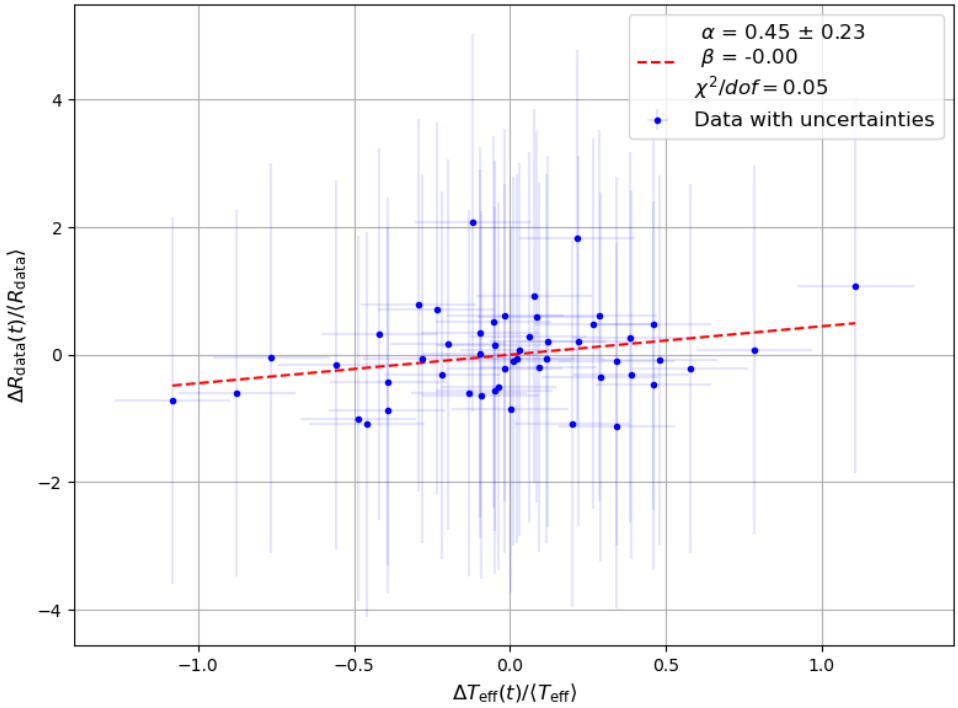

Figure A.38: Normalised effective temperature T_{eff} and ratio without detrending R_{data} of ORCA-11 showing the relative variation in percentage. The red line is a fit of the model in Equation 6.11. The errors are taken into account in the fit.

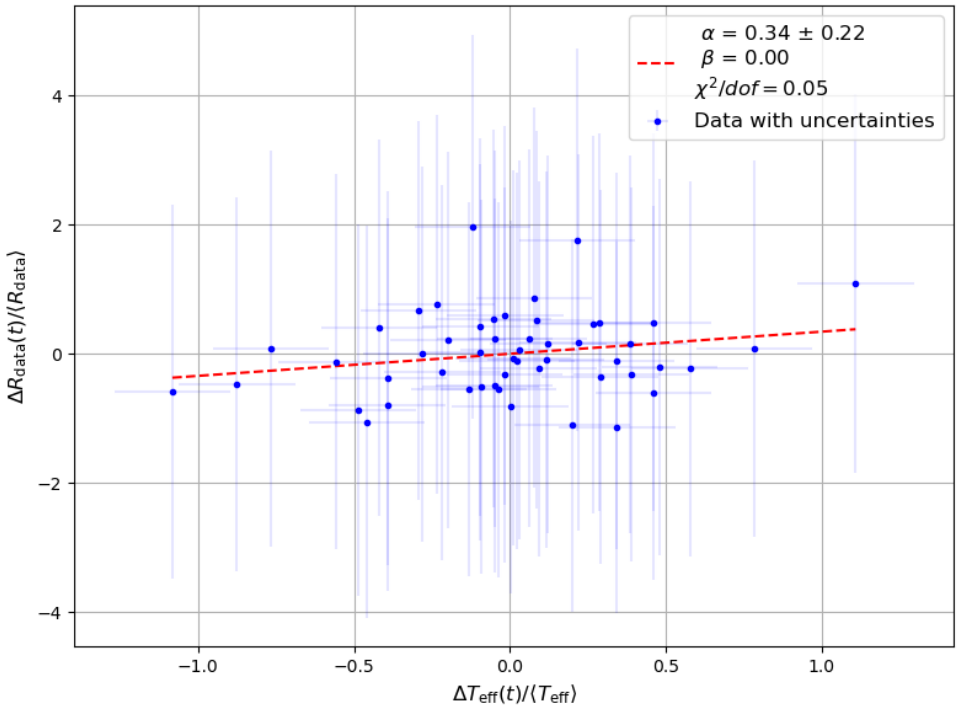

Figure A.39: Normalised effective temperature T_{eff} and ratio with detrending R_{data} of ORCA-11 showing the relative variation in percentage. The red line is a fit of the model in Equation 6.11. The errors are taken into account in the fit.

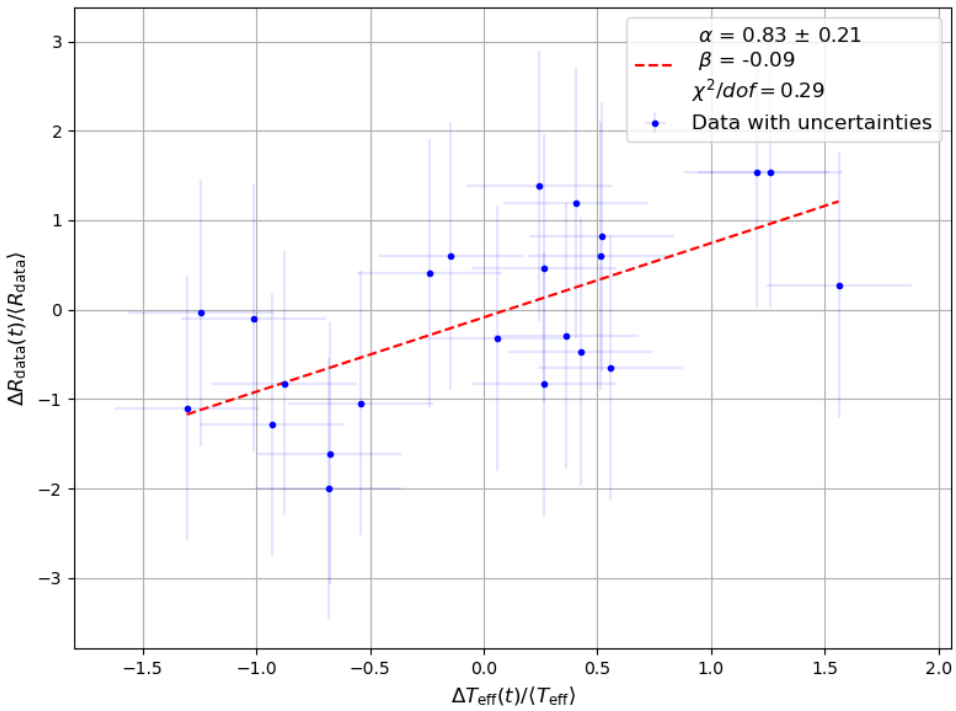

Figure A.40: Normalised effective temperature T_{eff} and ratio without detrending R_{data} of ORCA-11.1 showing the relative variation in percentage. The red line is a fit of the model in Equation 6.11. The errors are taken into account in the fit.

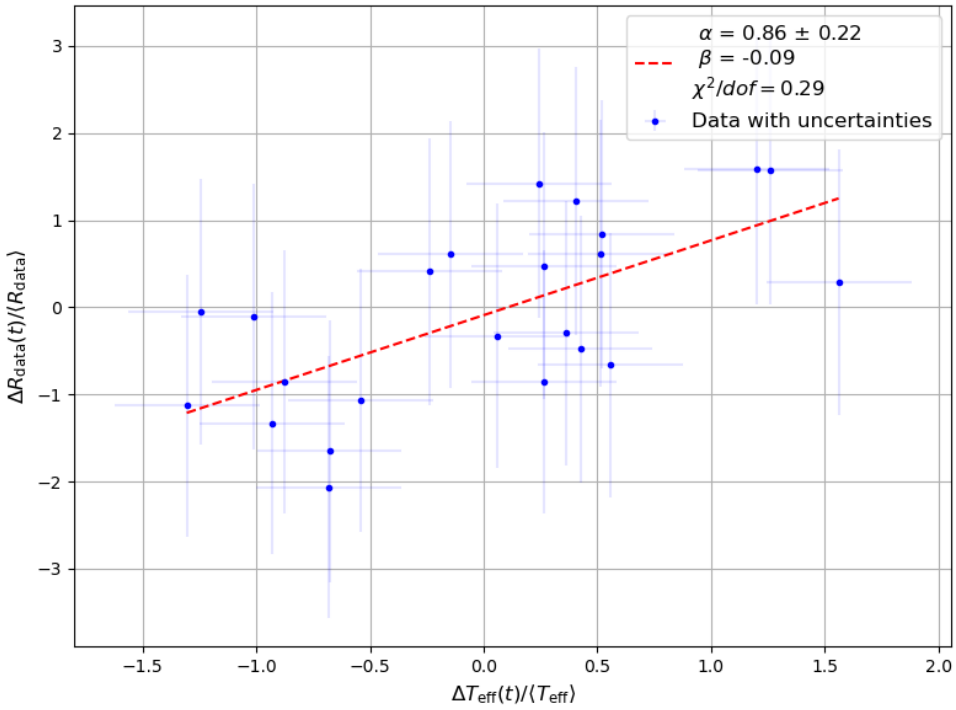

Figure A.41: Normalised effective temperature T_{eff} and ratio with detrending R_{data} of ORCA-11.1 showing the relative variation in percentage. The red line is a fit of the model in Equation 6.11. The errors are taken into account in the fit.

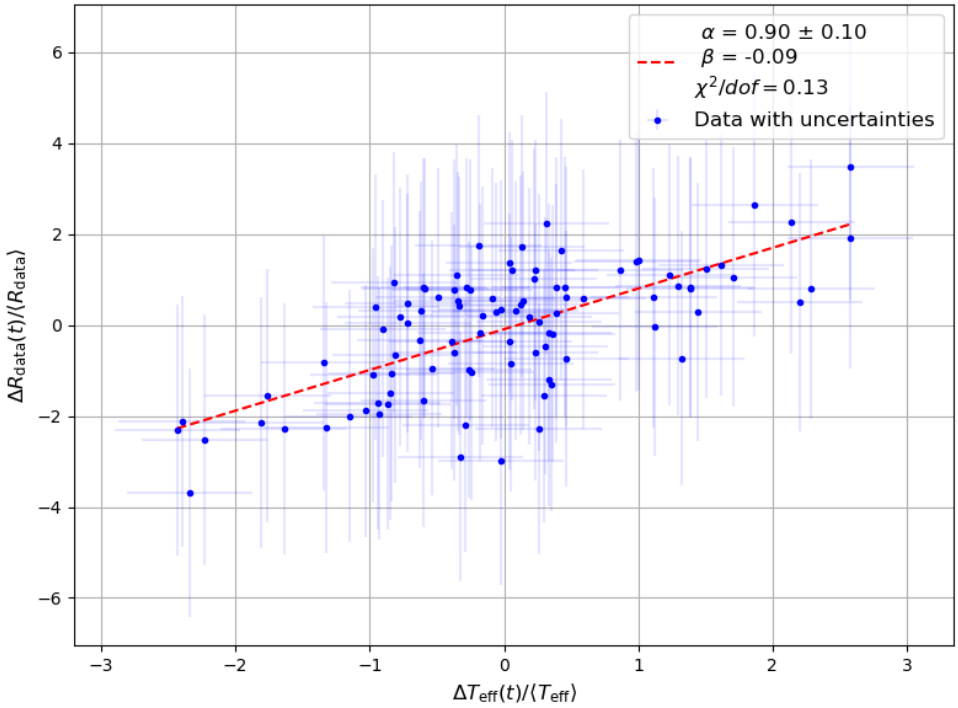

Figure A.42: Normalised effective temperature T_{eff} and ratio without detrending R_{data} of ORCA-15 showing the relative variation in percentage. The red line is a fit of the model in Equation 6.11. The errors are taken into account in the fit.

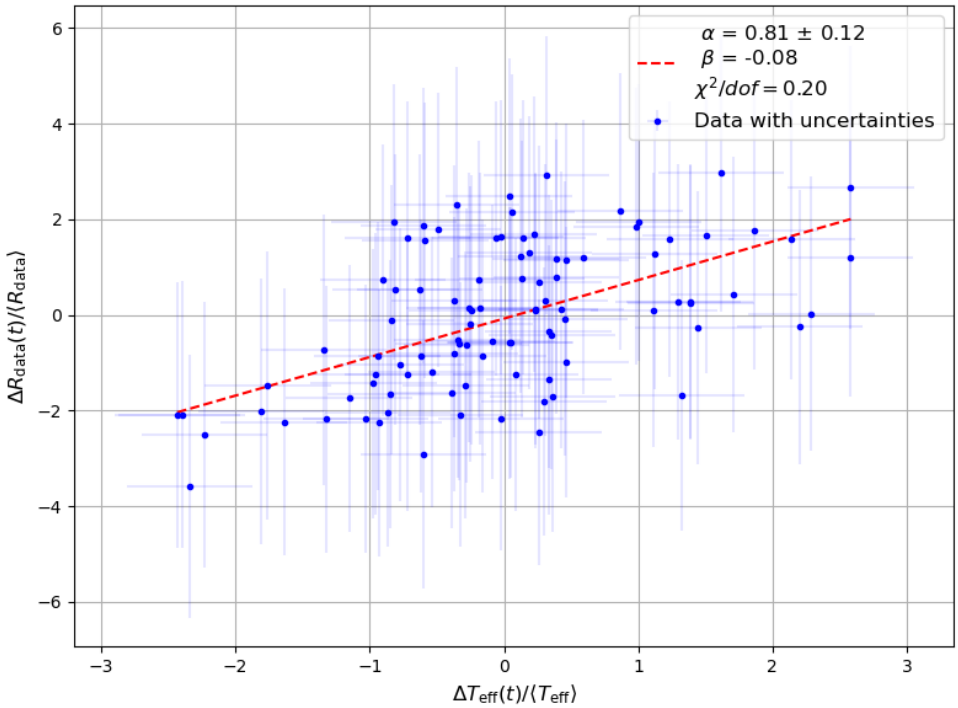

Figure A.43: Normalised effective temperature T_{eff} and ratio with detrending R_{data} of ORCA-15 showing the relative variation in percentage. The red line is a fit of the model in Equation 6.11. The errors are taken into account in the fit.

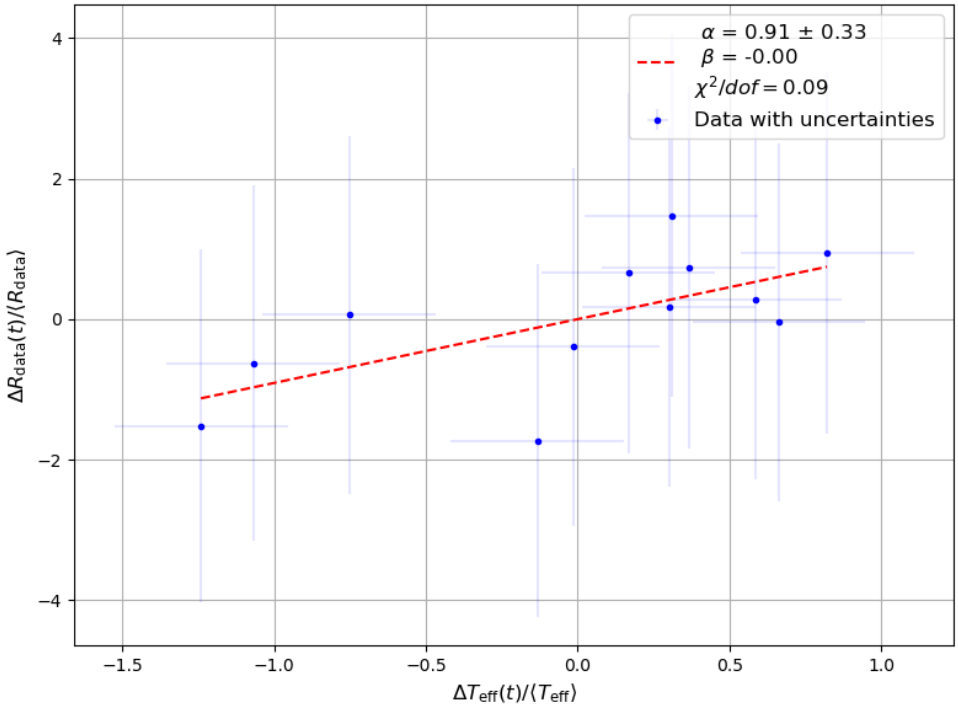

Figure A.44: Normalised effective temperature T_{eff} and ratio without detrending R_{data} of ORCA-15.1 showing the relative variation in percentage. The red line is a fit of the model in Equation 6.11. The errors are taken into account in the fit.

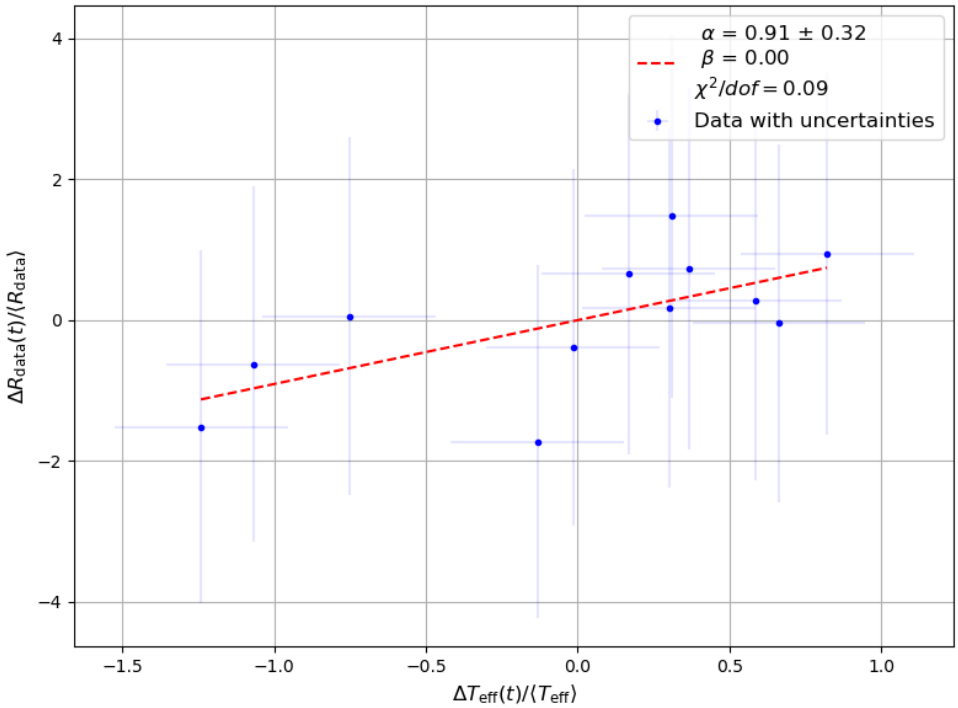

Figure A.45: Normalised effective temperature T_{eff} and ratio with detrending R_{data} of ORCA-15.1 showing the relative variation in percentage. The red line is a fit of the model in Equation 6.11. The errors are taken into account in the fit.

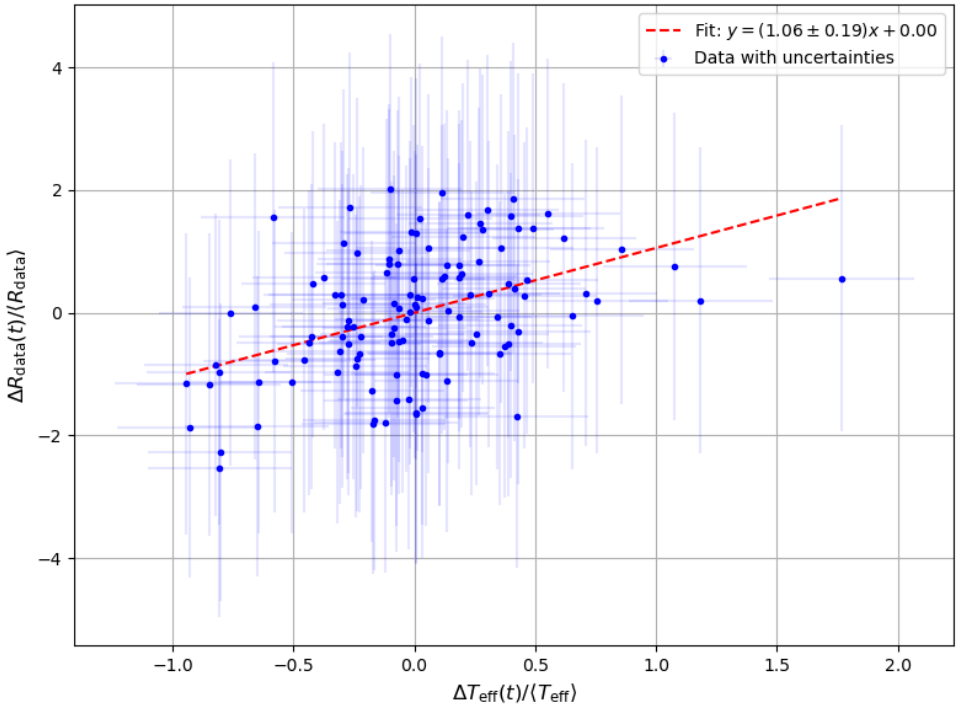

Figure A.46: Normalised effective temperature T_{eff} and ratio without detrending R_{data} of ORCA-18 showing the relative variation in percentage. The red line is a fit of the model in Equation 6.11. The errors are taken into account in the fit.

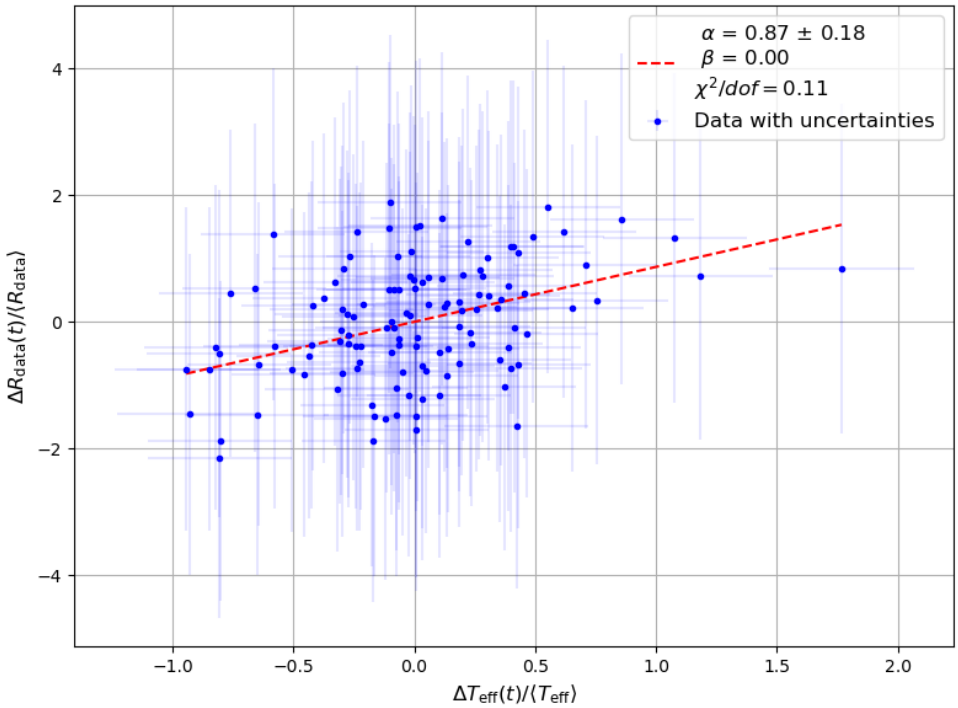

Figure A.47: Normalised effective temperature T_{eff} and ratio with detrending R_{data} of ORCA-18 showing the relative variation in percentage. The red line is a fit of the model in Equation 6.11. The errors are taken into account in the fit.

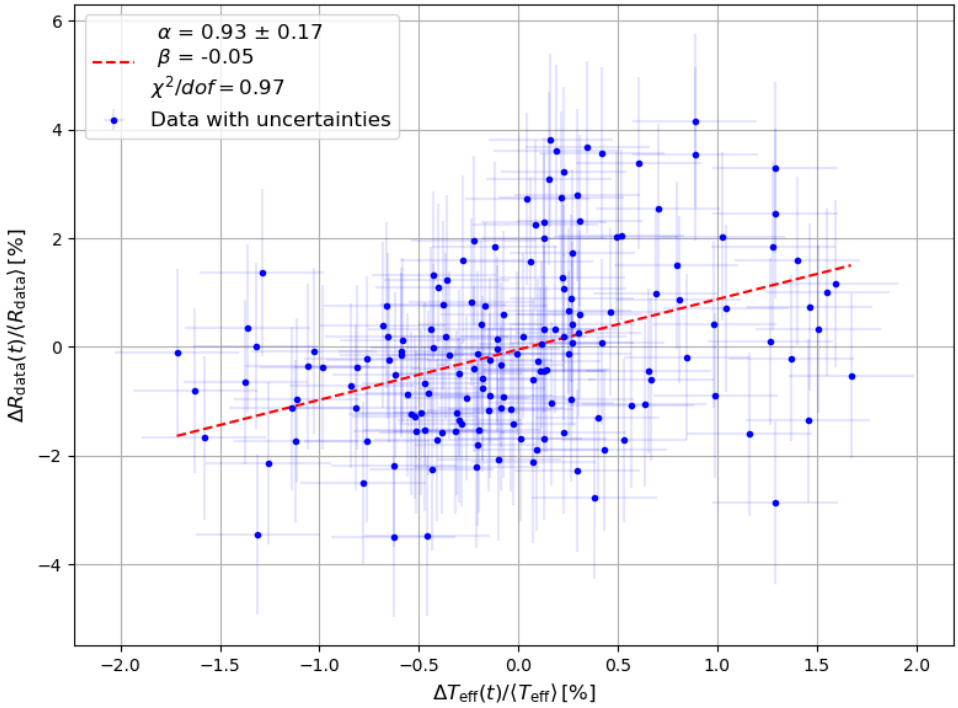

Figure A.48: Normalised effective temperature T_{eff} and ratio without detrending R_{data} of ARCA-21 showing the relative variation in percentage. The red line is a fit of the model in Equation 6.11. The errors are taken into account in the fit.

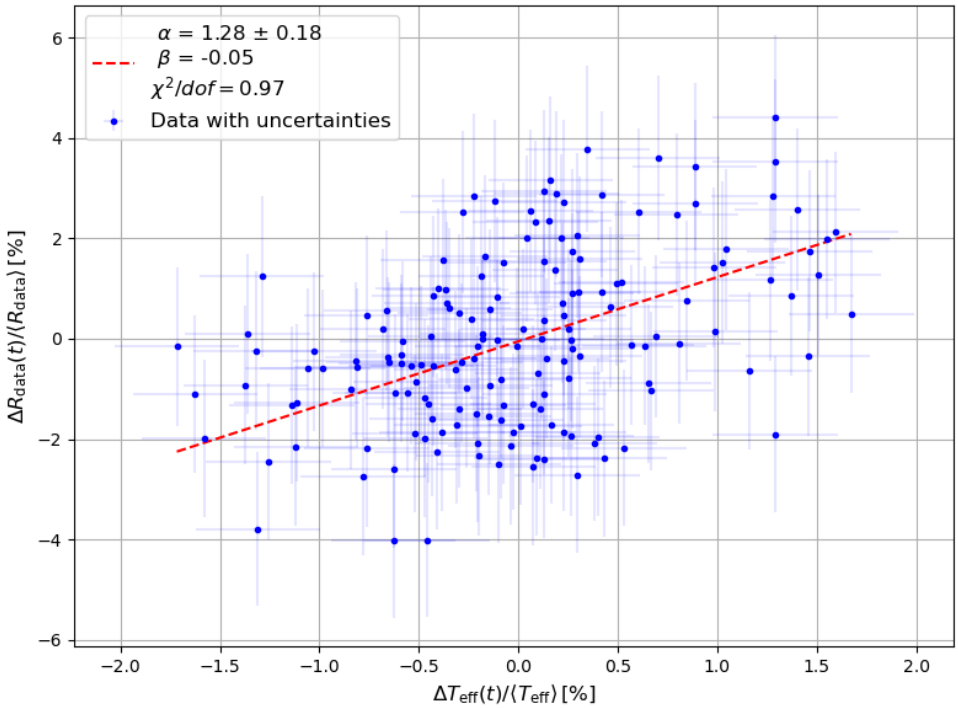

Figure A.49: Normalised effective temperature T_{eff} and ratio with detrending R_{data} of ARCA-21 showing the relative variation in percentage. The red line is a fit of the model in Equation 6.11. The errors are taken into account in the fit.

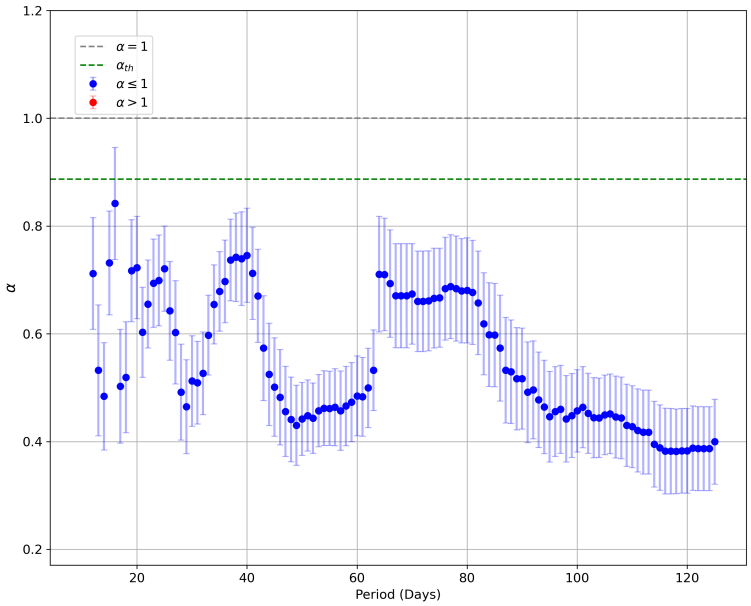

Figure A.50: The average effective temperature coefficient over a specific window or period is plotted for the ORCA-10 data without detrending. The red points show for which periods the coefficient is larger than 1 and the green dotted line shows what the coefficient theoretically should be.

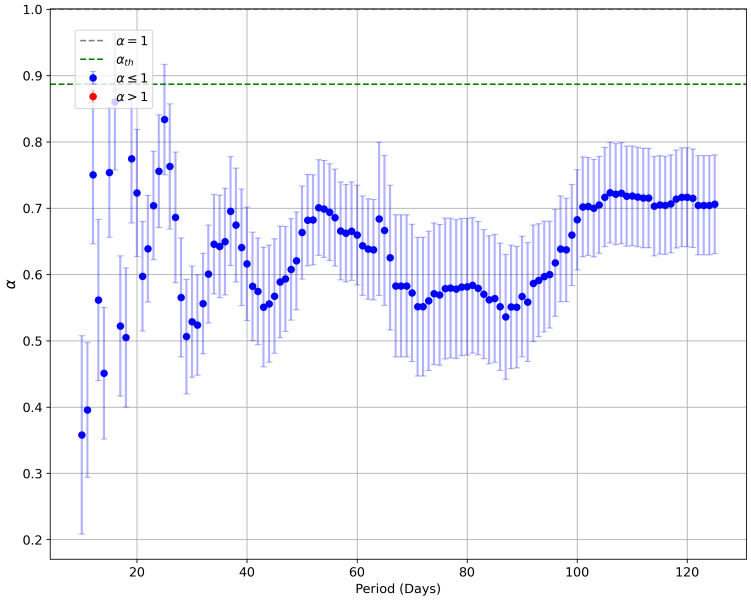

Figure A.51: The average effective temperature coefficient over a specific window or period is plotted for the ORCA-10 data with detrending. The red points show for which periods the coefficient is larger than 1 and the green dotted line shows what the coefficient theoretically should be.

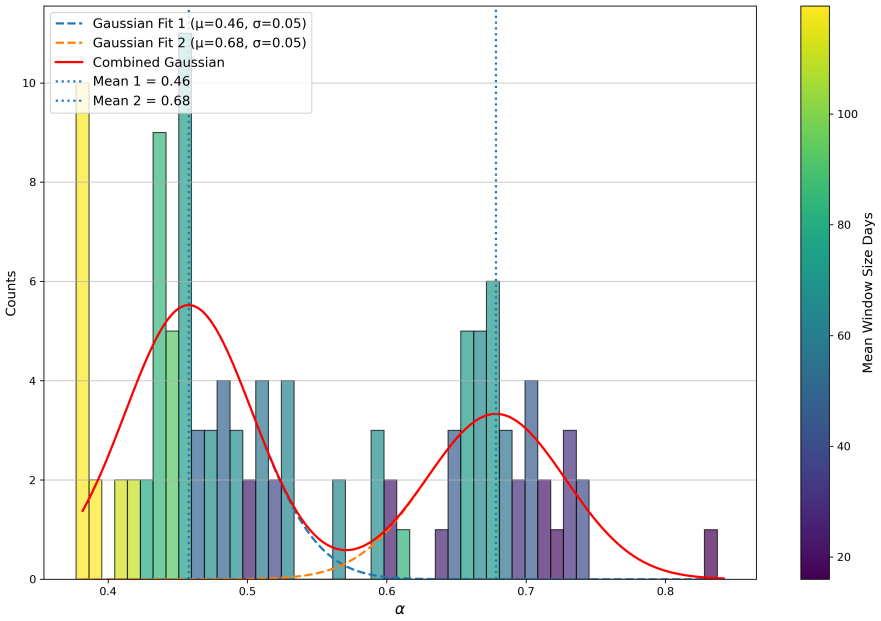

Figure A.52: Histogram of the average effective temperate coefficients of the ORCA-10 data without detrending. The colour of the bin indicates the mean window size of that bin. Two Gaussian distributions are fitted to the data.

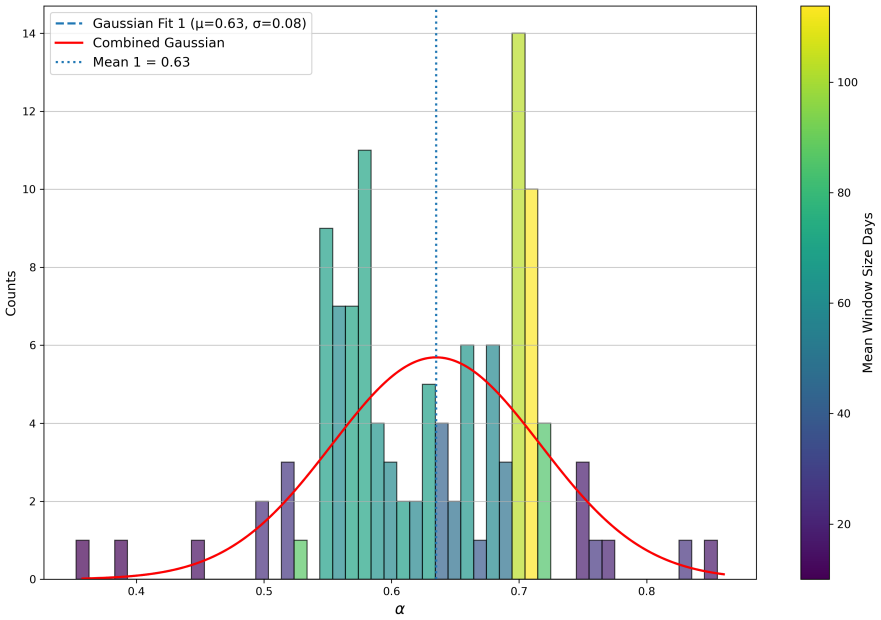

Figure A.53: Histogram of the average effective temperate coefficients of the ORCA-10 data without detrending. The colour of the bin indicates the mean window size of that bin. Two Gaussian distributions are fitted to the data.

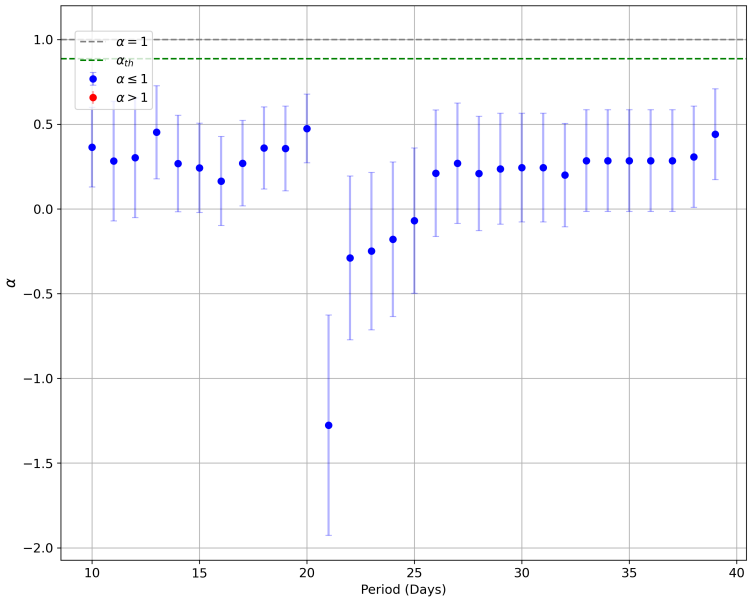

Figure A.54: The average effective temperature coefficient over a specific window or period is plotted for the ORCA-11 data without detrending. The red points show for which periods the coefficient is larger than 1 and the green dotted line shows what the coefficient theoretically should be.

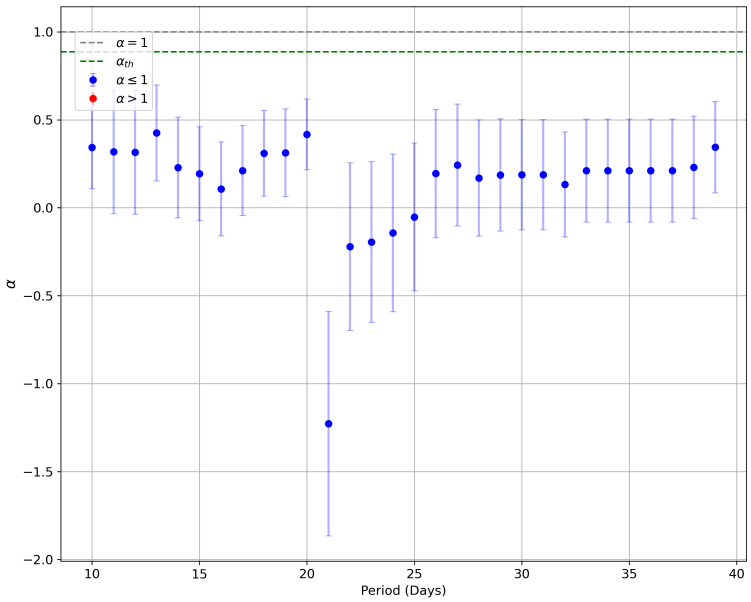

Figure A.55: The average effective temperature coefficient over a specific window or period is plotted for the ORCA-11 data with detrending. The red points show for which periods the coefficient is larger than 1 and the green dotted line shows what the coefficient theoretically should be.

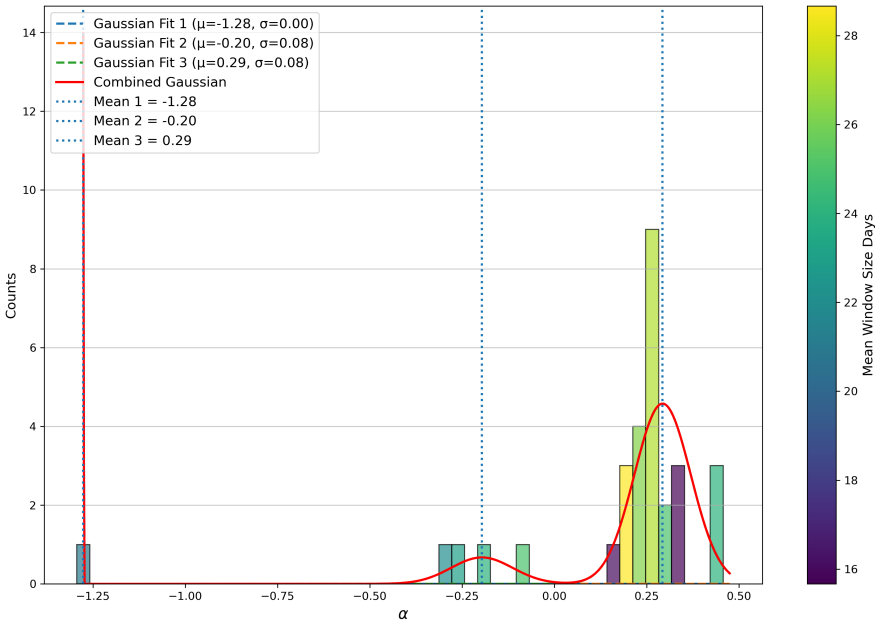

Figure A.56: Histogram of the average effective temperate coefficients of the ORCA-11 data without detrending. The colour of the bin indicates the mean window size of that bin. Two Gaussian distributions are fitted to the data.

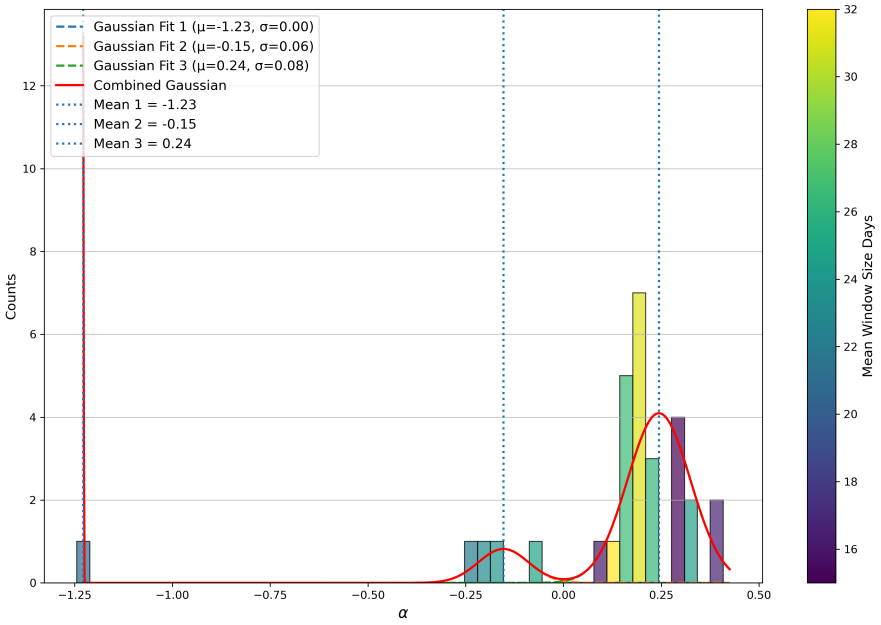

Figure A.57: Histogram of the average effective temperate coefficients of the ORCA-11 data without detrending. The colour of the bin indicates the mean window size of that bin. Two Gaussian distributions are fitted to the data.

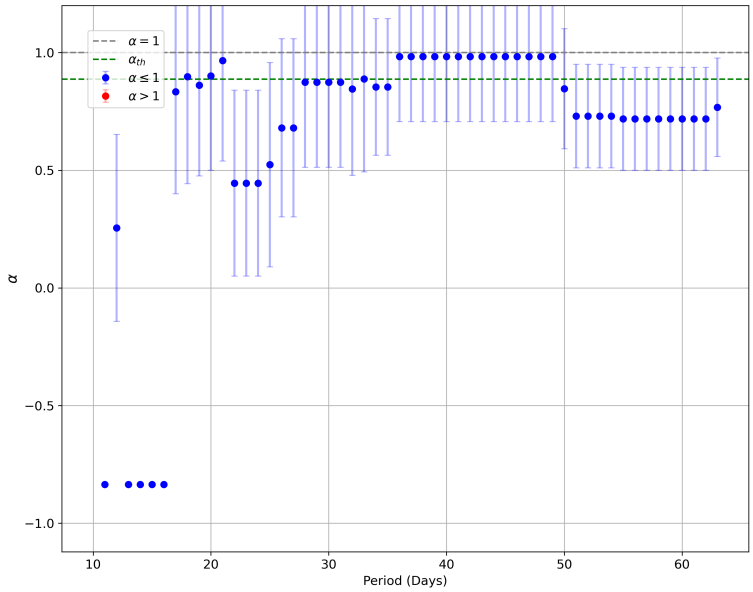

Figure A.58: The average effective temperature coefficient over a specific window or period is plotted for the ORCA-11.1 data without detrending. The red points show for which periods the coefficient is larger than 1 and the green dotted line shows what the coefficient theoretically should be.

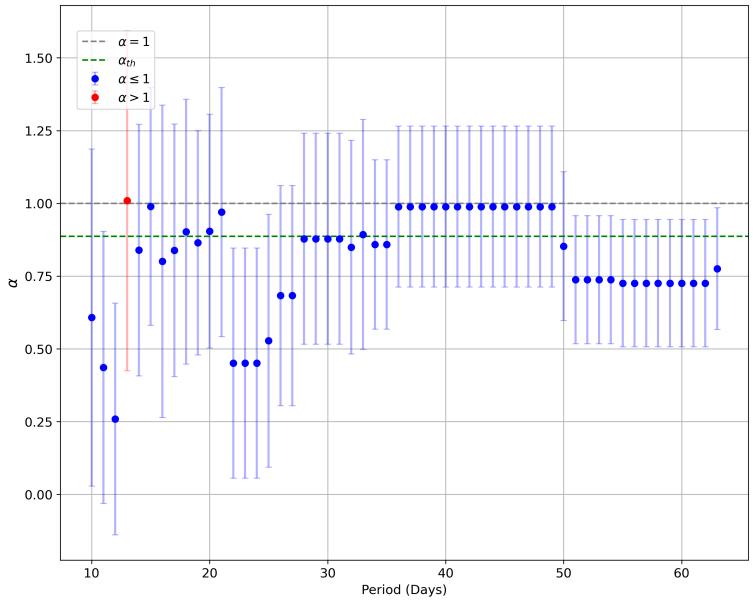

Figure A.59: The average effective temperature coefficient over a specific window or period is plotted for the ORCA-11.1 data with detrending. The red points show for which periods the coefficient is larger than 1 and the green dotted line shows what the coefficient theoretically should be.

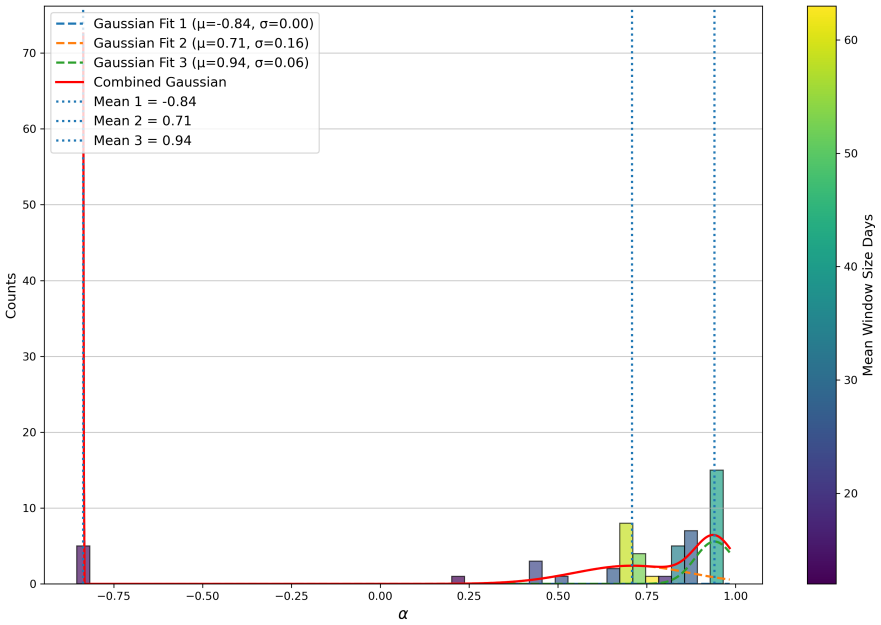

Figure A.60: Histogram of the average effective temperate coefficients of the ORCA-11.1 data without detrending. The colour of the bin indicates the mean window size of that bin. Two Gaussian distributions are fitted to the data.

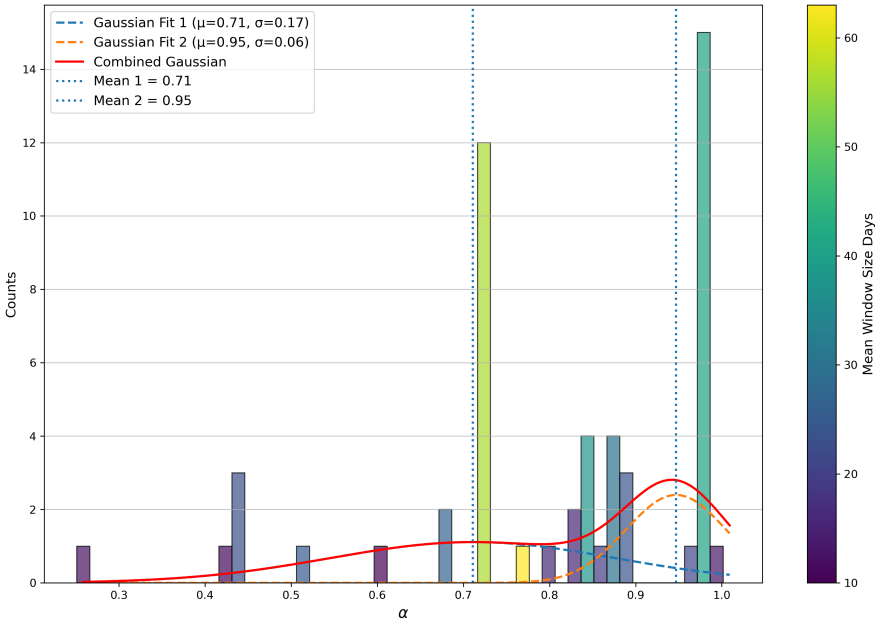

Figure A.61: Histogram of the average effective temperate coefficients of the ORCA-11.1 data without detrending. The colour of the bin indicates the mean window size of that bin. Two Gaussian distributions are fitted to the data.

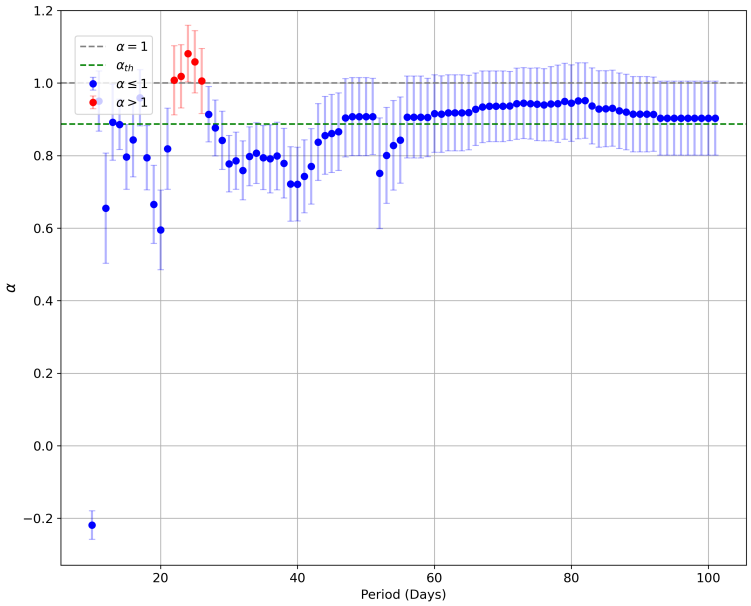

Figure A.62: The average effective temperature coefficient over a specific window or period is plotted for the ORCA-15 data without detrending. The red points show for which periods the coefficient is larger than 1 and the green dotted line shows what the coefficient theoretically should be.

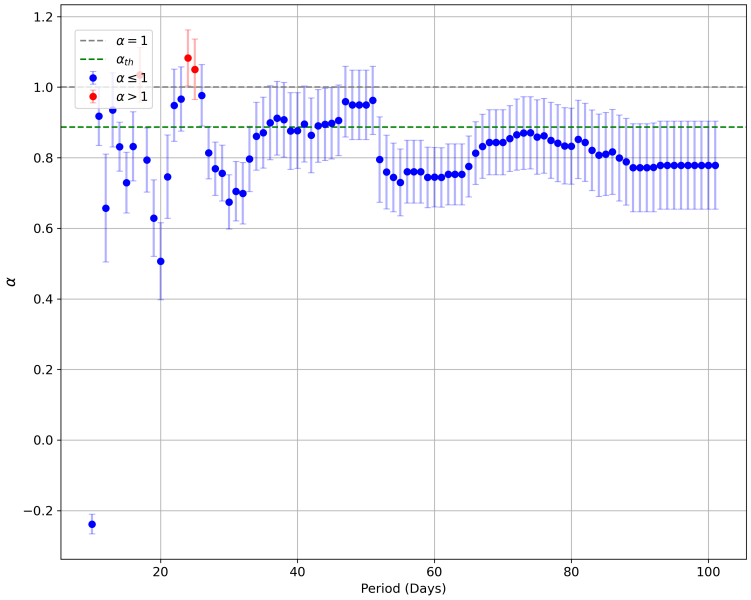

Figure A.63: The average effective temperature coefficient over a specific window or period is plotted for the ORCA-15 data with detrending. The red points show for which periods the coefficient is larger than 1 and the green dotted line shows what the coefficient theoretically should be.

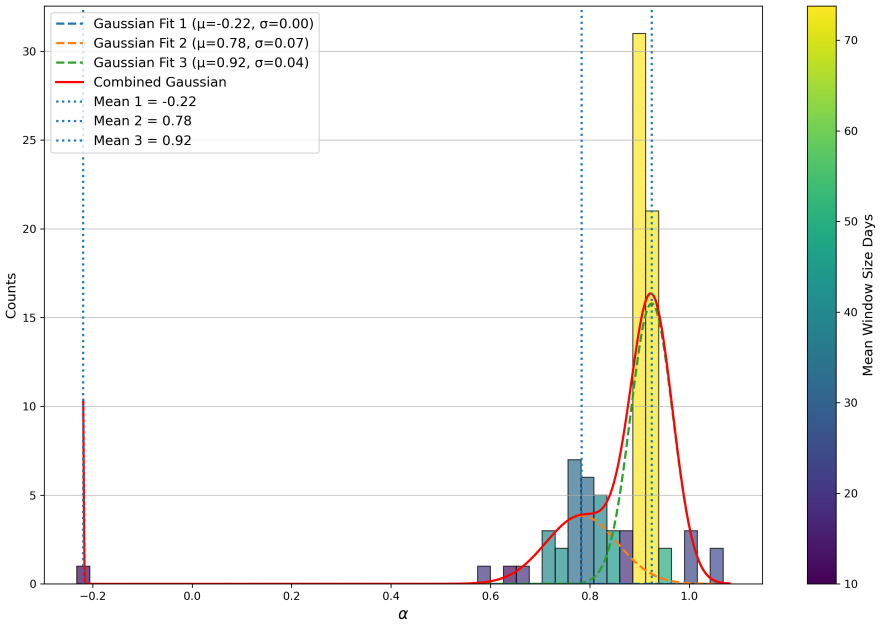

Figure A.64: Histogram of the average effective temperate coefficients of the ORCA-15 data without detrending. The colour of the bin indicates the mean window size of that bin. Two Gaussian distributions are fitted to the data.

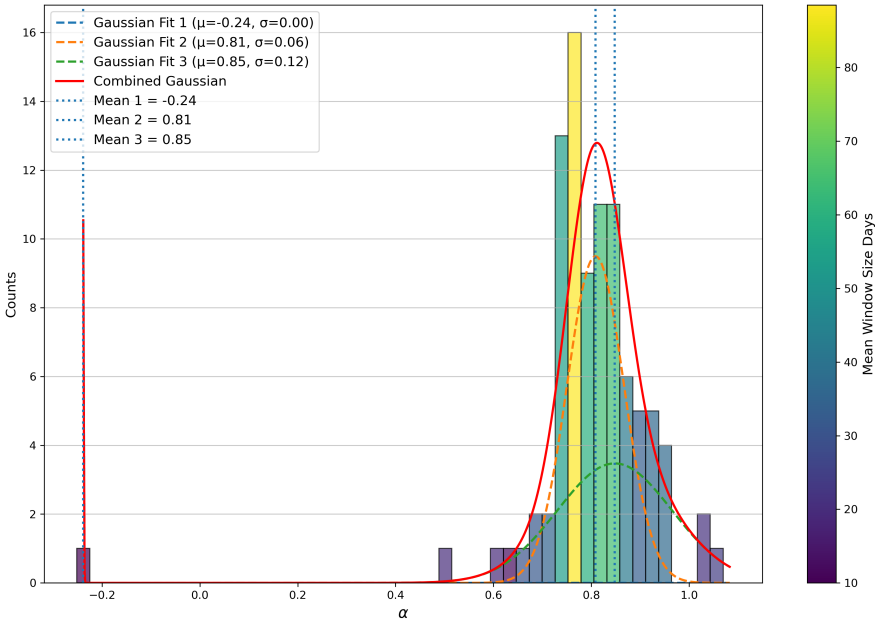

Figure A.65: Histogram of the average effective temperate coefficients of the ORCA-15 data without detrending. The colour of the bin indicates the mean window size of that bin. Two Gaussian distributions are fitted to the data.

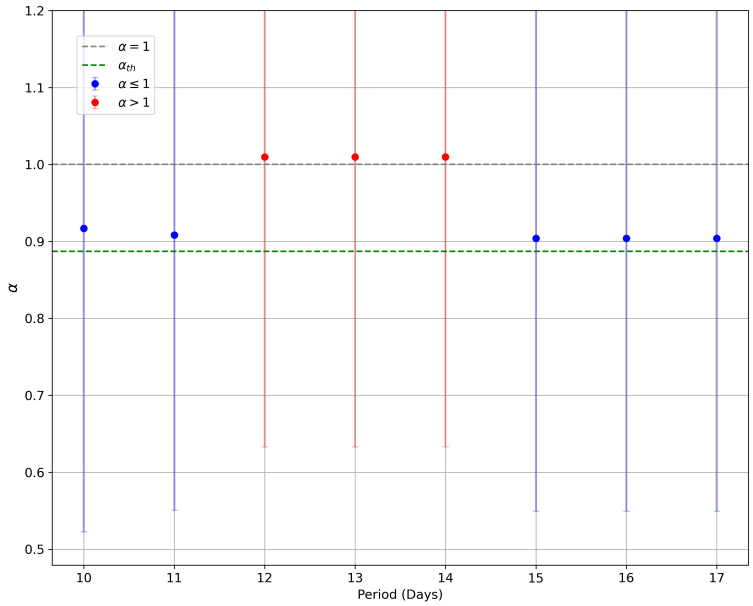

Figure A.66: The average effective temperature coefficient over a specific window or period is plotted for the ORCA-15.1 data without detrending. The red points show for which periods the coefficient is larger than 1 and the green dotted line shows what the coefficient theoretically should be.

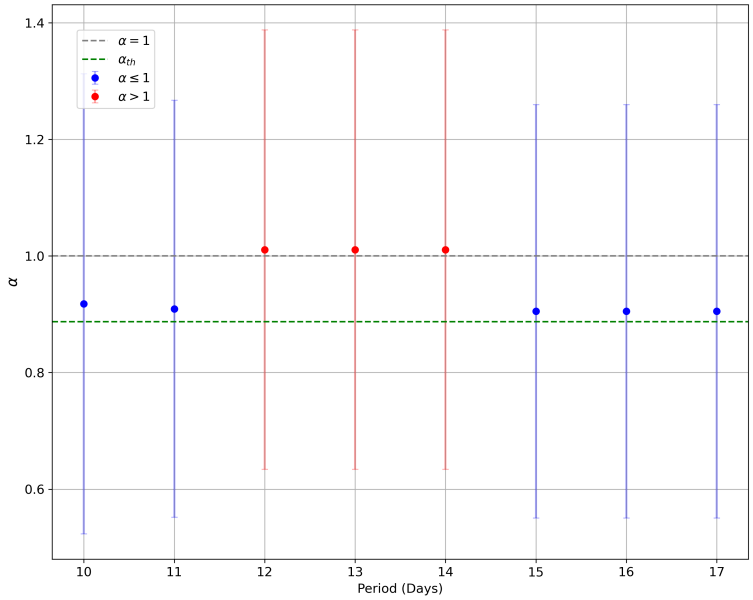

Figure A.67: The average effective temperature coefficient over a specific window or period is plotted for the ORCA-15.1 data with detrending. The red points show for which periods the coefficient is larger than 1 and the green dotted line shows what the coefficient theoretically should be.

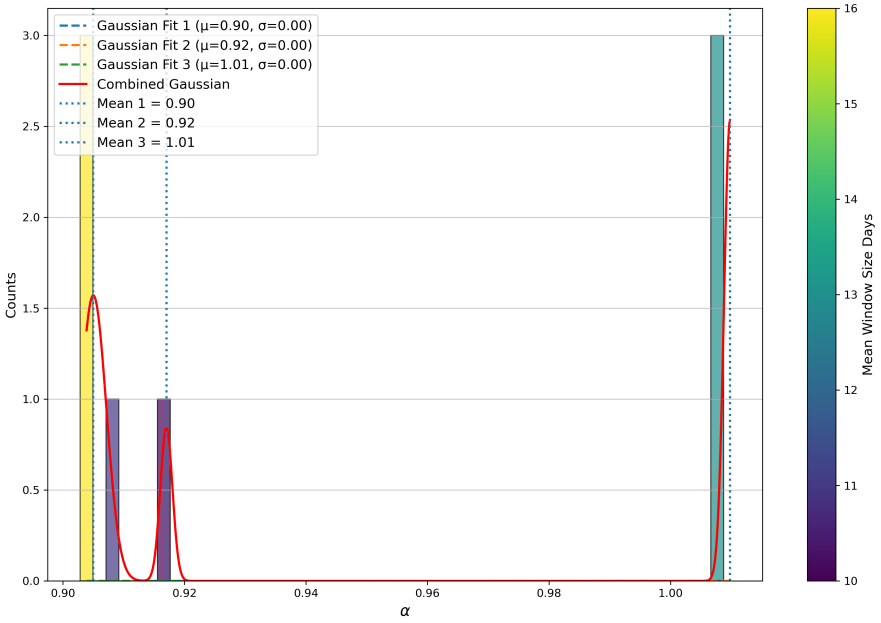

Figure A.68: Histogram of the average effective temperate coefficients of the ORCA-15.1 data without detrending. The colour of the bin indicates the mean window size of that bin. Two Gaussian distributions are fitted to the data.

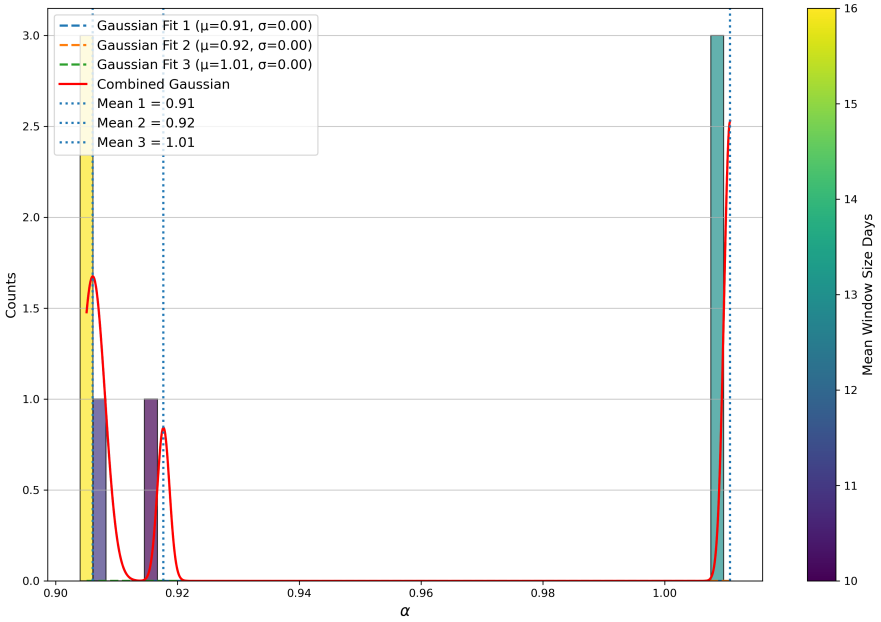

Figure A.69: Histogram of the average effective temperate coefficients of the ORCA-15.1 data without detrending. The colour of the bin indicates the mean window size of that bin. Two Gaussian distributions are fitted to the data.

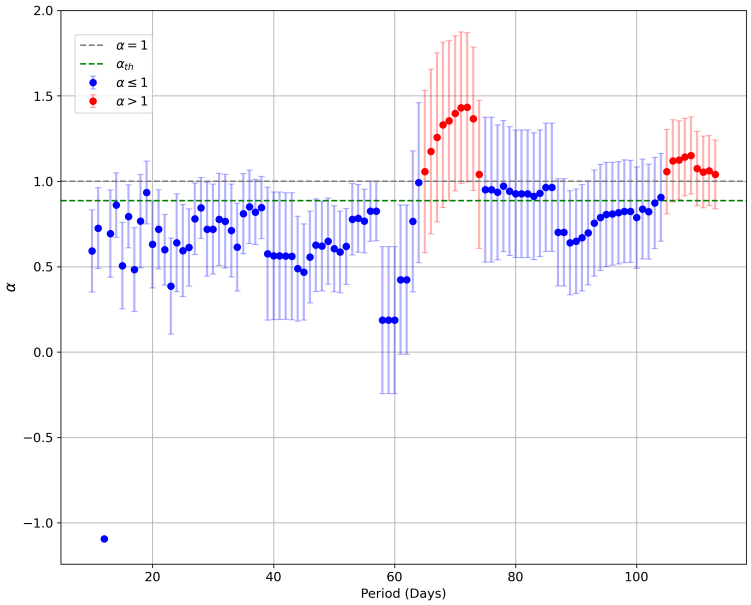

Figure A.70: The average effective temperature coefficient over a specific window or period is plotted for the ORCA-18 data without detrending. The red points show for which periods the coefficient is larger than 1 and the green dotted line shows what the coefficient theoretically should be.

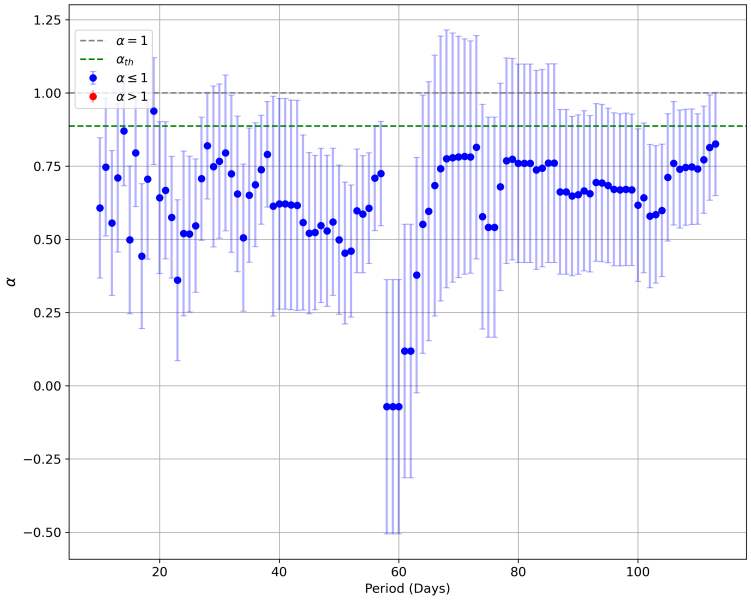

Figure A.71: The average effective temperature coefficient over a specific window or period is plotted for the ORCA-18 data with detrending. The red points show for which periods the coefficient is larger than 1 and the green dotted line shows what the coefficient theoretically should be.

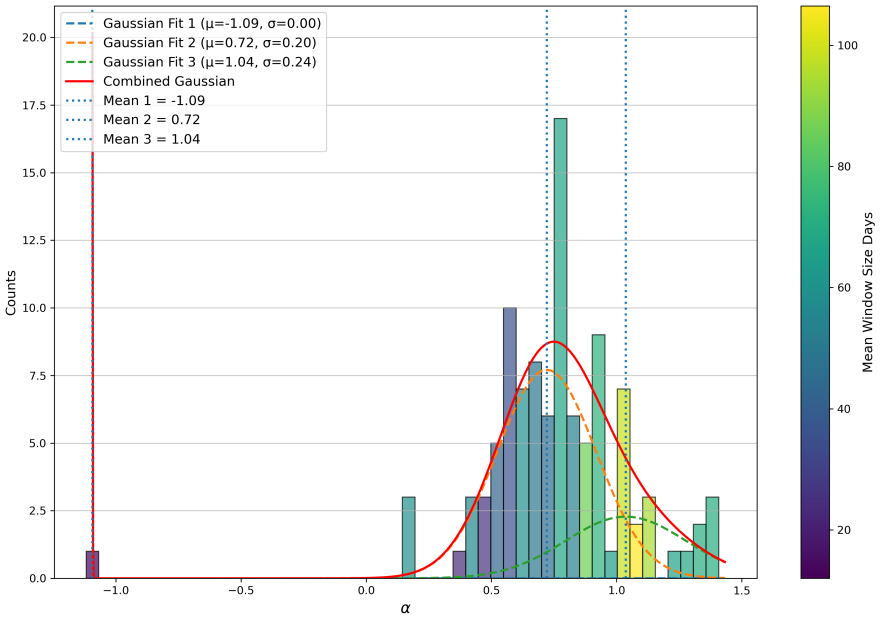

Figure A.72: Histogram of the average effective temperate coefficients of the ORCA-18 data without detrending. The colour of the bin indicates the mean window size of that bin. Two Gaussian distributions are fitted to the data.

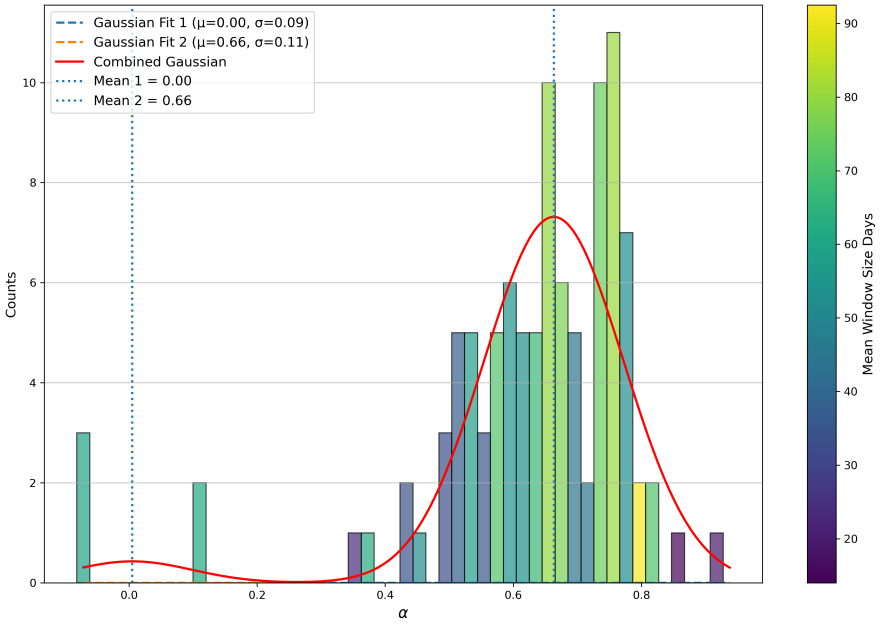

Figure A.73: Histogram of the average effective temperate coefficients of the ORCA-18 data without detrending. The colour of the bin indicates the mean window size of that bin. Two Gaussian distributions are fitted to the data.

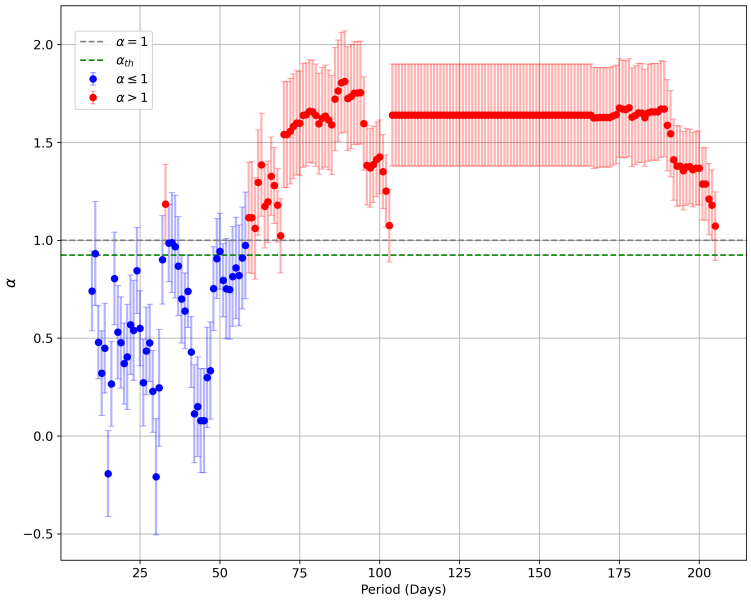

Figure A.74: The average effective temperature coefficient over a specific window or period is plotted for the ARCA-21 data without detrending. The red points show for which periods the coefficient is larger than 1 and the green dotted line shows what the coefficient theoretically should be.

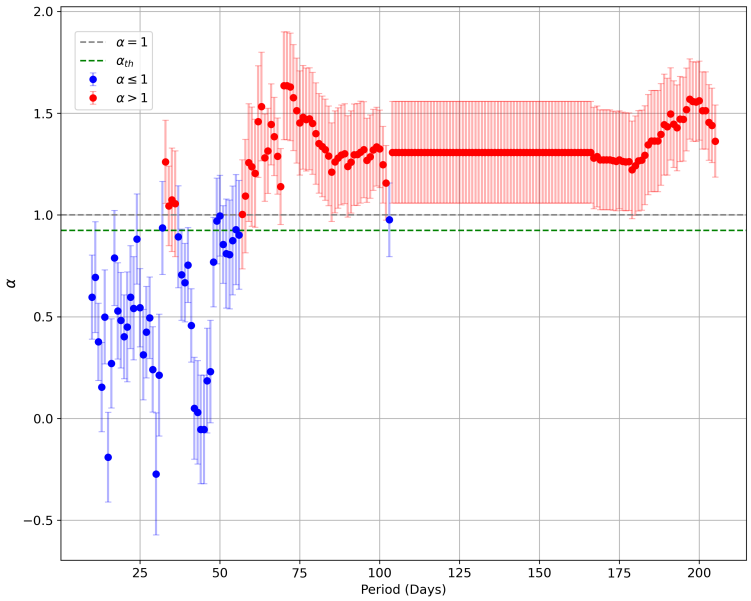

Figure A.75: The average effective temperature coefficient over a specific window or period is plotted for the ARCA-21 data with detrending. The red points show for which periods the coefficient is larger than 1 and the green dotted line shows what the coefficient theoretically should be.

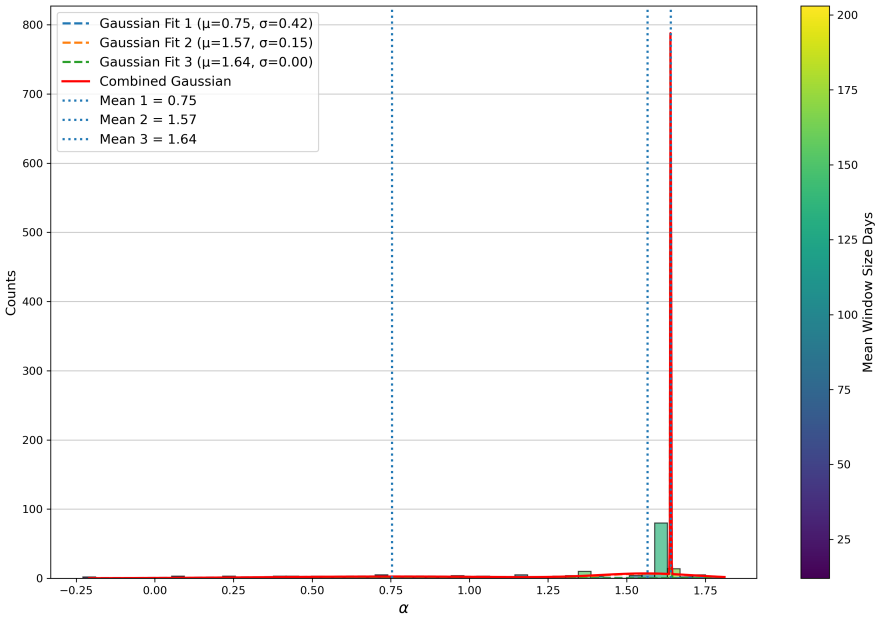

Figure A.76: Histogram of the average effective temperate coefficients of the ARCA-21 data without detrending. The colour of the bin indicates the mean window size of that bin. Two Gaussian distributions are fitted to the data.

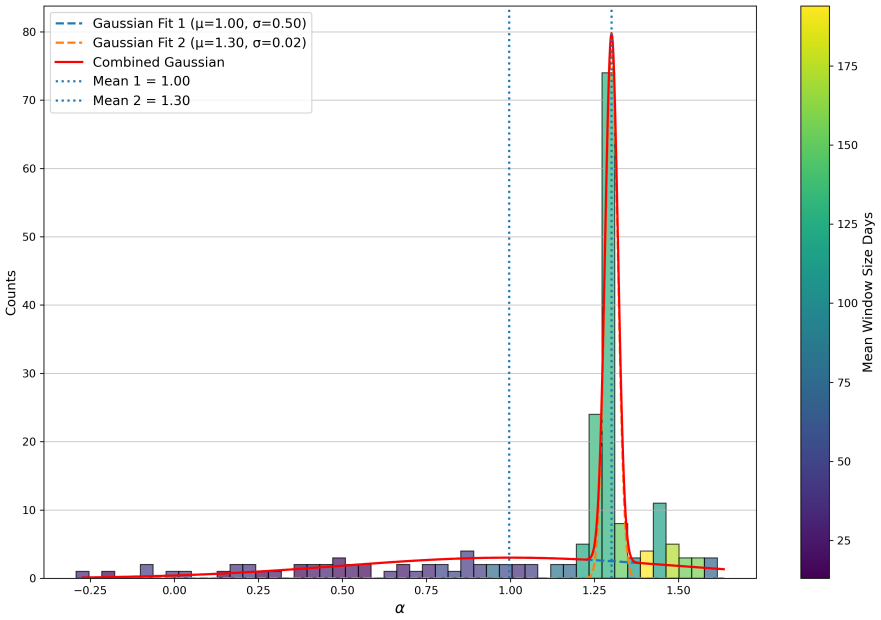

Figure A.77: Histogram of the average effective temperate coefficients of the ARCA-21 data without detrending. The colour of the bin indicates the mean window size of that bin. Two Gaussian distributions are fitted to the data.

A.1.2. 60-Minute Window Around Temperature Measurement

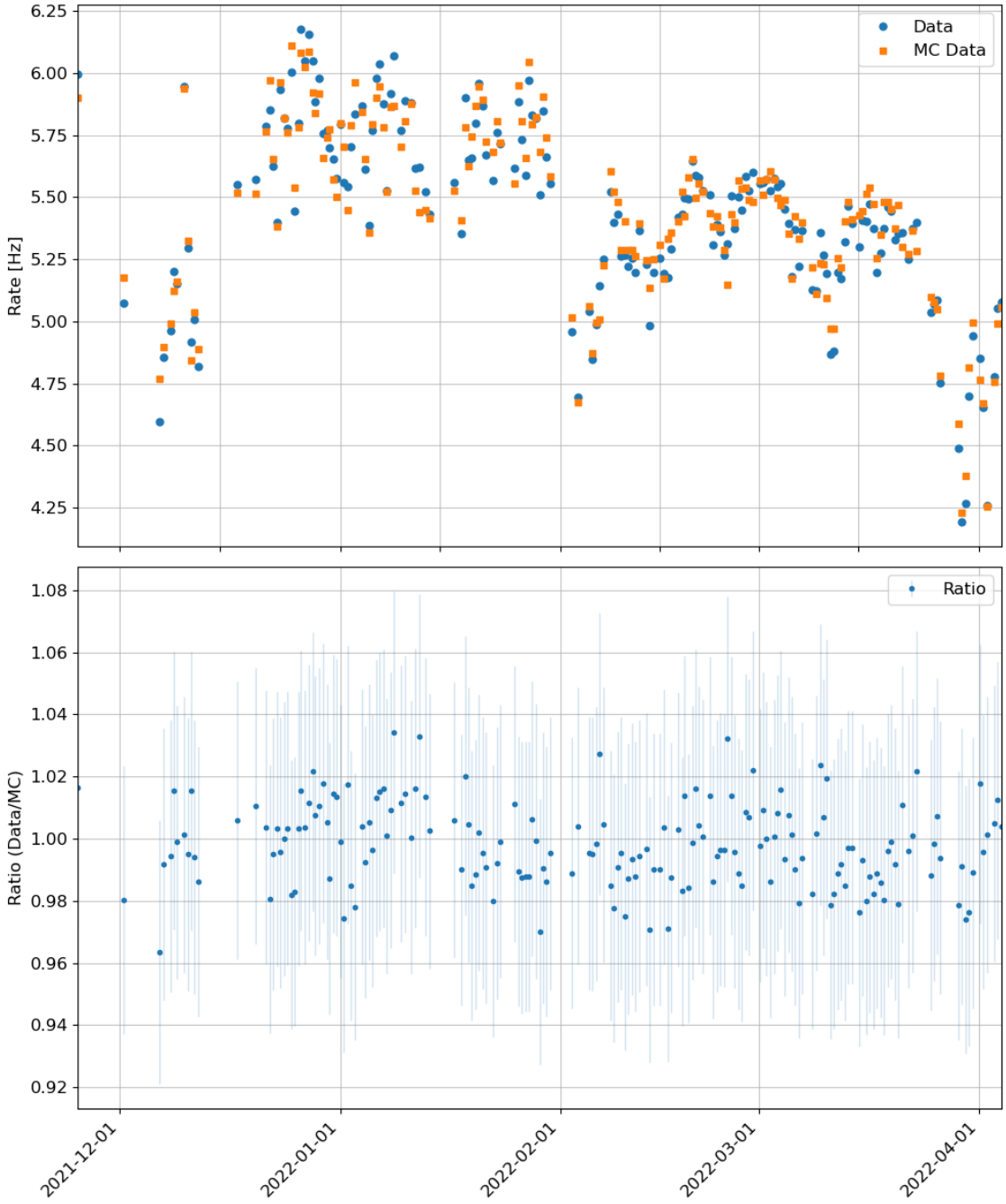

Figure A.78: Rate and ratio per 60-minute window around temperature measurements for ORCA-10 after cuts are applied. In the top part the count rates of the data and the Monte Carlo simulation are shown. In the bottom part the ratio of the two is shown.

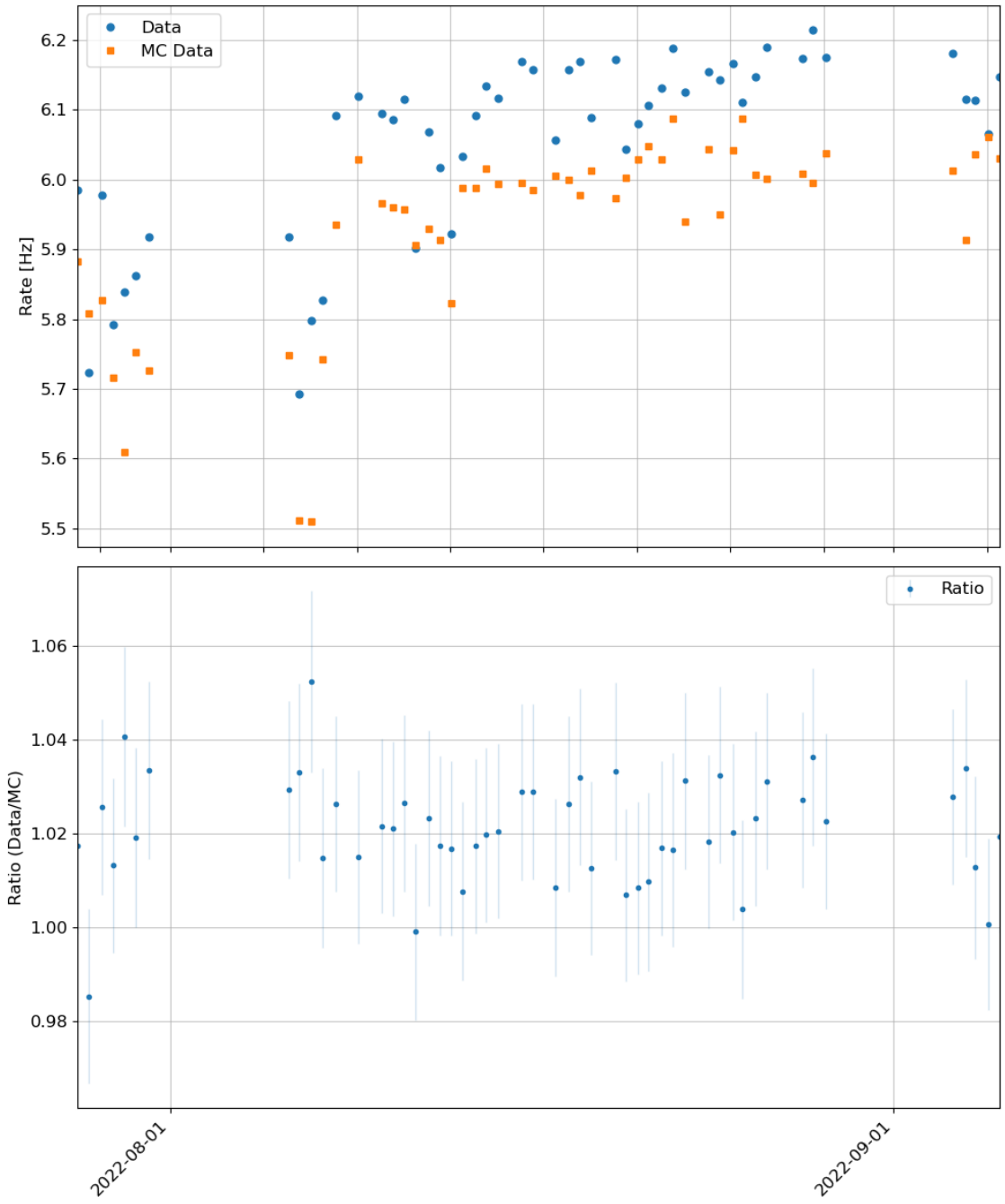

Figure A.79: Rate and ratio per 60-minute window around temperature measurements for ORCA-11 after cuts are applied. In the top part the count rates of the data and the Monte Carlo simulation are shown. In the bottom part the ratio of the two is shown.

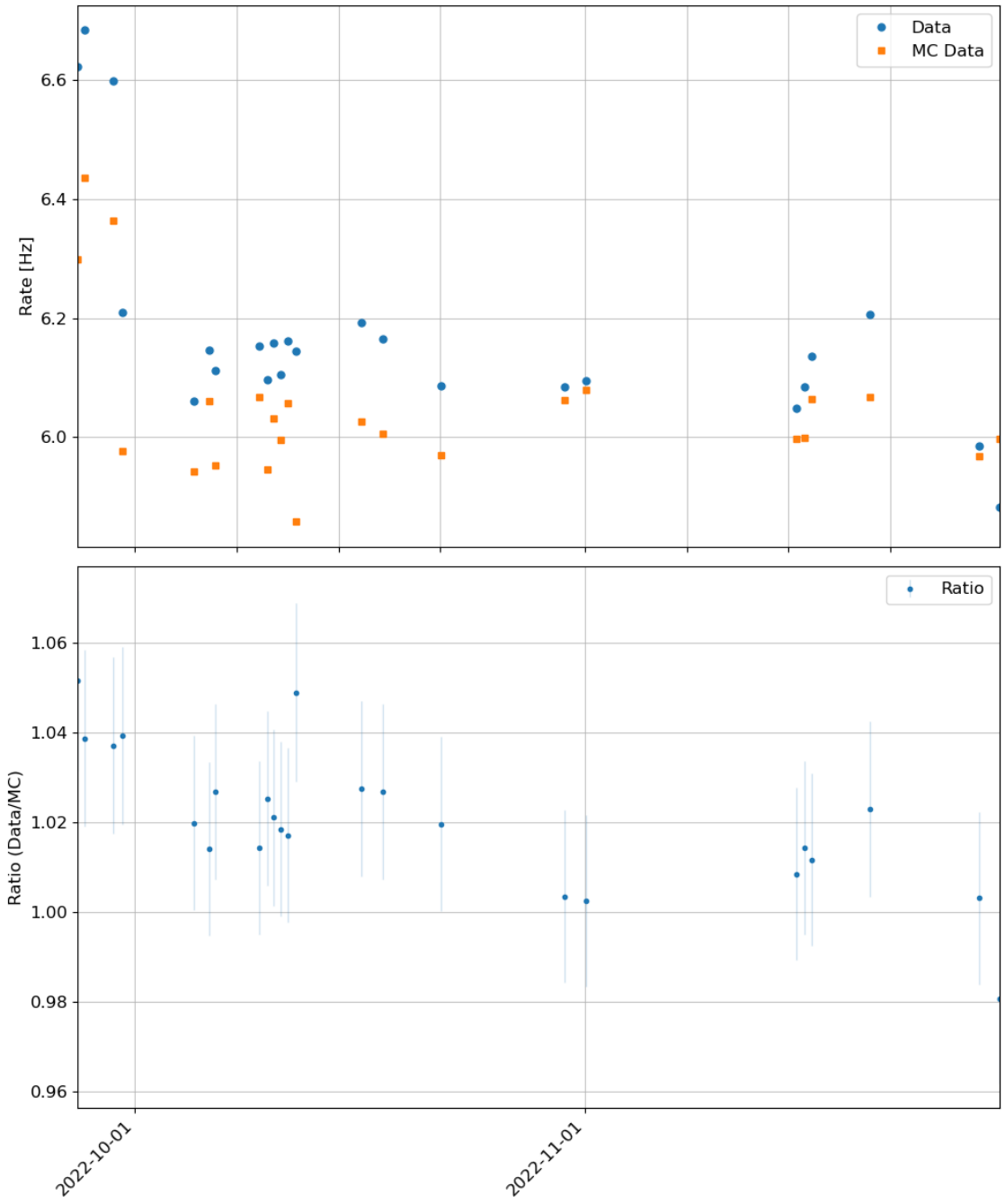

Figure A.80: Rate and ratio per 60-minute window around temperature measurements for ORCA-11.1 after cuts are applied. In the top part the count rates of the data and the Monte Carlo simulation are shown. In the bottom part the ratio of the two is shown.

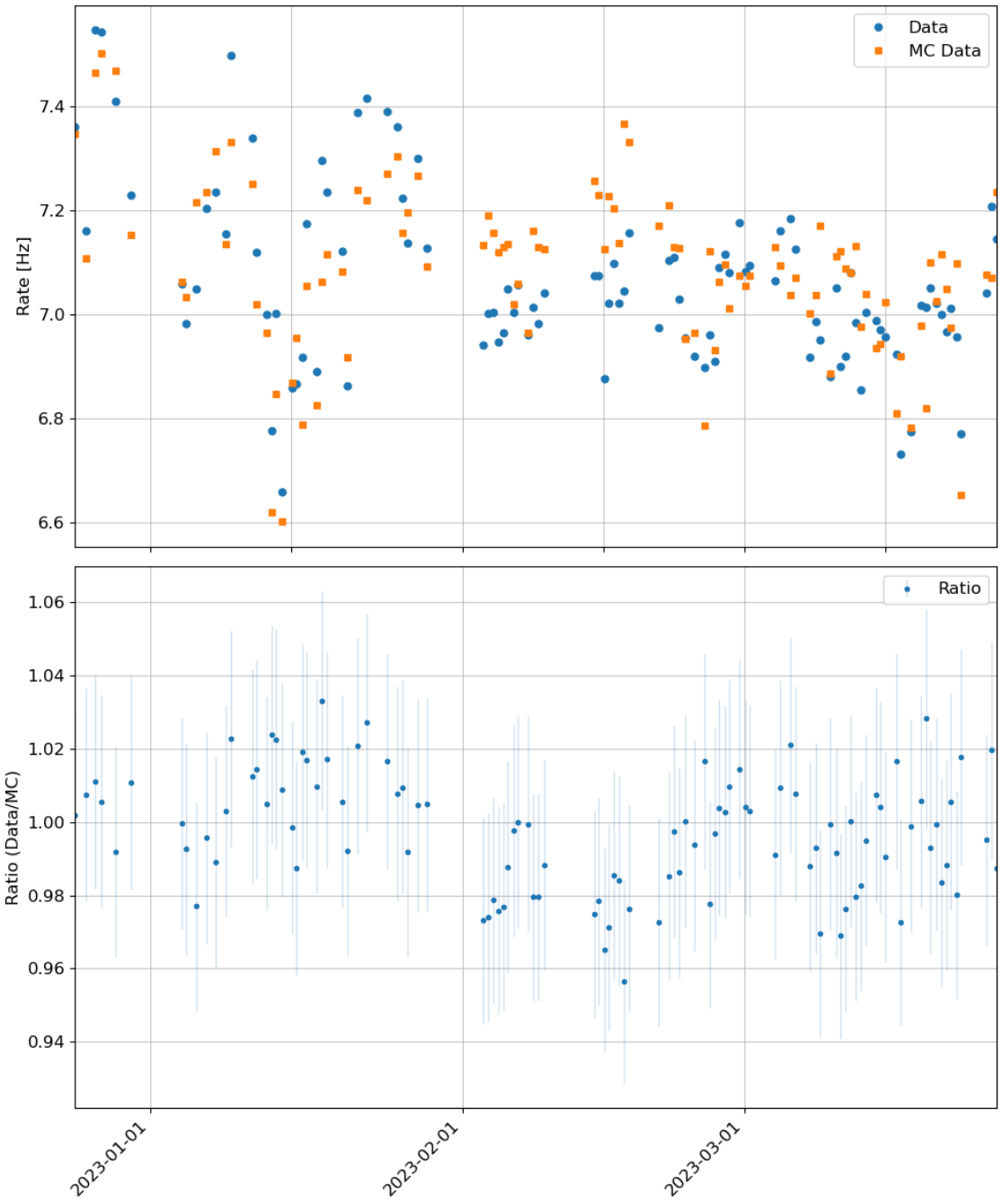

Figure A.81: Rate and ratio per 60-minute window around temperature measurements for ORCA-15 after cuts are applied. In the top part the count rates of the data and the Monte Carlo simulation are shown. In the bottom part the ratio of the two is shown.

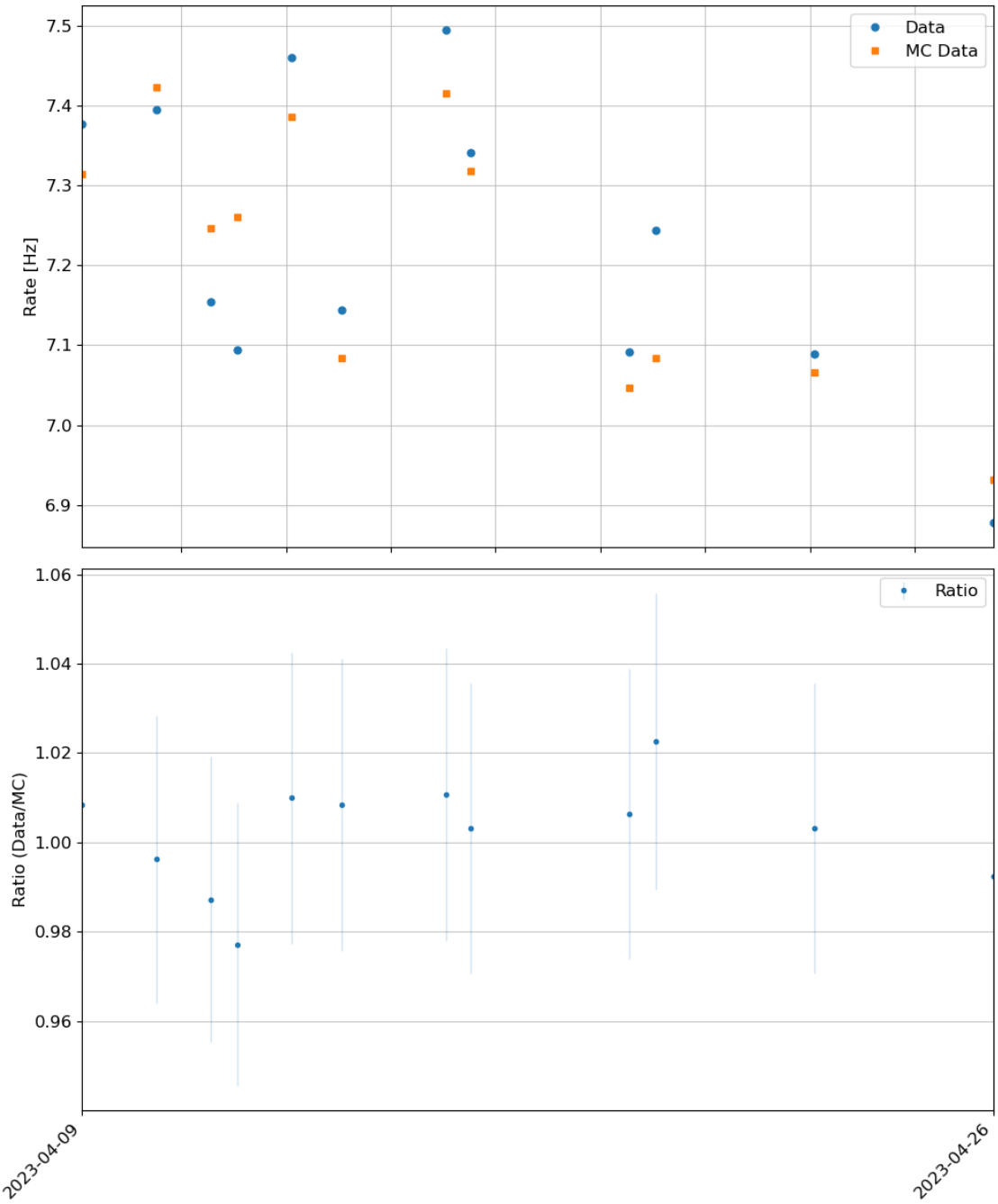

Figure A.82: Rate and ratio per 60-minute window around temperature measurements for ORCA-15.1 after cuts are applied. In the top part the count rates of the data and the Monte Carlo simulation are shown. In the bottom part the ratio of the two is shown.

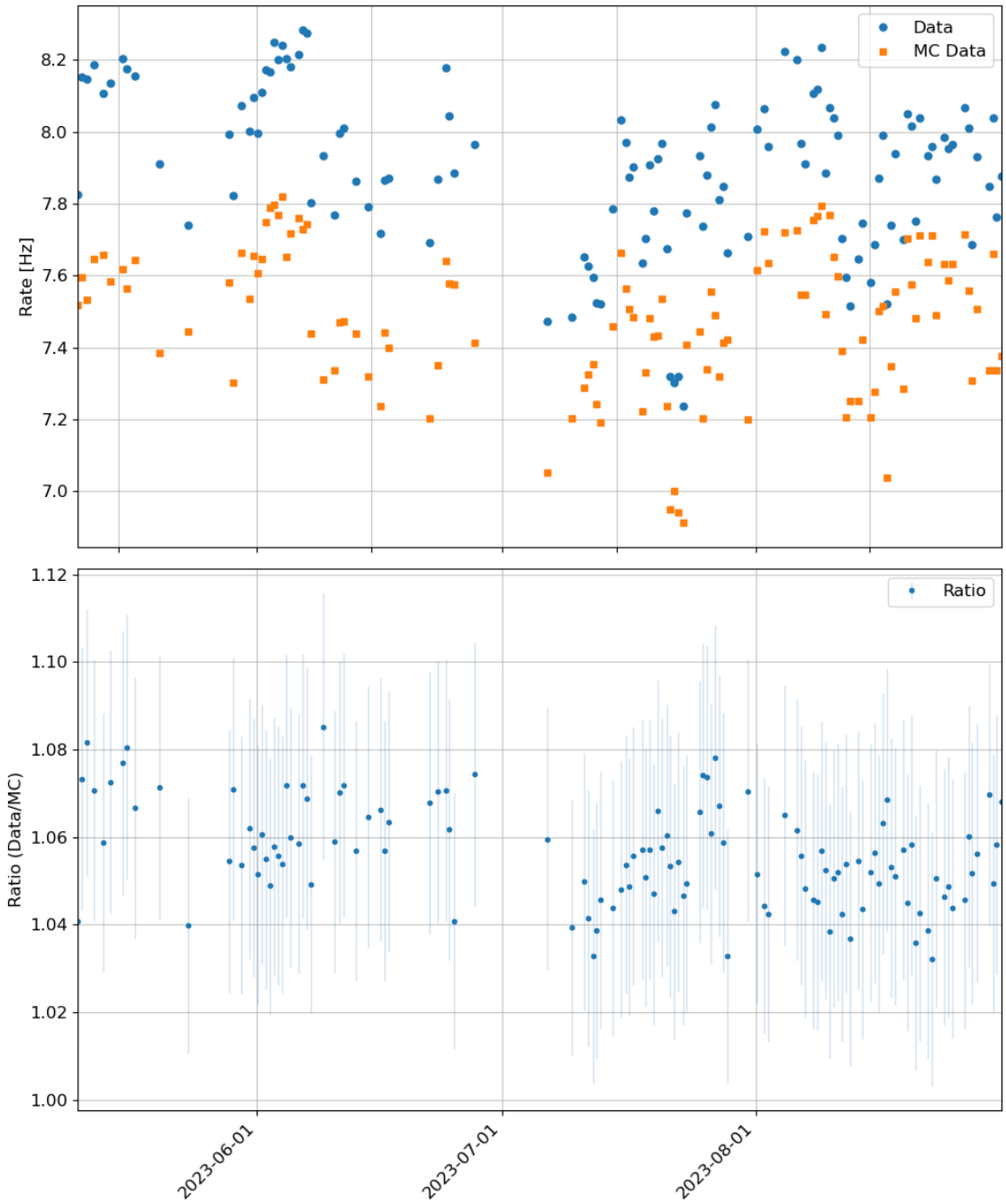

Figure A.83: Rate and ratio per 60-minute window around temperature measurements for ORCA-18 after cuts are applied. In the top part the count rates of the data and the Monte Carlo simulation are shown. In the bottom part the ratio of the two is shown.

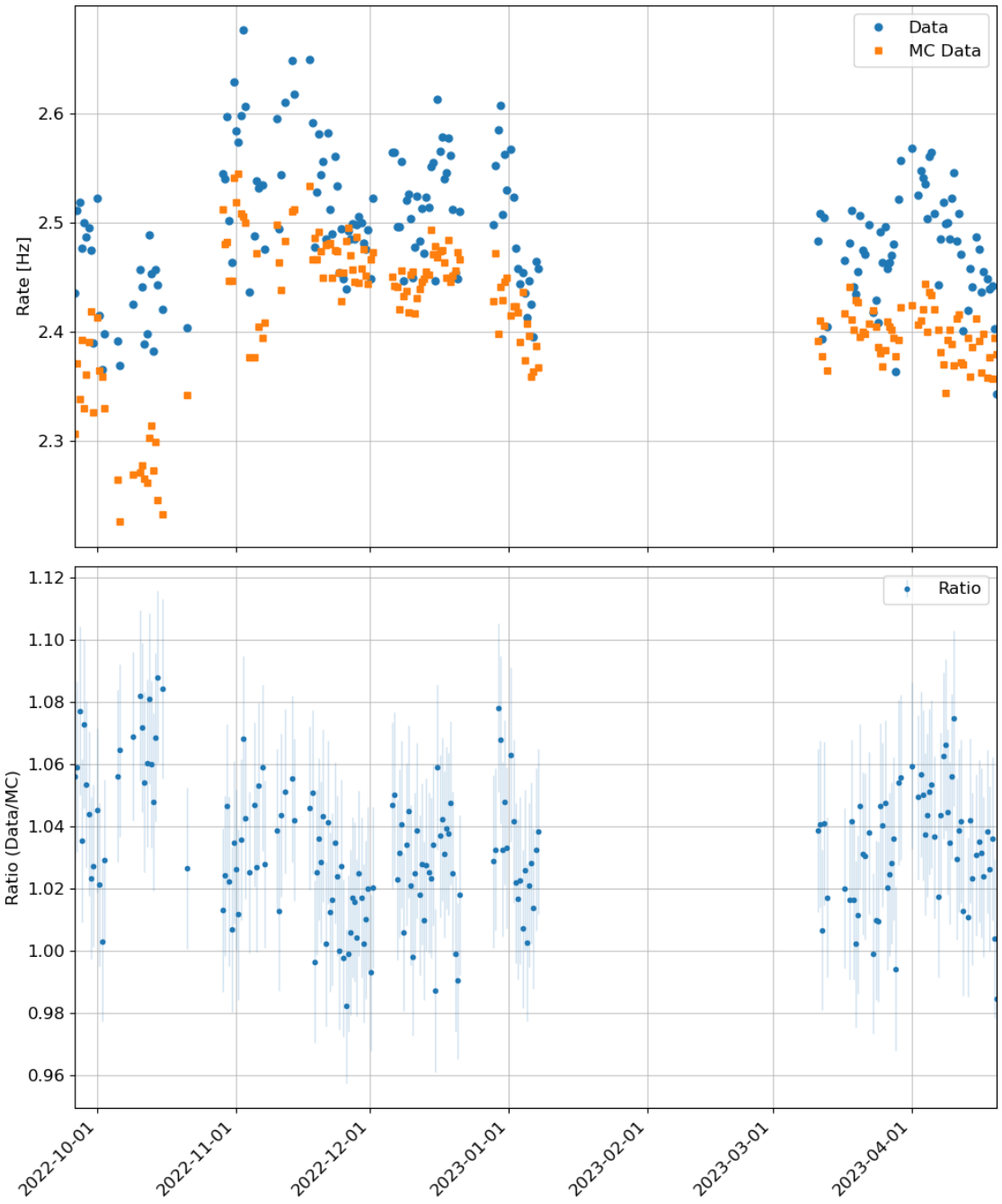

Figure A.84: Rate and ratio per 60-minute window around temperature measurements for ARCA-21 after cuts are applied. In the top part the count rates of the data and the Monte Carlo simulation are shown. In the bottom part the ratio of the two is shown.

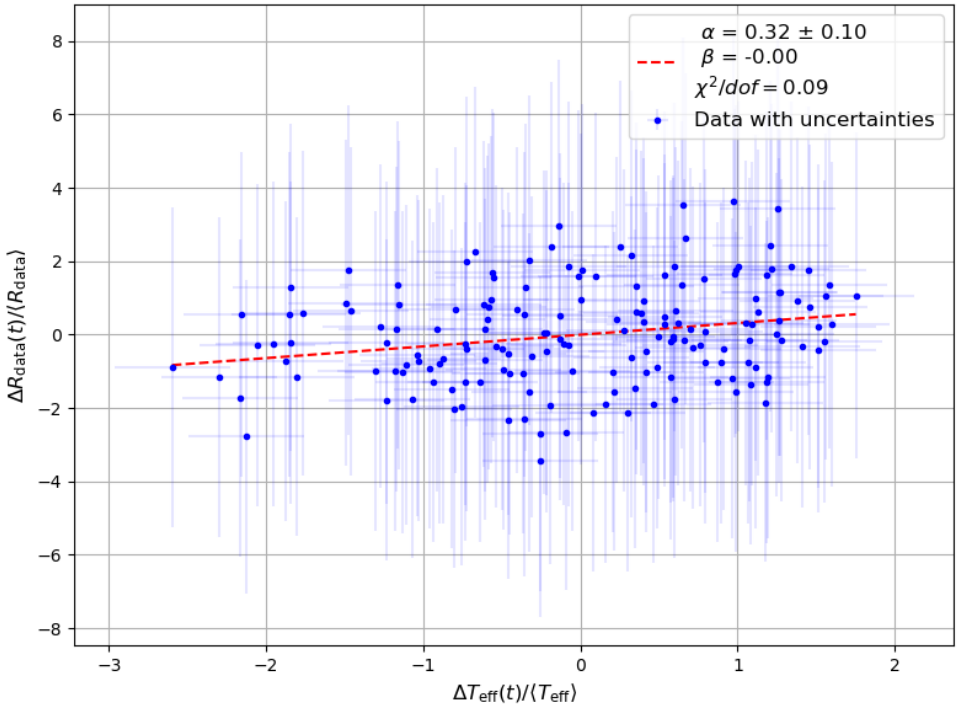

Figure A.85: Normalised effective temperature T_{eff} and ratio without detrending R_{data} of ORCA-10 showing the relative variation in percentage. The ratios are calculated in 60-minute windows around temperature measurements. The red line is a fit of the model in Equation 6.11. The errors are taken into account in the fit.

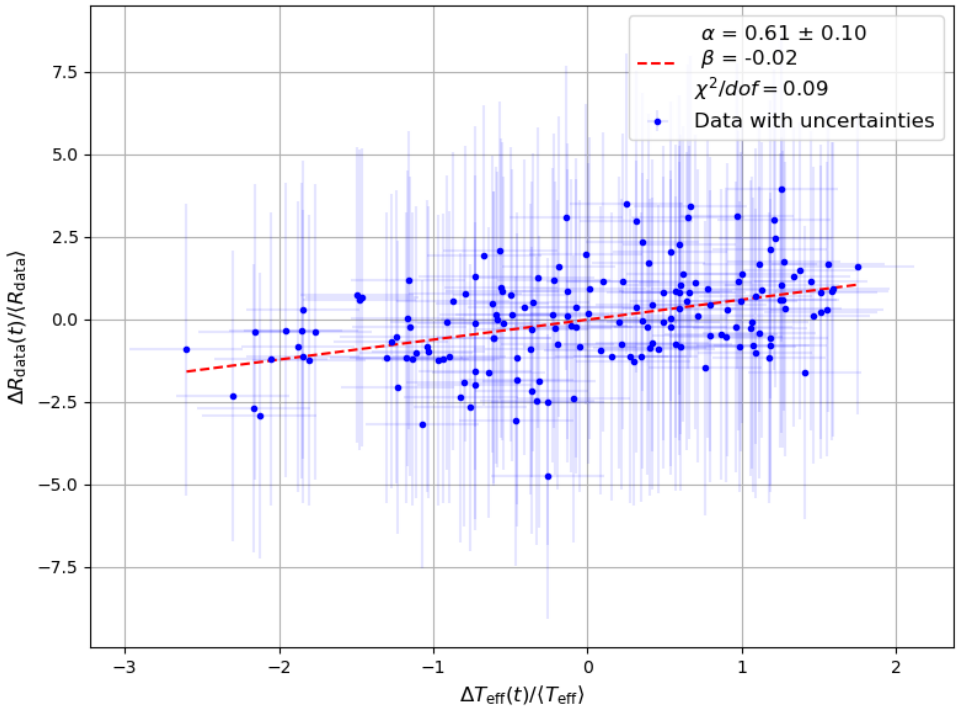

Figure A.86: Normalised effective temperature T_{eff} and ratio with detrending R_{data} of ORCA-10 showing the relative variation in percentage. The ratios are calculated in 60-minute windows around temperature measurements.The red line is a fit of the model in Equation 6.11. The errors are taken into account in the fit.

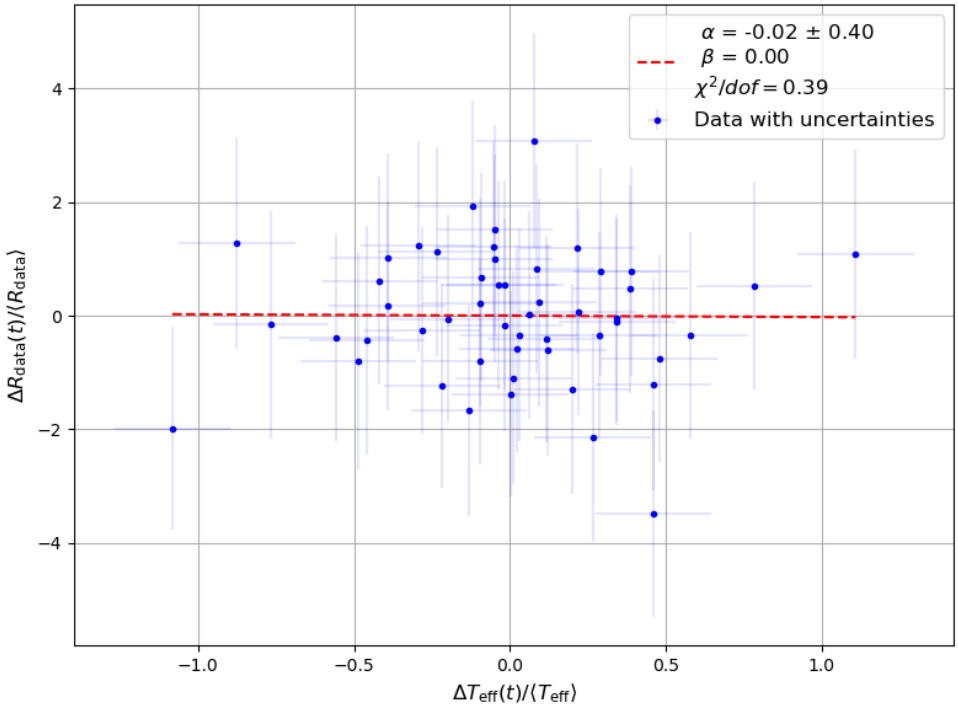

Figure A.87: Normalised effective temperature T_{eff} and ratio without detrending R_{data} of ORCA-11 showing the relative variation in percentage. The ratios are calculated in 60-minute windows around temperature measurements. The red line is a fit of the model in Equation 6.11. The errors are taken into account in the fit.

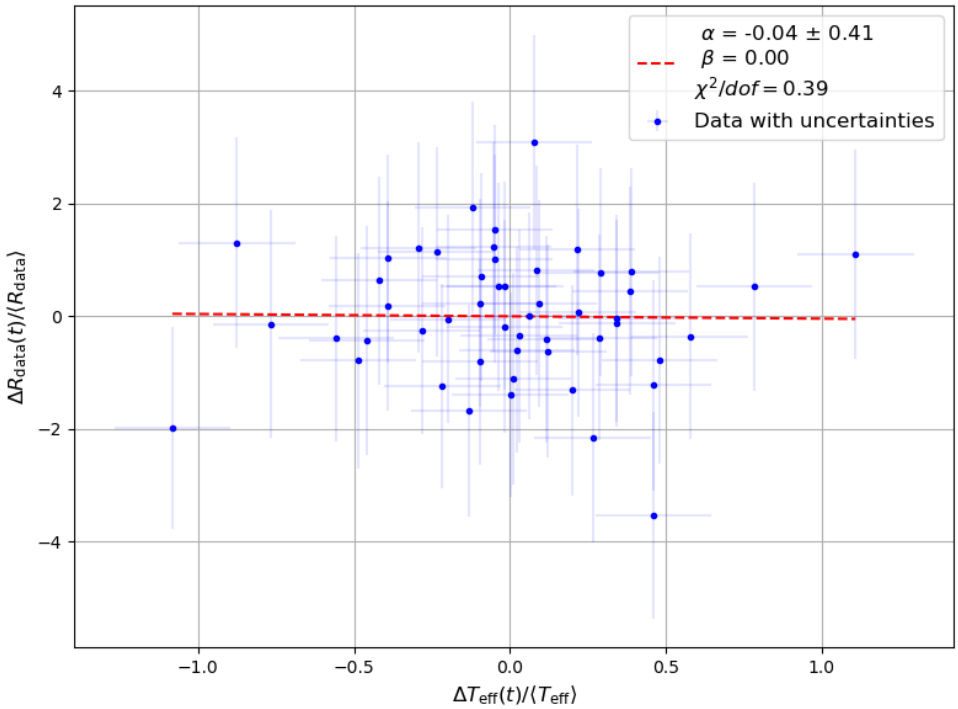

Figure A.88: Normalised effective temperature T_{eff} and ratio with detrending R_{data} of ORCA-11 showing the relative variation in percentage. The ratios are calculated in 60-minute windows around temperature measurements.The red line is a fit of the model in Equation 6.11. The errors are taken into account in the fit.

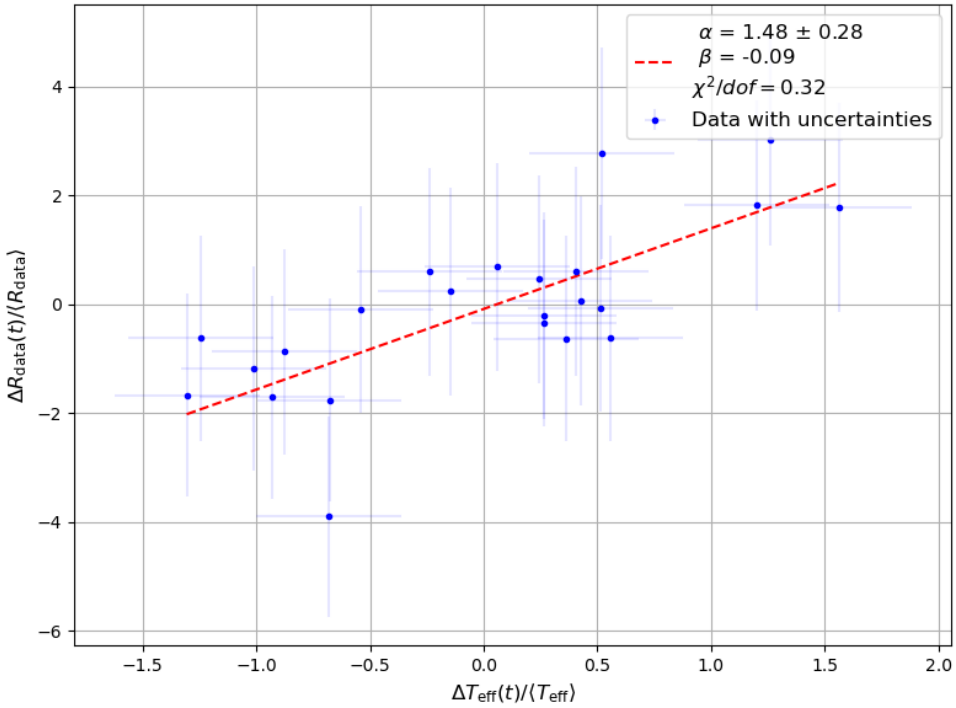

Figure A.89: Normalised effective temperature T_{eff} and ratio without detrending R_{data} of ORCA-11.1 showing the relative variation in percentage. The ratios are calculated in 60-minute windows around temperature measurements. The red line is a fit of the model in Equation 6.11. The errors are taken into account in the fit.

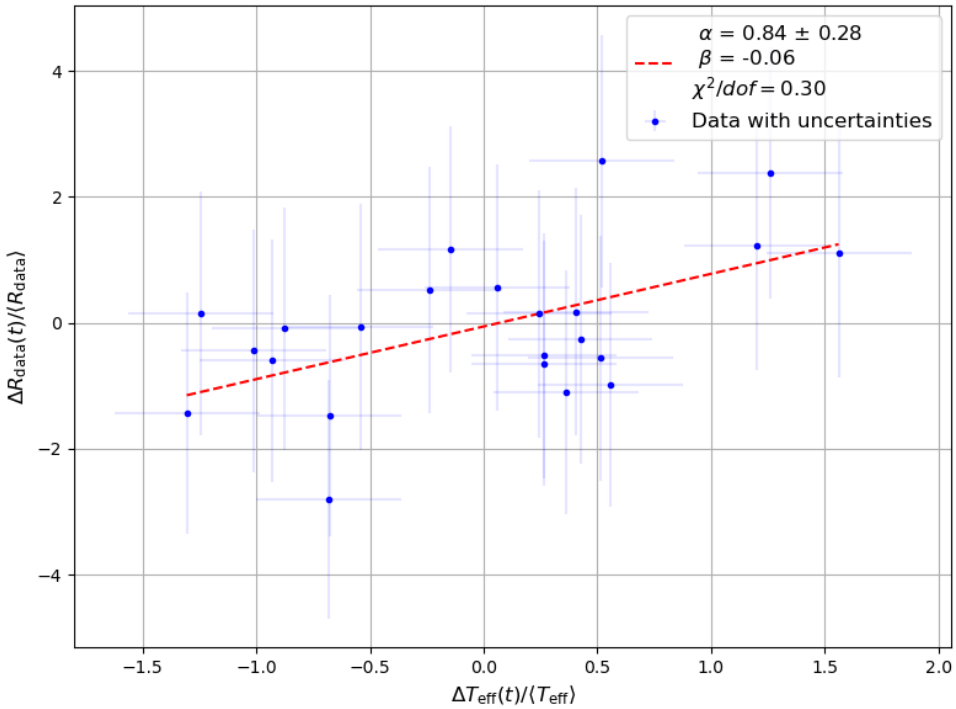

Figure A.90: Normalised effective temperature T_{eff} and ratio with detrending R_{data} of ORCA-11.1 showing the relative variation in percentage. The ratios are calculated in 60-minute windows around temperature measurements.The red line is a fit of the model in Equation 6.11. The errors are taken into account in the fit.

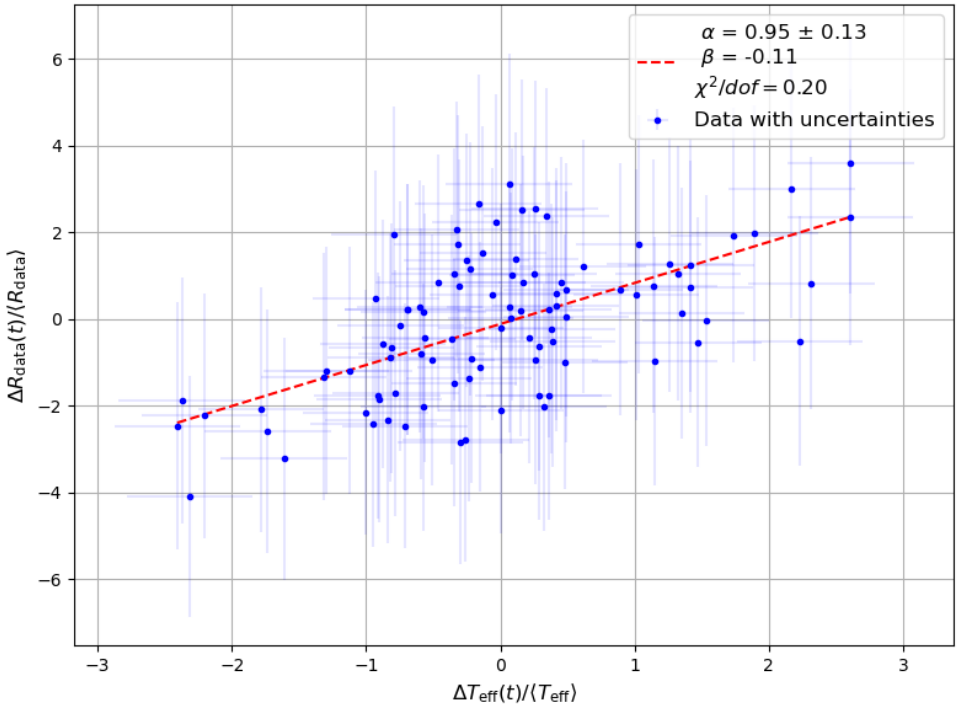

Figure A.91: Normalised effective temperature T_{eff} and ratio without detrending R_{data} of ORCA-15 showing the relative variation in percentage. The ratios are calculated in 60-minute windows around temperature measurements. The red line is a fit of the model in Equation 6.11. The errors are taken into account in the fit.

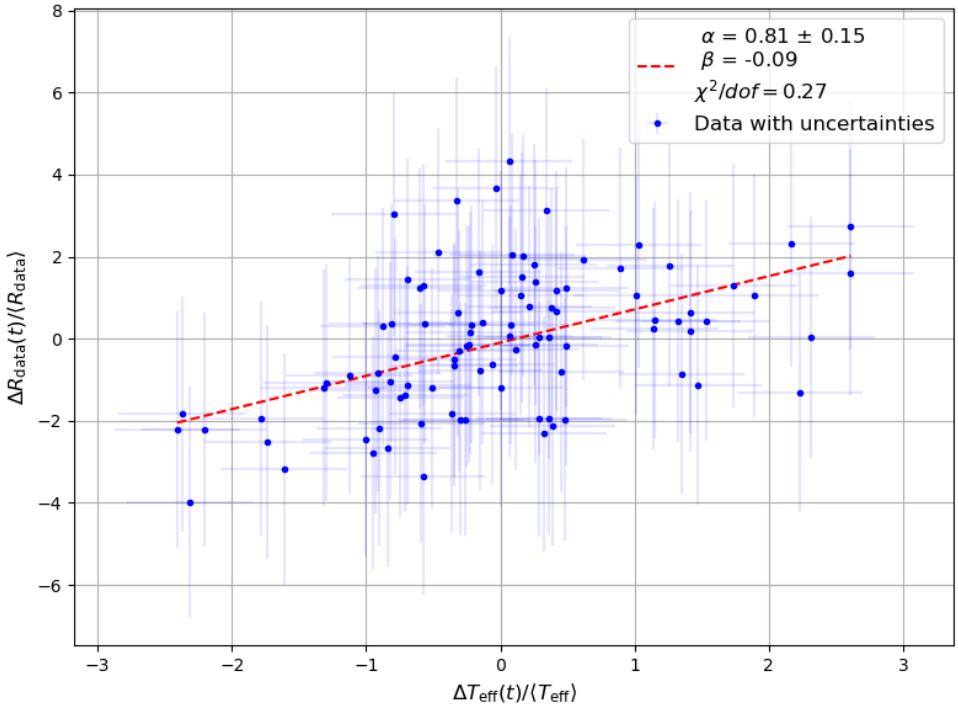

Figure A.92: Normalised effective temperature T_{eff} and ratio with detrending R_{data} of ORCA-15 showing the relative variation in percentage. The ratios are calculated in 60-minute windows around temperature measurements.The red line is a fit of the model in Equation 6.11. The errors are taken into account in the fit.

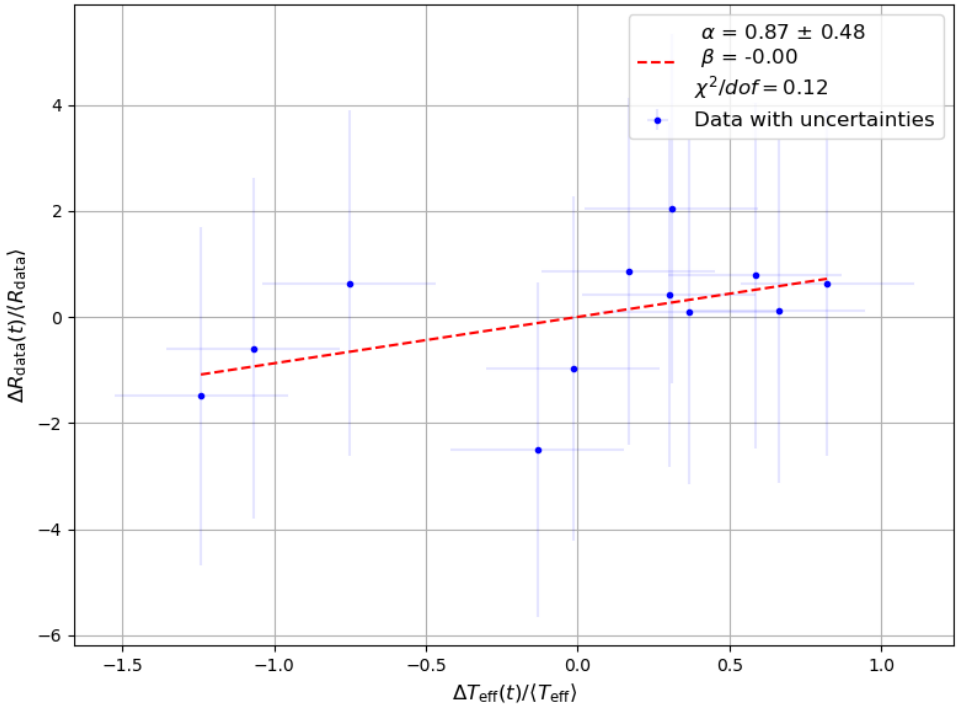

Figure A.93: Normalised effective temperature T_{eff} and ratio without detrending R_{data} of ORCA-15.1 showing the relative variation in percentage. The ratios are calculated in 60-minute windows around temperature measurements. The red line is a fit of the model in Equation 6.11. The errors are taken into account in the fit.

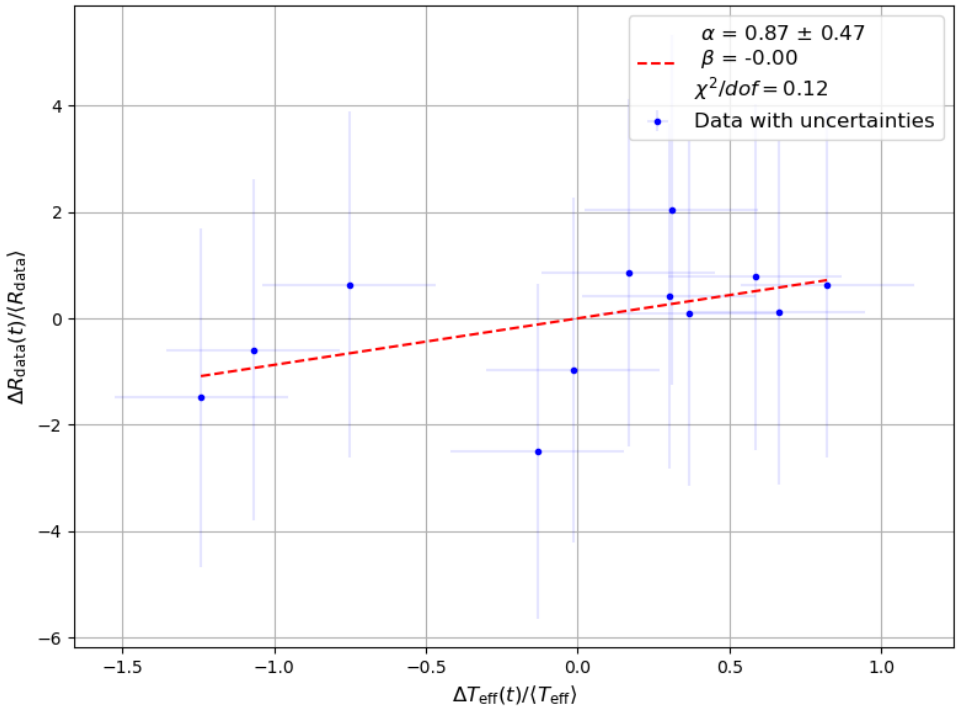

Figure A.94: Normalised effective temperature T_{eff} and ratio with detrending R_{data} of ORCA-15.1 showing the relative variation in percentage. The ratios are calculated in 60-minute windows around temperature measurements.The red line is a fit of the model in Equation 6.11. The errors are taken into account in the fit.

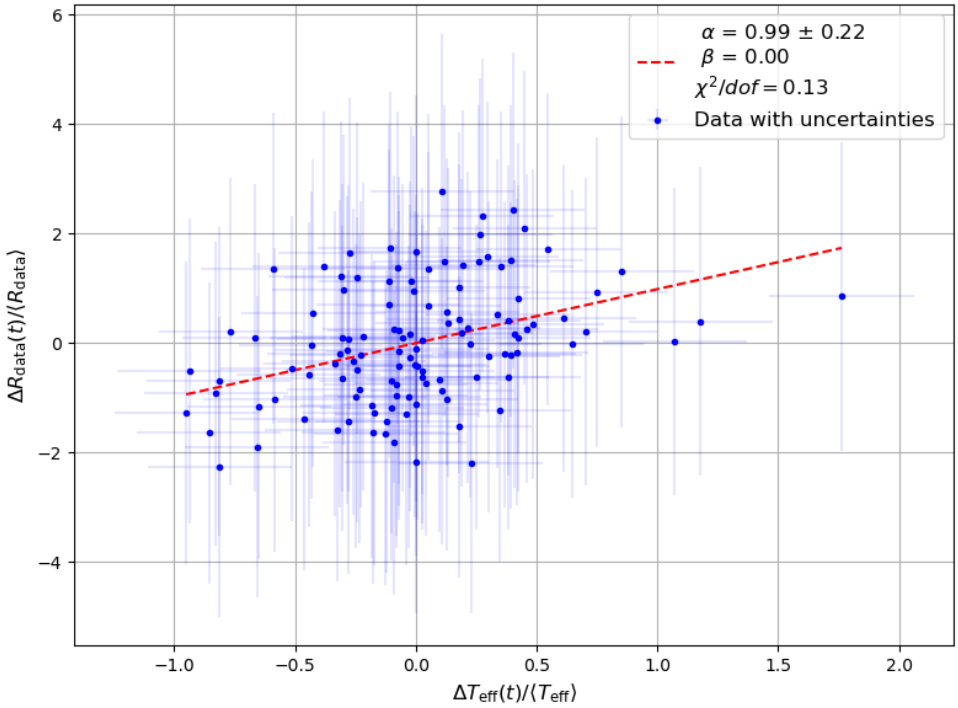

Figure A.95: Normalised effective temperature T_{eff} and ratio without detrending R_{data} of ORCA-18 showing the relative variation in percentage. The ratios are calculated in 60-minute windows around temperature measurements. The red line is a fit of the model in Equation 6.11. The errors are taken into account in the fit.

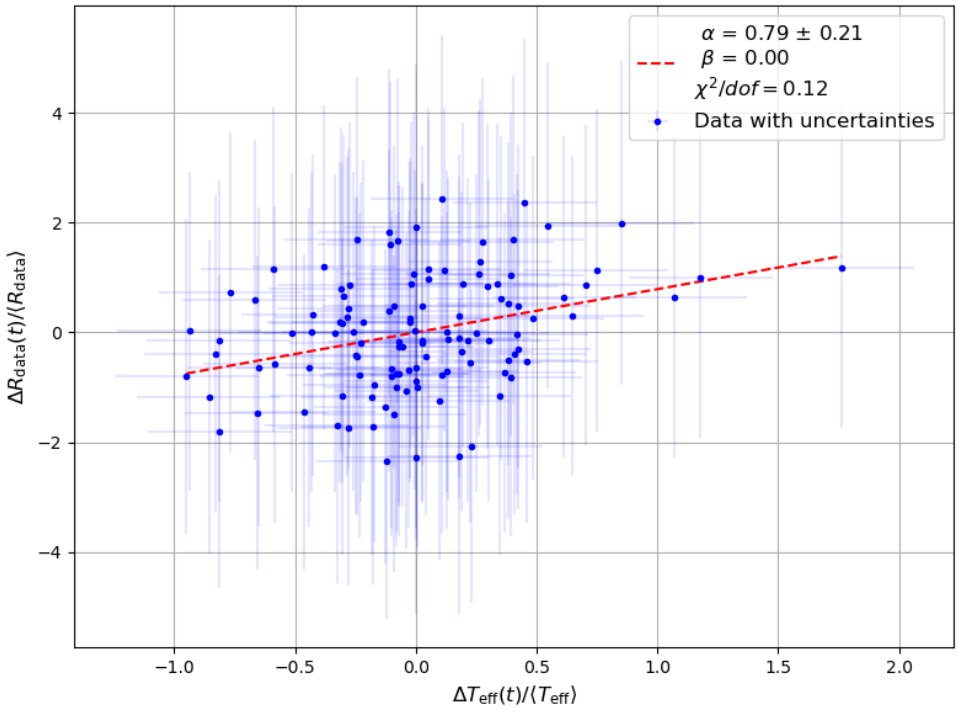

Figure A.96: Normalised effective temperature T_{eff} and ratio with detrending R_{data} of ORCA-18 showing the relative variation in percentage. The ratios are calculated in 60-minute windows around temperature measurements.The red line is a fit of the model in Equation 6.11. The errors are taken into account in the fit.

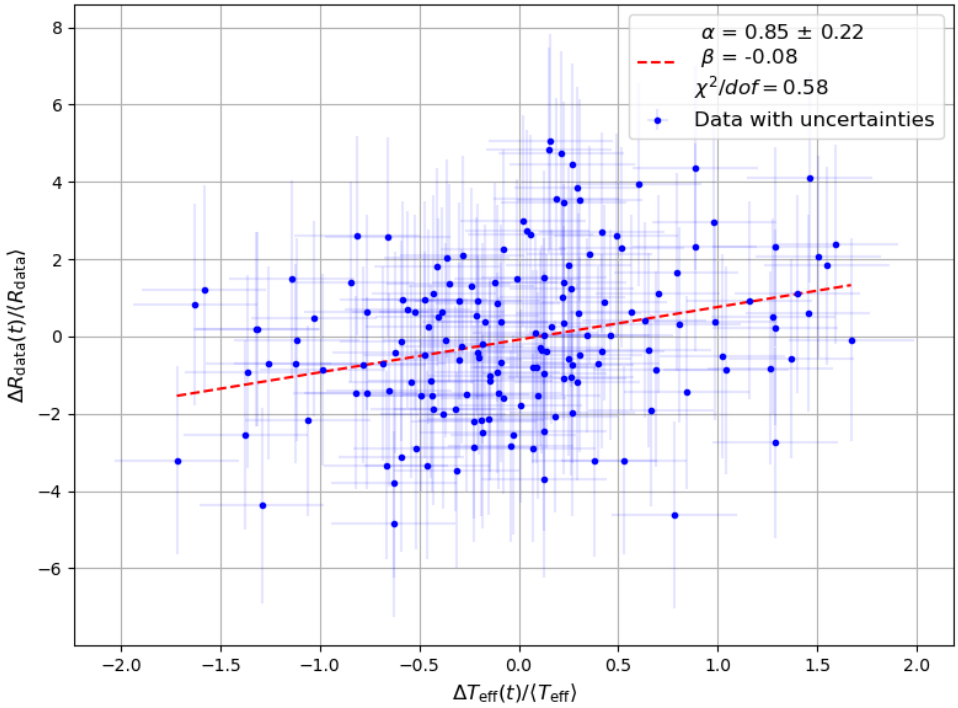

Figure A.97: Normalised effective temperature T_{eff} and ratio without detrending R_{data} of ARCA-21 showing the relative variation in percentage. The ratios are calculated in 60-minute windows around temperature measurements. The red line is a fit of the model in Equation 6.11. The errors are taken into account in the fit.

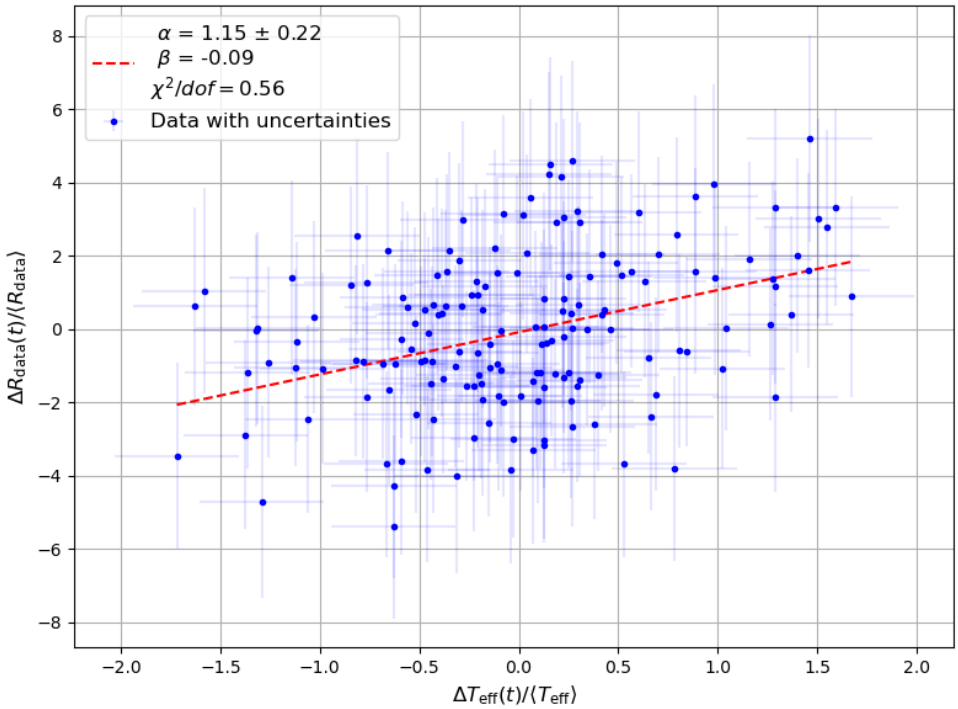

Figure A.98: Normalised effective temperature T_{eff} and ratio with detrending R_{data} of ARCA-21 showing the relative variation in percentage. The ratios are calculated in 60-minute windows around temperature measurements.The red line is a fit of the model in Equation 6.11. The errors are taken into account in the fit.

A.2. ERA5

A.2.1. 60-Minute Window Around Temperature Measurement

Figure A.99: Rate and ratio per 60-minute window around temperature measurements for ORCA-10 after cuts are applied. In the top part the count rates of the data and the Monte Carlo simulation are shown. In the bottom part the ratio of the two is shown.

Figure A.100: Rate and ratio per 60-minute window around temperature measurements for ORCA-11 after cuts are applied. In the top part the count rates of the data and the Monte Carlo simulation are shown. In the bottom part the ratio of the two is shown.

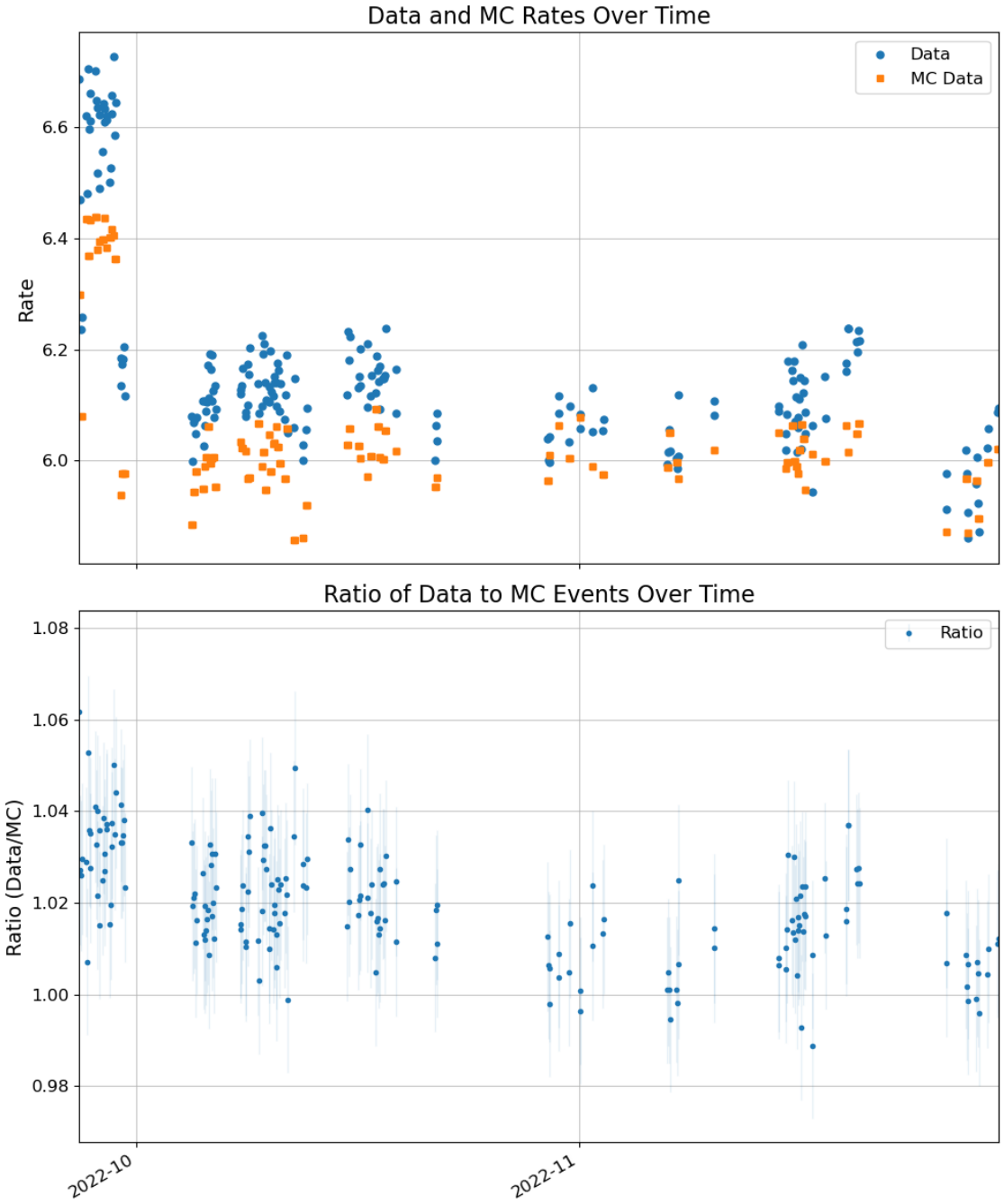

Figure A.101: Rate and ratio per 60-minute window around temperature measurements for ORCA-11.1 after cuts are applied. In the top part the count rates of the data and the Monte Carlo simulation are shown. In the bottom part the ratio of the two is shown.

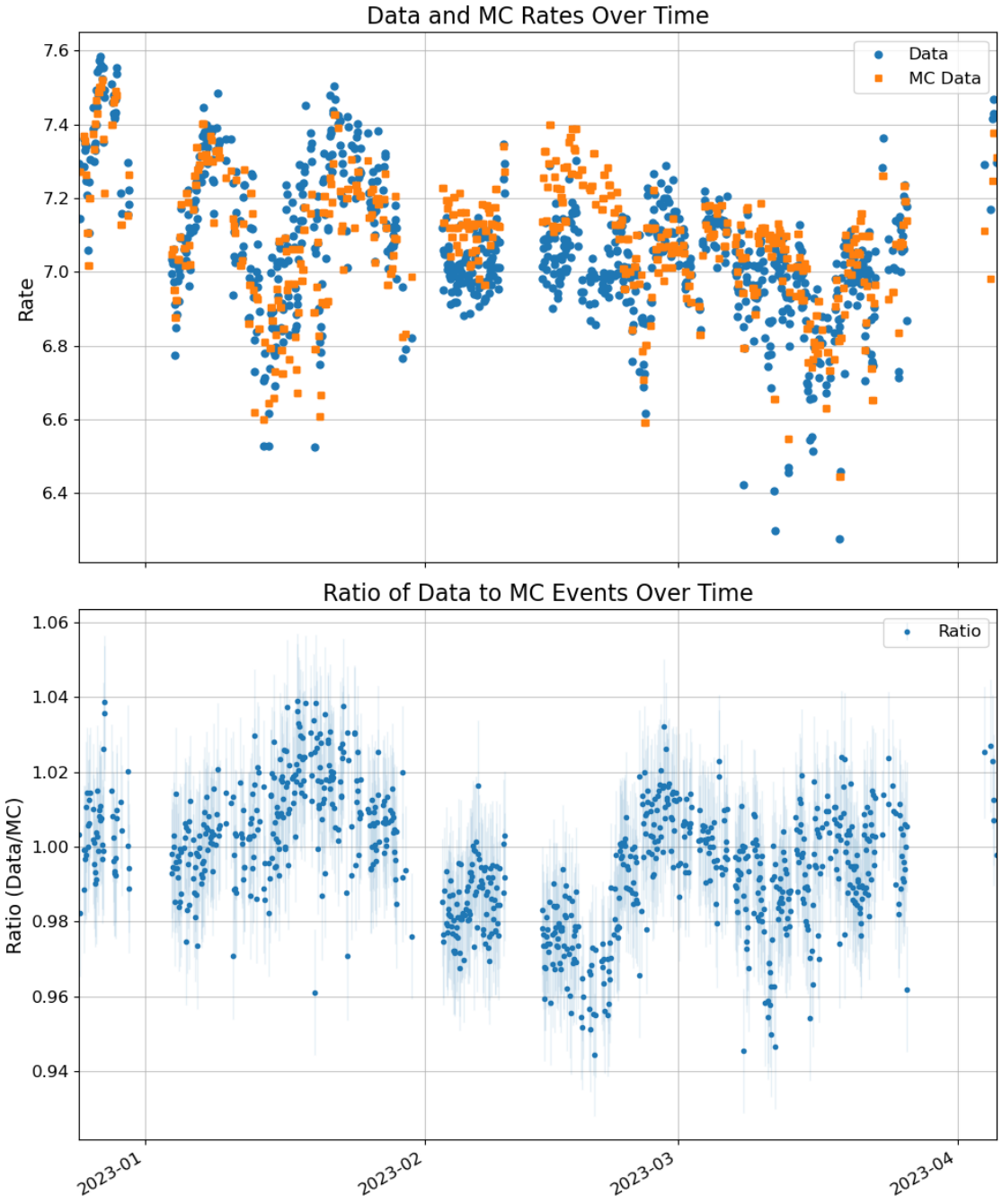

Figure A.102: Rate and ratio per 60-minute window around temperature measurements for ORCA-15 after cuts are applied. In the top part the count rates of the data and the Monte Carlo simulation are shown. In the bottom part the ratio of the two is shown.

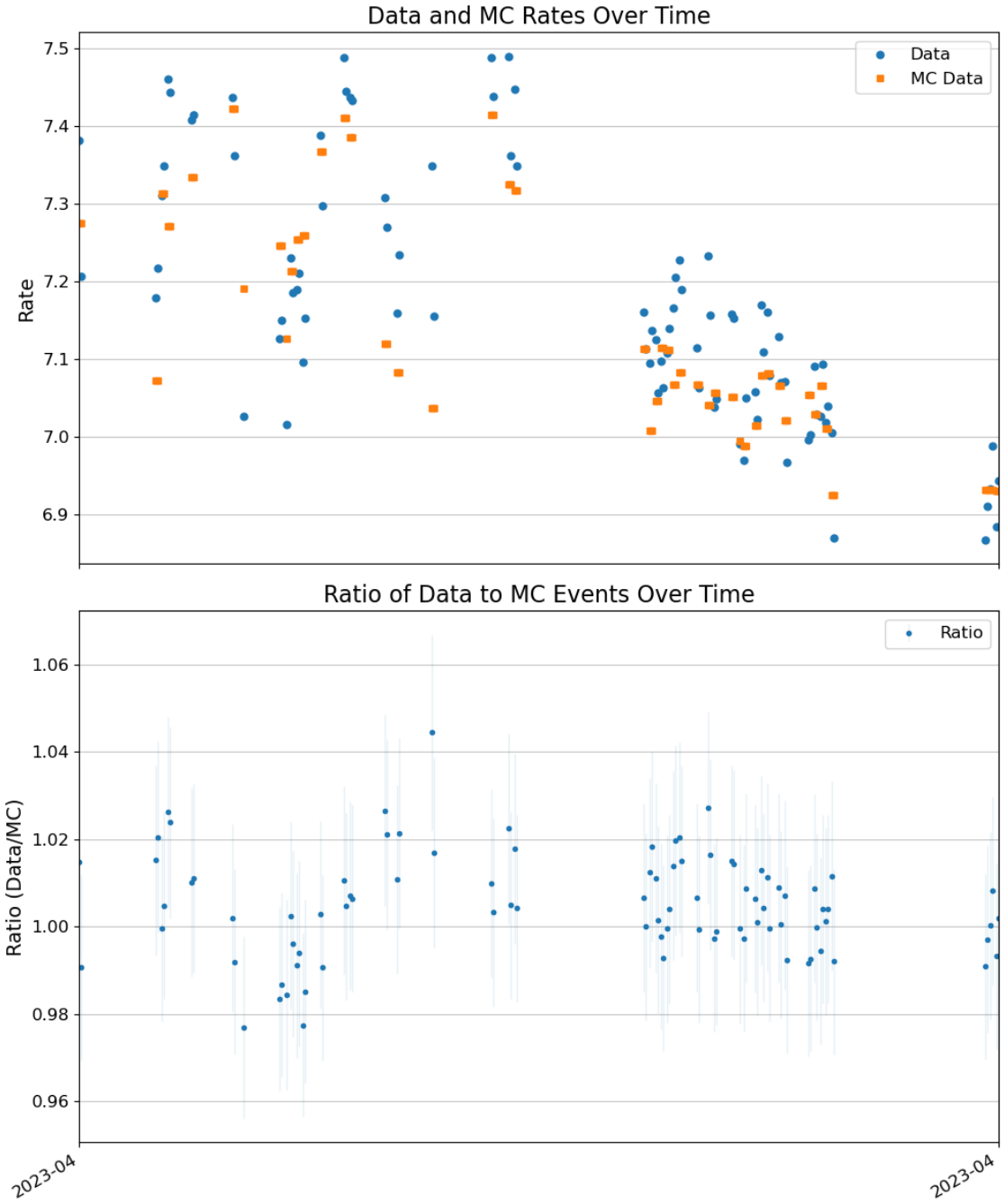

Figure A.103: Rate and ratio per 60-minute window around temperature measurements for ORCA-15.1 after cuts are applied. In the top part the count rates of the data and the Monte Carlo simulation are shown. In the bottom part the ratio of the two is shown.

Figure A.104: Rate and ratio per 60-minute window around temperature measurements for ORCA-18 after cuts are applied. In the top part the count rates of the data and the Monte Carlo simulation are shown. In the bottom part the ratio of the two is shown.

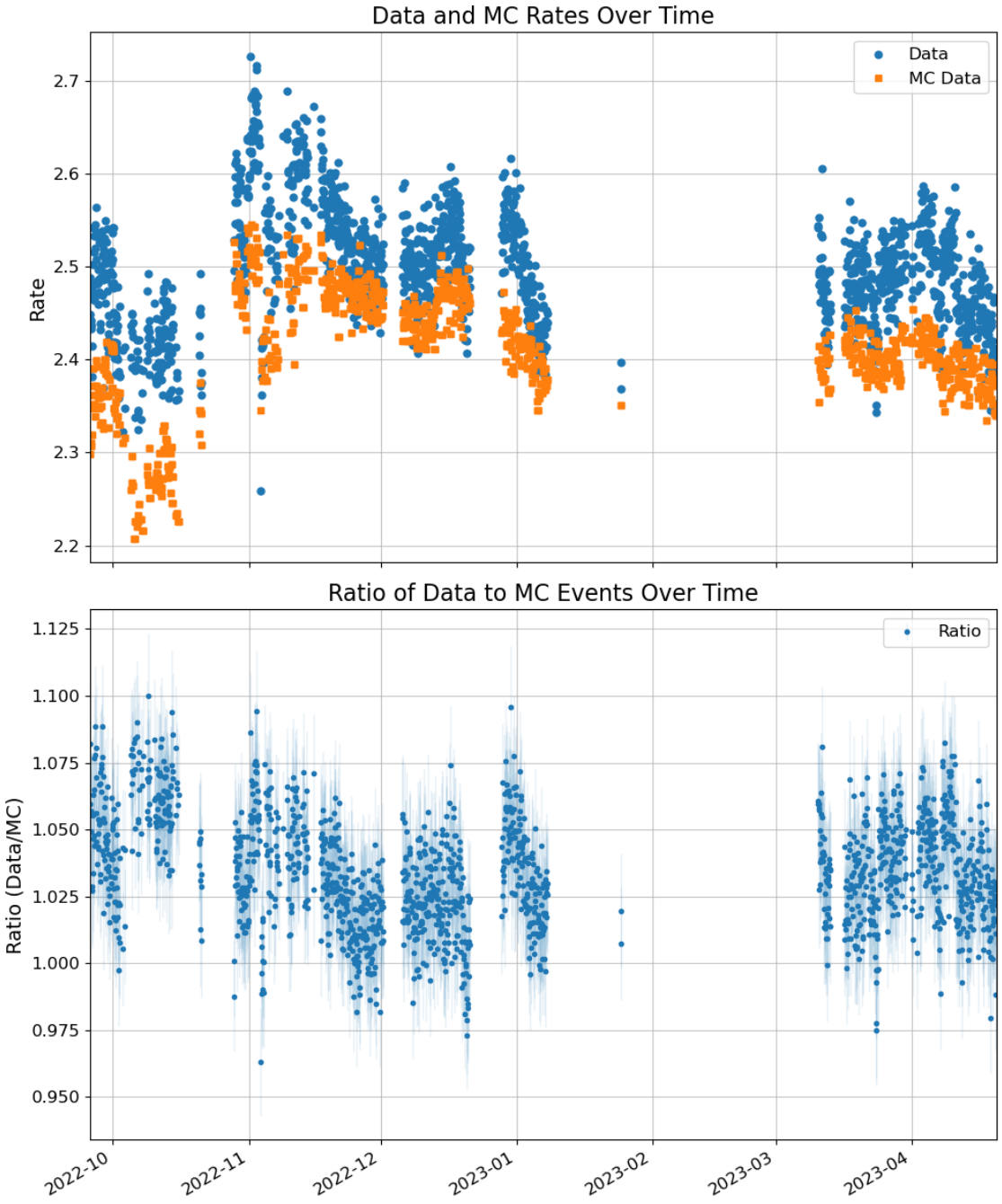

Figure A.105: Rate and ratio per 60-minute window around temperature measurements for ARCA-21 after cuts are applied. In the top part the count rates of the data and the Monte Carlo simulation are shown. In the bottom part the ratio of the two is shown.

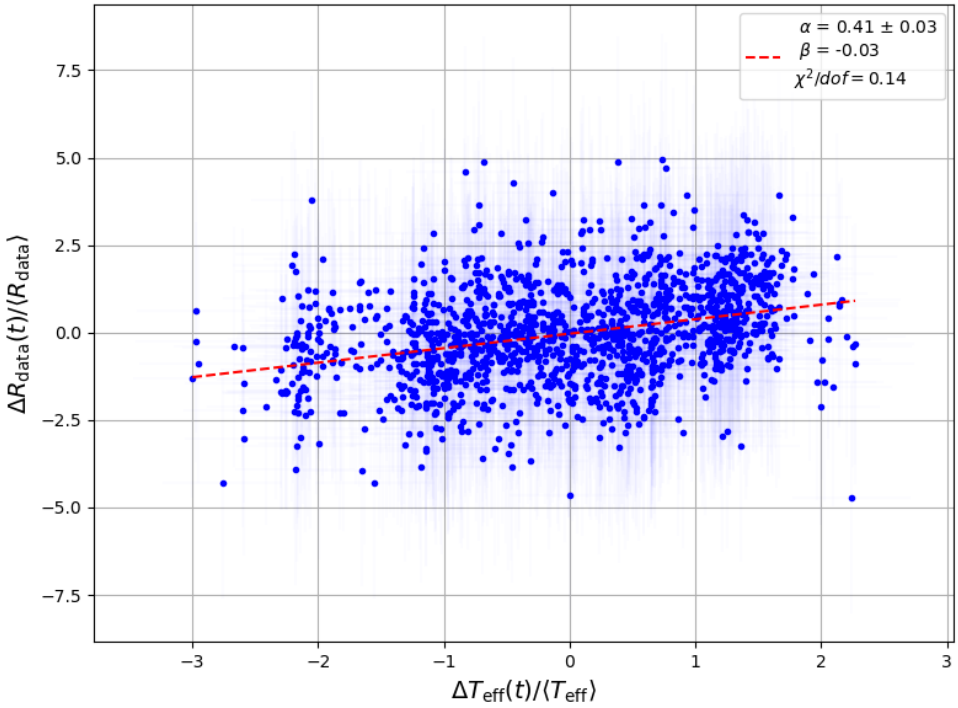

Figure A.106: Normalised effective temperature T_{eff} and ratio without detrending R_{data} of ORCA-10 showing the relative variation in percentage. The ratios are calculated in 60-minute windows around temperature measurements. The red line is a fit of the model in Equation 6.11. The errors are taken into account in the fit.

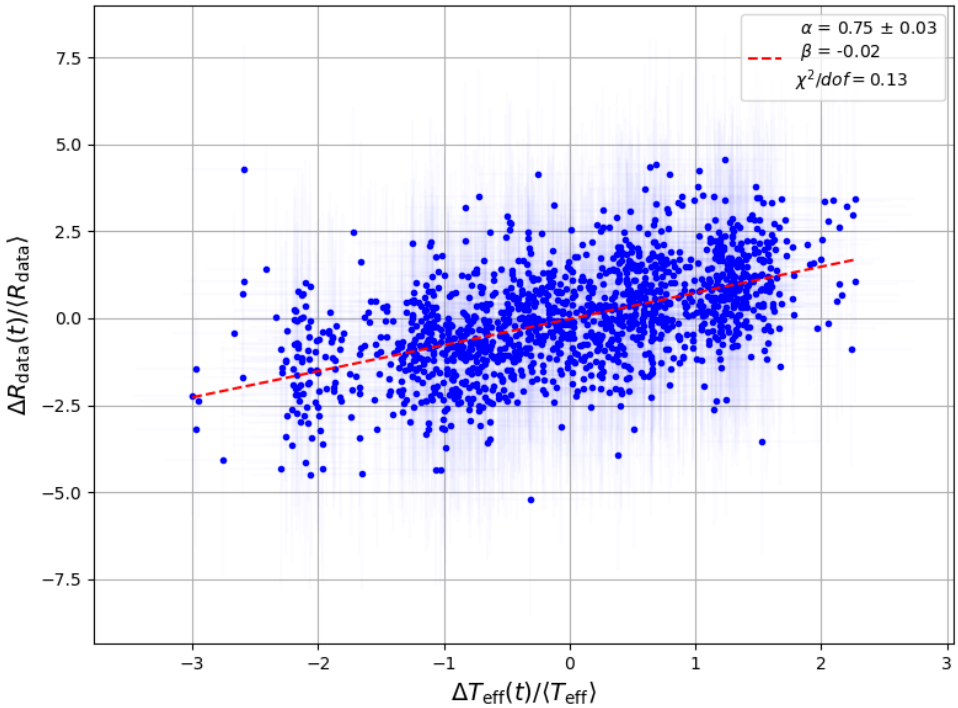

Figure A.107: Normalised effective temperature T_{eff} and ratio with detrending R_{data} of ORCA-10 showing the relative variation in percentage. The ratios are calculated in 60-minute windows around temperature measurements.The red line is a fit of the model in Equation 6.11. The errors are taken into account in the fit.

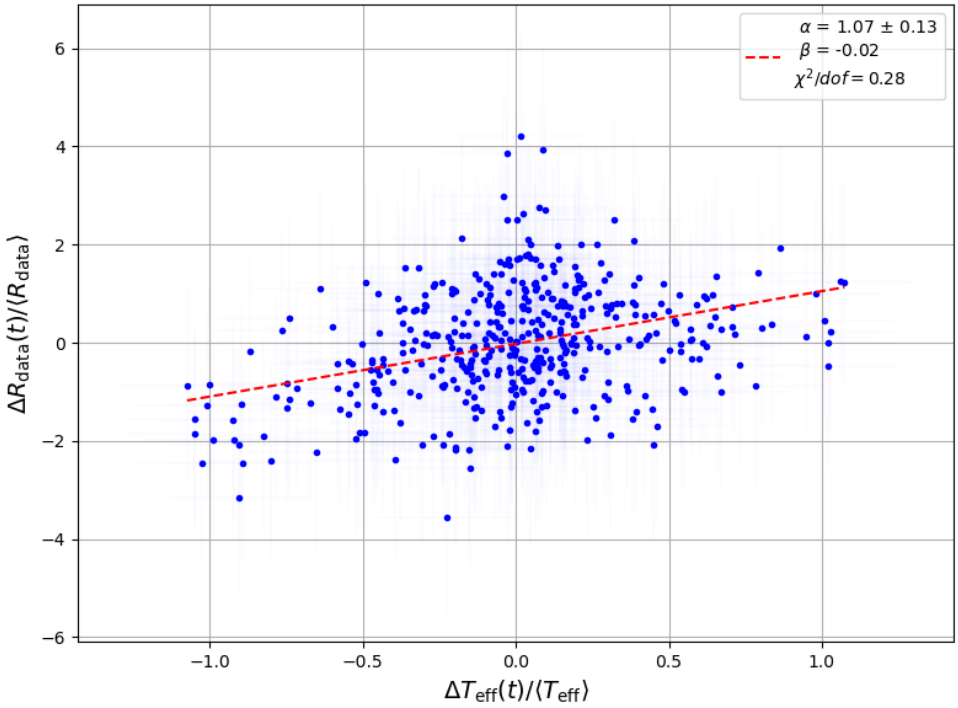

Figure A.108: Normalised effective temperature T_{eff} and ratio without detrending R_{data} of ORCA-11 showing the relative variation in percentage. The ratios are calculated in 60-minute windows around temperature measurements. The red line is a fit of the model in Equation 6.11. The errors are taken into account in the fit.

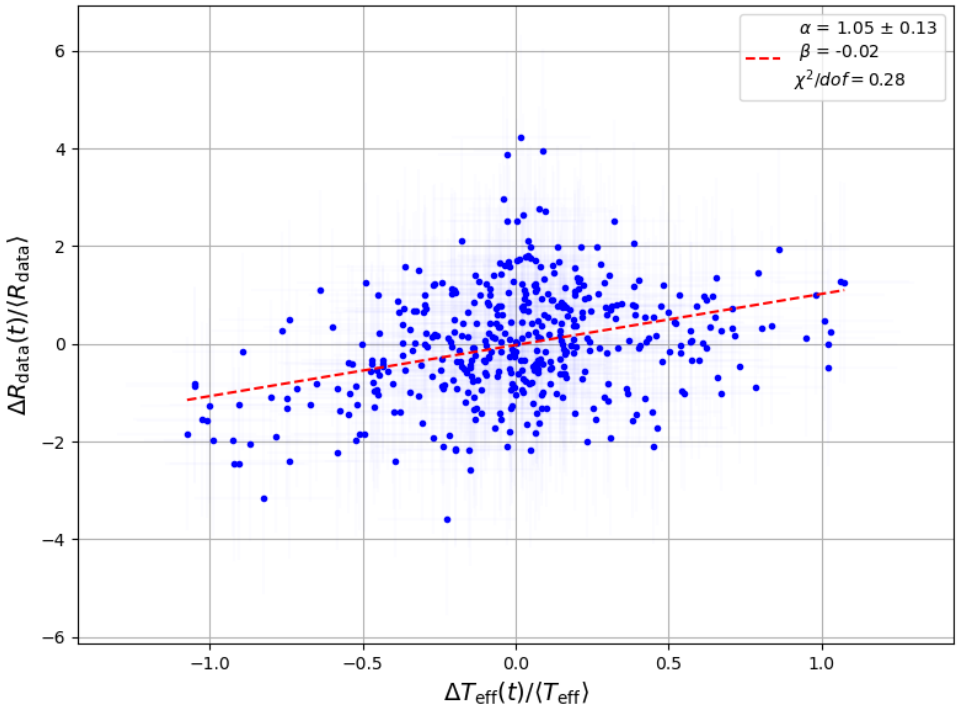

Figure A.109: Normalised effective temperature T_{eff} and ratio with detrending R_{data} of ORCA-11 showing the relative variation in percentage. The ratios are calculated in 60-minute windows around temperature measurements.The red line is a fit of the model in Equation 6.11. The errors are taken into account in the fit.

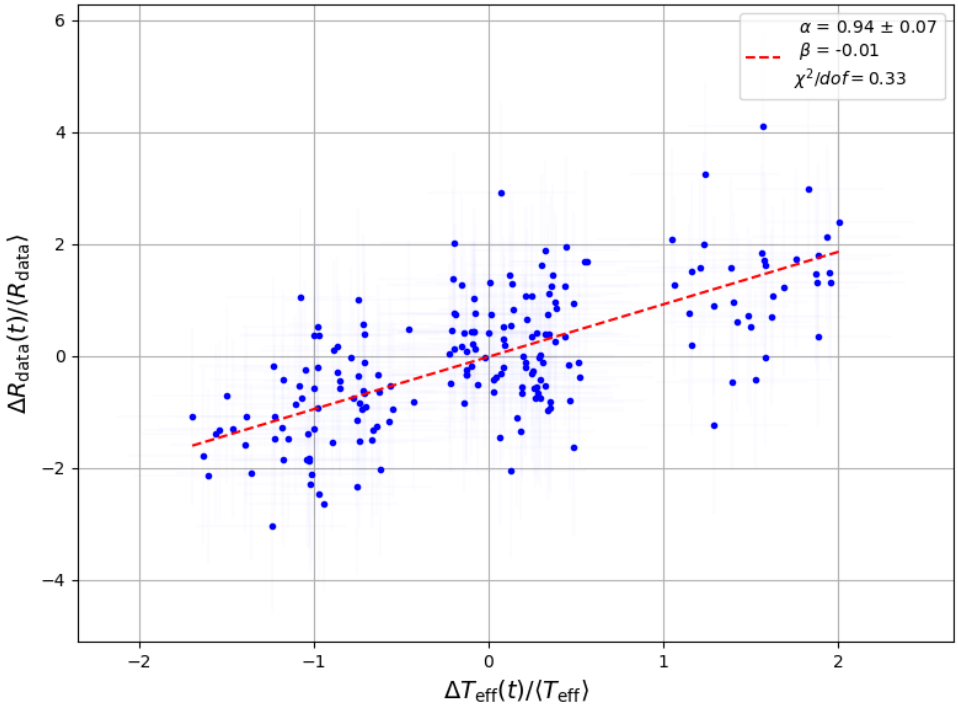

Figure A.110: Normalised effective temperature T_{eff} and ratio without detrending R_{data} of ORCA-11.1 showing the relative variation in percentage. The ratios are calculated in 60-minute windows around temperature measurements. The red line is a fit of the model in Equation 6.11. The errors are taken into account in the fit.

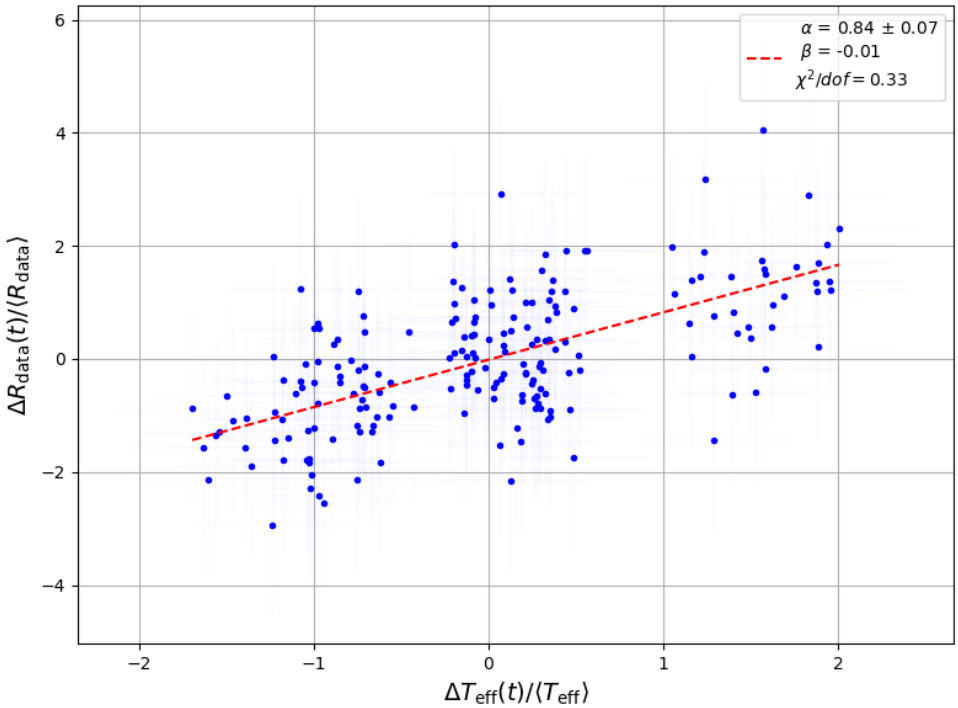

Figure A.111: Normalised effective temperature T_{eff} and ratio with detrending R_{data} of ORCA-11.1 showing the relative variation in percentage. The ratios are calculated in 60-minute windows around temperature measurements.The red line is a fit of the model in Equation 6.11. The errors are taken into account in the fit.

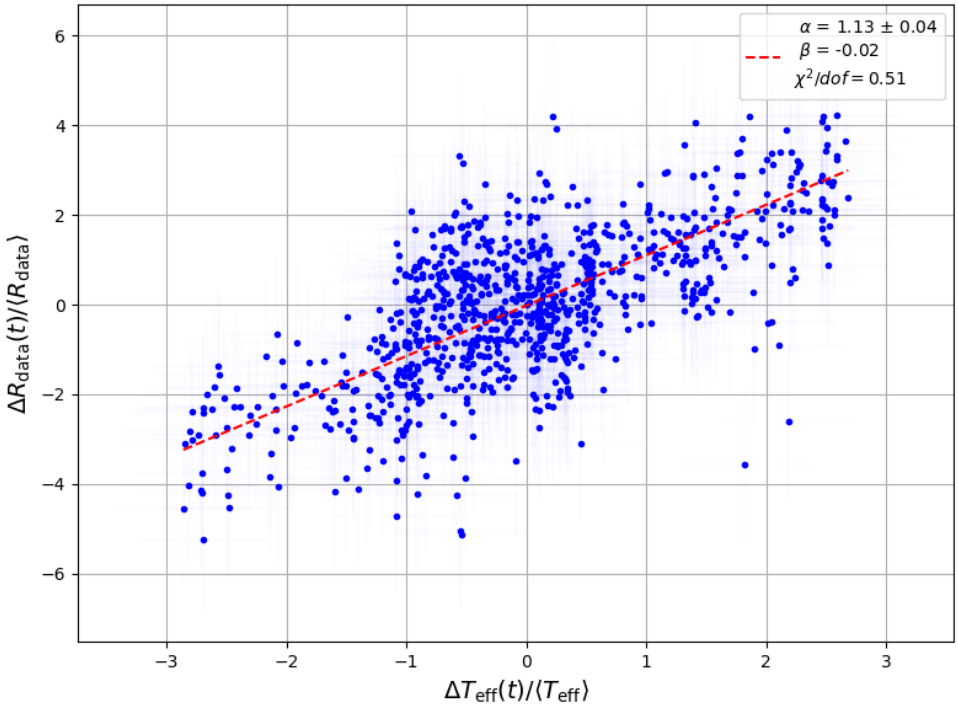

Figure A.112: Normalised effective temperature T_{eff} and ratio without detrending R_{data} of ORCA-15 showing the relative variation in percentage. The ratios are calculated in 60-minute windows around temperature measurements. The red line is a fit of the model in Equation 6.11. The errors are taken into account in the fit.

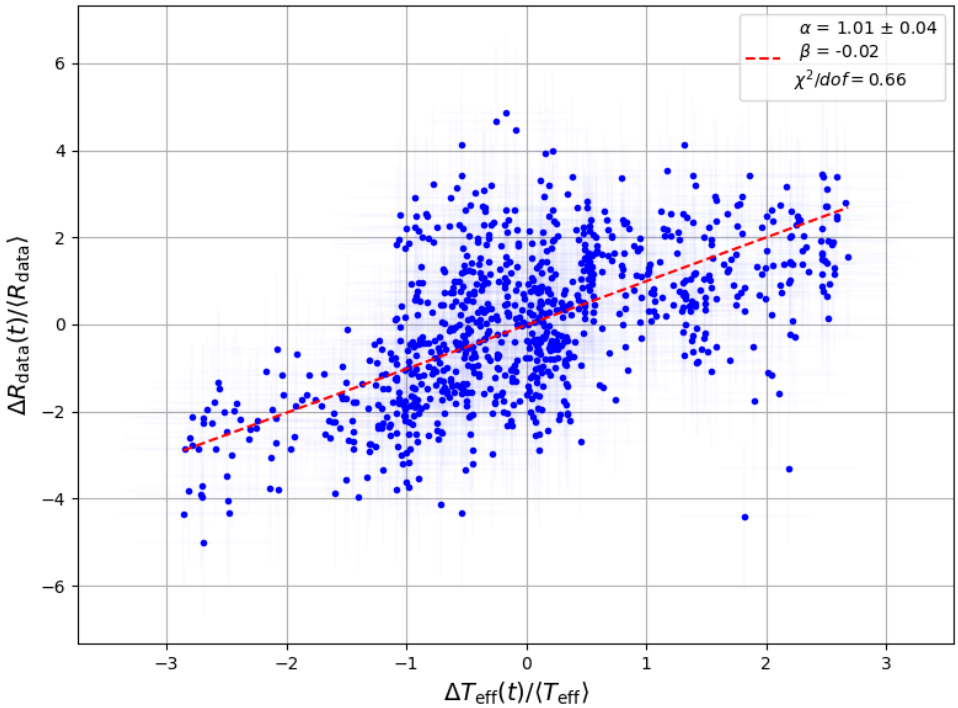

Figure A.113: Normalised effective temperature T_{eff} and ratio with detrending R_{data} of ORCA-15 showing the relative variation in percentage. The ratios are calculated in 60-minute windows around temperature measurements.The red line is a fit of the model in Equation 6.11. The errors are taken into account in the fit.

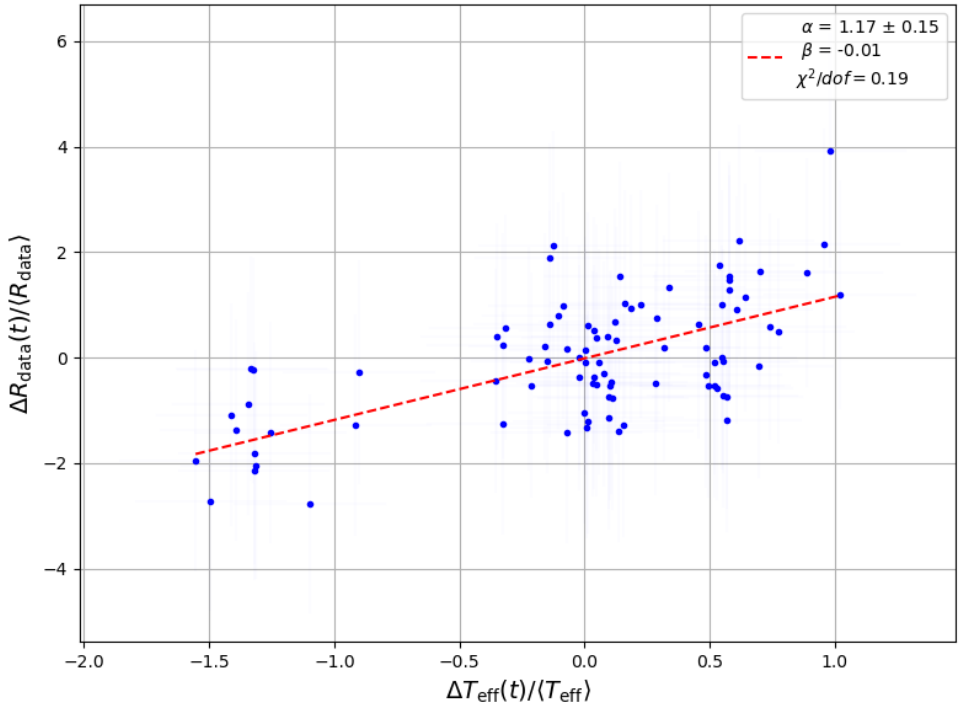

Figure A.114: Normalised effective temperature T_{eff} and ratio without detrending R_{data} of ORCA-15.1 showing the relative variation in percentage. The ratios are calculated in 60-minute windows around temperature measurements. The red line is a fit of the model in Equation 6.11. The errors are taken into account in the fit.

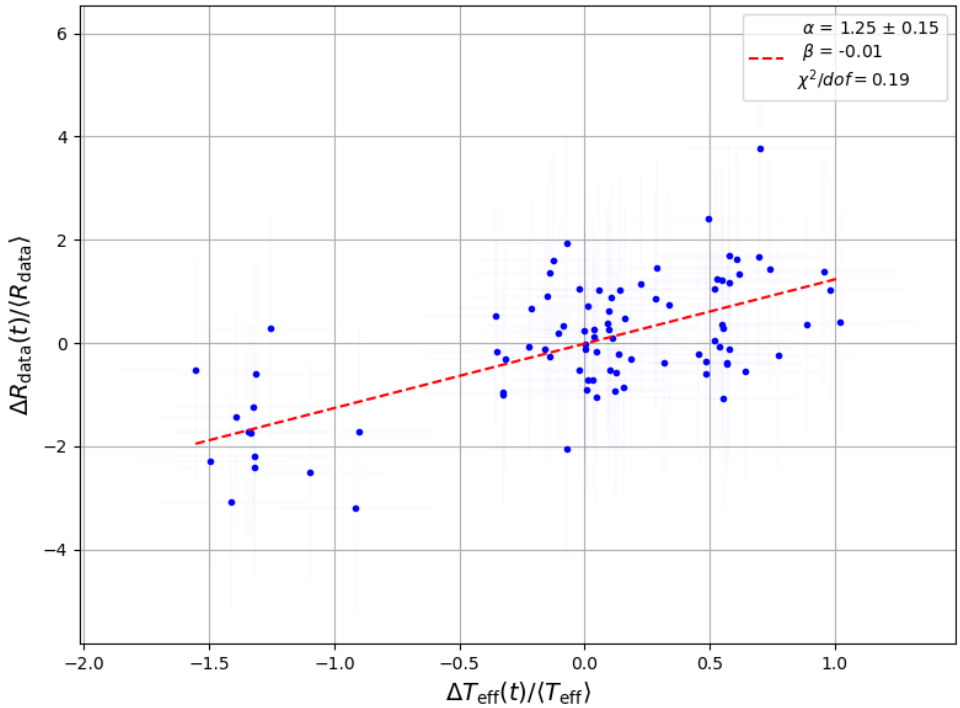

Figure A.115: Normalised effective temperature T_{eff} and ratio with detrending R_{data} of ORCA-15.1 showing the relative variation in percentage. The ratios are calculated in 60-minute windows around temperature measurements.The red line is a fit of the model in Equation 6.11. The errors are taken into account in the fit.

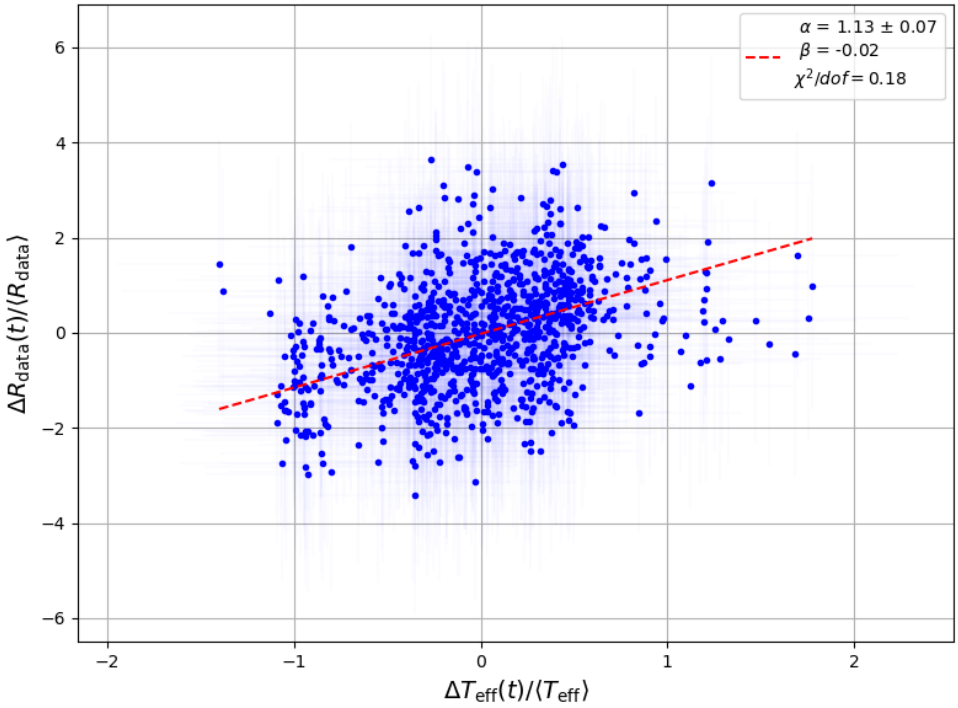

Figure A.116: Normalised effective temperature T_{eff} and ratio without detrending R_{data} of ORCA-18 showing the relative variation in percentage. The ratios are calculated in 60-minute windows around temperature measurements. The red line is a fit of the model in Equation 6.11. The errors are taken into account in the fit.

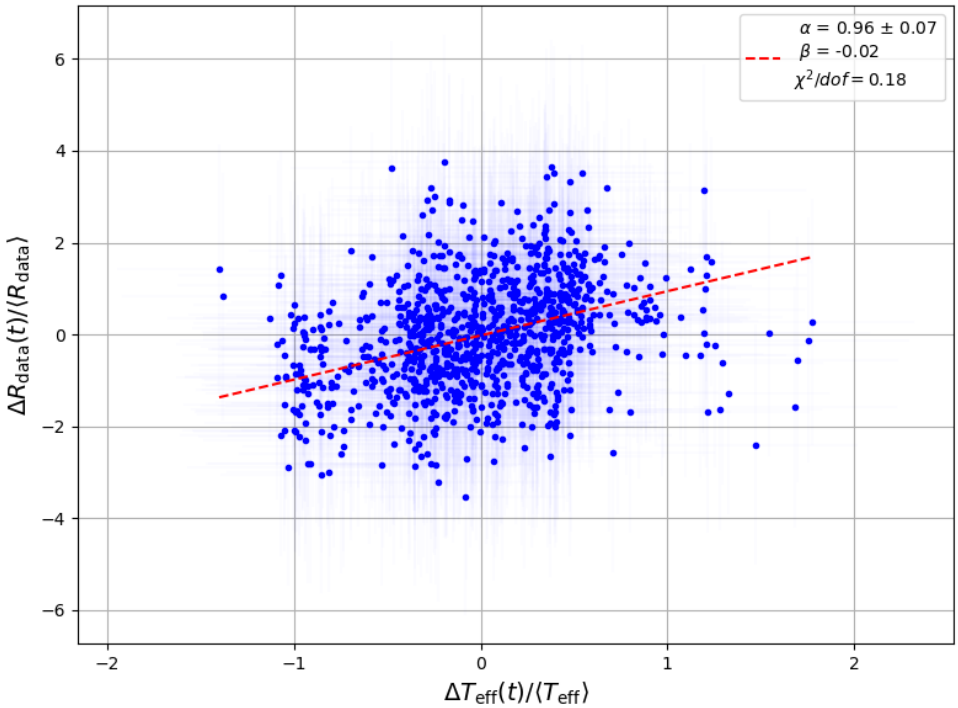

Figure A.117: Normalised effective temperature T_{eff} and ratio with detrending R_{data} of ORCA-18 showing the relative variation in percentage. The ratios are calculated in 60-minute windows around temperature measurements.The red line is a fit of the model in Equation 6.11. The errors are taken into account in the fit.

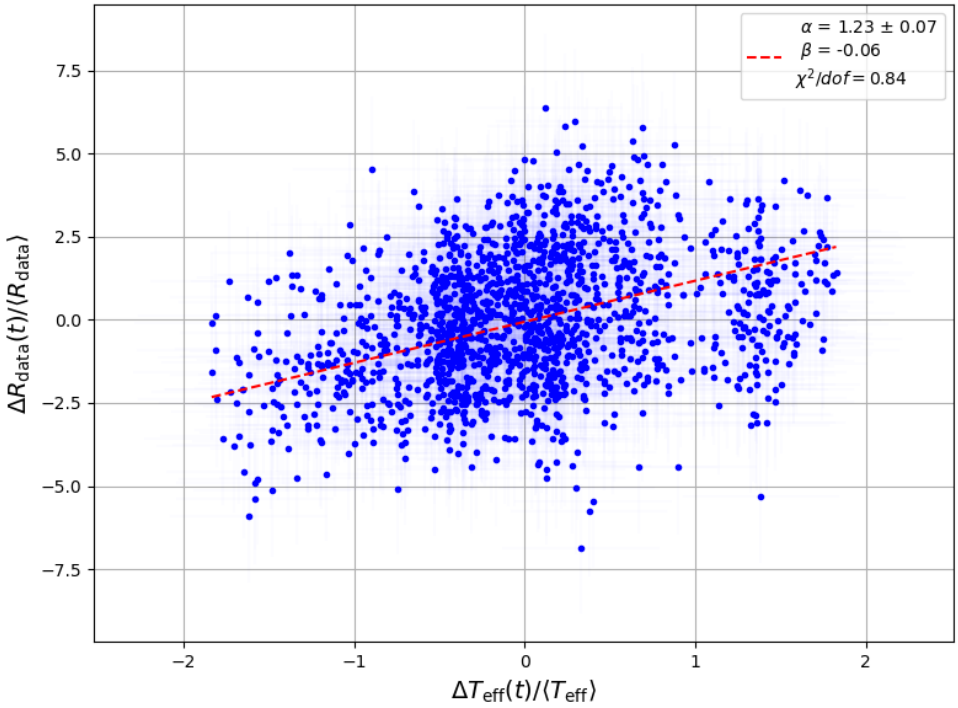

Figure A.118: Normalised effective temperature T_{eff} and ratio without detrending R_{data} of ARCA-21 showing the relative variation in percentage. The ratios are calculated in 60-minute windows around temperature measurements. The red line is a fit of the model in Equation 6.11. The errors are taken into account in the fit.

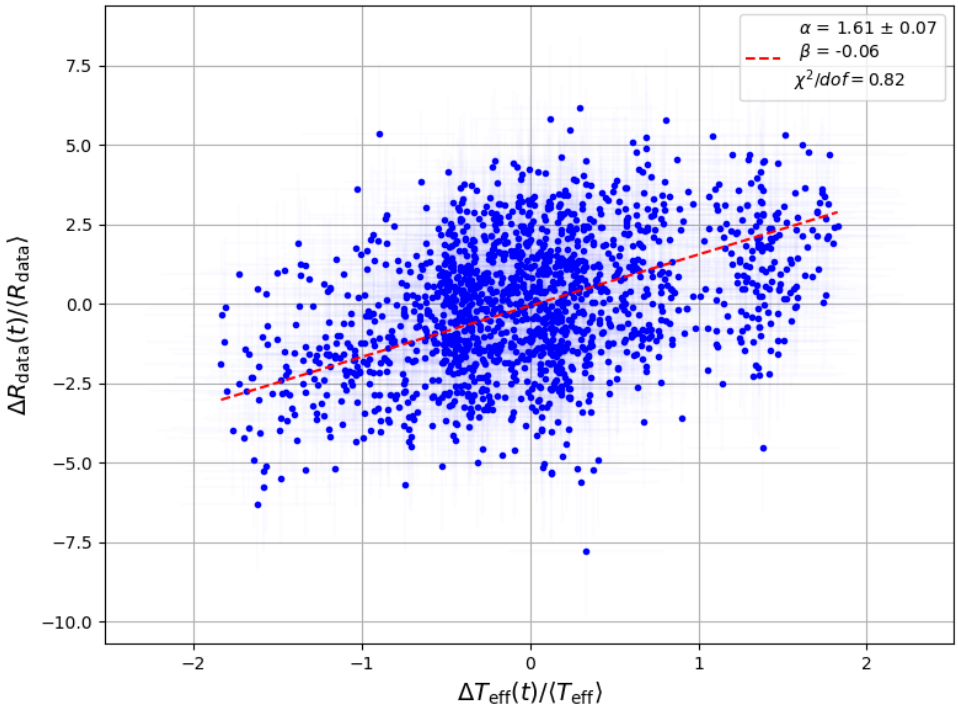

Figure A.119: Normalised effective temperature T_{eff} and ratio with detrending R_{data} of ARCA-21 showing the relative variation in percentage. The ratios are calculated in 60-minute windows around temperature measurements.The red line is a fit of the model in Equation 6.11. The errors are taken into account in the fit.

A.2.2. Binned analysis

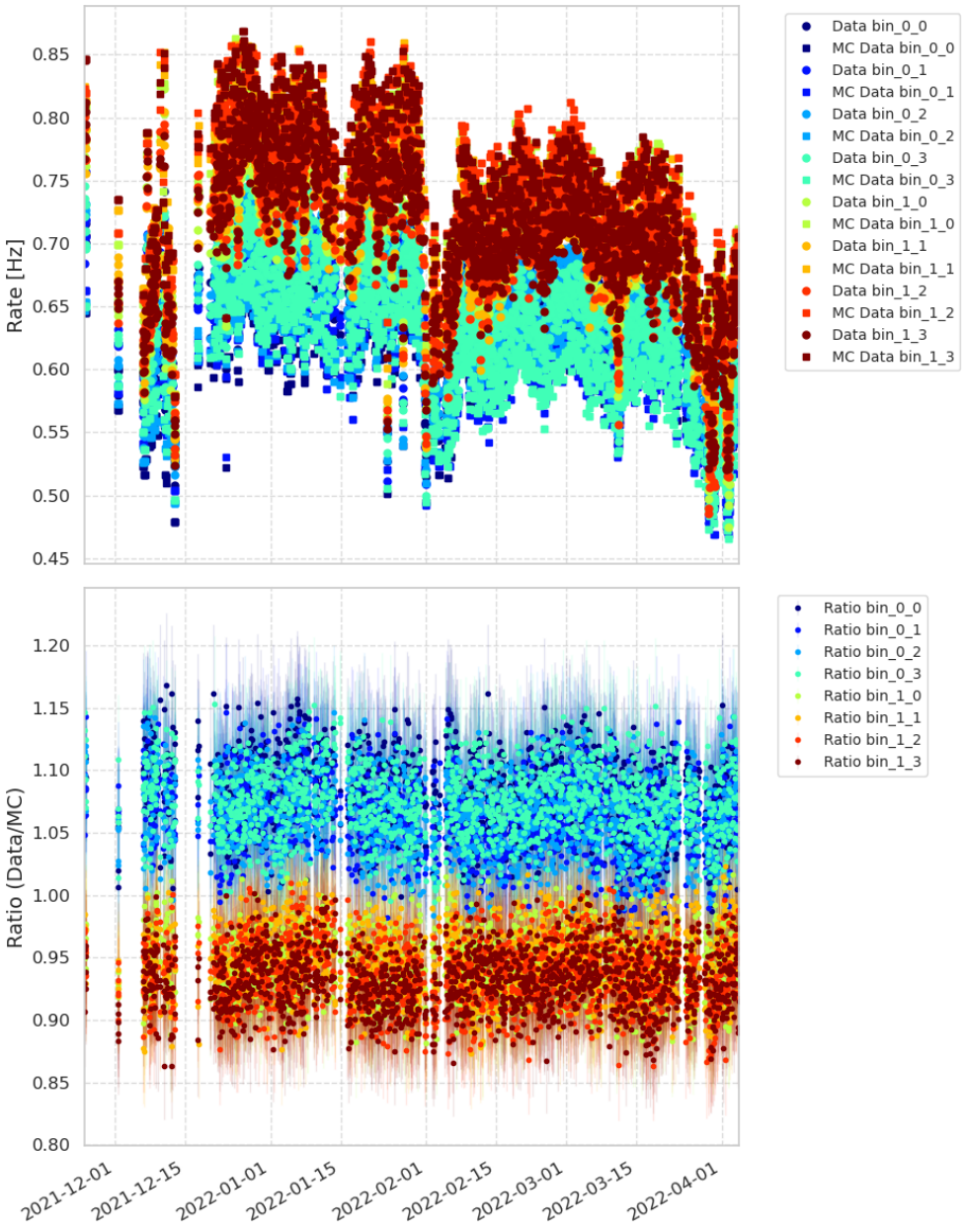

Figure A.120: Rate and ratio per bin per 60-minute window around temperature measurements for ORCA-10 after cuts are applied. In the top part the count rates of the data and the Monte Carlo simulation are shown. In the bottom part the ratio of the two is shown.

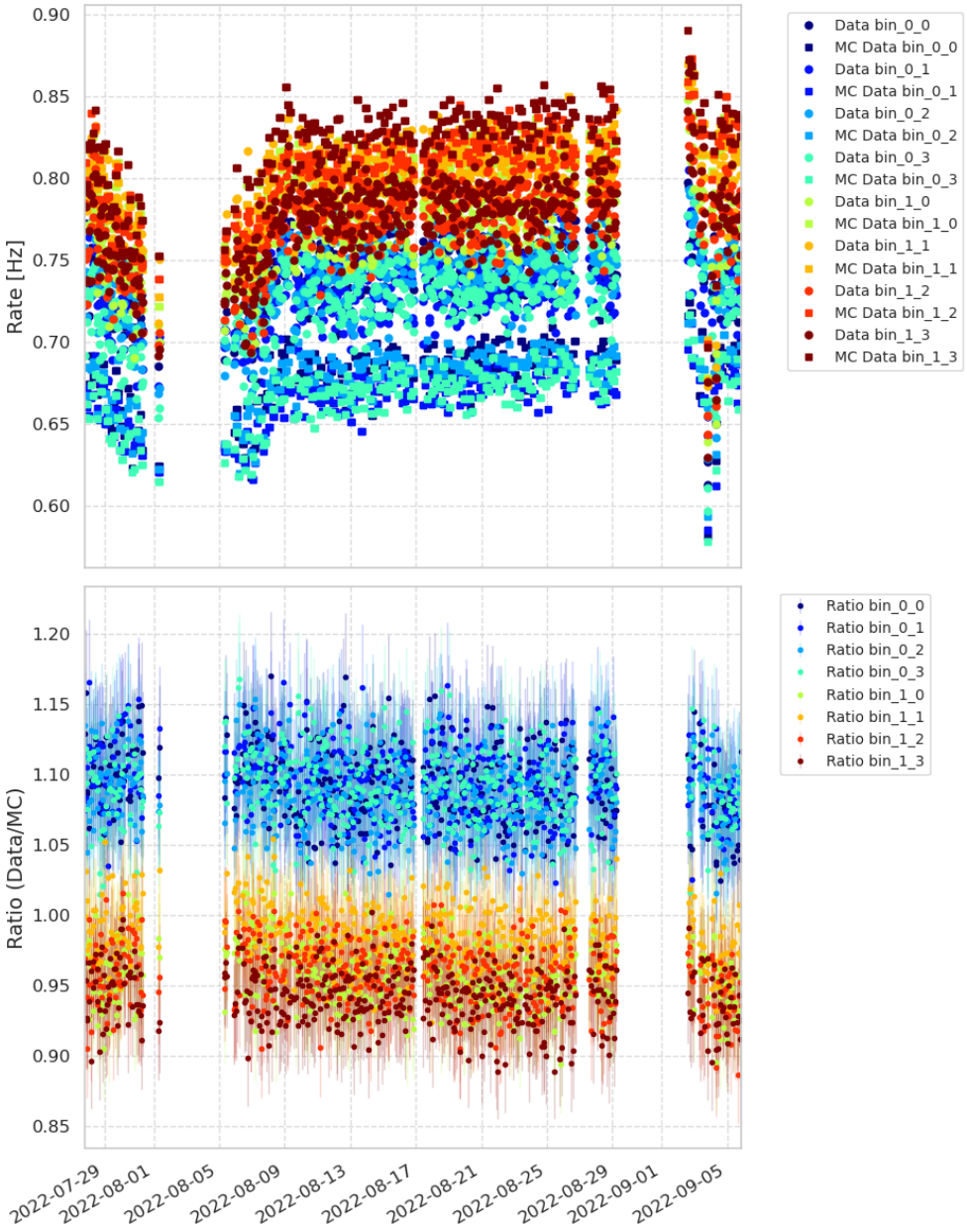

Figure A.121: Rate and ratio per bin per 60-minute window around temperature measurements for ORCA-11 after cuts are applied. In the top part the count rates of the data and the Monte Carlo simulation are shown. In the bottom part the ratio of the two is shown.

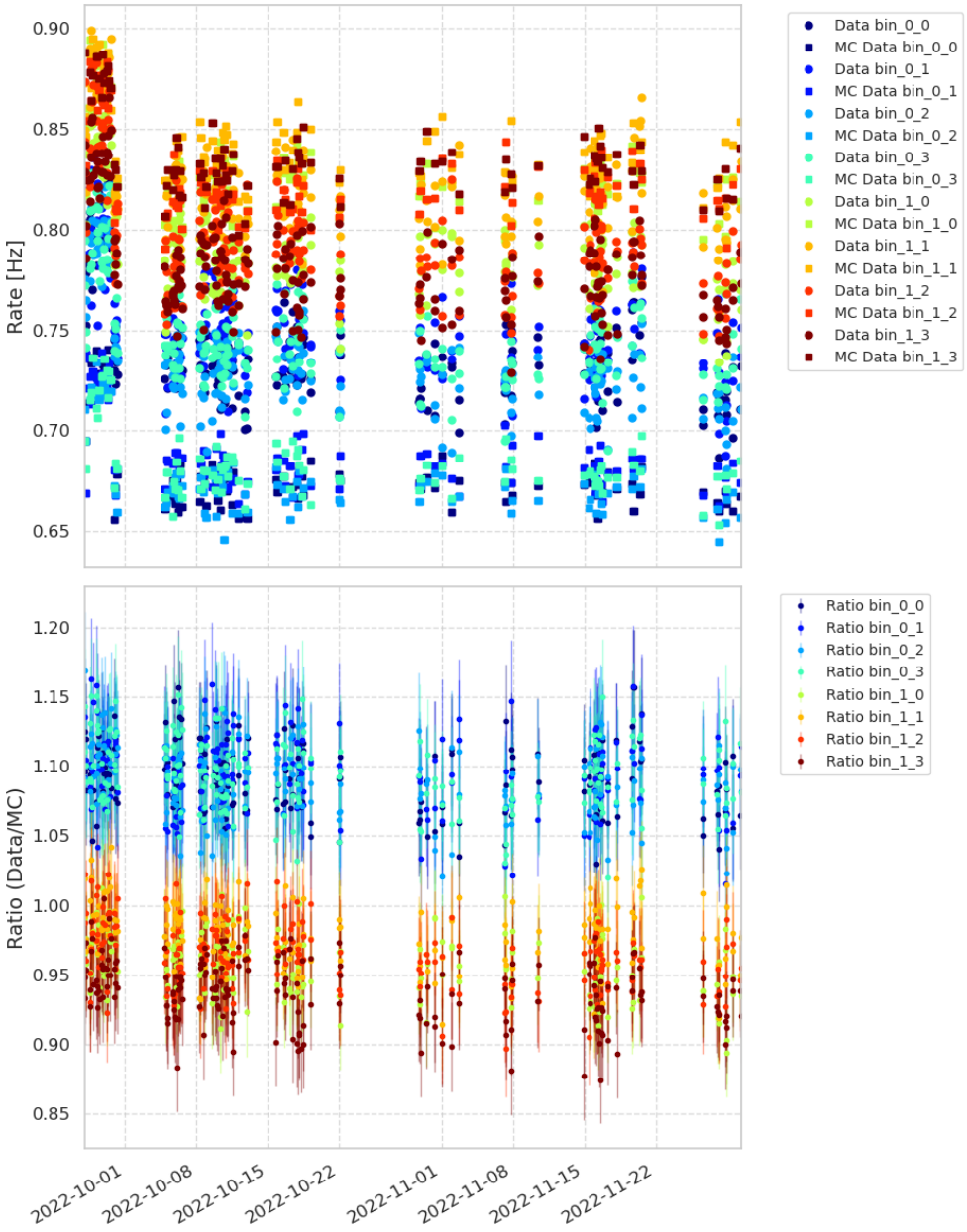

Figure A.122: Rate and ratio per bin per 60-minute window around temperature measurements for ORCA-11.1 after cuts are applied. In the top part the count rates of the data and the Monte Carlo simulation are shown. In the bottom part the ratio of the two is shown.

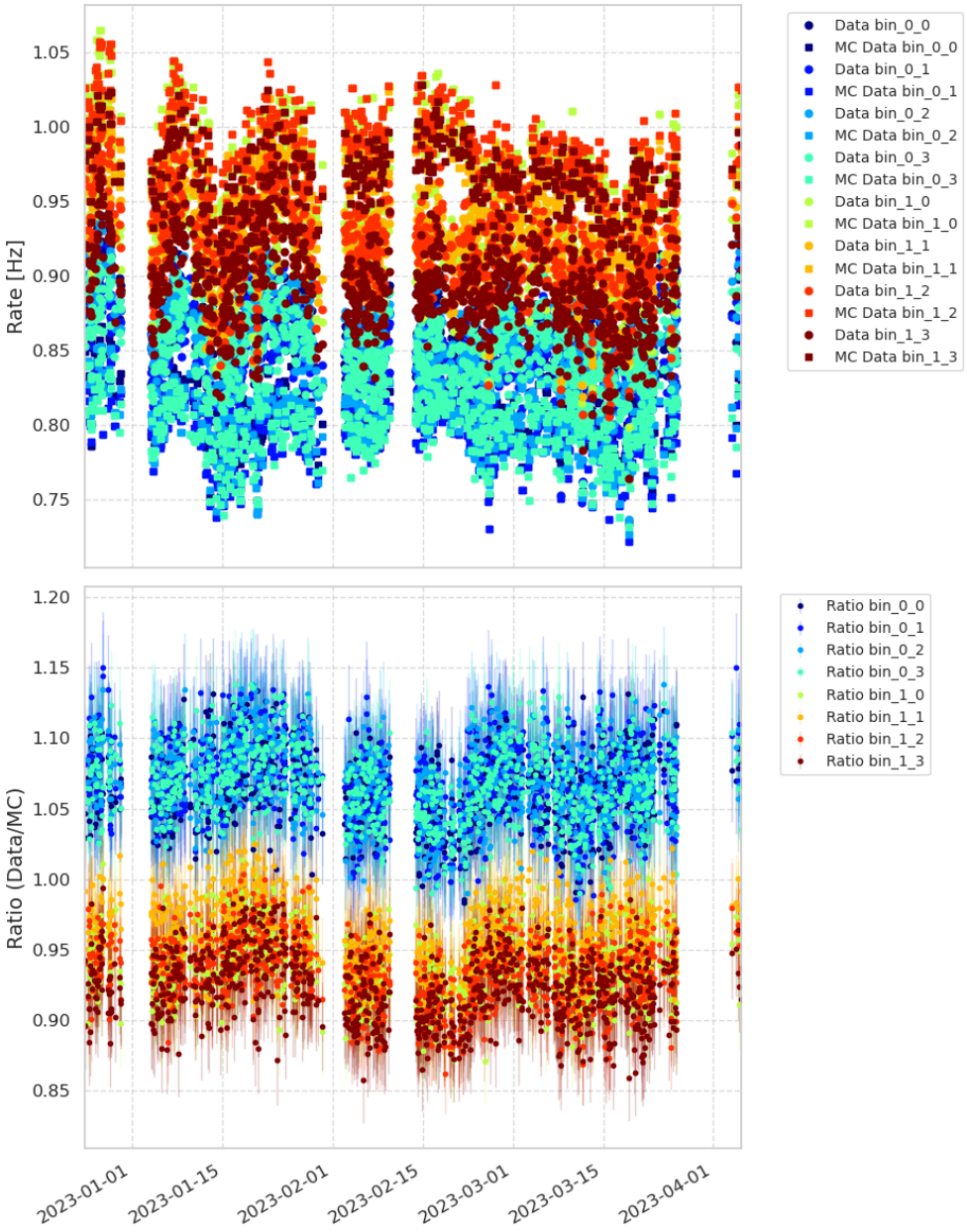

Figure A.123: Rate and ratio per bin per 60-minute window around temperature measurements for ORCA-15 after cuts are applied. In the top part the count rates of the data and the Monte Carlo simulation are shown. In the bottom part the ratio of the two is shown.

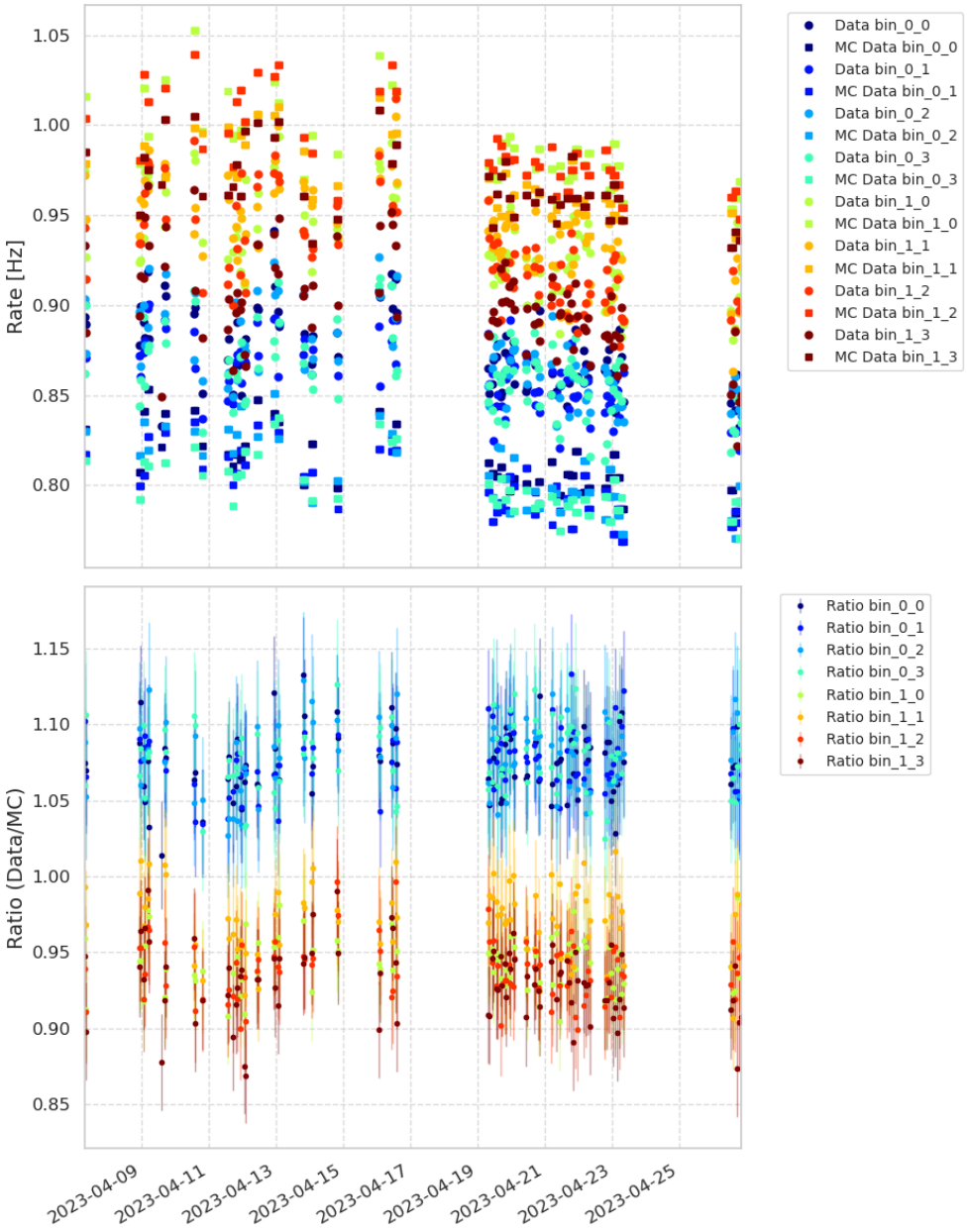

Figure A.124: Rate and ratio per bin per 60-minute window around temperature measurements for ORCA-15.1 after cuts are applied. In the top part the count rates of the data and the Monte Carlo simulation are shown. In the bottom part the ratio of the two is shown.

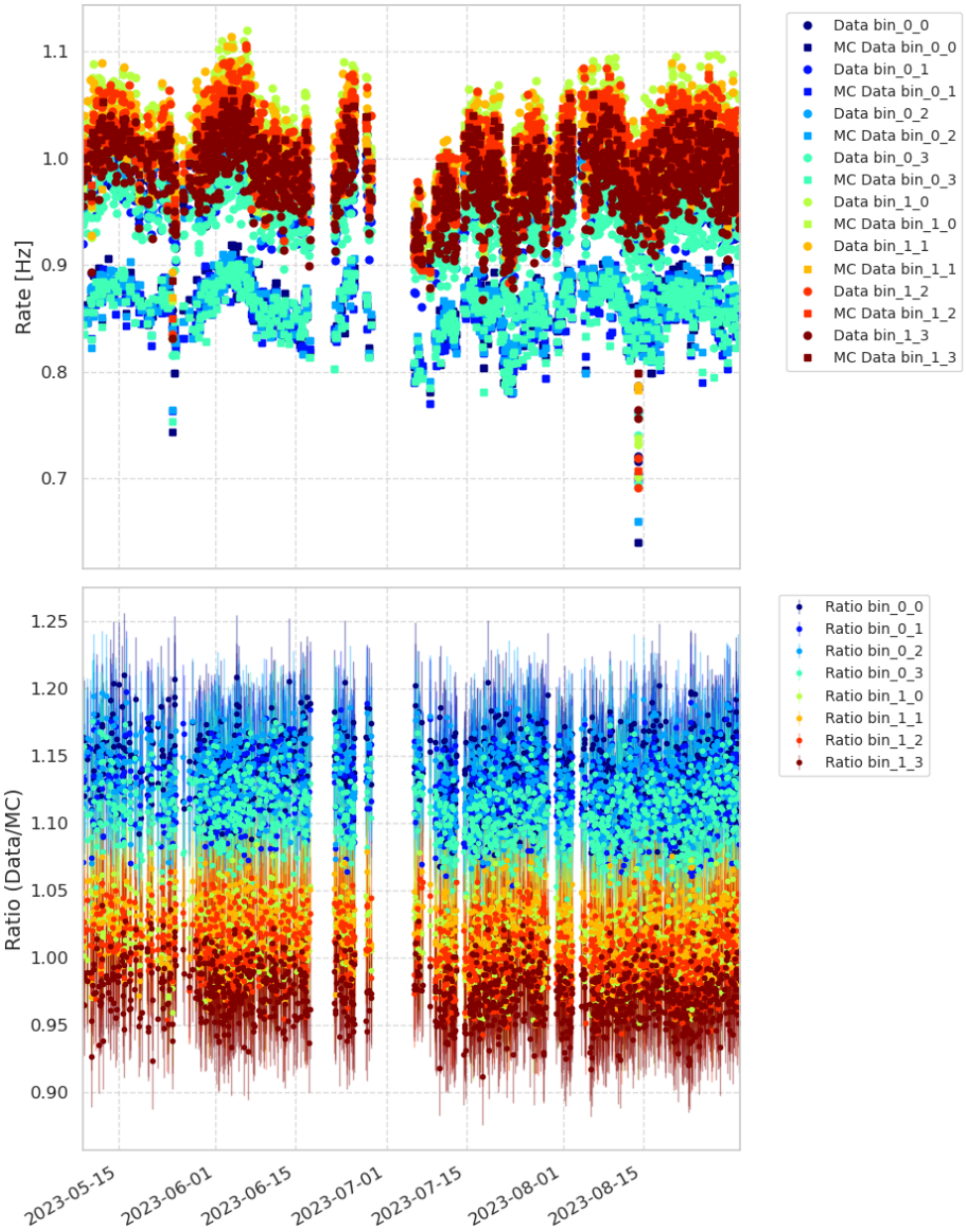

Figure A.125: Rate and ratio per bin per 60-minute window around temperature measurements for ORCA-18 after cuts are applied. In the top part the count rates of the data and the Monte Carlo simulation are shown. In the bottom part the ratio of the two is shown.

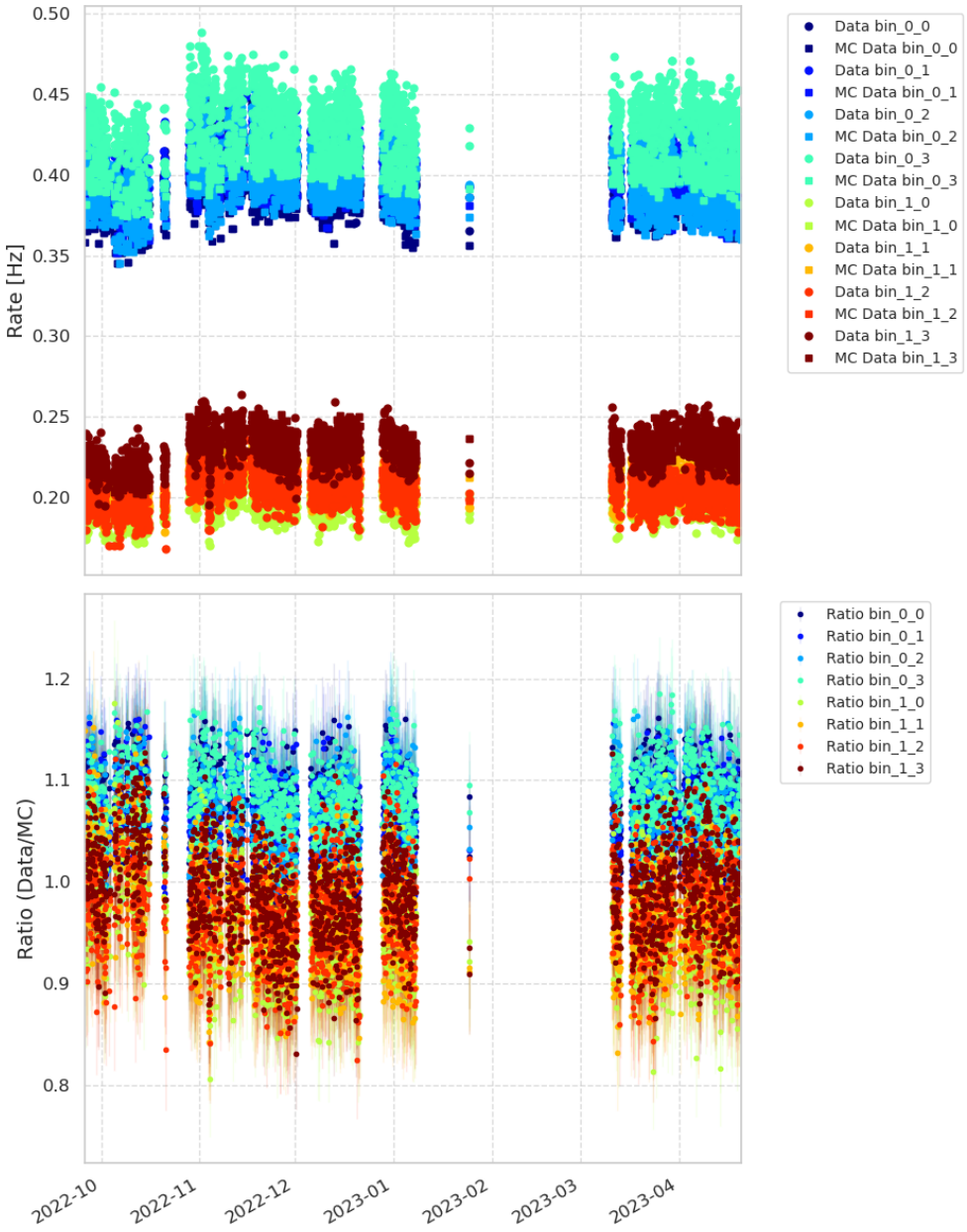

Figure A.126: Rate and ratio per bin per 60-minute window around temperature measurements for ARCA-21 after cuts are applied. In the top part the count rates of the data and the Monte Carlo simulation are shown. In the bottom part the ratio of the two is shown.

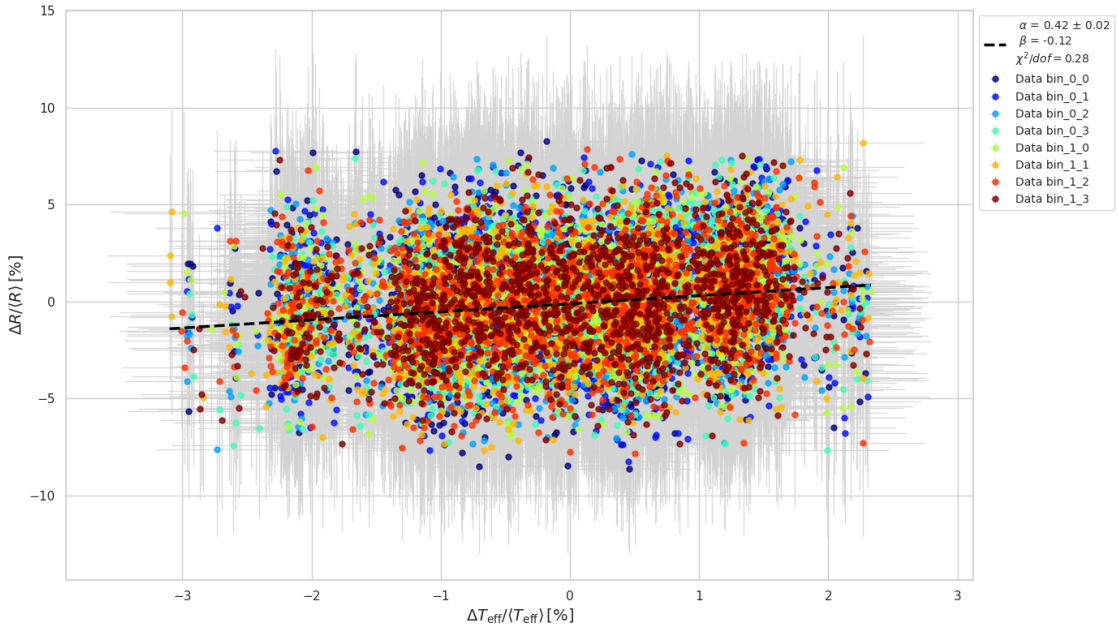

Figure A.127: Normalised effective temperature T_{eff} and ratio without detrending R_{data} of ORCA-10 showing the relative variation in percentage for each bin plotted together. The black line is a fit of the model in Equation 6.11 though all the data points combined. The errors are taken into account in the fit.

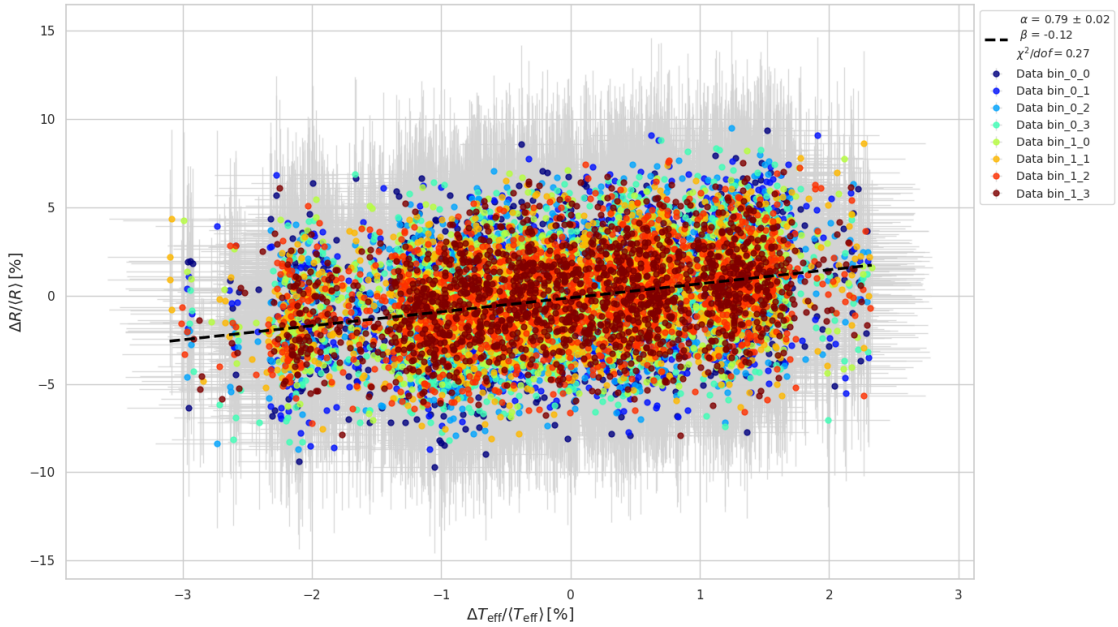

Figure A.128: Normalised effective temperature T_{eff} and ratio with detrending R_{data} of ORCA-10 showing the relative variation in percentage for each bin plotted together. The black line is a fit of the model in Equation 6.11 though all the data points combined. The errors are taken into account in the fit.

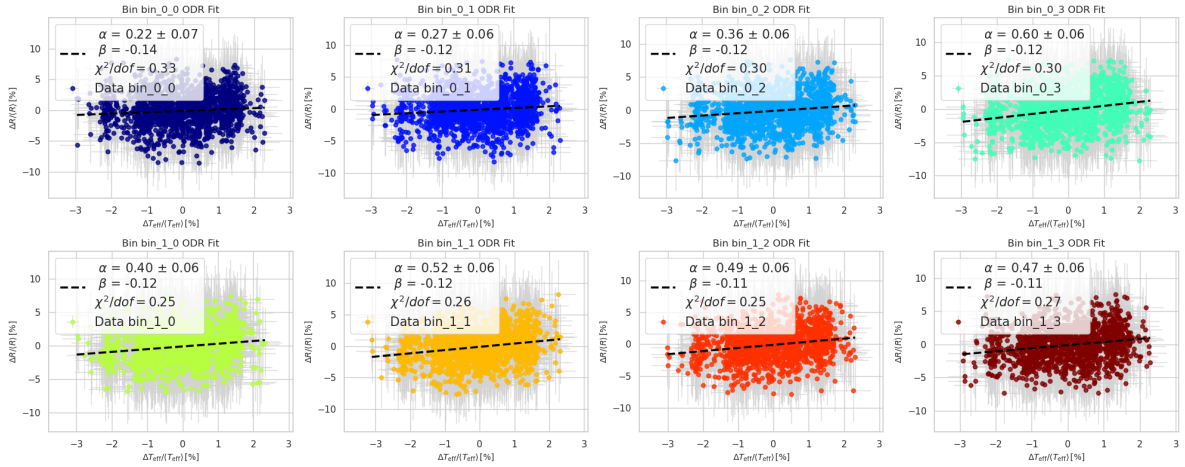

Figure A.129: Normalised effective temperature T_{eff} and ratio without detrending R_{data} of ORCA-10 showing the relative variation in percentage for each separate bin. The black line in each plot is a fit of the model in Equation 6.11 though the data of each bin separate. The errors are taken into account in the fit.

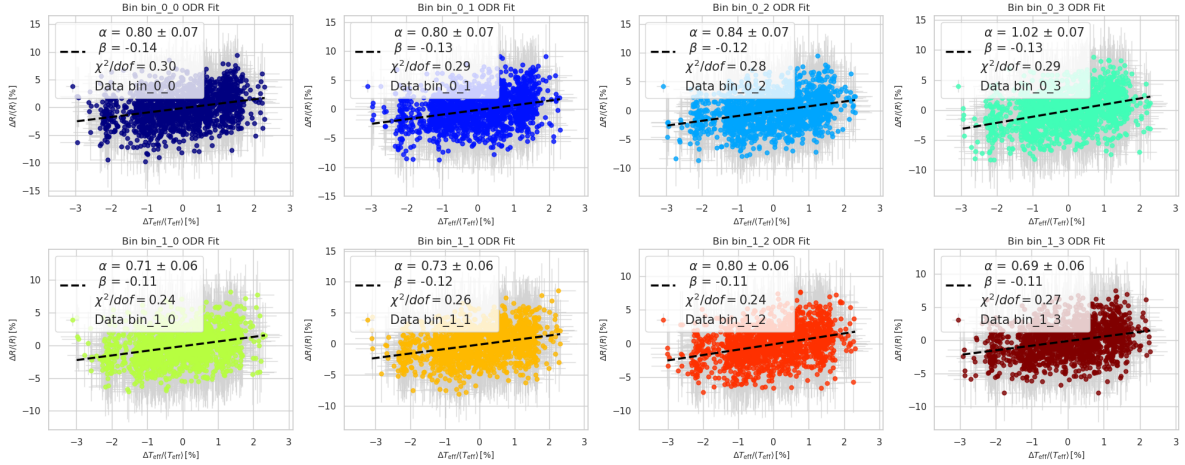

Figure A.130: Normalised effective temperature T_{eff} and ratio with detrending R_{data} of ORCA-10 showing the relative variation in percentage for each separate bin. The black line in each plot is a fit of the model in Equation 6.11 though the data of each bin separate. The errors are taken into account in the fit.

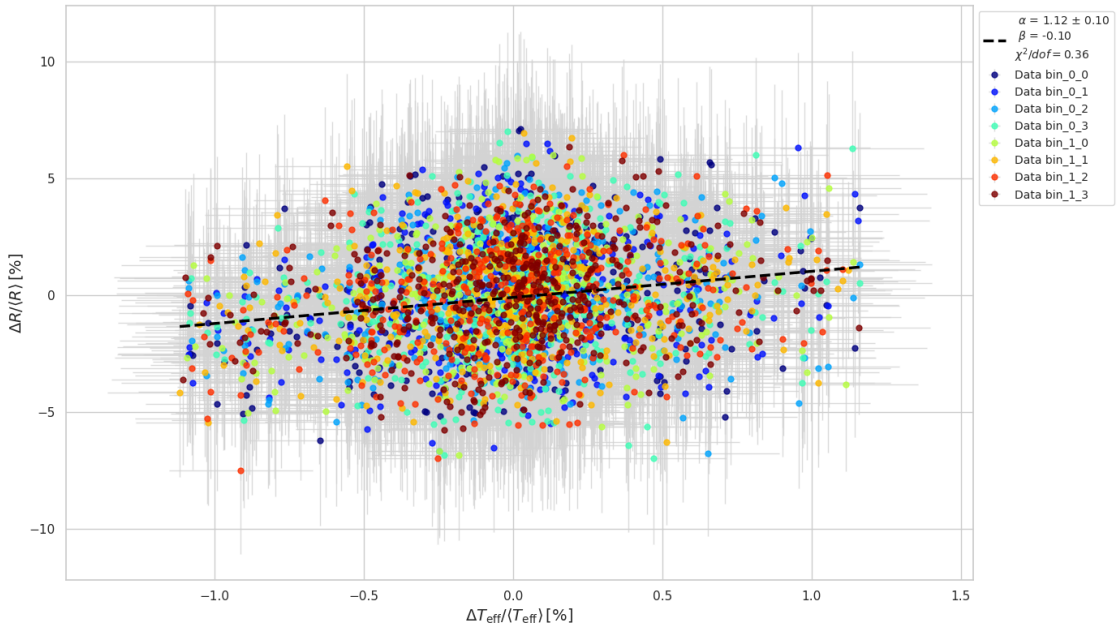

Figure A.131: Normalised effective temperature T_{eff} and ratio without detrending R_{data} of ORCA-11 showing the relative variation in percentage for each bin plotted together. The black line is a fit of the model in Equation 6.11 though all the data points combined. The errors are taken into account in the fit.

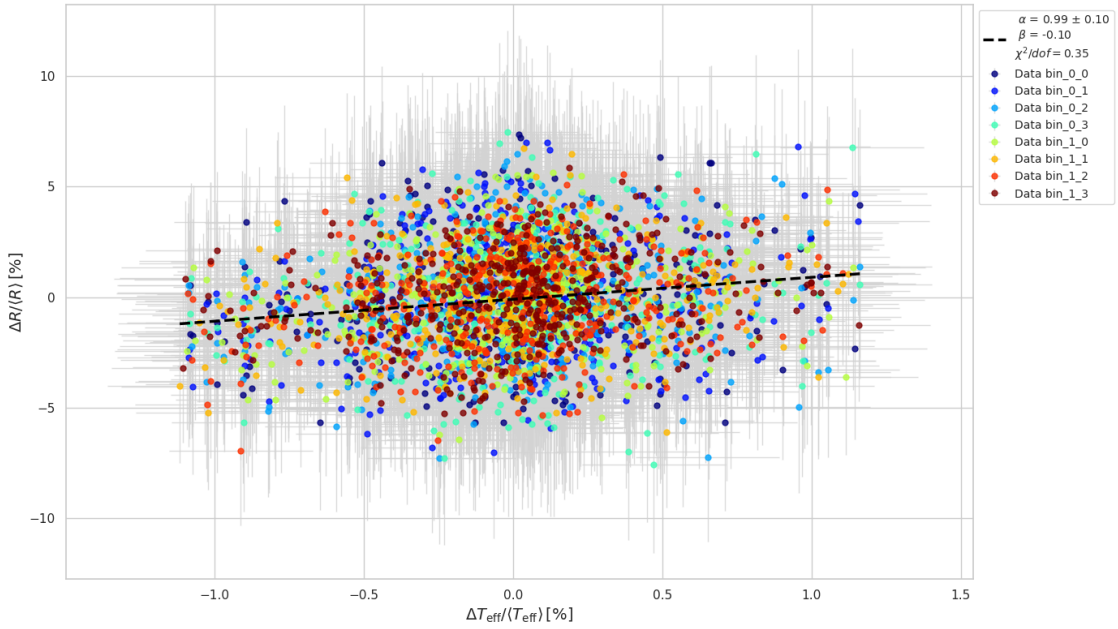

Figure A.132: Normalised effective temperature T_{eff} and ratio with detrending R_{data} of ORCA-11 showing the relative variation in percentage for each bin plotted together. The black line is a fit of the model in Equation 6.11 though all the data points combined. The errors are taken into account in the fit.

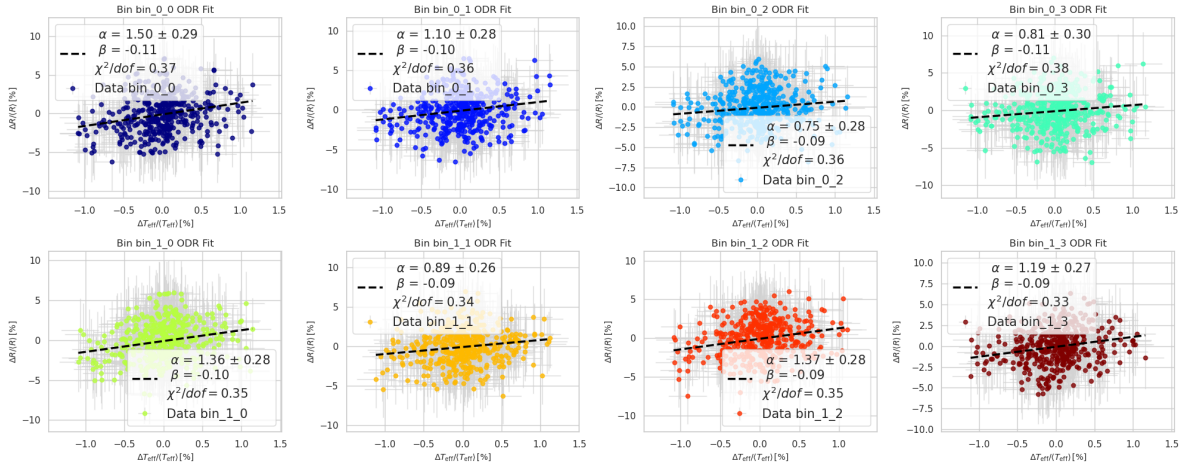

Figure A.133: Normalised effective temperature T_{eff} and ratio without detrending R_{data} of ORCA-11 showing the relative variation in percentage for each separate bin. The black line in each plot is a fit of the model in Equation 6.11 though the data of each bin separate. The errors are taken into account in the fit.

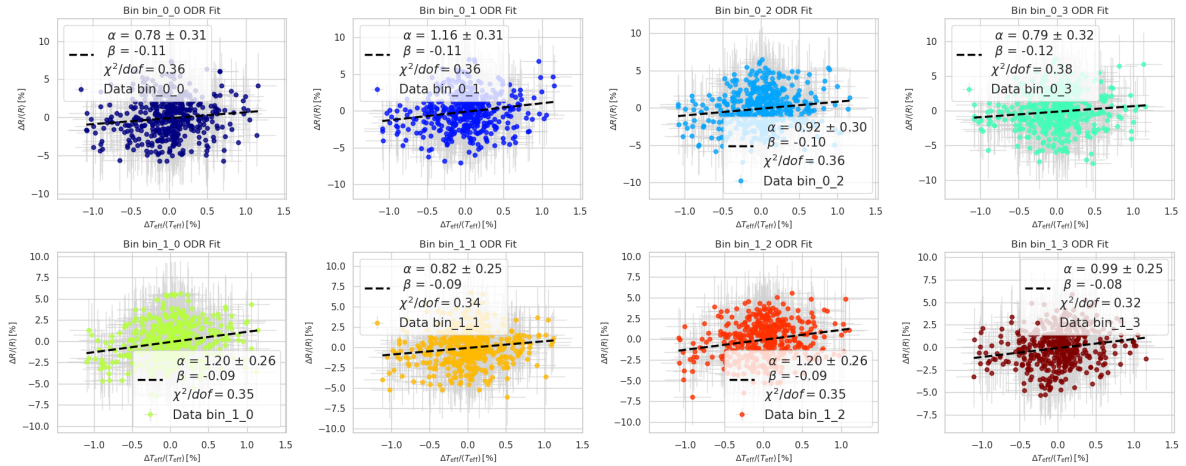

Figure A.134: Normalised effective temperature T_{eff} and ratio with detrending R_{data} of ORCA-11 showing the relative variation in percentage for each separate bin. The black line in each plot is a fit of the model in Equation 6.11 though the data of each bin separate. The errors are taken into account in the fit.

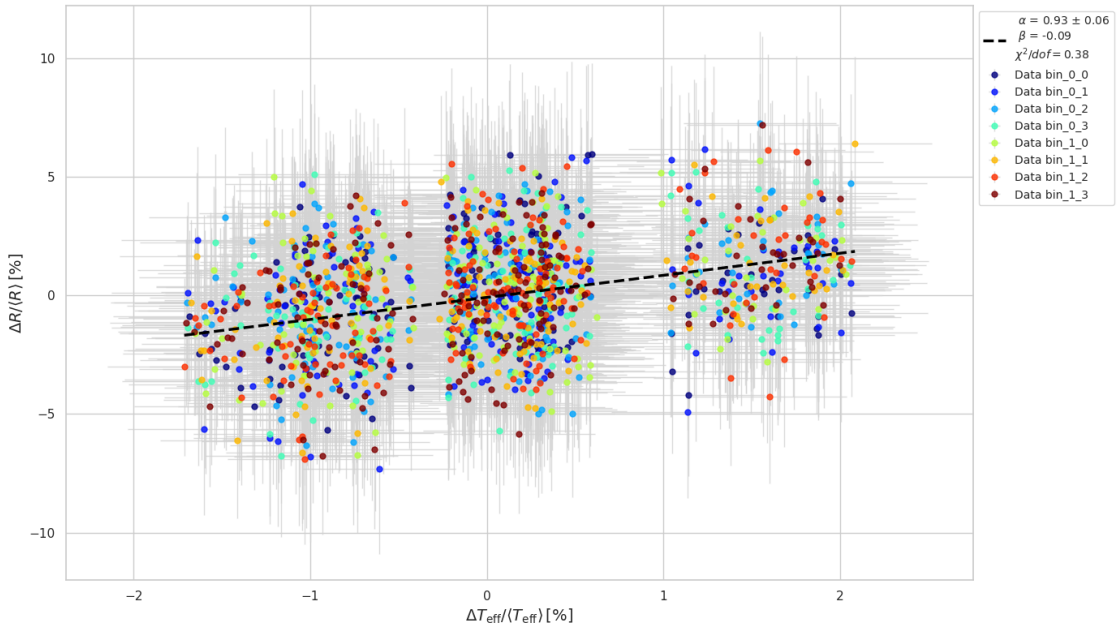

Figure A.135: Normalised effective temperature T_{eff} and ratio without detrending R_{data} of ORCA-11.1 showing the relative variation in percentage for each bin plotted together. The black line is a fit of the model in Equation 6.11 though all the data points combined. The errors are taken into account in the fit.

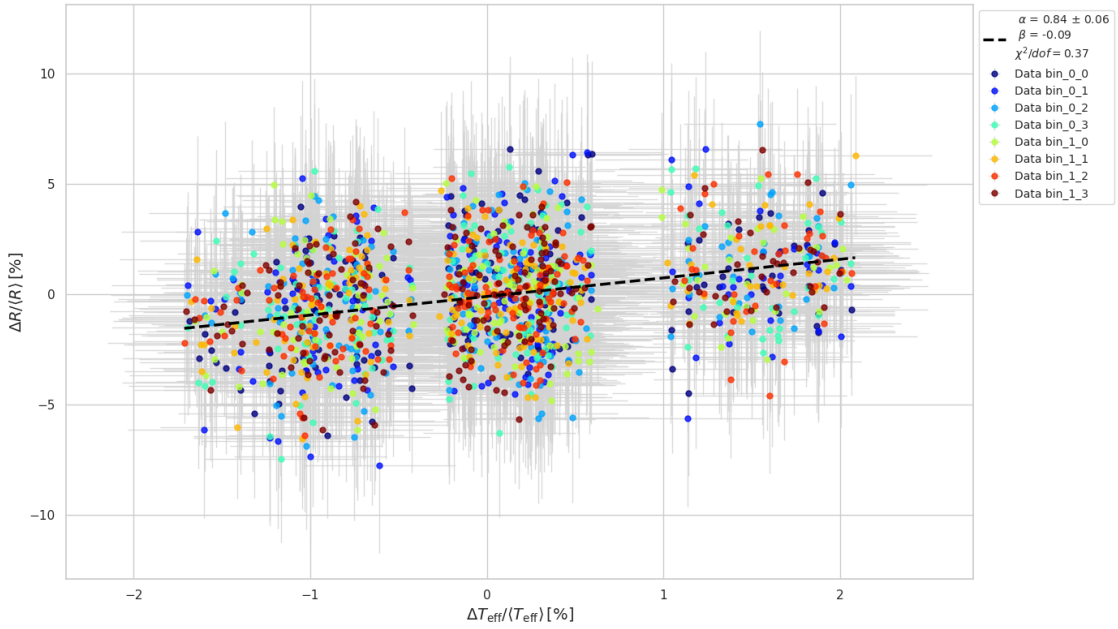

Figure A.136: Normalised effective temperature T_{eff} and ratio with detrending R_{data} of ORCA-11.1 showing the relative variation in percentage for each bin plotted together. The black line is a fit of the model in Equation 6.11 though all the data points combined. The errors are taken into account in the fit.

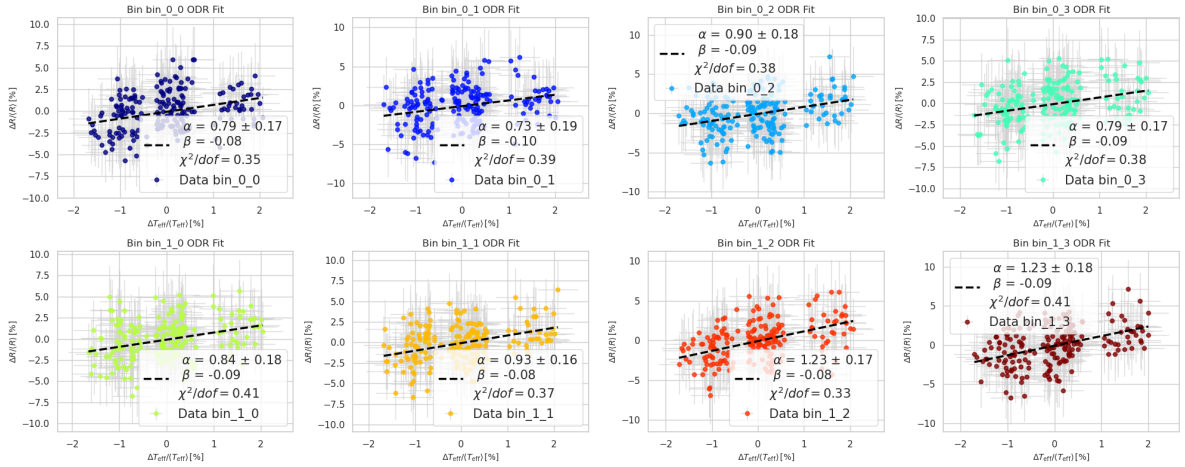

Figure A.137: Normalised effective temperature T_{eff} and ratio without detrending R_{data} of ORCA-11.1 showing the relative variation in percentage for each separate bin. The black line in each plot is a fit of the model in Equation 6.11 though the data of each bin separate. The errors are taken into account in the fit.

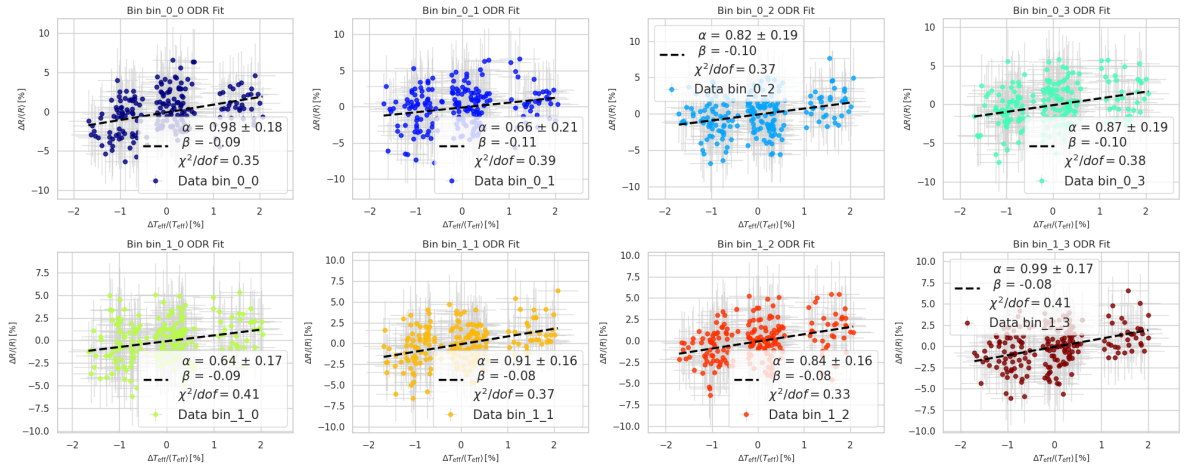

Figure A.138: Normalised effective temperature T_{eff} and ratio with detrending R_{data} of ORCA-11.1 showing the relative variation in percentage for each separate bin. The black line in each plot is a fit of the model in Equation 6.11 though the data of each bin separate. The errors are taken into account in the fit.

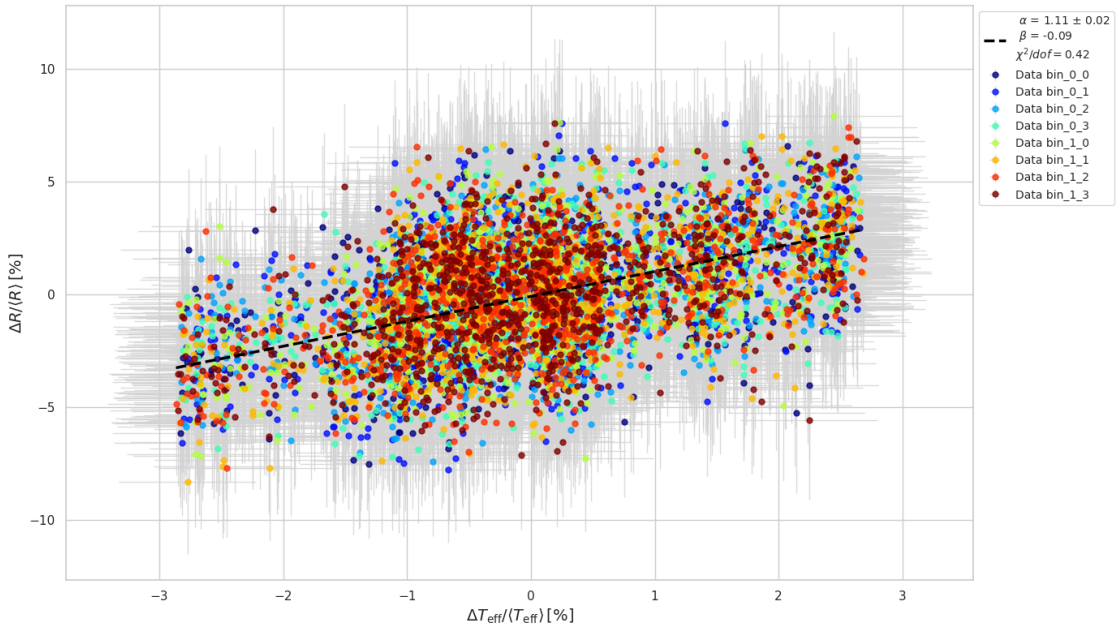

Figure A.139: Normalised effective temperature T_{eff} and ratio without detrending R_{data} of ORCA-15 showing the relative variation in percentage for each bin plotted together. The black line is a fit of the model in Equation 6.11 though all the data points combined. The errors are taken into account in the fit.

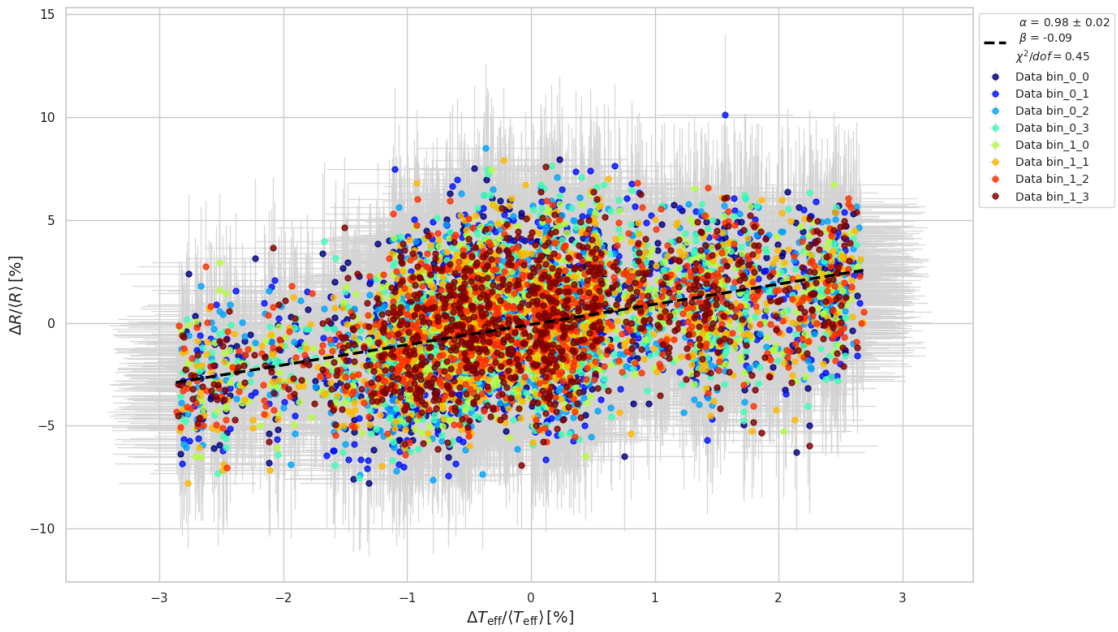

Figure A.140: Normalised effective temperature T_{eff} and ratio with detrending R_{data} of ORCA-15 showing the relative variation in percentage for each bin plotted together. The black line is a fit of the model in Equation 6.11 though all the data points combined. The errors are taken into account in the fit.

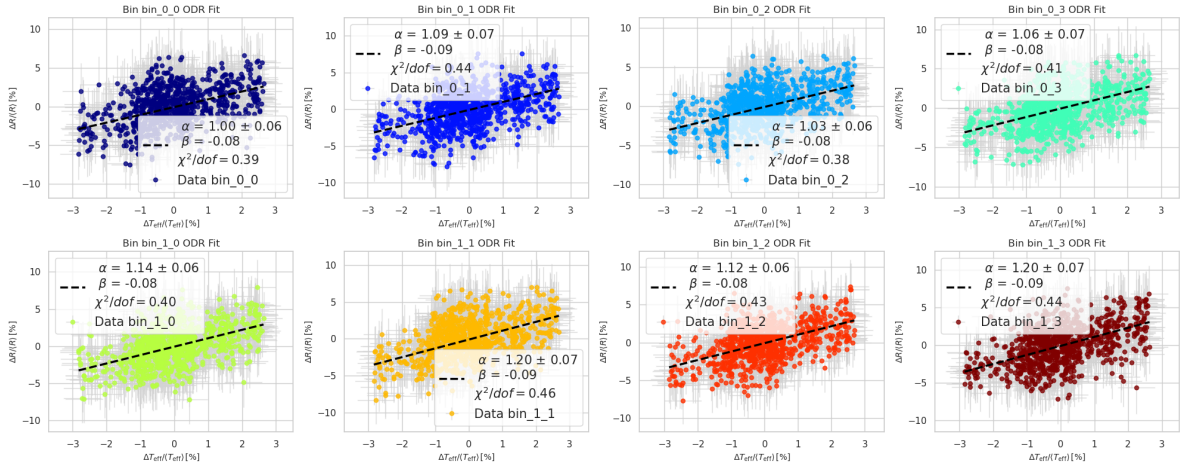

Figure A.141: Normalised effective temperature T_{eff} and ratio without detrending R_{data} of ORCA-15 showing the relative variation in percentage for each separate bin. The black line in each plot is a fit of the model in Equation 6.11 though the data of each bin separate. The errors are taken into account in the fit.

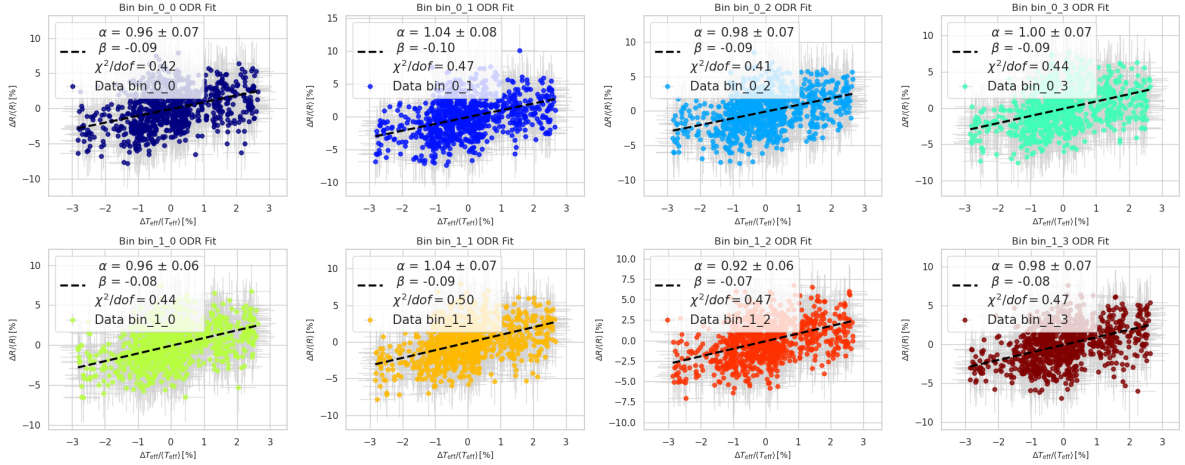

Figure A.142: Normalised effective temperature T_{eff} and ratio with detrending R_{data} of ORCA-15 showing the relative variation in percentage for each separate bin. The black line in each plot is a fit of the model in Equation 6.11 though the data of each bin separate. The errors are taken into account in the fit.

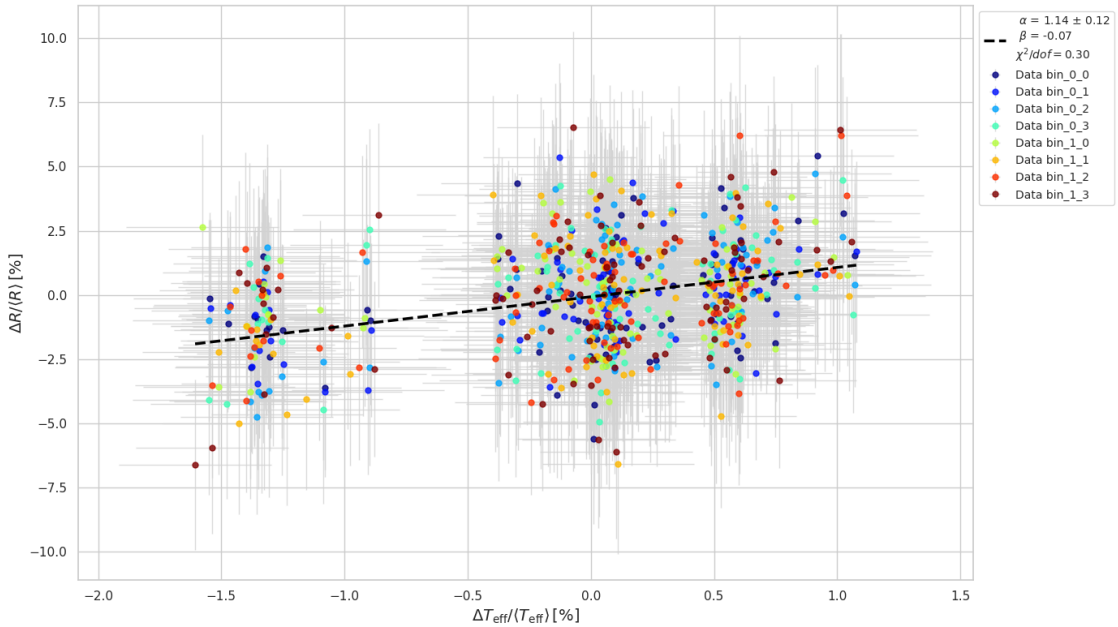

Figure A.143: Normalised effective temperature T_{eff} and ratio without detrending R_{data} of ORCA-15.1 showing the relative variation in percentage for each bin plotted together. The black line is a fit of the model in Equation 6.11 though all the data points combined. The errors are taken into account in the fit.

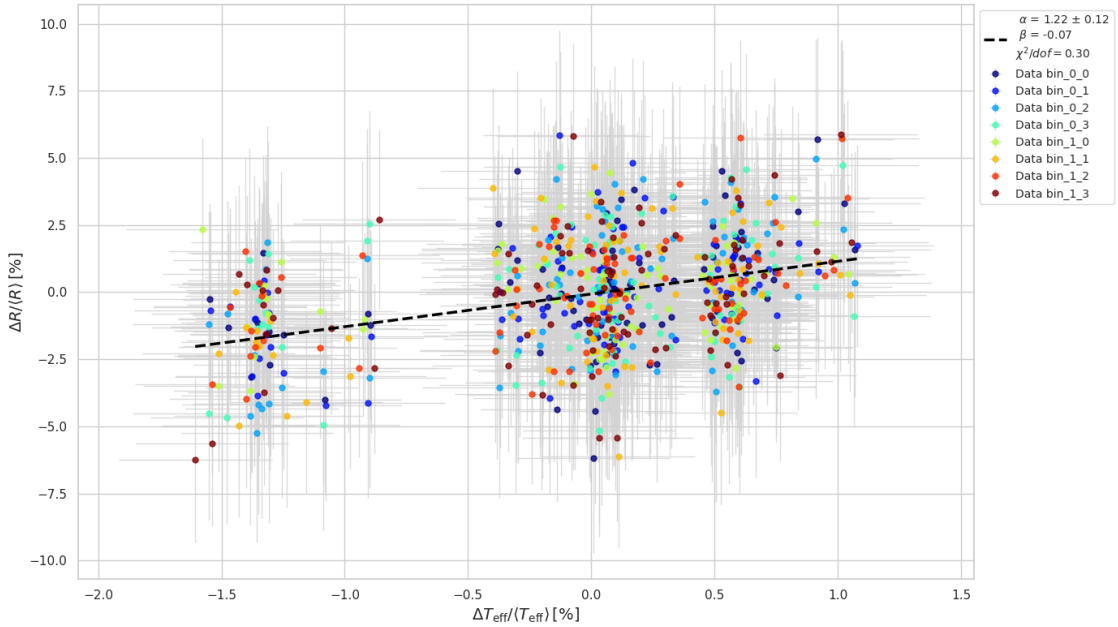

Figure A.144: Normalised effective temperature T_{eff} and ratio with detrending R_{data} of ORCA-15.1 showing the relative variation in percentage for each bin plotted together. The black line is a fit of the model in Equation 6.11 though all the data points combined. The errors are taken into account in the fit.

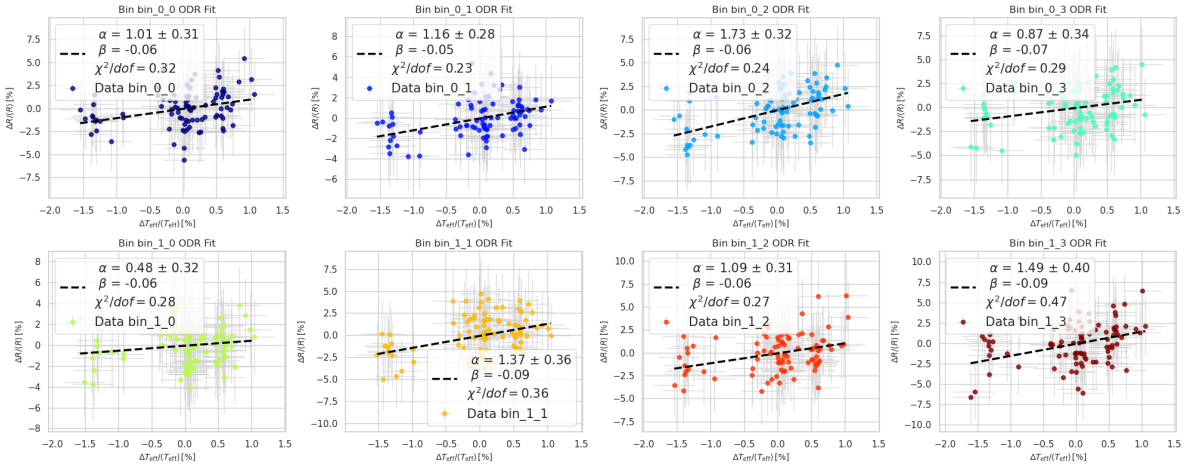

Figure A.145: Normalised effective temperature T_{eff} and ratio without detrending R_{data} of ORCA-15.1 showing the relative variation in percentage for each separate bin. The black line in each plot is a fit of the model in Equation 6.11 though the data of each bin separate. The errors are taken into account in the fit.

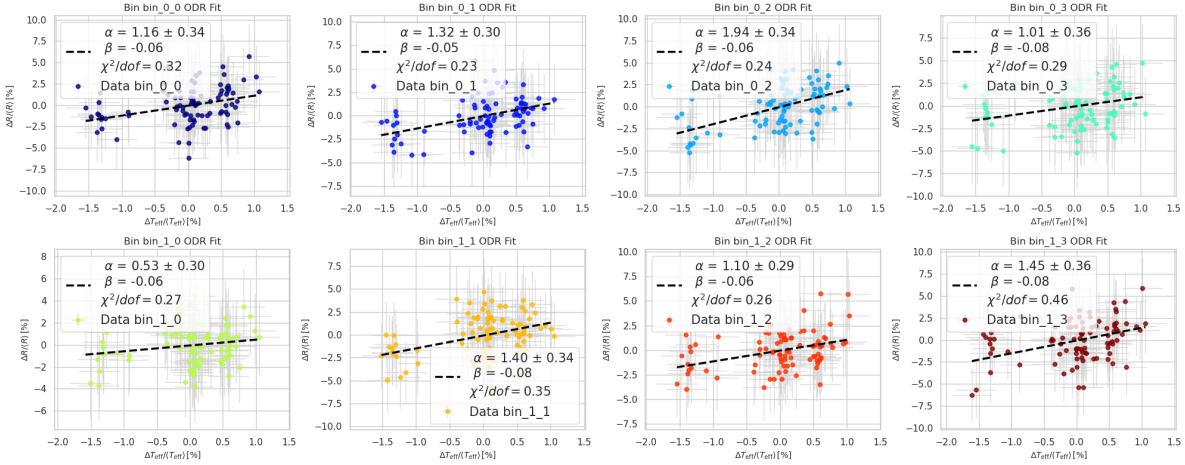

Figure A.146: Normalised effective temperature T_{eff} and ratio with detrending R_{data} of ORCA-15.1 showing the relative variation in percentage for each separate bin. The black line in each plot is a fit of the model in Equation 6.11 though the data of each bin separate. The errors are taken into account in the fit.

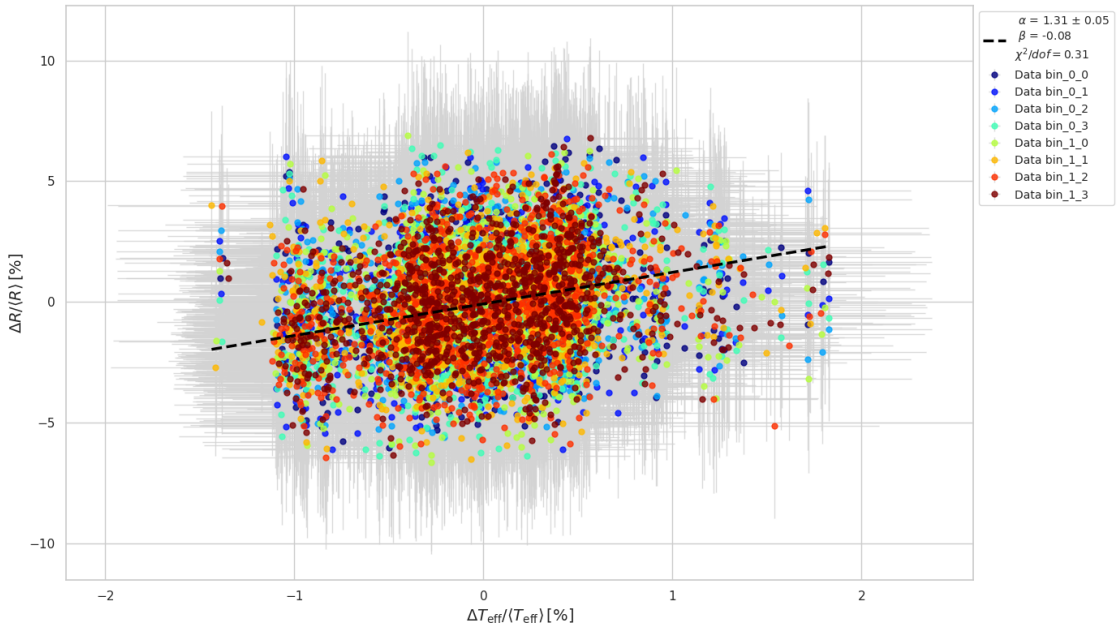

Figure A.147: Normalised effective temperature T_{eff} and ratio without detrending R_{data} of ORCA-18 showing the relative variation in percentage for each bin plotted together. The black line is a fit of the model in Equation 6.11 though all the data points combined. The errors are taken into account in the fit.

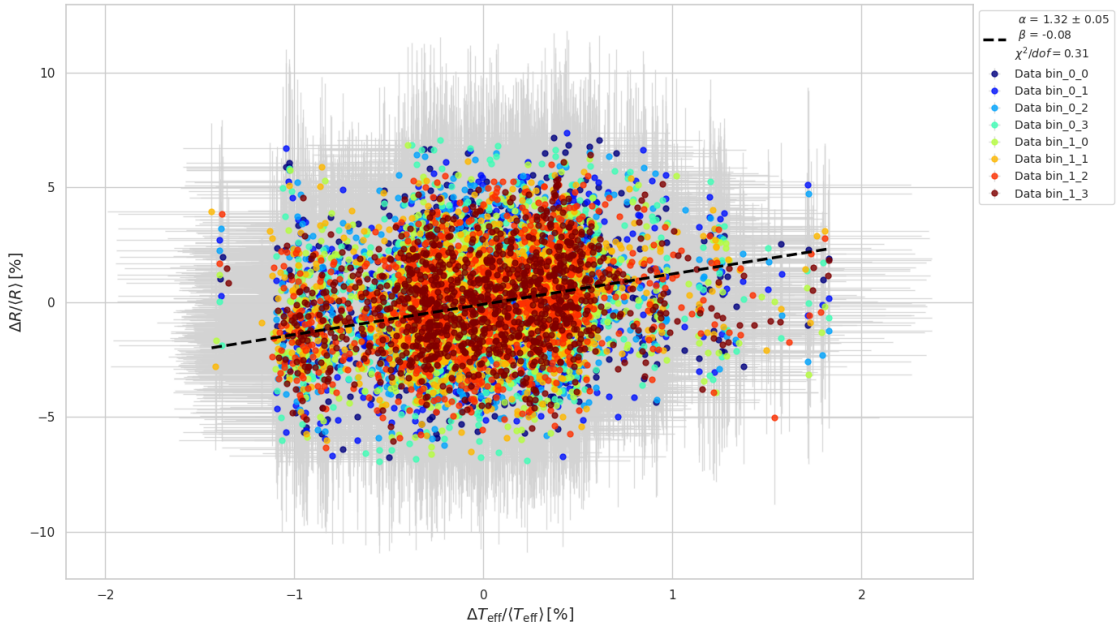

Figure A.148: Normalised effective temperature T_{eff} and ratio with detrending R_{data} of ORCA-18 showing the relative variation in percentage for each bin plotted together. The black line is a fit of the model in Equation 6.11 though all the data points combined. The errors are taken into account in the fit.

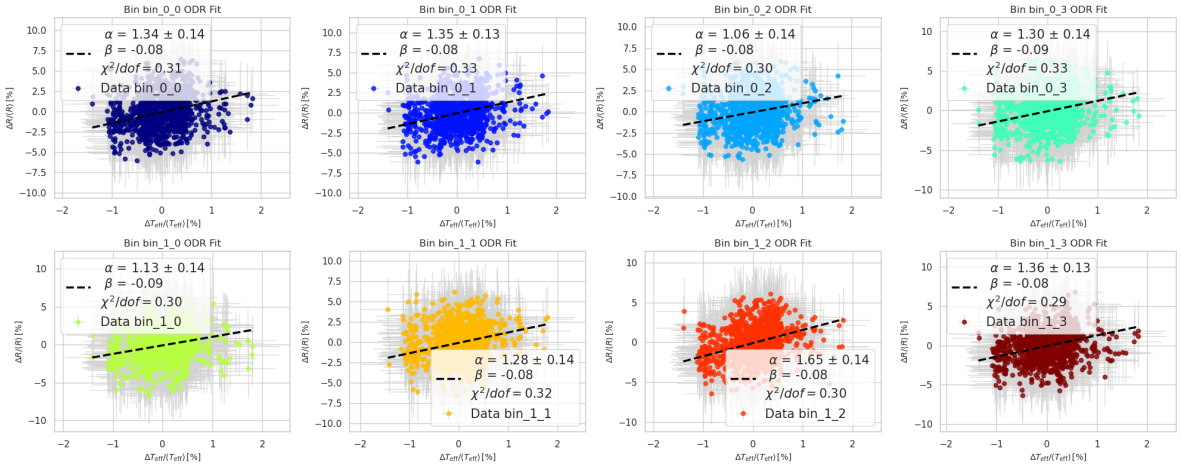

Figure A.149: Normalised effective temperature T_{eff} and ratio without detrending R_{data} of ORCA-18 showing the relative variation in percentage for each separate bin. The black line in each plot is a fit of the model in Equation 6.11 though the data of each bin separate. The errors are taken into account in the fit.

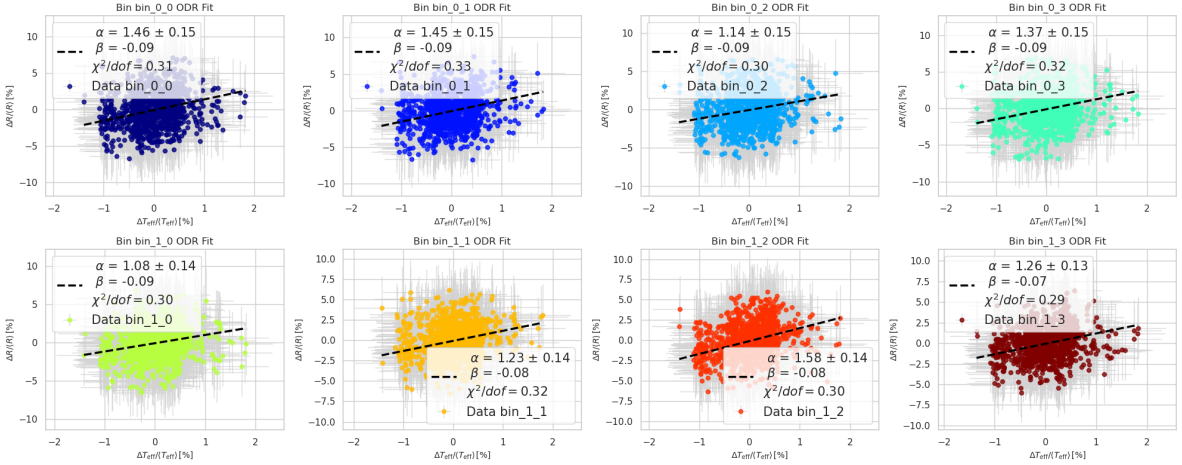

Figure A.150: Normalised effective temperature T_{eff} and ratio with detrending R_{data} of ORCA-18 showing the relative variation in percentage for each separate bin. The black line in each plot is a fit of the model in Equation 6.11 though the data of each bin separate. The errors are taken into account in the fit.

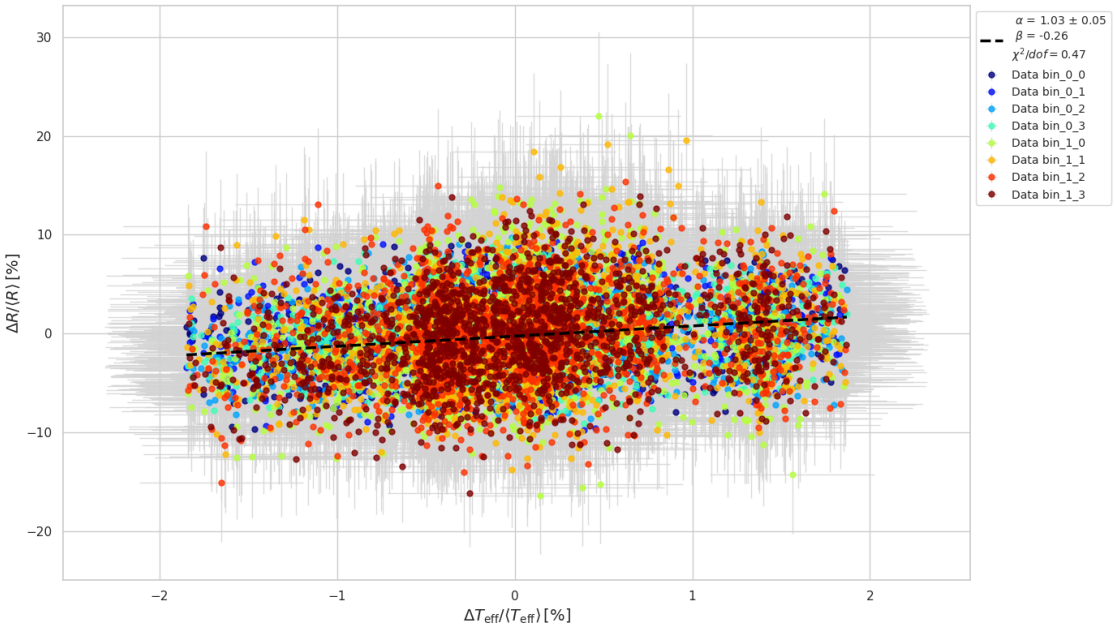

Figure A.151: Normalised effective temperature T_{eff} and ratio without detrending R_{data} of ARCA-21 showing the relative variation in percentage for each bin plotted together. The black line is a fit of the model in Equation 6.11 though all the data points combined. The errors are taken into account in the fit.

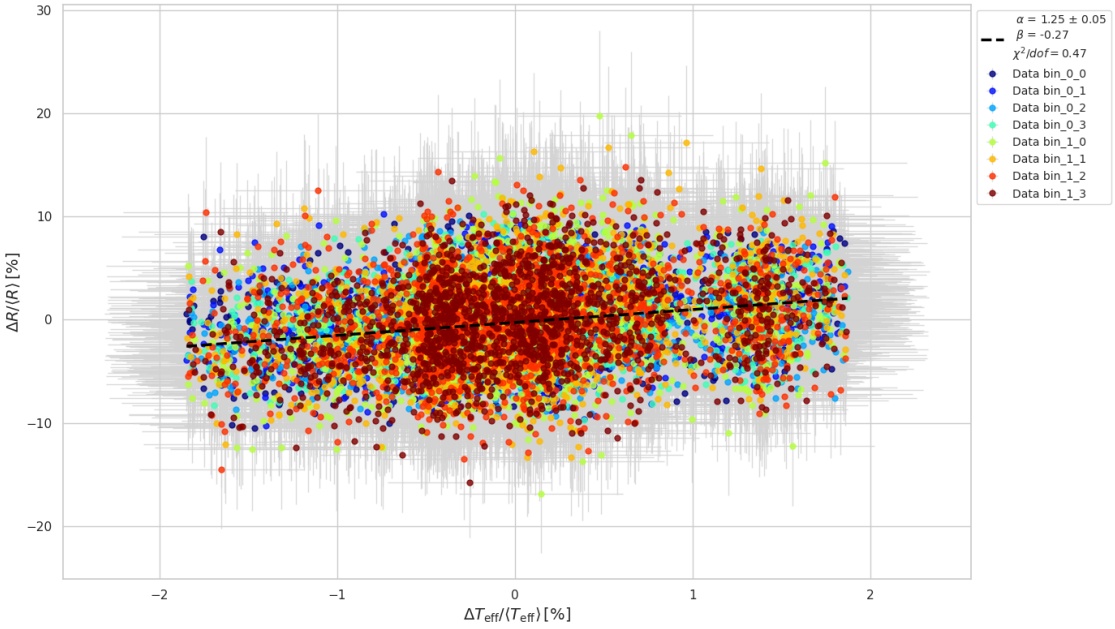

Figure A.152: Normalised effective temperature T_{eff} and ratio with detrending R_{data} of ARCA-21 showing the relative variation in percentage for each bin plotted together. The black line is a fit of the model in Equation 6.11 though all the data points combined. The errors are taken into account in the fit.

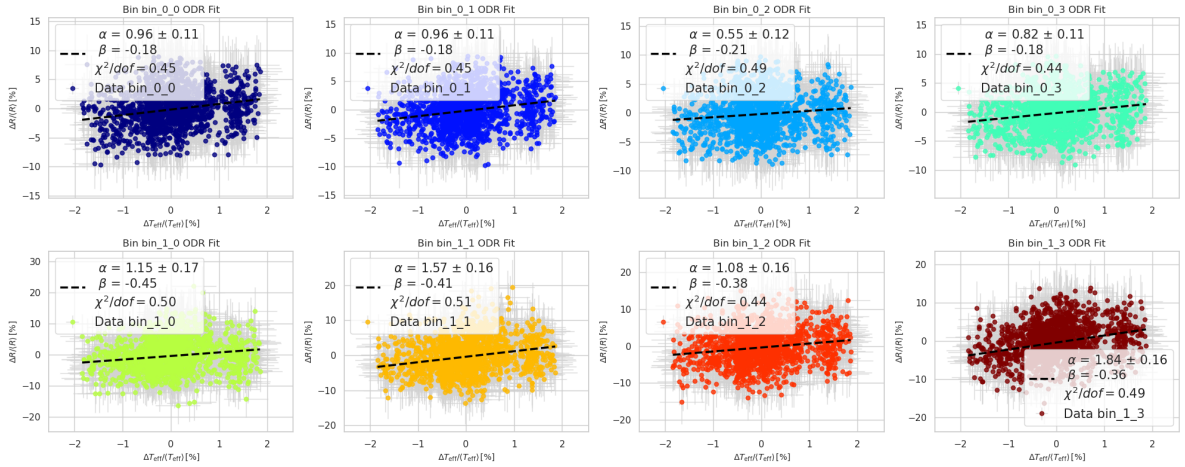

Figure A.153: Normalised effective temperature T_{eff} and ratio without detrending R_{data} of ARCA-21 showing the relative variation in percentage for each separate bin. The black line in each plot is a fit of the model in Equation 6.11 though the data of each bin separate. The errors are taken into account in the fit.

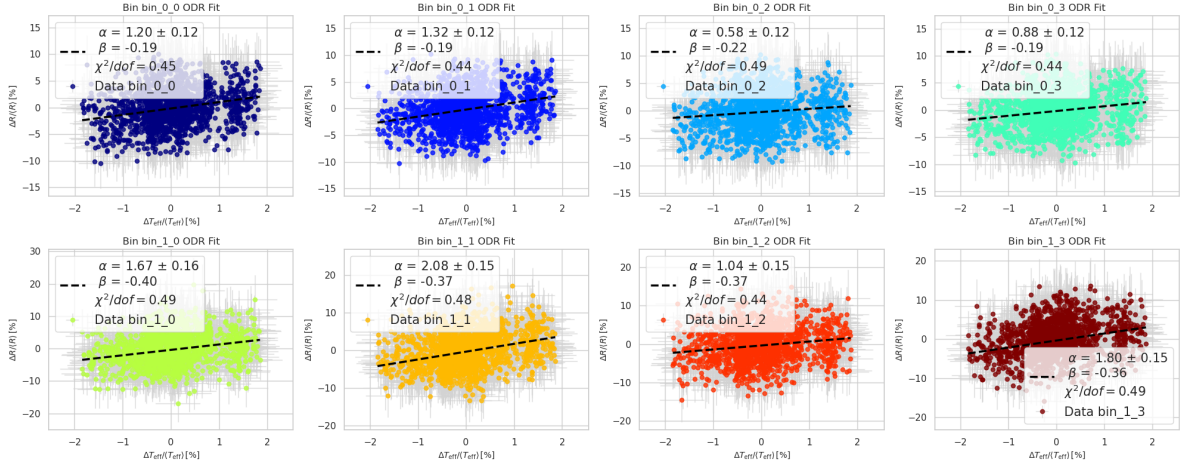

Figure A.154: Normalised effective temperature T_{eff} and ratio with detrending R_{data} of ARCA-21 showing the relative variation in percentage for each separate bin. The black line in each plot is a fit of the model in Equation 6.11 though the data of each bin separate. The errors are taken into account in the fit.